Delft University of Technology

Noise emissions and annoyance of sustainable aviation systems
Identifying noise sources and validating noise prediction models

von den Hoff, B.

DOI
10.4233/uuid:e97e1d99-11f0-46f3-9be9-2f8eeddde3bc

Publication date
2025

Document Version
Final published version

Citation (APA)
von den Hoff, B. (2025). *Noise emissions and annoyance of sustainable aviation systems: Identifying noise sources and validating noise prediction models*. [Dissertation (TU Delft), Delft University of Technology]. https://doi.org/10.4233/uuid:e97e1d99-11f0-46f3-9be9-2f8eeddde3bc

Important note
To cite this publication, please use the final published version (if applicable).
Please check the document version above.

Copyright
Other than for strictly personal use, it is not permitted to download, forward or distribute the text or part of it, without the consent of the author(s) and/or copyright holder(s), unless the work is under an open content license such as Creative Commons.

Takedown policy
Please contact us and provide details if you believe this document breaches copyrights.
We will remove access to the work immediately and investigate your claim.

This work is downloaded from Delft University of Technology.
For technical reasons the number of authors shown on this cover page is limited to a maximum of 10.

Noise emissions and annoyance of sustainable aviation systems

Identifying noise sources and validating noise prediction models

Bieke
von den Hoff

NOISE EMISSIONS AND ANNOYANCE OF SUSTAINABLE AVIATION SYSTEMS

IDENTIFYING NOISE SOURCES AND VALIDATING NOISE PREDICTION MODELS

NOISE EMISSIONS AND ANNOYANCE OF SUSTAINABLE AVIATION SYSTEMS

IDENTIFYING NOISE SOURCES AND VALIDATING NOISE PREDICTION MODELS

Dissertation

for the purpose of obtaining the degree of doctor
at Delft University of Technology,
by the authority of the Rector Magnificus Prof. dr. ir. T.H.J.J. van der Hagen,
chair of the Board for Doctorates,
to be defended publicly on
Wednesday 2 July 2025 at 12:30

by

Bieke VON DEN HOFF

Master of Science in Aerospace Engineering,
Delft University of Technology, Delft, the Netherlands,
born in Weert, the Netherlands.

This dissertation has been approved by the promotors:

Prof. dr. ir. M. Snellen
Em. Prof. dr. D.G. Simons

Composition of the doctoral committee:

Rector Magnificus,	chairperson
Prof. dr. ir. M. Snellen	Delft University of Technology, promotor
Em. Prof. dr. D.G. Simons	Delft University of Technology, promotor
Independent members:	
Prof. dr. ir. C.H. Venner	University of Twente
Prof. dr. ir. G.J.T. Leus	Delft University of Technology
Prof. dr. ir. P.M. Bluyssen	Delft University of Technology
Prof. dr. ir. J.M. Hoekstra	Delft University of Technology
Dr. ir. A. Amiri Simkooei	Delft University of Technology

Funding: First flow of funds.

Keywords: Phased Microphone Arrays, Beamforming, Acoustic Imaging, Aircraft Noise, Propeller Noise, Psychoacoustics.

Printed by: Proefschriftspecialist

Front & Back: Outline of the phased microphone array structure that was used in this dissertation.

Copyright © 2025 by B. von den Hoff

ISBN 978-94-6384-800-8

An electronic version of this dissertation is available at
http://repository.tudelft.nl/.

The scientist is not a person who gives the right answers;
he is one who asks the right questions.

Claude Levi-Strauss

Contents

Summary **xi**

Samenvatting **xiii**

1 Introduction **1**
- 1.1 The need for climate sustainable aviation . . . 2
- 1.2 Negative impact of aircraft noise . . . 3
- 1.3 Assessing aircraft noise . . . 4
- 1.4 Approaches to reducing aircraft noise . . . 5
- 1.5 Thesis objectives and outline . . . 6

2 An overview of aircraft noise sources **9**
- 2.1 Airframe noise . . . 11
  - 2.1.1 Landing gear . . . 12
  - 2.1.2 Wings . . . 13
  - 2.1.3 High-lift devices . . . 14
  - 2.1.4 Cavity noise . . . 15
- 2.2 Turbofan engine noise . . . 15
  - 2.2.1 Inlet noise . . . 16
  - 2.2.2 Core noise . . . 17
  - 2.2.3 Exhaust noise . . . 18
- 2.3 Propeller noise . . . 19
  - 2.3.1 Thickness noise . . . 20
  - 2.3.2 Loading noise . . . 21
  - 2.3.3 Broadband noise . . . 22
- 2.4 Installation noise . . . 23
- 2.5 Shielding of noise . . . 23

3 Methods to identify acoustic sources **25**
- 3.1 Microphone arrays . . . 26
  - 3.1.1 Microphones . . . 26
  - 3.1.2 Array lay-out . . . 28
  - 3.1.3 Data Acquisition System . . . 29
  - 3.1.4 Calibration of microphone arrays . . . 30
- 3.2 Acoustic imaging . . . 32
  - 3.2.1 Conventional Time Domain Beamforming . . . 33
  - 3.2.2 Rotating Source Identifier . . . 34
  - 3.2.3 Conventional Frequency Domain Beamforming . . . 36
  - 3.2.4 Improved source identification methods . . . 37
  - 3.2.5 Global Optimisation . . . 38

4 Sound quality aspects **41**
4.1 Critical bands . . . 43
4.2 Loudness . . . 43
4.3 Tonality . . . 44
4.4 Sharpness . . . 46
4.5 Roughness . . . 47
4.6 Fluctuation strength . . . 48
4.7 Impulsiveness . . . 49
4.8 Psychoacoustic Annoyance factor . . . 50
4.9 Considerations in psychoacoustic experimental design . . . 52

5 Assessment of Global Optimisation for source identification **55**
5.1 Introduction . . . 56
5.2 Experimental setup . . . 57
5.2.1 Choice of optimal DE settings . . . 58
5.3 Application on multi-source case . . . 59
5.3.1 Sources at same normal distance . . . 59
5.3.2 Sources at different normal distances . . . 61
5.3.3 Sources with different levels . . . 62
5.4 Energy function adaptations for complex source environments . . . 63
5.4.1 Energy function for broadband sources . . . 63
5.4.2 Energy function for asynchronous measurements . . . 63
5.5 Performance with respect to other imaging method . . . 65
5.6 Conclusions and outlook . . . 66

6 Noise emissions of taxibotted versus conventional taxiing operations **69**
6.1 Introduction . . . 70
6.2 Experiment setup . . . 70
6.3 Noise emission comparison of taxibotted and taxiing operations . . . 73
6.3.1 Comparison of taxibotted and conventional taxiing measurements . 73
6.3.2 Source identification on a taxibotted pass-by . . . 75
6.3.3 Source identification on a taxiing pass-by . . . 77
6.3.4 Noise source around the landing gear . . . 77
6.4 Impact of noise emissions on surroundings . . . 79
6.5 Conclusions and outlook . . . 79

7 Noise emissions and annoyance of the Skymaster for different propellers **81**
7.1 Introduction . . . 82
7.2 Measurement campaigns . . . 82
7.2.1 Ground measurements . . . 83
7.2.2 Flyover measurements . . . 85
7.3 Noise emission comparison of the 2-bladed and 3-bladed propellers . . . 86
7.3.1 Ground measurements . . . 87
7.3.2 Flyover measurements . . . 93
7.4 Noise annoyance comparison of the 2-bladed and 3-bladed propellers . . . 96
7.5 Conclusions and outlook . . . 100

8 Propeller noise model validation with in-flight noise measurements of a Pipistrel Velis Electro 103
8.1 Introduction . . . 104
8.2 Measurement campaigns . . . 105
8.2.1 Ground measurements . . . 105
8.2.2 Flyover measurements . . . 106
8.2.3 3D scans of propeller . . . 107
8.3 Decomposition of noise sources during ground measurements . . . 108
8.4 Validation of a tonal propeller noise prediction model . . . 110
8.4.1 Helix propeller noise model . . . 111
8.4.2 Validation of spectra at overhead position . . . 112
8.4.3 Polar directionality during flyover . . . 114
8.4.4 Influence of shaft angle of attack on noise predictions . . . 115
8.5 Conclusions and outlook . . . 117

9 Psychoacoustic annoyance of electric propeller aircraft 119
9.1 Introduction . . . 120
9.2 Characteristics of Pipistrel Velis and Virus . . . 120
9.3 Listening experiments . . . 123
9.3.1 Graphical user interface (GUI) . . . 123
9.3.2 Sound stimuli . . . 124
9.3.3 Participants . . . 124
9.3.4 Experimental procedure . . . 125
9.4 Conventional sound analysis . . . 125
9.5 Sound quality metrics of the flyovers . . . 126
9.6 Comparison of predicted with experienced annoyance . . . 129
9.7 Conclusions and outlook . . . 131

10 Conclusion and Outlook 133
10.1 Reflection on objectives . . . 134
10.2 Recommendations for future research . . . 138

A Acoustic characterisation of a listening room 141
A.1 Introduction . . . 142
A.2 Facility description . . . 143
A.2.1 Structural components and sound-absorbing elements . . . 143
A.2.2 Audio equipment description . . . 146
A.2.3 Audio equipment calibration . . . 147
A.2.4 Graphical User Interface and experimental procedure . . . 148
A.3 Acoustic characterisation . . . 151
A.3.1 Background noise levels . . . 151
A.3.2 Reverberation time . . . 152
A.3.3 Free-field propagation assessment . . . 154
A.3.4 Transmission loss of the walls . . . 155
A.3.5 Comparison with other listening laboratories . . . 157
A.4 Conclusions . . . 157

Bibliography **159**

Curriculum Vitæ **179**

List of publications **181**

Acknowledgements **183**

SUMMARY

Sustainable aviation is achieved when the negative impact of aviation on people, planet, and profit is minimised. Aviation impacts people through the noise it produces. Exposure to high noise levels for prolonged periods of time can lead to sleeping disorders, hypertension, and hearing issues. Therefore, the new generation of aircraft should be designed such that the noise emissions are reduced. Additionally, reducing noise annoyance is important as the human perception of aircraft noise is not only influenced by sound pressure levels.

Reducing the noise emissions and annoyance is only possible when the noise sources of an aircraft are known and can be predicted accurately during the design process. The objective of this dissertation is therefore to identify sources and validate aircraft noise prediction models that can be used for reducing noise emissions and noise annoyance in the design process. This is specifically applied to currently operational sustainable aviation systems.

The first step to improve design methods is to accurately identify the noise source. Acoustic imaging methods applied to phased microphone array data provide acoustic source maps indicating the location and spectrum of a specific source. The proposed global optimisation method was able to outperform conventional methods by identifying individual sources within a three-dimensional multi-source environment at half the Rayleigh resolution frequency. This method proved successful in a controlled environment with known sources in an anechoic room. The next step entails applying the method to identify noise sources in noisier environments and eventually apply it to commercial aircraft flyovers.

It is not always necessary to apply advanced acoustic imaging methods to study the noise emissions. One of the aviation systems studied through conventional beamforming and directionality assessment was the hybrid-electric taxiing robot TaxiBot. The aircraft engines can remain turned off during taxiing manoeuvres with the TaxiBot thereby reducing fuel emissions and noise emissions. Taxiing operations with the TaxiBot reduced the noise emissions up to 7 dB at the source during a pass-by, compared to conventional aircraft taxiing operations. This is especially valuable for ground workers on an airport.

The noise impact of aviation, however, reaches further outside the airport during take-off, landing, and low altitude flights. During these operations the noise emission of sustainable aircraft will be especially important and thus needs to be studied. Many proposed sustainable aircraft contain propeller-driven propulsion system. Therefore, the noise sources on two propeller-driven aircraft, i.e., the Cessna Skymaster and Pipistrel Velis, were analysed. These measurements showed that the propeller was the dominant noise source during flight. For the Cessna Skymaster the engine contributed to the noise at lower frequencies up to 300 Hz. Two acoustic imaging methods, conventional beamforming and rotating source identifier, were applied to separate the rotating

sources from the non-moving source during an engine run-up on the ground. This process was repeated for the Pipistrel Velis which lacks the engine noise source. However, the influence of ground recirculation as well as the potential presence of cyclostationary sources hampered a spectral decomposition.

The flyover measurements of the Pipistrel Velis were used to validate a tonal propeller noise prediction model based on Hanson's Helicoidal Surface Theory. These type of models are generally validated with measurements from a wind-tunnel experiment where only the propeller is present. In this case, the model is validated with a full-scale propeller at general operating conditions. The validation showed that the model was able to predict the first few tonal harmonics of the blade passing frequency well, but could be improved for higher harmonics by incorporating unsteady loading noise. The outputs of this prediction model should be auralised to simulate a flyover with a propeller aircraft and subsequently validated with listening experiments. When these steps will be performed, the model can give insight on the noise emissions and noise annoyance during the design process of a propeller aircraft.

As a last step the psychoacoustic annoyance of electric propeller-driven aircraft has been assessed. The predicted psychoacoustic annoyance indicated a 50% reduction of annoyance between the electric Pipistrel Velis and its combustion engine replacement. Listening experiments found that the electric version reduced annoyance by 30%. Especially the sound quality metrics roughness and loudness differed between the aircraft models. These results form a starting base to improve psychoacoustic annoyance models to better predict annoyance for propeller aircraft.

In conclusion, this research showed that propeller tonal noise predictions models are able to provide a first prediction of noise emissions for small propeller-driven aircraft. Additionally a starting point has been created for the assessment of propeller noise annoyance. In the future, these combined advancements can aid in designing aircraft for lower noise annoyance.

SAMENVATTING

Duurzame luchtvaart wordt bereikt wanneer de negatieve impact van de luchtvaart op mensen, de planeet en de winst wordt geminimaliseerd. De luchtvaart heeft invloed op mensen via het geluid dat het produceert. Blootstelling aan hoge geluidsniveaus gedurende langere tijd kan leiden tot slaapstoornissen, overspanning en gehoorproblemen. Daarom moet de nieuwe generatie vliegtuigen zo worden ontworpen dat de geluidsemissies worden verminderd. Bovendien is het belangrijk om geluidsoverlast te verminderen, omdat de menselijke perceptie van vliegtuiggeluid niet alleen wordt beïnvloed door geluidsdrukniveaus.

Het verminderen van geluidsemissies en -overlast is alleen mogelijk wanneer de geluidsbronnen van een vliegtuig bekend zijn en nauwkeurig kunnen worden voorspeld tijdens het ontwerpproces. Het doel van dit proefschrift is daarom om geluidsbronnen te identificeren en modellen voor geluidsvoorspellingen te verbeteren zodat in het ontwerpproces de geluidsemissies en geluidsoverlast verminderd kunnen worden. Dit wordt specifiek toegepast op actuele operationele duurzame luchtvaartsystemen.

Om ontwerpmethoden te kunnen verbeteren, moeten de geluidsbronnen nauwkeurig worden geïdentificeerd. Akoestische beeldvormingsmethoden die worden toegepast op drukmetingen van een opstelling van microfoons, leveren akoestische bronkaarten op die de locatie en het spectrum van een specifieke bron aangeven. De globale optimalisatiemethode die wordt gebruikt in dit proefschrift, was in staat om conventionele methoden te overtreffen door individuele bronnen te identificeren binnen een driedimensionale omgeving met meerdere bronnen. De bronnen werden geïdentificeerd tot de helft van de Rayleigh resolutie frequentie. Deze methode bleek succesvol in een gecontroleerde omgeving met bekende bronnen in een echovrije ruimte. De volgende stap omvat het toepassen van de methode om geluidsbronnen te identificeren in een omgeving met meer ruis, en de methode uiteindelijk toe te passen op geluidsmetingen aan commerciële vliegtuigen.

Het is niet altijd nodig om geavanceerde akoestische beeldvormingsmethoden toe te passen om de geluidsemissies te bestuderen. Een van de luchtvaartsystemen die bestudeerd werd door middel van conventionele beamforming en directionaliteitskaarten, was de hybride-elektrische taxirobot TaxiBot. De vliegtuigmotoren kunnen uitgeschakeld blijven tijdens taximanoeuvres met de TaxiBot, waardoor brandstofemissies en geluidsemissies worden verminderd. Taxiën met de TaxiBot verminderde de geluidsemissies met maximaal 7 dB bij de bron tijdens een pass-by, vergeleken met conventioneel taxiën. Deze geluidsreductie is met name waardevol voor grondwerkers op een luchthaven.

De geluidsimpact van de luchtvaart reikt echter verder dan de luchthaven tijdens het opstijgen, landen en vliegen op lage hoogte. Tijdens deze operaties zullen de geluidsemissies van duurzame vliegtuigen vooral belangrijk zijn en dus moeten deze worden bestudeerd. Veel voorgestelde duurzame vliegtuigen bevatten een propeller-aangedreven

voortstuwingssysteem. Daarom werden de geluidsbronnen op twee propeller-aangedreven vliegtuigen, namelijk de Cessna Skymaster en Pipistrel Velis, geanalyseerd. Deze metingen toonden aan dat de propeller de dominante geluidsbron was tijdens de vlucht. Voor de Cessna Skymaster droeg de motor bij aan het geluid bij lagere frequenties tot 300 Hz. Twee akoestische beeldvormingsmethoden, conventionele beamforming en roterende bronidentificatie, werden toegepast om de roterende bronnen te scheiden van de niet-bewegende bron tijdens een motorstart op de grond. Dit proces werd herhaald voor de Pipistrel Velis die de motorgeluidsbron mist. De invloed van grondrecirculatie en de mogelijke aanwezigheid van cyclostationaire bronnen belemmerden echter een spectrale ontleding.

De vlucht-metingen van de Pipistrel Velis werden gebruikt om een tonaal propeller geluidsvoorspellingsmodel te valideren op basis van *Hanson's Helicoidal Surface Theory*. Dit soort modellen worden over het algemeen gevalideerd met metingen van een windtunnelexperiment waarin alleen een propeller gemeten wordt. In deze dissertatie wordt het model gevalideerd met een propeller op ware grootte onder realistische operationele omstandigheden. De validatie toonde aan dat het model de eerste harmonische tonen van de *blade passing frequency* goed kon voorspellen, maar verbeterd kon worden voor hogere harmonische tonen door instabiele blad belasting mee te nemen in het model. De uitkomsten van dit voorspellingsmodel moeten geauraliseerd worden om een vlucht met een propellervliegtuig te simuleren en die auralisatie kan vervolgens gevalideerd worden met luisterexperimenten. Wanneer deze stappen zijn uitgevoerd, kan het model inzicht geven in de geluidsemissies en geluidshinder tijdens het ontwerpproces van een propellervliegtuig.

Als laatste stap is de psychoakoestische hinder van een elektrisch propellervliegtuig beoordeeld. De voorspelde psychoakoestische hinder gaf een vermindering van 50% van de hinder aan tussen de elektrische Pipistrel Velis en het vergelijkbare model met verbrandingsmotor. Luisterexperimenten toonden aan dat de elektrische versie de hinder met 30% verminderde. Vooral de geluidskwaliteitsmetrieken ruwheid en luidheid verschilden tussen de vliegtuigmodellen. Deze resultaten vormen een startpunt om psychoakoestische hindermodellen te verbeteren om hinder voor propellervliegtuigen beter te voorspellen.

Dit onderzoek toonde aan dat tonale geluidsvoorspellingsmodellen voor propellers in staat zijn om een eerste voorspelling te doen van geluidsemissies voor kleine propellervliegtuigen. Daarnaast is er een startpunt gecreëerd voor de beoordeling van propeller geluidshinder. In de toekomst kunnen deze gecombineerde punten helpen om vliegtuigen te ontwerpen met een lagere geluidshinder.

NOMENCLATURE

Symbols (Greek)

α	Shaft angle of attack (non-axial inflow angle)
α_w	Weighted absorption
$\boldsymbol{\xi}_j$	Grid/source map coordinate of source j
Δf	Frequency resolution
$\Delta t_{j,n}$	Propagation delay from source j to microphone n
Ω	Angular velocity
ϕ	Phase shift
ϕ_0	Phase lag blade offset
ϕ_a	Source azimuthal angle
ϕ_s	Sweep phase
Ψ_V	Chordwise loading distribution
σ	Standard deviation
θ	Polar/observer angle or blade azimuth

Symbols (Latin)

$\boldsymbol{d}$	Descendant population member
$\boldsymbol{m}$	Original population member
$\boldsymbol{s}$	Partner population member
$\boldsymbol{x}(x, y, z)$	Cartesian coordinates
SPL	Sound pressure level
B	Number of blades
C	Aerodynamic coefficient
c	Speed of sound
C_{meas}	Measured cross-spectral matrix

C_{mod}	Modelled cross-spectral matrix
D	Propeller diameter
D_{array}	Array aperture
E_{CSM}	Energy function based on CSM
F	Differential evolution mutation factor
f	Frequency
FS	Fluctuation strength
g	Steering vector component
I	Impulsiveness
J	Advance ratio
J_{mB}	Bessel function for m^{th} harmonic and B blades
k'	Time sample
K	Tonality metric
k_x	Wavenumber
K_{src}	Number of sources
L_p	Sound pressure level
M	Mach number
N	Loudness
N_{forward}	Number of forward computations
N_{gen}	Number of generations in optimization
N_{mic}	Number of microphones
N_{runs}	Number of optimization runs
P	Spectral components of sound pressure
p	Sound pressure amplitude
p_c	Crossover probability in DE
p_{ref}	Reference pressure
PA	Psychoacoustic annoyance
q	Population size in DE

R	Roughness
r	Radius
R_{Rayleigh}	Rayleigh spatial resolution limit
s'	Blade loading harmonic
S	Sharpness
s	Source power
T	Thrust
t	Time
t_b	Blade thickness
V	Free-stream or flight velocity
w_I	Weighting factor for impulsiveness
w_S	Weighting factor for sharpness and loudness
w_T	Weighting factor for tonality
w_{FR}	Weighting factor for fluctuation strength and roughness
z_C	Critical band

Superscripts

*	Complex conjugate transpose

Subscripts

0	Ambient or baseline condition
5	5th percentile (as in N_5, K_5, S_5)
γ	Generation index
∞	Free-stream or far-field condition
c	Centre
D	Drag-related value
j	Source/grid index
L	Lift-related value
m	Harmonic index
n	Microphone index

r	Radial section index
t	Blade tip
u	Search parameter index

Acronyms

ADC	Analogue-to-Digital Converter
BPF	Blade Passing Frequency
CBW	Critical Bandwidth
CFDB	Conventional Frequency Domain Beamforming
CSM	Cross-Spectral Matrix
CTDB	Conventional Time Domain Beamforming
DAS	Data Acquisition System
DE	Differential Evolution
FPGA	Field Programmable Gate Array
GO	Global Optimisation
HLD	High Lift Device
JND	Just Noticeable Difference
LG	Landing Gear
OSPL	Overall Sound Pressure Level
PALILA	PsychoAcoustic Listening Laboratory
PCB	Printed Circuit Board
PSF	Point Spread Function
ROSI	Rotating Source Identifier
SQM	Sound Quality Metric
TL	Transmission Loss

1

Introduction

We want the air to unite the peoples,
and not to divide them.

Philip Cunliffe-Lister, 1st Earl of Swinton

Aviation is facing two large sustainability challenges: reducing climate emissions and reducing noise emissions. There are different approaches to making aviation more climate sustainable; however, for an approach to be truly successful and sustainable, it needs to be societally sustainable as well. This means that the impact on the society needs to be limited, especially for airport neighbourhoods which are suffering from reduced air quality and increased noise annoyance. This research thus focuses on the impact of sustainable aviation on noise annoyance. This introduction chapter first explains the need for sustainable aviation and links it to the impact of noise annoyance through reduced wellbeing. After establishing the relevance of both subjects and linking them, a brief overview on how to assess aircraft sound is provided. Based on that, potential noise reduction strategies are discussed. Lastly, the thesis objectives and outline are presented.

Aviation is at the intersection of what the World Health Organisation (WHO) considers the two worst forms of environmental pollution for the European region: air pollution and noise pollution [1–4]. Air pollution is mainly caused by burning fossil fuels, which not only influences local air quality but also the global climate, with loss of healthy life years as a main human consequence. Noise pollution has the same consequence, with an estimated Disability-Adjusted Life Years (DALYs) of 15,100 to 35,800 in 2017 due to aviation alone [5]. Fundamentally addressing the impact of aviation will require new aircraft designs that are truly sustainable.

1.1. THE NEED FOR CLIMATE SUSTAINABLE AVIATION

There is a clear need for sustainable aircraft from the climate impact perspective as aviation contributes 3% to 5% to total anthropogenic climate impact, which considers CO_2 and non-CO_2 effects [6–8], and this percentage is expected to grow for two main reasons. Firstly, other sectors are reducing their climate impact at a high pace, meaning that a standstill in aviation would increase the share. Secondly, emerging economies are predicted to have a strong growth in aviation. The opportunity and choice for flying are mostly linked to the economic position of a country and its inhabitants [9, 10]. Since the financial position of inhabitants in developing countries like India and China improved recently, more people are able to afford flying rather than the 10% currently [11, 12]. Hence even if a standstill in growth in Western countries would occur, the aviation sector and its climate impact as a whole still grows.

Recently, some movements have been calling for a reduction in aviation due to the emissions and impact of a single flight [13]. Regulatory bodies are becoming increasingly sensitive to this reasoning and are looking at reducing aviation's impact for example by restraining airports and increasing the cost of flight tickets. However, this might disproportionately impact previously under-served communities. They have yet to benefit from the potential economical and cultural benefits of flying and restricting aviation would reduce their chances. Besides that, curtailing aviation would reduce the possibility to globally connect people and cultures which can aid in improving social cohesion and reduce cultural tensions which have been recently on the rise [14]. Thus, the large sum that is invested in making aviation more climate sustainable [9, 15] could be a fairer solution than curtailing aviation.

However, climate impact is not the only driver of sustainability. For something to be truly sustainable, it must be bearable, viable, and equitable to become successful as is explained by the Venn diagram on sustainability in Figure 1.1. Currently the focus of the aviation sector is on profit with some attention being paid to planet, but the impact on people in terms of health, wellbeing, and quality of life receives less focus. Aircraft noise and climate emissions will have an impact on health and hence influence the people-part of sustainability according to the Venn diagram.

Thus, there is a strong need for sustainable aviation in terms of reducing climate impact and addressing the planet-part of sustainability, while also checking the box of profit in the Venn diagram. Yet, simultaneously the people-part should not be neglected, and in specific the impact of noise on health and well-being.

Figure 1.1: Venn diagram outlining the key considerations for sustainability [16].

1.2. NEGATIVE IMPACT OF AIRCRAFT NOISE

Aircraft noise is described as noise, and not sound, due to the negative connotation humans have with it. In order to better understand why some sounds are considered annoying, i.e., noise, a field called psychoacoustics has been developed that looks at a range of characteristics of sound beyond pressure levels and decibels. This field links acoustics to psychological human perception and helps to understand why two sound sources that have the same overall sound level can be perceived very differently, in the most extreme case one as annoying and one as pleasant [17, 18]. This difference is caused by sound characteristics such as the perception of loudness, presence of strong tones, and presence of high frequency sound [19–22].

Besides these psychological stimuli, sound can trigger a physiological reaction such as increased adrenaline levels because it may signal danger. These reactions have severe negative effects on physical and mental health and wellbeing. According to studies noise annoyance can cause sleeping disorders, hypertension, decreased performance, hearing issues, and ultimately cardiovascular diseases through the stress mechanism [4, 23, 24]. There are even studies that link high aircraft noise exposure to impaired cognitive development in children [25]. Simultaneously, studies are showing that the cost of lost healthy life years are substantial to society [5, 26]. This does not even include the depreciation of property such as housing around major airports, which is an additional stress factor for the community [27].

This detrimental effect of noise is already a point of concern for the current fleet of aircraft, which is dominated by medium-haul, tube-and-wing, narrow-bodies such as the B737-series or A320 as depicted in Figure 1.2a. Some aircraft in the current fleet however have engines installed over the wing like the Fokker 70 in Figure 1.2b, which reduces the observed engine noise [28], but not sufficiently so. Therefore, regulatory bodies such as EASA, ICAO, and WHO are providing ever more stringent guidelines and

regulations to reduce the emitted noise levels for every generation of aircraft [29].

The next generation of aircraft is focused on reducing climate impact with a different design. Often, this leads to designs with propellers as they are found to be more (fuel) efficient on short- or medium-haul distances at low speeds [30, 31]. These designs commonly have propeller-driven electric engines or hydrogen-burning turboprops [32], which can be located in a single spot as with the Pipistrel in Figure 1.2c or distributed over the wing span such as the render of DLR in Figure 1.2d. However, there are worries of the noise impact for these newer designs as propellers cause significant noise annoyance [33, 34]. While there are some studies investigating if an electric aircraft produces less noise than a similar piston-engine aircraft [35, 36], there is still more research needed for the propeller as source of noise emission and annoyance. Thus in order for this next generation of aircraft to be considered truly sustainable, their noise annoyance should be effectively addressed. Therefore it is essential to understand the potential noise sources first.

(a) Conventional tube-and-wing aircraft [37]

(b) Fokker 70, Engine placement over the wing [38]

(c) Pipistrel Velis Electro [39]

(d) Distributed propulsion [40]

Figure 1.2: Different aircraft configurations.

1.3. ASSESSING AIRCRAFT NOISE

The negative impacts due to excessive noise, can only be addressed if the sources of the noise are known. There are several methods to characterise and identify the noise source of an aircraft which can be roughly grouped in experimental methods and numerical models [41].

Experimental methods include microphone measurements of a scale or full-size ob-

ject, measured in a wind-tunnel or in field measurements. The advantage of wind-tunnel measurements is the high degree of control over the experiment. Several conditions can be tested and repeated, there is a controlled flow, and all model parameters are known. However, it is not possible to test a full-size aircraft in a wind-tunnel thereby introducing scaling issues on top of lacking installation effects, such as wake impingement on the structure, and other effects, such as engine noise shielding by the wing.

Experimental measurements in the field, around an airport, have the benefit of capturing interaction and full-scale effects [42] as they are based on real-life operational conditions. Thus, the human perception of aircraft noise is most reliably caught by field measurements. The drawback in field experiments is however the difficulty of controlling the conditions of the experiment, the increased distance between the microphone and the source, and inaccuracies introduced by the environment (e.g. wind, rain, background noise). It also proved difficult to retrieve accurate data on the flight path and some geometrical and engine parameters of the aircraft [43].

Numerical models can be used when an experimental measurement is not feasible, for example in the design phase before the prototype is built. These numerical models vary significantly in level of detail and computational expense. The most accurate prediction can be done through simulations with Computational AeroAcoustics, which models the sound generation mechanism based on aerodynamics and the sound propagation mechanism based on the acoustic wave equation [44]. While these methods are highly accurate and can provide in-depth details about the source generation, they are computationally expensive as it is time consuming to resolve the entire flow field [41].

Typically, these computational simulations and experimental test are too time expensive to be used during the design process for aircraft, meaning that cheaper models should be used to predict noise. The noise prediction models (1) can be fully based on previous empirical data without design parameters, or (2) can include some design parameters of the major noise sources, or (3) can include a parametric model of each source [45]. The fully empirical models (best-practice models) are not considered here, as they are only able to determine the overall noise level of existing aircraft and are not able to reflect on design choices or individual sources [46]. The same reasoning holds for category 2 where often only a split between airframe and engine spectra is made. This leaves semi-empirical models such as PANAM [47], sonAIR [48], or ANOPP [49] which are based on noise predictions for individual components. These models can be used to design for lower noise emissions, but unfortunately they are often not fully validated [42]. A potential consequence to not having validated models is the risk of having a final design that does not meet the requirements and regulations. This would mean a delay in the introduction of much needed truly sustainable aircraft.

1.4. APPROACHES TO REDUCING AIRCRAFT NOISE

The impact of perceived aircraft noise can be reduced by emitting less noise or by reducing the propagation of noise. The corresponding measures are typically divided into operational methods, receiver-based methods, and source-based methods.

Operational methods reduce the perceived noise through scheduling and route alterations. On the scheduling side, night curfews would be an option, as well as planning carefully when aircraft with a large noise footprint take off. It might be worthwhile to in-

vestigate if it is better to have one single loud event really standing out, or have the loud event be partially masked within multiple flyovers. Routing alterations are also possible. Some airports are already testing continuous descent approaches and avoiding densely populated areas [50]. These methods can be implemented in the short term, but are dependent on weather conditions and air traffic control options. Additionally, rerouting could increase the fuel consumption and thus negatively impact local air quality and the global climate.

Receiver-based methods mostly include alterations in the urban landscape or on buildings [51]. For example, special window glazing exists that dampens the vibrations and noise. DeNoize even is developing anti-noise windows [52]. Another option for the built environment would be to change the facade design such that it scatters noise in all directions or such that it reflects less noise. Additionally, special landscaping that acts as sound barriers can be applied [53]. These methods provide relief, but the effect can change drastically when moving from inside to outside, or to a different part of the surroundings where the noise source is directly audible.

Source-based methods are particularly useful because they provide a uniform reduction in noise for everyone in the surrounding area. Several retrofit options for engines exist already, such as installing engines with acoustic liners to reduce tonality or adding chevrons to the exhaust to reduce jet mixing noise [54]. As engine noise was reduced tremendously over the past years, airframe noise became more important, in particular during landing [42, 45]. Airframe sources are mostly based on flow-object interaction or installation effects. To reduce these sources slat covers, porous trailing-edge inserts, and landing bay covers amongst others have been suggested. Apart from retrofits, an option for new designs would be to provide shielding of the main sources by placing a noise barrier between the source and observer for example by placing the engines over the wing [55]. However, these design changes to the aircraft require more implementation time as the design, testing, and certification of aircraft can easily take years.

For all these options there are two important take-aways. Firstly, it is important to focus on treating the most annoying noise source, which is not necessarily the loudest noise source, as this will have the largest impact on well-being. Therefore, it is important to perform psychoacoustic annoyance research. Secondly, treating the source is typically the most effective solution to reduce noise levels as it is independent of propagation effects. Source reduction is also the most fair solution as it reduces the impact for all receivers equally, regardless of their position under the route or distance to noise barriers.

1.5. THESIS OBJECTIVES AND OUTLINE

The previous sections show that there is a strong need for sustainable aviation, rather sooner than later. Yet, future generation aircraft will only be accepted by society if the perceived noise annoyance is deemed acceptable. Annoyance goes beyond the pure physics of noise, into the subjective perception of sound by human hearing, and therefore is more important to reduce than just a decibel level.

The most efficient way to reduce noise annoyance of future (sustainable) aircraft is to use noise prediction models during the design phase and design for lower noise annoyance. However, these models still need to be validated and extended with psychoa-

coustic metrics, rather than only noise emission predictions. Understanding and validating prediction models can best be done with measurements on full-scale operational aircraft, from which a source of interest is isolated. These measurements can then be used for psychoacoustic tests in listening rooms. The combination of these research gaps (noise of sustainable aviation and psychoacoustic noise levels) leads to this thesis' objective: *to identify noise sources and validate noise prediction models to improve the assessment of noise emissions and annoyance in sustainable aviation systems.* The main objective has been divided into four sub-objectives that have been researched in consecutive order:

1. Improve acoustic imaging methods to identify in three-dimensional space, the location and level of a noise source.

2. Use acoustic imaging methods on microphone array measurements of sustainable aviation systems during normal operations to identify their noise sources.

3. Use the identified noise sources of propellers to validate a propeller noise prediction model.

4. Perform listening experiments with the noise measurements to assess the psychoacoustic annoyance of electric propeller aircraft.

The outcome of the last step provides the base for future research which should incorporate the prediction of annoyance and sound quality metrics into noise prediction models. The procedure is presented in Figure 1.3, in several ways. First, the blue activities present the activities needed to achieve the sub-objectives. Secondly, the information inputs and subsequent outputs of the blocks are presented, above and below respectively. Thirdly, there are trends visible in the outline: (1) from global noise level to a source level, (2) from present day aircraft to future aircraft, and (3) from only levels to a full source description.

This dissertation is structured according to the outline and the consecutive research objectives. However, the thesis starts by providing the reader with the necessary background information in three theory chapters, the first of which describes potential aircraft noise sources in Chapter 2. These noise sources can be identified in overall amplitude, frequency spectrum, and location with acoustic imaging methods that are applied to microphone arrays. The background on microphone arrays and imaging methods can be found in Chapter 3. Each noise source also has a certain psychoacoustic characterisation, which is composed of its sound quality metrics. The sound quality metrics are treated in Chapter 4.

Chapter 5 addresses Objective 1 where the application of Global Optimisation as a source identification method is discussed. The method has been applied to a controlled measurement for which three broadband noise sources, scattered in three dimensions, were recorded in an anechoic room.

Objective 2 is covered in Chapters 6, 7, and 8 by applying methods from Chapter 3 to three different systems, respectively the TaxiBot, Skymaster, and Pipistrel Velis. Chapter 6 compares the noise sources and noise emissions of taxiing with a hybrid-electric taxiing robot versus conventional taxiing on aircraft engines. Chapter 7 investigates the

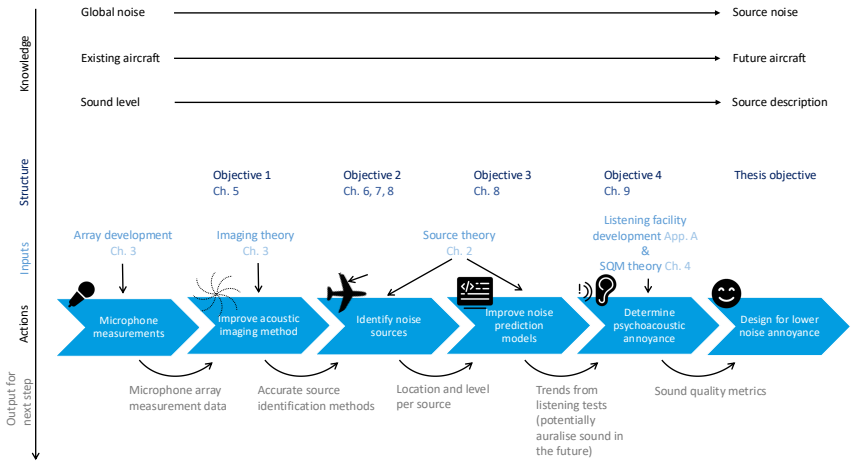

Figure 1.3: Necessary research steps from microphone measurements to lower noise annoyance.

noise sources and emissions of a fuel-engine propeller aircraft, the Cessna Skymaster. Chapter 8 investigates the noise sources and emissions of an electric-engine propeller aircraft. The chapters focusing on propeller aircraft aim to provide a method to separate propeller and engine noise sources. This separation can be helpful to perform Objective 3 which is a validation of the propeller tonal noise prediction model Helix. The validation is also covered in Chapter 8 as the Pipistrel Velis source assessment is used directly for the model validation and hence the information is best kept together.

The noise measurements of the electric Pipistrel Velis and its combustion engine counterpart (Pipistrel Virus) were used for listening experiments in the psychoacoustic listening facility to fulfil Objective 4. Chapter 9 analyses these experiments on sound quality metrics and the perceived annoyance versus the predicted annoyance.

Finally, Chapter 10 provides a conclusion which reflects on the main research objective and proposes future work based on the findings of this thesis.

The chapters are based on papers by the author as presented on conferences or in journals. However, the theory and methodology have been extracted and bundled in Chapters 2, 3, and 4 to avoid repeating the same theory and methodology in each chapter.

2

An overview of aircraft noise sources

Big whirls have little whirls,
That feed on their velocity;
And little whirls have lesser whirls,
And so on to viscosity.

Lewis Fry Richardson

This chapter describes all noise sources that could be present on an aircraft. It starts with describing the most common airframe noise sources which aircraft have irrespective of their propulsion method. It then progresses to engine noise, including the inner workings of a turbofan engine and the noise of a propfan. As a side-effect of the installation of the propulsion system on the airframe, several interaction noise sources are formed which increase the noise emission. The placement of the propulsion system can however be optimised to reduce perceived noise through shielding. For all types of sources, the sound generation mechanism, the typical frequency range, and directionality are described.

The main aircraft components that can generate noise are indicated in Figure 2.1. The source mechanisms of each of these components will be explained in this chapter. In Figure 2.1 the aircraft is configured with turbofan engines, but this chapter also includes an explanation for the noise of turboprop engines. In general the noise sources of the propulsion system are: fan (or propeller) noise, combustion noise, compressor and turbine noise, and exhaust jet noise [49]. For turboprops the exiting speed of the jet is far lower than for turbofans, thus making the contribution of the fan more relevant with respect to jet noise.

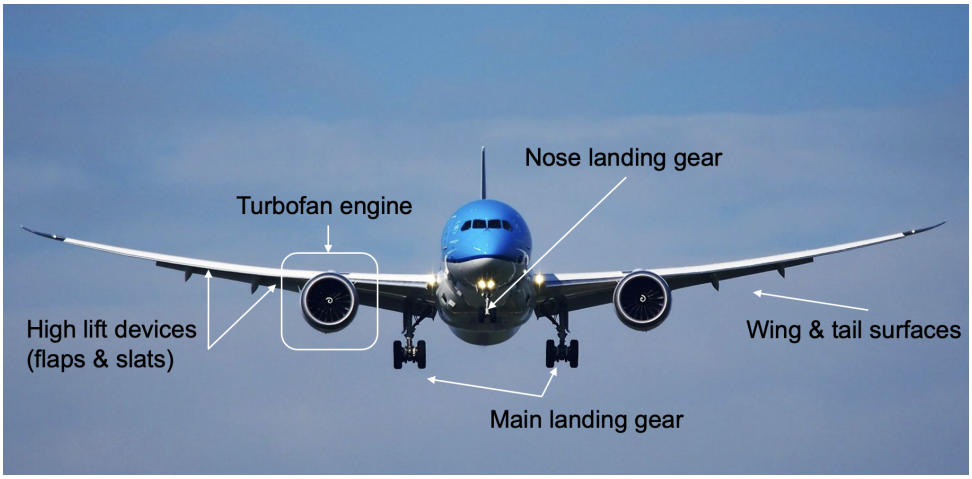

Figure 2.1: Noise sources on an aircraft during approach. Airframe sources are red, engine sources are blue.

Whether a noise source is perceived as dominant, depends on the flight phase with corresponding operational conditions and the angle between the observer and the aircraft. The flight phases are split in take-off, cruise, and landing. In this dissertation the cruise phase is not covered as sound propagated from such high altitudes results in on-ground noise levels below background noise levels.

To understand the noise levels of different aircraft components during different flight phases, Figure 2.2 shows Overall Sound Pressure Level (OSPL) for a modelled A320 with CFM56-5B4 engines at overhead position for a take-off and a landing. The simulation parameters are based on operational conditions as measured at Schiphol Amsterdam Airport and reported in Vieira et al. [42]. The overhead position is defined as polar angle $\theta = 90°$, which is the angle between an aircraft and a receiver, while the azimuthal or sideline angle ϕ_a equals 0° [56]. See also Figure 2.3 for the definition of ϕ_a and θ.

Figure 2.2 shows that the main difference between landing and take-off is the lower noise levels for all engine components in landing when the engine is turning idle. The airframe noise level is comparable for both operations, but the composition of noise is very different. During take-off, the main contributors are the deployed high-lift devices (HLD), i.e., slats and flaps. Yet, during landing the landing gear (LG) reach similar levels as the HLD.

It is interesting to see that most of the airframe noise in take-off is produced by the

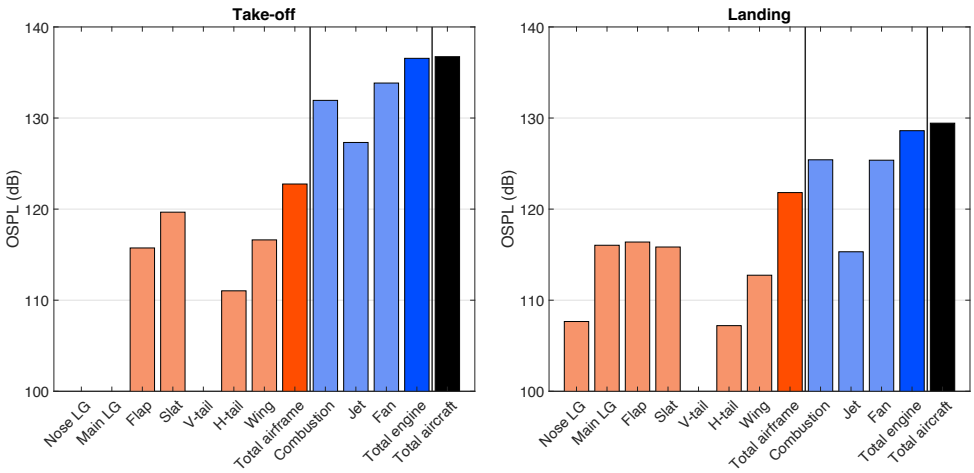

Figure 2.2: Typical OSPL per noise source on a simulated A320 with CFM56-5B4, predicted with the model ANOPP. The simulation parameters are based on operational conditions as measured at Schiphol Amsterdam Airport and reported in [42].

HLD. These airframe sources will have an increased importance in the future as during the past decades attention has been focused on making jet engines more silent [57]. Noise reductions on the engines will lead to an increased relative importance for airframe noise, especially during landing when the engines turn idle and thus are even more silent. Additionally, aircraft fly at a lower altitude during landing for an extended distance compared to take-off operations, thus resulting in higher ground levels thereby substantiating the need for airframe noise reduction.

2.1. AIRFRAME NOISE

Airframe noise is generated through the interaction of the airflow with the different structural components on the aircraft [45]. These noise generation mechanisms are related to turbulent boundary layers, turbulent wake interaction, or vortex shedding from bluff bodies. In this section, the noise generation mechanism, the source directionality (also named directivity), and the most influential source parameters are explained. Semi-empirical noise prediction models are not explained here, but the interested reader is referred to PANAM, ANOPP, FLULA, and IESTA [47, 49, 58, 59].

The directivity is the non-uniform sound level around a sphere for which three fundamental shapes are identified, being the monopole, dipole, and quadrupole [60, 61]. The cardioid shape occurs often and is thus also described here. Most of the sound sources can be described as a combination of these fundamental directivity shapes. Examples of these shapes are included in Figure 2.4. A monopole source occurs when mass is introduced or removed from a certain parcel of space. The dipole is caused by force variations in time or in location in a certain space. The quadrupole is generated through velocity fluctuations on the parcel. The monopole is the most efficient sound radiator, while a quadrupole radiates least efficient [62, 63].

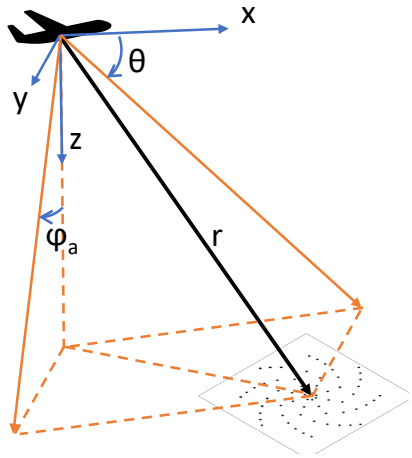

Figure 2.3: Flight path angles ϕ_a and θ with respect to a receiver position [42].

The following sections will make use of these definitions to describe the directionality of individual components. The axis of the dipole is the line joining the positive and negative source, i.e., from 0° to 180°. For the cardioid shape the axis is defined the same as for the dipole, thus running through 0° and 180°. The cardioid shape occurs when a source is acoustically non-compact, meaning the size of the eddies is smaller than the object, for example at high acoustic frequencies or for large objects, in which case the eddies interact with only a part of the object causing local pressure fluctuations [61].

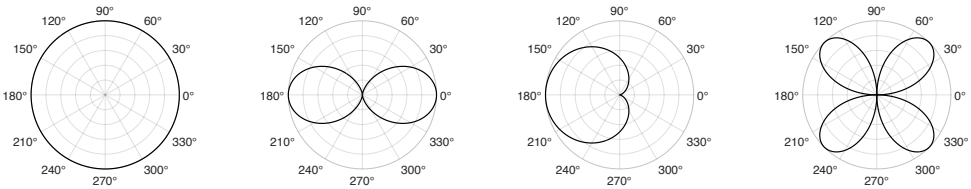

(a) Monopole
p^2 independent of θ

(b) Dipole
$p^2 \propto \cos^2\theta$

(c) Cardioid
$p^2 \propto \sin^2\theta/2$

(d) Quadrupole
$p^2 \propto \sin^2 2\theta$

Figure 2.4: Directionality shapes of some basic polar patterns.

2.1.1. LANDING GEAR

The bluff body of the wheels of the landing gear as well as the rod causes turbulent flow separation and vortex shedding, and this turbulent wake impinges on other airframe parts downstream [64]. The small struts of the landing gear also cause periodic vortex shedding and due to the different sizes this combines to broadband noise, yet this source is small compared to the noise of the wheels and rod [65]. The pin holes act as cavities and create tonal noise when the grazing turbulent flow excites the resonance in the cavity [66]. Recently, some Airbus aircraft have been found to exhibit strong tonal peaks at

the nose main landing gear, which could require a revision of the relative importance of sources [67].

Generally, semi-empirical noise models take into account the vortex shedding only and not the noise sources created by the cavities [47, 68]. Thus, dimensions of the LG such as wheel diameter, strut length, number of wheels, and fairing are relevant. The models also include a velocity term, as the aerodynamic noise scales with V^6 [64]. For the nose LG the impinging flow velocity is the free-stream velocity, however for the main LG the flow recirculates under the wing, which reduces the impinging flow velocity and thus can lead to reductions in noise levels [45].

As the wake vortex dynamics cause unsteady lift forces on the components, the radiated pattern in polar directivity behaves as a dipole, with the axis perpendicular to the inflow velocity vector [69, 70]. In the azimuthal direction, the landing gear noise source is often modelled as a monopole. The struts do not contribute to total noise levels directly under the aircraft where the sideline angle is zero [68]. The sideline angle defines the maximum contribution of the struts to 90° angles, i.e., the dipole main axis is perpendicular to the inflow and the strut axis. Yet, the total directivity of the landing gear was experimentally found to be almost omnidirectional for some aircraft types [65, 71].

2.1.2. WINGS

Airfoil noise sources can be divided into different generation mechanisms as shown in Figure 2.5, being turbulent trailing edge noise, trailing edge bluntness noise, separation or stall noise, tip noise, and laminar boundary layer instability noise [72]. Only turbulent trailing edge noise is taken into account for this dissertation.

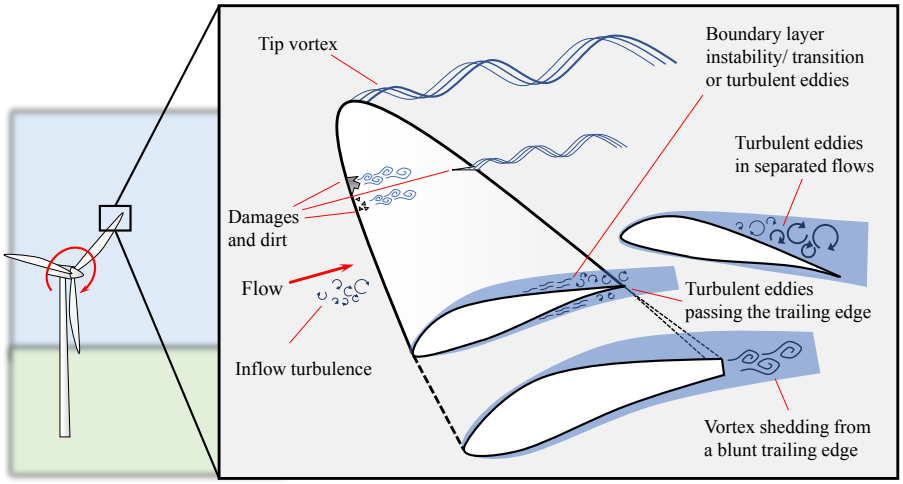

Figure 2.5: Airfoil noise sources schematic [73].

Clean surfaces such as the wings or horizontal tail surfaces, but also the vertical tail, generate noise as the turbulent flow which developed over the surface in the boundary layer is convected over the trailing edge. This sudden acoustic impedance change creates

scattering of broadband noise to the far-field [1]. While this noise is of turbulent nature, its directivity is not quadrupole-like as turbulence close to a surface or sharp edge behaves like a dipole due to the fluctuating lift force it imposes on the wing [61]. The far-field polar directivity is additionally dominated by the relative size of the eddies compared to the wing chord, which radiates more noise upstream.

Semi-empirical noise prediction models thus include boundary layer thickness and general wing dimensions to define the acoustic power, for which the model is generally taken as the flat-plate turbulent boundary layer model to simplify the computation [75]. Note that different wing surfaces, such as the horizontal tail, vertical tail, and wing can be modelled with the same equations yet different boundary layer and dimension inputs. Noise of wing surfaces scales with V^5 for non-compact dipoles or V^6 for compact dipoles [45].

2.1.3. HIGH-LIFT DEVICES

High-lift devices comprise various types of flaps and slats which deflect the air stream to generate additional lift during climb or descent. However, their attachment to the wing surface causes noise in several ways as can be seen in Figure 2.6. Slats generate additional noise as they introduce a slat cove which acts as cavity, while simultaneously turbulent flow scatters of the trailing edge of the slat [76, 77]. In semi-empirical models, the slat is mostly modelled similar to the clean wing surface, thus the cove cavity effect, slat junction noise, or cusp noise are not taken into account. Slat noise scales similarly as the wing noise [78].

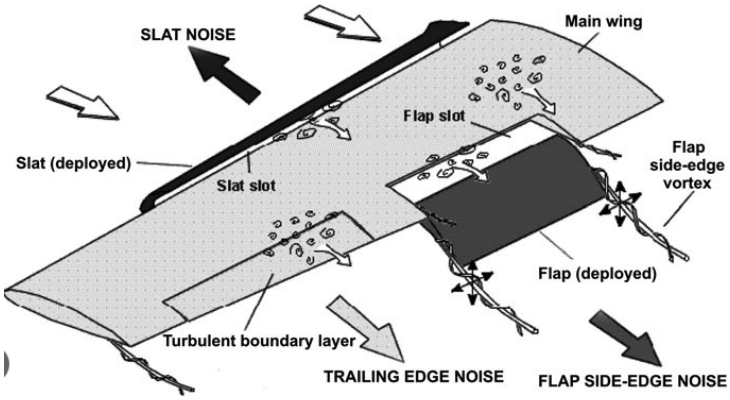

Figure 2.6: Schematic of flow around high-lift devices that could cause noise [79].

Flaps generate additional noise as they interact with the turbulent flow convected off the clean wing trailing edge [49, 80]. Additionally, vortices might arise at the flap side edges. The deflection angle of the flap defines the additional noise that is generated by the flap, where a higher deflection can lead to higher noise levels depending on the increase of loading. Throughout history, different flap models have been produced with

[1] The acoustic far-field is defined as a distance (1) greater than the largest dimension of the object, or (2) a distance larger than the dominant wavelength [74].

varying levels of slots. A higher number of slots (or increased complexity) increases the noise levels [78]. Models for flap noise are mostly based on the flap deflection angle and flap dimensions relative to the wing, without any boundary layer characteristics. The flap directivity is a dipole tilted at the flap deflection angle for polar angle, and an asymmetrical dipole for the azimuthal angle with a larger lobe towards the ground. Flap noise scales with V^6 [78].

2.1.4. CAVITY NOISE

Cavity noise occurs at open pin holes, inlets, and even at surface dents due to damage and presents itself as a tonal peak in the spectrum. Small open or closed orifices can act as a resonator when air flows over its top. The flow causes a velocity shear layer between the still standing air inside the cavity and the fast moving air outside the cavity. This shear layer rolls up in Kelvin-Helmholtz instability vortices. These vortices impinge on the downstream edge of the cavity [81]. Here, the acoustic impedance change causes acoustic scattering upstream. At certain frequencies, this acoustic pressure field locks the instability which feeds the roll-up of vortices [82]. Simultaneously the vortical structure might also trigger the resonance mode of the cavity due to standing waves, at a quarter wavelength of the depth, causing an additional tone [83]. The noise generation mechanism is outlined schematically in Figure 2.7.

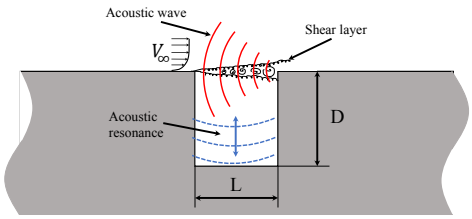

Figure 2.7: Cavity noise feedback loop [84].

The frequency of the cavity is determined by the cavity geometry. For the vortical acoustic coupling, this is dependent on the diameter of the cavity and the convection velocity [82]. For the resonance mode, also the depth of the cavity has to be taken into account to predict the frequency of the tone. As cavities are often of small size, it generates high frequency tones that are especially annoying to the human ear. Fortunately, cavity noise can be solved by closing the orifice.

2.2. TURBOFAN ENGINE NOISE

To understand the noise that is generated in the turbofan, its working mechanism and principle components are explained first. The noise generation mechanism of each part is explained in the subsequent sections. Most aircraft are configured with turbofan engines, which comprise of five stages to generate thrust. Figure 2.8 shows the stages as fan - compressor - combustion chamber - turbine - nozzle/exhaust [85].

In a turbofan engine, the fan draws in incoming airflow at a low velocity, directing a portion to the engine core while bypassing the rest around the core to create additional

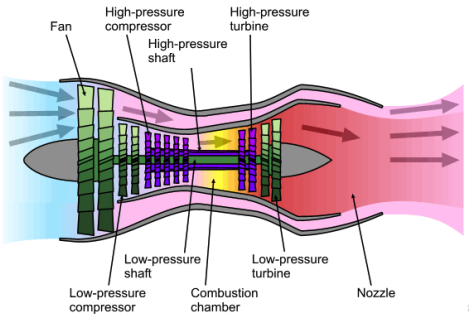

Figure 2.8: Schematic of turbofan engine with low by-pass ratio and mixed exhaust. Nowadays, the by-pass ratio is increased for increased efficiency [86].

thrust and cool the engine. This bypass air, particularly in high bypass ratio engines, significantly contributes to total thrust. Inside the compressor, stators and rotors increase the pressure of the air, ensuring it reaches the combustor at the correct pressure and temperature. Fuel is injected into the combustor, where it mixes with the air and ignites. This expanding gas is forced out through the exhaust, a process in which the chemical energy is transferred to kinetic energy. This drives a coaxial shaft connected to the turbine, which then drives the compressor and fan. Finally, the high-velocity jet exiting the nozzle, combined with the bypass airflow, generates thrust.

2.2.1. INLET NOISE

At the inlet of the engine, the fan and compressor stage cause significant noise emissions. While they are present on the front of the engine, the inlet noise radiates strongly toward the rear direction, with a noise peak at 120° and no variation in the azimuthal direction [87]. While the engine is idling during approach, the fan is still loaded, causing significant noise in both take-off and landing. This noise exhibits strong tonal peaks at the Blade Passage Frequency (BPF) and its harmonics, as well as broadband noise due to the blade wake turbulence and unsteady engine inflow.

Several noise sources are present in the fan: discrete tones from the rotating components propagating from the inlet and exhaust, broadband noise from both inlet and exhaust, and buzz-saw noise. Inlet flow distortion can also be present but is only relevant during starting and ground roll operations [80]. The discrete tones are caused by rotor-stator interaction mostly, which happens periodically when the rotating blade passes the stationary vanes [87]. The corresponding frequency can be specified by the number of blades and the rotational speed as the BPF which is calculated as

$$\mathrm{BPF} = \frac{B \cdot \mathrm{RPM}}{60} \tag{2.1}$$

where RPM is the rotational speed (rotations per minute) and B the number of blades. Tones are also present at integer multiples of the BPF, but at decreasing strength. These harmonics exist due to changes in RPM or changes in loading over the cycle. The noise mechanism for the exhaust tones is the same, but propagates from the bypass exhaust.

The buzz-saw noise is also caused by the rotating fan, but specifically when the local tip Mach number becomes supersonic during take-off [78]. In that case, each blade generates a shock wave which coalesces with that of others in the inlet to form a single shock wave. This pattern repeats itself every full rotation, hence occurring at a lower frequency than the BPF, i.e., the shaft frequency. Buzz-saw noise also has strong harmonics at integer multiples of the shaft frequency and radiates only forwards.

Finally the inlet and exhaust broadband noise is generated through turbulence in the blade wakes, unsteady inflow, or turbulence in boundary layers. The turbulence is related to different vortical sizes hence emitting noise over a wide range of frequencies [78].

The fan noise can be modelled mostly based on the number of rotor and stator blades, the mass flow rate over the fan, and the diameter of each stage (to determine the tip speed). Additionally, the effect of acoustic liners can be taken into account. Acoustic liners are placed inside the engine fairing to reduce fan noise. The liner consists of small protrusions that act as Helmholtz resonators, thereby attenuating sound at a specific range of frequencies and directivity angles [88]. This can be modelled through the length of the lining area, the duct diameter, and potentially the protrusion size.

2.2.2. CORE NOISE

Engine core noise is the noise from the combustion chamber and the turbine stages combined. It is of broadband nature peaking around 500 Hz, bound by jet noise at lower frequencies and fan noise at higher frequencies. The combustion noise radiates to the rear of the engine, thus present in the directionality in the aftward arc, with a maximum around 120° [78].

Direct combustion noise is caused by the fuel burning which adds heat energy to the flow, which expands the gas mixture. However, this heat release is unsteady resulting in fluctuating expansions and contractions of air, thereby creating pressure fluctuations and thus sound. Additionally, the acoustic waves cause flame unsteadiness which enhances the effect. The direct combustion noise travels downstream, where it impinges on the turbine blades. The blades reflect the wave back to the flame, inducing even more unsteadiness, and propagate downstream to the exhaust.

Indirect combustion noise originates from unsteady combustion which causes non-uniformities in air temperature or essentially variances in entropy, which are accelerated past the turbine blades [89]. Due to the acceleration of air, shear layers arise which results in vortices. The energy of the vortical structures and entropy fluctuations, both pressure perturbations, is transferred to acoustic energy when they interact at the combustor exit after the turbine stage. All noise sources from the engine core are summarised schematically in Figure 2.9.

The combustion noise models can be based on the mass flow rate and temperature differences over the different combustion stages in the engine [90]. These parameters are often difficult to find and should rather be modelled with a gas turbine performance model, such as GSP or GasTurb [42].

Figure 2.9 omits that the turbine also generates noise in a similar way as the inlet fan; tonal noise due to wake-impingement from one row of vanes to the next, as well as broadband noise due to the unsteady inflow and turbulent wake [91]. These can be

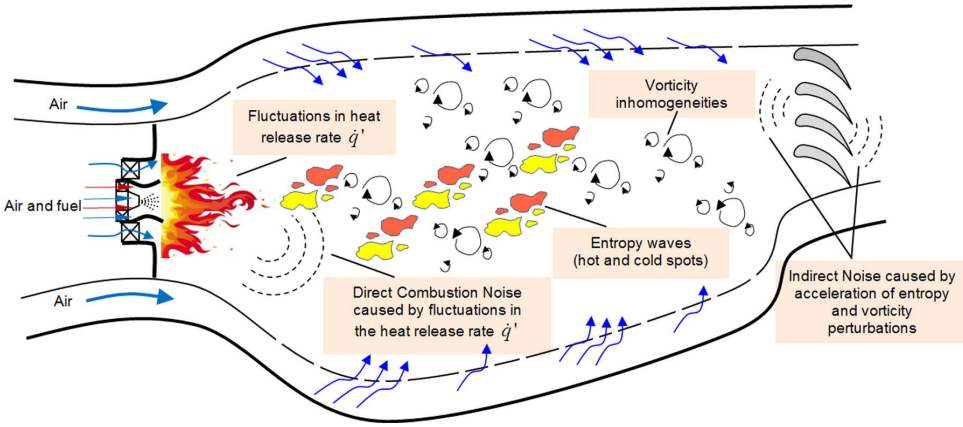

Figure 2.9: Noise sources in the combustion chamber, between the flame and the turbine stages [89].

modelled similarly as the fan model.

2.2.3. EXHAUST NOISE

Exhaust noise is the dominant part of jet noise during take-off, which contributes to the engine noise spectrum in a broadband way but is most perceptible at low frequencies until roughly 200 Hz [78, 91]. At higher frequencies combustion noise and fan noise are the main engine noise contributors. Yet, jet exhaust noise can be dominant depending on the polar angle as jet noise is generated at the exhaust and travels downstream, so the directionality peak lies around $\theta = 150°$ (see Figure 2.3) [42].

Generally, there are three different regions where turbulence noise is generated: (1) the inner shear layer between the core and bypass airflow, (2) the outer shear layer between the bypass and ambient airflow, and (3) the core mixing region with the surrounding air flow [92]. These regions are indicated in Figure 2.10.

Small-scale turbulence mostly forms around the outer shear layer close to the exhaust, causing high frequency noise content. Through downstream propagation and mixing with ambient air, the velocity in the potential core reduces. In this region, large-scale turbulence is present. Especially the large-scale turbulence is of importance for jet exhaust noise as it defines the spectrum at lower frequencies [93]. The transitional region includes mid-scale turbulent structures and hence is responsible for the acoustic power at mid-range frequencies [94]. Shock noise is omitted in the current work as all aircraft used here fly in the subsonic regime.

Jet noise can be modelled based on the effective velocity and convective Mach number for each jet region. The use of chevrons should be included, as they influence the region of noise radiation. The jet noise theoretically scales with V_{jet}^8 for the turbulence mixing region [60], but many semi-empirical models found that the scaling power depends on the temperature difference between the jet and the ambient air [45, 92]. For higher temperature jet streams, entropy fluctuations start forming which reduce the exponent to a value between 6 and 8 [61, 91].

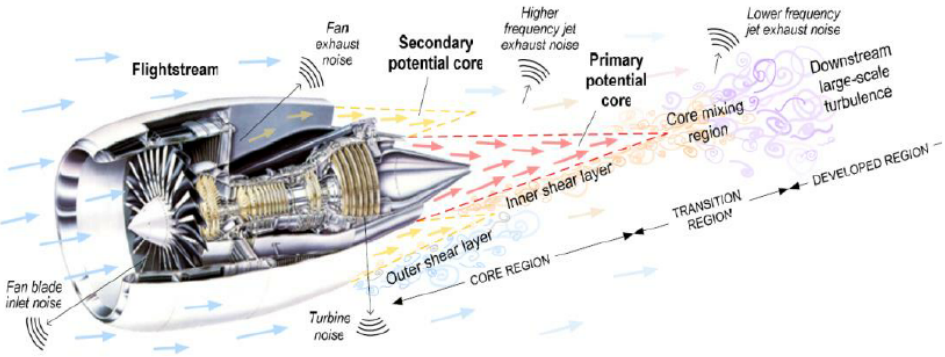

Figure 2.10: Regions of flow mixing at the jet exhaust [95]

2.3. PROPELLER NOISE

Propeller-driven aircraft have a turboprop engine as in Figure 2.11 or a propeller coupled to an electric engine which thus has no combustion noise sources. As the noise generation mechanism of the engine parts was discussed in the previous section, solely the noise caused by the moving propeller is explained in this section.

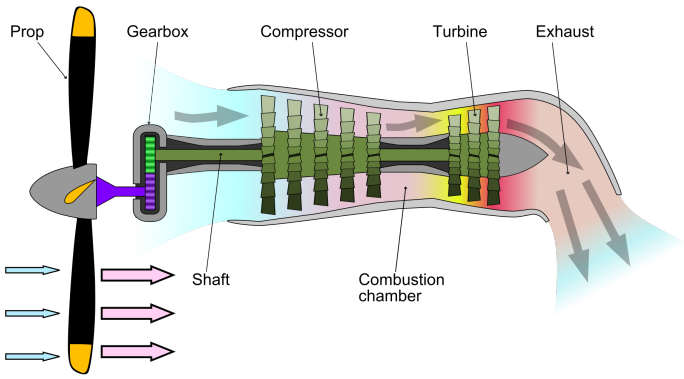

Figure 2.11: Schematic of turboprop engine with fuel-burning engine [86].

In general, propeller noise is recognisable by the strong tonal component which is caused by the blades passing a parcel of air which is excited into a pressure fluctuation every time. The frequency of the tone corresponding to this is the BPF, see Equation 2.1. Thickness and loading noise cause the pressure fluctuations resulting in this tonal component, while vortex and turbulence noise contributes to the broadband component [62].

As this dissertation contains a chapter on the results of tonal propeller noise modelling (Chapter 8), the corresponding model is introduced in this theory chapter. The

work focused on the model Helicoidal Surface Theory of Hanson, which includes merely the steady periodic propeller noise sources [96, 97]. The combined propeller noise in the time-domain in the far-field is modelled as a Fourier Series as

$$p(\boldsymbol{x}, t) = \sum_{m=-\infty}^{\infty} P_{mB} e^{-imB\Omega t} \tag{2.2}$$

where $\boldsymbol{x}$ is a receiver location, P_{mB} is the pressure Fourier Transform at the mth harmonic of the BPF for a propeller with B blades, and Ω the angular velocity. P_{mB} consists of the effects of thickness, lift, and drag noise as $P_{mB} = P_{Vm} + P_{Lm} + P_{Dm}$, which are introduced in the following sections. For brevity and in keeping with the level of detail of this chapter, the description and implementation are presented here but without a detailed explanation of every individual parameter. Instead, a general overview of the key components is given, focusing on their relationships and overall significance within the equation.

2.3.1. THICKNESS NOISE

A blade passing through a parcel of air, moves the air physically aside which can be seen as a mass ejection. Thus, thickness noise is a monopole source for which the directionality is depicted in Figure 2.4a [62]. Note that this explanation is as perceived from the air parcel which is at a fixed, still-standing, reference frame with respect to the propeller blade.

The strength of the monopole is proportional to the mass ejected per time and therefore to the volume of air displaced, where the volume is strongly related to the thickness of the airfoil [98]. The blade length is not important in this matter as the monopole is described for a specific airfoil section along the blade, which is later integrated over all radial sections.

However, for a forward-moving propeller aircraft, an observer in the far-field will not perceive thickness noise as a monopole source. The forward motion of the source introduces a Doppler-shifted term and hence a subsonically moving monopole is perceived as a dipole due to the introduction of a $\cos^2\theta$-term in the derivations [99].

Thickness noise is strongly related to the local velocity, with a higher velocity resulting in higher noise levels. Hence, thickness noise is stronger at radial sections close to the tip. However, for low Mach numbers the contribution of thickness noise is smaller than that of loading noise [98]. At higher velocities, i.e., higher RPM or larger blade diameter, thickness noise may be assumed to have a larger contribution than loading noise. The tip Mach number is defined as

$$M_t = \frac{2\pi \cdot (\mathrm{RPM}/60) \cdot (D/2)}{c} \tag{2.3}$$

in which D is the propeller diameter and c the speed of sound. The local (radial) Mach number can be derived from this by replacing R with the local radius.

The helicoidal surface theory accounts for the thickness noise as a volume displacement based on the volume of an airfoil section, which is included in

$$P_{Vm} = -\frac{\rho_0 c^2 B \sin\theta e^{imB\left(\frac{\Omega_D r}{c} - \frac{\pi}{2}\right)}}{8\pi\left(\frac{y}{D}\right)(1 - M_x \cos\theta)} \cdot \frac{1}{2}\int_0^{r_t} M_r^2 e^{i(\phi_0+\phi_s)} J_{mB}\left(\frac{mBzM_t \sin\theta}{1 - M_x \cos\theta}\right) \cdot 2k_x^2 t_b \Psi_V(k_x) dz \tag{2.4}$$

for which the purpose and significance of certain components of the equation are explained below. The equation uses geometric variables such as the radius r, diameter D, the blade thickness t_b, and position defined by x, y, z and observer angle θ. The operational variables include the angular velocity Ω, the Mach numbers at the tip M_t, at the radial section M_r, and of flight velocity M_x. k_x is the non-dimensional wave number in x-direction, m is the harmonic number, and B is the number of blades. ϕ_s denotes the phase lag due to blade sweep, whereas ϕ_0 denotes the phase lag due to blade offset.

1. $\sin\theta$ incorporates the diminishing noise towards the front and rear axes of the propeller.
2. $e^{imB\left(\frac{\Omega_D r}{c} - \frac{\pi}{2}\right)}$ creates a sinusoid at a certain frequency for which the remainder of the equation provides the assigned amplitude.
3. $(1 - M_x \cos\theta)$ is the Doppler factor which shifts the directivity pattern forward due to the source motion.
4. $\int_0^{r_t} ...dz$ is the actual thickness noise computation through an integration over radial sections of a source term (item 7) times a radiation efficiency (item 6).
5. $e^{i(\phi_0+\phi_s)}$ includes a phase lag due to propeller sweep, but can also incorporate phase lags due to other angle offsets.
6. $J_{mB}\left(\frac{mBzM_t \sin\theta}{1-M_x \cos\theta}\right)$ is the radiation efficiency, modelled by a Bessel function, for which the order mB defines which harmonics play a role and the argument $\frac{mBzM_t \sin\theta}{1-M_x \cos\theta}$ defines the strength for a specific order.
7. $t_b \Psi_V(k_x)$ includes the the local thickness multiplied by the thickness source term which includes the chordwise thickness distribution. The argument of the chordwise wavenumber indicates the non-compactness of the source which can cause interference from the signals of different chord positions.

2.3.2. LOADING NOISE

Loading noise is caused by the pressure field on the passing blade which causes a resulting pressure field in the surrounding air parcel, thus locally resulting in a dipole source for which the directionality is described in Figure 2.4b [62]. The maximum of the lobe is pointed in the direction of the lift or drag force. However, under subsonic forward motion of the propeller, the thrust directionality in the far-field changes from a dipole into a quadrupole which is described in Figure 2.4d [62].

The resultant force field of a propeller blade section can be decomposed into the torque (blade induced drag) and thrust (blade lift) forces which act in different directions. Torque acts in the propeller rotation plane parallel to the incoming flow, while

thrust acts perpendicular to the blade section and thus normal to the rotation plane [62]. The strength of these forces determines the strength of the noise source, with higher forces leading to more noise. An estimate for the blade loading can be made based on the advance ratio J which is defined as

$$J = \frac{V_\infty}{(\mathrm{RPM}/60)D}. \tag{2.5}$$

For a certain forward velocity V_∞, a high RPM results in a low advance ratio and implies a high blade loading.

The helicoidal surface theory incorporates the sectional lift and drag dipole into its loading noise component. The lift dipole is 90° out of phase with the thickness monopole and oriented normal to the convection direction, and the drag dipole is oriented in the convection direction.

The loading forces are ideally steady during a full rotation, but this is unfortunately not realistic. Small variations occur causing unsteady loading due to disturbances in the air flow such as gusts, re-circulation effects, or a changing blade pitch. These unsteady effects cause the presence of blade loading harmonics and hence harmonics of the BPF [100, 101]. Unsteady loading can be present at the rotation axis, whereas purely steady loading has no contribution along that axis.

The pressure Fourier Transforms of each loading source according to Hanson's model are

$$P_{Lm} = -\frac{\rho_0 c^2 B \sin\theta e^{imB\left(\frac{\Omega_D r}{c} - \frac{\pi}{2}\right)}}{8\pi\left(\frac{y}{D}\right)(1 - M_x \cos\theta)} \cdot \frac{1}{2}\int_0^{r_t} M_r^2 e^{i(\phi_0+\phi_s)} J_{mB}\left(\frac{mBzM_t \sin\theta}{1 - M_x\cos\theta}\right) \cdot i k_y C_L \Psi_L(k_x) dz \tag{2.6}$$

and

$$P_{Dm} = -\frac{\rho_0 c^2 B \sin\theta e^{imB\left(\frac{\Omega_D r}{c} - \frac{\pi}{2}\right)}}{8\pi\left(\frac{y}{D}\right)(1 - M_x \cos\theta)} \cdot \frac{1}{2}\int_0^{r_t} M_r^2 e^{i(\phi_0+\phi_s)} J_{mB}\left(\frac{mBzM_t \sin\theta}{1 - M_x\cos\theta}\right) \cdot i k_x C_D \Psi_D(k_x) dz \tag{2.7}$$

for which the main difference with respect to the thickness definition in Equation 2.4 is the $C_L\Psi_L(k_x)$ and $C_D\Psi_D(k_x)$ source distribution. C_L and C_D are the lift and drag coefficients of the blade section.

Unsteady forces can be included as well as blade loading harmonics through adding a Fourier Series in Equation 2.6 and 2.7. These sinusoids are created at all blade loading harmonics s' but not all of them weigh equally into the final equation. The weighting of the loading harmonics is determined by the order of the Bessel function which now is determined by $mB - s'$ as well as the loading force [101].

2.3.3. BROADBAND NOISE

Apart from the tonal components, the propeller noise spectra also include broadband noise albeit of less importance. The broadband noise originates partially from vortex noise and partially is turbulence induced. All turbulent fluctuations at the edge of the

blade scatter as dipole source [61]. Again, the areas near the blade tips will have the highest amplitude due to the noise scaling with V^6 [62].

Additionally, inflow turbulence might be present which can create leading edge noise [98]. The tonal components of propeller noise are stronger than the broadband components, but broadband propeller noise models do exist such as that of Amiet and of Brooks, Pope, Marconi [75, 102].

2.4. INSTALLATION NOISE

Whereas all previous sections described noise sources that were formed by one of the aircraft components specifically, installation noise is an additional source caused by an aerodynamic interaction of components. It is not always present and is highly dependent on placing of the components with respect to each other, with one object affecting the other. Placement does not only comprise scattering or reflecting of an acoustic wave against an object, but can also entail the creation of a new source as the wake of a source hits another object. This is most apparent in the installation of engines.

Propeller engines suffer from pylon and wing wake interactions, where the turbulent wake or strong vorticity from the propeller hits the wing surface creating new sources through force fluctuations [103]. Jet engines suffer from the jet stream impinging on the pressure side (lower side) of the wing surface or on the wing trailing edge [104, 105]. Another well-known installation effect is the shedding of turbulent vortices from the landing gear impinging on deflected flaps [54].

2.5. SHIELDING OF NOISE

The previous section discussed additional noise sources occurring due to placement of aircraft components, however, the placement can also be optimised to reduce the perceived noise on ground, commonly named shielding. This occurs when a barrier is present between the source and the receiver, such as an engine mounted above the wing.

The barrier surface will reflect the noise in a similar way as jet-installation noise, and hence, it introduces an installation noise source above the wing, but it simultaneously obstructs the direct path of the noise from source to receiver thereby reducing the perceived noise below the wing [55, 106, 107]. A part of the noise will still be perceived by the observer as there is diffraction of noise around the edges of the barrier. The barrier effectiveness is therefore strongly dependent on the frequency of the source which determines diffraction, but is also dependent on the source's directionality.

3

METHODS TO IDENTIFY ACOUSTIC SOURCES

We can't solve problems by using the same kind of thinking we used when we created them.

Albert Einstein

In the previous chapter the different aircraft noise sources were discussed. However, humans only hear an aircraft as a single source, so how can we establish the contribution of the separate sources? This can be achieved through the application of acoustic imaging methods on microphone array data, which results in the location and frequency spectrum per noise source. To understand how noise signals can be measured, this chapter first introduces the working mechanism of microphones and phased microphone arrays. The first acoustic imaging method introduced here, conventional time domain beamforming, covers the intuitive basics and provides an analogy to the human auditory system. After that, the adaptation for rotating sources is provided. The more efficient frequency domain implementation of conventional beamforming is also described, along with an overview of improved methods. Lastly, a global optimisation approach to identify acoustic source is presented.

Post-processing methods, so-called acoustic imaging methods, are applied to measurements of phased microphone arrays to accurately identify source positions by utilising the differences in sound wave arrival times at different microphones. By using multiple microphones arranged in a specific configuration, these arrays can capture sound signals from various directions simultaneously. The configuration can be optimised to have a good performance over a wide range of frequencies.

3.1. MICROPHONE ARRAYS

The microphone arrays used in this dissertation all consist of the four main components outlined in Figure 3.1. The following sections will discuss the hardware components, in the order from left to right as outlined in the figure.

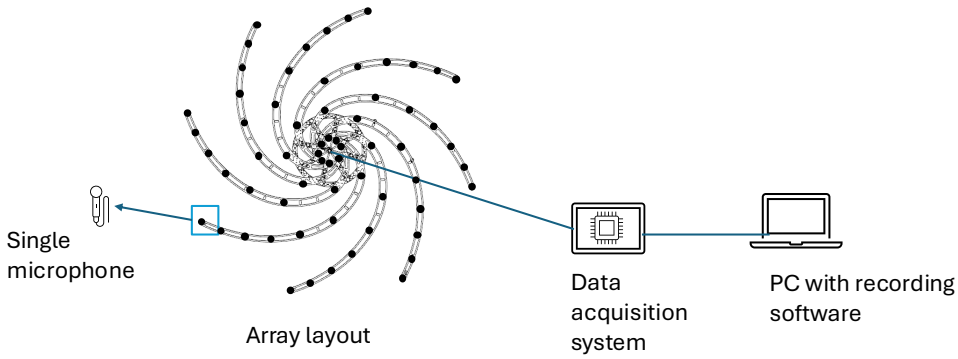

Figure 3.1: Components needed for a phased microphone array setup.

3.1.1. MICROPHONES

Microphones convert acoustic pressure waves into electrical signals that can be further processed. The two main types of microphones in use today are electret microphones and MEMS microphones, with MEMS microphones increasingly dominating consumer electronics [108]. This dissertation utilises data from both types. The working mechanisms, along with their respective advantages and disadvantages, are discussed in the following sections.

PRE-POLARIZED CONDENSER MICROPHONES

Pre-polarised condenser microphones were the standard for a long time due to their relatively low weight, small size, and low power consumption [109]. Figure 3.2 shows the components of a condenser microphone, specifically an electret microphone.

Electret microphones use a pre-polarised diaphragm made from an electret material, which can hold a constant charge, thereby eliminating the need for external polarisation via a power supply [110]. The pre-polarised diaphragm deflects in response to incoming pressure waves, changing the capacitance between the electret plate and the pick-up plate (also called the backplate). A changing capacitance gives a changing

voltage. Because these fluctuations are very small, the microphone signal needs to be well shielded from interfering noise. A transistor is used to maintain high impedance, preventing charge leakage from the electret material, and to amplify the small voltage fluctuations.

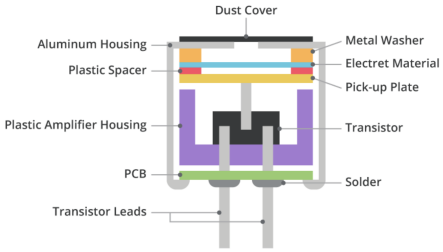

Figure 3.2: Diagram of an Electret microphone from [111].

MEMS MICROPHONES

Micro-ElectroMechanical Systems (MEMS) microphones are available in both analogue and digital versions. The only difference between analogue and digital MEMS microphones is that the digital ones include an Analogue-to-Digital Converter (ADC) on the Printed Circuit Board (PCB). Like electret microphones, MEMS microphones create a capacitor using a membrane and a backplate, but the layout of MEMS is horizontal rather than vertically stacked, as shown in Figure 3.3 [112].

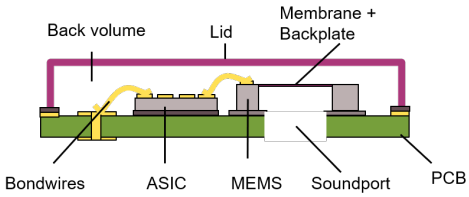

Figure 3.3: Diagram of a MEMS microphone from [111].

MEMS microphones are generally much smaller than condenser microphones, making them ideal for applications where space is limited, such as in mobile phones or hearing aids. Additionally, MEMS microphones have more stable sensitivity over a wide operating temperature range, allowing for a broader range of applications. Their improved resistance to water and dust damage in the latest designs also makes them more advantageous compared to electret microphones. However, they can suffer from resonance frequencies around 20 kHz due to the small cavity required in the transducer to receive acoustic waves.

For microphone arrays, a key advantage of using MEMS is the more uniform frequency response among MEMS microphones from the same batch. However, Merino-Martinez et al. [113] found that arrays using digital MEMS microphones had higher side-

lobe levels compared to those using conventional condenser microphones. This is a notable disadvantage, although the cause remains unknown.

3.1.2. ARRAY LAY-OUT

The layout of the array, particularly the positioning of one microphone relative to another, affects the array's performance. This performance is measured through spatial resolution and spatial aliasing (grating lobes), defined by main lobe width and maximum sidelobe level, respectively [114, 115]. These key performance indicators are illustrated in Figure 3.4. Three main factors influence these indicators: array periodicity, array aperture, and the minimum distance between two microphones.

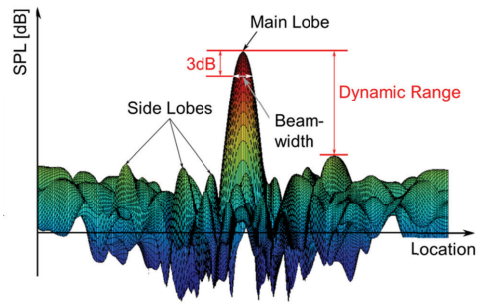

Figure 3.4: Array response to a single source of unit strength, also known as the Point Spread Fuction (PSF), from [116].

Array periodicity describes how repetitive the pattern is; for example, an equally spaced line array has high periodicity, whereas a more random pattern has lower periodicity. Arrays with high periodicity have sidelobes that reflect the array shape and are relatively high in level [117]. In contrast, random arrays have lower sidelobe levels, and their locations are more spread out over the source map. The theoretical limit of the sidelobe level depends on the number of microphones in the array [74] and is given by $L_{\text{main lobe}} - 3 + 10\log_{10}(N_{\text{mic}})$ dB [117]. This often leads to spiral or concentric circle arrangements with an odd number of microphones.

The array's aperture influences the beamwidth of the main lobe; a larger aperture results in a narrower main lobe. A narrower main lobe is crucial for accurately identifying source locations and is necessary when multiple sources are closely spaced to prevent the overlap of main lobes. A large aperture is also beneficial for measuring sources at large distances or at low frequencies. The relationship between these factors is defined by the Rayleigh resolution limit as [118]

$$R_{\text{Rayleigh}} = 1.22\frac{cz}{D_{\text{array}}f} \tag{3.1}$$

where c is the speed of sound, z is the distance between the source and the centre of the array, D is the array aperture, and f is the frequency of interest. R represents the minimum distance at which two sources can be separated and still identified individually in the source map.

The distance between microphones affects the formation of grating lobes or spurious sources, i.e., spatial aliasing. Grating lobes are sidelobes with a level equal to the source level, which can significantly interfere with source identification in the source map [119]. Grating lobes result from spatial aliasing: when more than half a wavelength fits between two sampling points (microphones), the signal may be misidentified as a lower frequency, potentially causing phase matches across the array. Therefore, the minimum distance between microphones should be no more than half the wavelength of the highest frequency of interest. A smaller inter-microphone distance also reduces coherence loss between recorded signals [120]. Typically, the highest microphone density, i.e., closest spacing, is found at the centre of the array to improve source localisation near the centre of the scan plane.

Various array layouts have been proposed over time, with optimisations and improvements tailored to specific applications [120–123]. The Underbrink log-spiral arm array, as used for most measurement campaigns in this dissertation and depicted in Figure 3.1, is among the best-performing arrays across a broad frequency range. It offers a narrow main lobe width for a given number of microphones due to the extensive spread of the arms, while simultaneously providing high microphone density at the array's centre to reduce sidelobe levels [114].

3.1.3. DATA ACQUISITION SYSTEM

The Data Acquisition System (DAS) used in this dissertation is an in-house designed system tailored to the specific requirements of microphone type, sampling frequency, and outdoor use. Figure 3.5 presents the design schematic of the DAS.

Microphones are grouped into bundles of eight per identical channel board. Each microphone signal passes through a gain block, which functions as the pre-amplifier, to boost the voltage signal and minimise noise interference. This pre-amp, which includes an operational amplifier (opamp), is the only point of gain application in the system. Users can choose between low and high gain, with high gain being advantageous for very quiet experiments.

The analogue data from each microphone is first processed through a low-pass filter before being converted to a digital signal. This low-pass filter removes high-frequency components, typically caused by electronic interference, and acts as an anti-aliasing filter. Without this filter, high-frequency components above half the sampling frequency could alias, or distort, into lower frequencies during the analogue-to-digital conversion. To simplify and reduce the cost of the filter design, oversampling and later decimation are employed, allowing for a more straightforward low-pass filter.

Oversampling permits the use of a lower-order passive low-pass filter, followed by a lower-order digital Finite Impulse Response (FIR) filter after the ADC, which is generally more cost-effective, particularly for high-order filters. The anti-alias/low-pass filter implemented is a Sallen-Key filter [124], with a 20 kHz cutoff frequency and 96 dB attenuation at 1 MHz. These passive filters are simpler to implement, less expensive, induce minimal processing delay, and offer greater stability.

After anti-alias filtering, the signal is converted to a differential signal by the ADC driver, then processed through the ADC. The ADC operates in two stages: the first stage, a state-machine, converts the continuous incoming signal into a pulse-width modulated

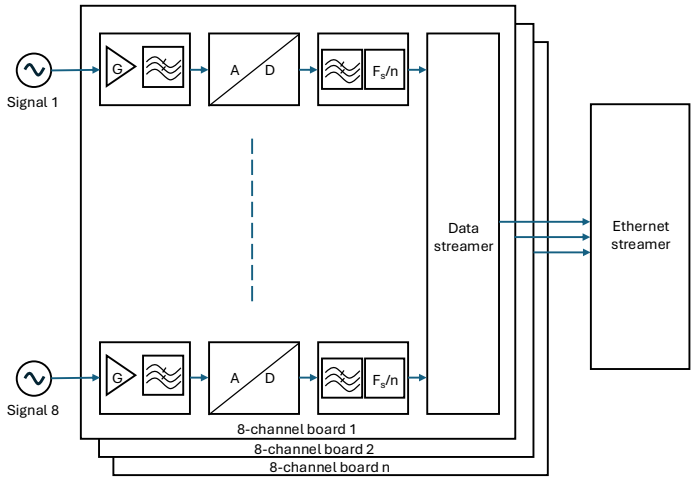

Figure 3.5: Block diagram of the data acquisition system, running from the data received by the microphone (analogue) to the data received by the computer (digital).

signal; the second stage converts these pulses into a 16-bit digital word. Additionally, a de-bounce filter is included to limit voltage signal changes, thereby reducing cross-talk.

The ADC can sample two input channels simultaneously, after which an Field Programmable Gate Array (FPGA) collects data from all eight input channels (microphones) and processes it for the streamer FPGA. All components up to and including the ADC comprise a modular front-end, which allows for future changes of microphone types. In such cases, the pre-amp may need to be replaced to accommodate new impedance matching. Figure 3.6 illustrates the detailed schematic of the DAS front-end.

After acquisition of the data from 4 ADCs, the acquisition FPGA filters the data. A two-stage digital filter is used to reduce the sampling frequency to the final 62.5 kHz, with a cut-off frequency of 20 kHz. This two-stage filter minimises the number of coefficients needed compared to a single-stage filter. The stages of the filter are shown in Figure 3.7.

Following the decimation filter, the signal is transferred to the back-end, which includes the data streamer and the Ethernet streamer. The data streamer gathers the filtered data and bundles it for the Ethernet streamer. To prevent sampling delays to the PC and to ensure that system information is sent before the samples, the streamer employs two buffers.

3.1.4. CALIBRATION OF MICROPHONE ARRAYS

Calibrating microphone arrays is more complex than calibrating individual microphones. While single microphone calibration typically involves an amplitude correction at a sin-

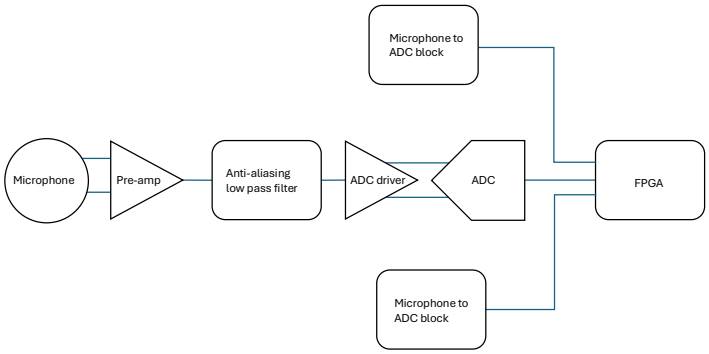

Figure 3.6: Throughput of the microphone signal. The front-end with the pre-amp is modular to allow for other microphone sets in the future, such as low-noise microphones (in need of higher gains) or microphones with a better accuracy.

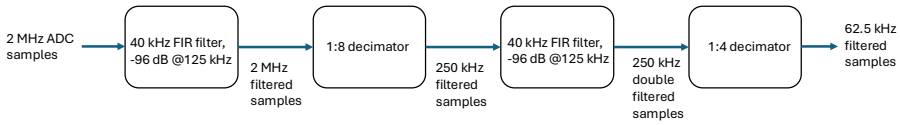

Figure 3.7: Double staged FIR filter to reduce the 2 MHz sampling from the ADC to 62.5 kHz sampling as requested (with a cut-off/roll-off at 20 kHz).

gle frequency to match a reference, microphone arrays require additional considerations. Specifically, it is crucial to ensure that all microphones are in phase with each other, as beamforming techniques depend on phase differences in the measured signals to determine source locations [125]. These phase differences should not be affected by general phase offsets between microphones.

Traditionally, microphones are calibrated using a pistonphone that emits a tone at 250 Hz or 1 kHz with an Overall Sound Pressure Level (OSPL) of 94 dB [126]. Ideally, this calibration should be performed before each measurement campaign. This method is effective for microphones with a flat and stable frequency response. However, field measurement microphones are exposed to various weather conditions, which can lead to frequency degradation over time. Additionally, some microphones have a non-flat frequency response. In such cases, the Bruel and Kjaer (B&K) Multifunction Acoustic Calibrator type 4226, which calibrates microphones at 11 different octave-band frequencies, is used [127].

Phase calibration of microphone arrays must account for the entire measurement chain, from the microphone through all filters in the DAS to the laptop, as phase shifts can occur at any conversion or filtering stage. Phase calibration can be achieved by using a sound pulse or clap at a known location. The expected phase difference across

the array can be calculated based on the microphones' positions relative to the pulse source. However, this method requires precise knowledge of the pulse and microphone positions and a large anechoic room to avoid interference with the emitted signal. Alternatively, two microphones can be placed in a T-shaped piece, see Figure 3.8, opposite each other at the T-bar with the stem of the T connected to a pistonphone [128]. If the T-shaped piece is perfectly symmetrical, the microphones should record the same amplitude and phase. Although this method is more time-consuming, it provides more accurate results for large arrays and eliminates the need for a large anechoic chamber. The B&K 4226 pistonphone can be used with a T-shaped piece to calibrate the phase response of microphones across a broad frequency range.

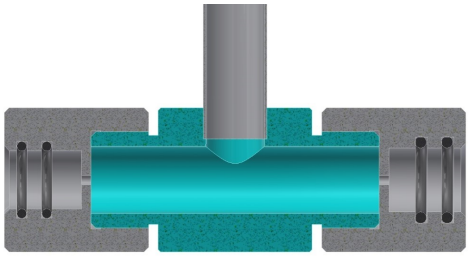

Figure 3.8: Technical drawing of the T-shaped calibration piece as designed for this PhD.

Calibration is applied in the frequency domain by correcting the Fourier-transformed pressure with amplitude correction and phase shift as follows:

$$P_{\text{calibrated},n}(f) = P_{\text{uncalibrated},n}(f) \cdot p_{\text{cal},n}(f) e^{-i\Delta\phi_{\text{cal},n}(f)} \tag{3.2}$$

where p_{cal} is the amplitude correction factor and $\Delta\phi_{\text{cal}}$ is the phase shift correction for a specific frequency f between microphone n and a reference microphone. In practice, these correction values are applied at a centre frequency f_c of the corresponding frequency band.

For the time domain correction there are two common approaches: (1) Apply the corrections in the frequency domain according to Equation 3.2 and then perform the inverse Fourier transform, or (2) split the full time domain signal into partial signals with passband filters, correct each passband by multiplying with p_{cal} and shifting the signal with Δt of the corresponding band, and then sum the corrected signals. Since the signal is discretized, the time shift Δt is implemented as a shift in samples. Both methods have been applied in this dissertation, depending on the acoustic imaging algorithm used.

3.2. ACOUSTIC IMAGING

The earliest techniques of acoustic imaging date back to before the First World War, although they were limited in resolution [129]. The concept of "seeing" with sound, however, is much older. Many mammals use this ability in various ways. The term "seeing

sound" might seem unusual, but it refers to the additional information available to listeners about sound sources. For example, humans can determine whether a car is on the left or right side without turning their head to visually confirm its presence.

The location of a sound source can be inferred by the brain from the sound waves arriving at the ears. Humans have a uniquely shaped ear on each side of the head, causing sound waves to arrive slightly differently at each ear. The received signals vary in level, arrival time, and high-frequency content of the spectrum. The differences in the spectrum are due to unique reflections from the pinna. For sources equidistant from both ears, this spectral information is used. When the source is not equidistant to the ears, the brain relies on the arrival time and level differences between them. A source closer to the left ear will be heard earlier and louder on that side than on the right ear. Thus, listeners can approximate the source's location. To refine the location, listeners move their head until the ear receives the strongest signal, thereby orienting towards the source.

This simplified model of human hearing is analogous to state-of-the-art acoustic imaging systems. In these systems, microphones replace the ears, and the brain is substituted by a data acquisition system with processing algorithms. Additionally, an entire microphone array, instead of just two microphones, improves the accuracy of source location estimation.

3.2.1. CONVENTIONAL TIME DOMAIN BEAMFORMING

Conventional Time Domain Beamforming (CTDB), also known as delay-and-sum beamforming, refers to the process of creating an acoustic image or acoustic source map based on the signals in the time domain. Figure 3.9 shows the steps taken for a line microphone array.

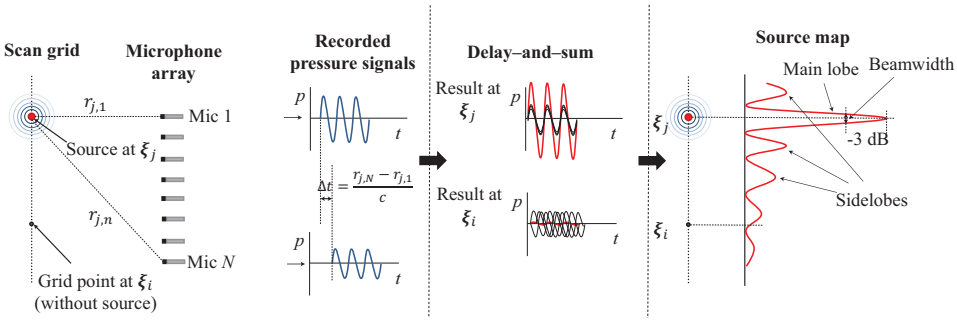

Figure 3.9: Schematic representation of delay-and-sum beamforming from [41].

In the example in Figure 3.9, the sound wave from a source at position $\boldsymbol{\xi}_j$ arrives first at the nearest microphone (microphone 1) and last at the farthest microphone (microphone N). The difference in arrival time is proportional to the difference in distance the sound wave has to travel to each microphone. Each received signal is corrected for this time delay so that the signals align in time before being summed - this is the delay-and-sum process. When the arrival time differences are accurately calculated based on the true source location, summing the aligned signals results in a high output. Correcting

this output for the number of microphones results in the OSPL. Since the exact source location is usually unknown, a scan grid with potential source locations is established.

For each potential location j, the arrival time differences across microphones are calculated, the microphone signals are delayed accordingly, and then summed over all microphones for each time step. When the delayed signals align, constructive interference results in a high value in the source map. Conversely, destructive interference occurs when the signals do not align, indicating that they do not originate from the same source. The summed receiver signal is then divided by the number of microphones to estimate the emitted pressure signal $p(\boldsymbol{\xi}_j)$. The estimated effective pressure $p_{\text{eff}}(\boldsymbol{\xi}_j)$ of grid point j is derived from $p(\boldsymbol{\xi}_j)$ as the root-mean-square (rms) over time, which is used to compute the OSPL as

$$\text{OSPL}(\boldsymbol{\xi}_j) = 10\log_{10}\left(\frac{\overline{p_{\text{eff}}(\boldsymbol{\xi}_j)^2}}{p_{\text{ref}}^2}\right) \tag{3.3}$$

where p_{ref} is the reference pressure of 20 µPa corresponding to the hearing threshold [130]. The results of this extensive search over all grid points are typically presented as a source map, with values assigned to each evaluated grid point. Depending on the application, the OSPL value can be corrected for the distance z between the source and the centre of the microphone array through a spherical spreading correction of $20\log_{10}(z)$.

Destructive interference does not always result in a zero sum. For some grid points (or source directions), the signals may partially interfere. This can happen when analysing locations close to the main source, contributing to the main lobe width, or for other positions in the source map that create similar time delay patterns, resulting in sidelobes. The source map in Figure 3.9 demonstrates the source map for a single source, i.e., the so-called Point Spread Function (PSF).

3.2.2. ROTATING SOURCE IDENTIFIER

CTDB relies on the assumption that the source is not moving, meaning that the time delay from source to receiver remains constant over time. When a moving source is present in the scan plane, applying CTDB results in a smeared appearance of the source in the source map, as illustrated in Figure 3.10a for rotating sources. This occurs because the delayed signals partially constructively interfere at each grid point the source passes, leading to a blurred representation. Thus, identifying moving sources can be challenging with a stationary acoustic imaging method.

To address this issue, two main approaches can be employed. The first is to define the grid such that it follows the source movement. This method involves moving the grid along the expected path of the source. It is commonly used for rotating sources and will be detailed in this section. Another method to correct for source movement is to adjust the time delay calculation to incorporate the source's movement. It is typically applied to sources moving in a straight line and will be discussed in Section 3.2.3.

The ROtating Source Identifier (ROSI) builds upon the delay-and-sum beamforming principle but incorporates a rotating scan plane synchronised with the source's estimated trajectory based on the rotational speed of the source. Specifically, the grid point location is adjusted at every time step to match the source's path, and then the time delay between the grid point and the receiver at each time step is calculated. After that,

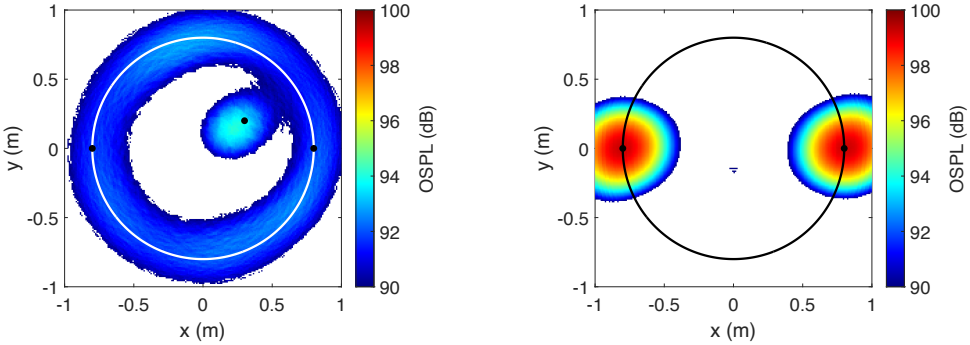

(a) CTDB

(b) ROSI

Figure 3.10: Acoustic imaging methods applied to a simulation of two rotating sources and one stationary source. The sources rotate counterclockwise at 2000 RPM and each have an OSPL of 100 dB. The starting position of the sources is at (0.8,0) and (-0.8,0). The stationary source has an OSPL of 95 dB and is located at (0.3, 0.2). The rotation circle is indicated in the figures, as well as the location (a black dot) of the stationary source for CTDB and the rotating sources for ROSI.

the received signal is reconstructed to the emitted signal for each time sample k'. By applying this approach, the source map can be significantly improved, as illustrated by the enhanced map in Figure 3.10b where the two rotating sources are now present at their starting location.

The grid point location $\boldsymbol{\xi}_{j,k'} = [x_j(k'), y_j(k'), z_j(k')]$ is calculated as

$$x_j(k') = x_c + R_j \cos(\psi)\cos(\Omega t(k') + \theta_j) \tag{3.4}$$

$$y_j(k') = y_c + R_j \sin(\Omega t(k') + \theta_j) \tag{3.5}$$

$$z_j(k') = z_c + R_j \sin(\psi)\cos(\Omega t(k') + \theta_j) \tag{3.6}$$

where (x_c, y_c, z_c) indicates the centre of rotation, ψ represents the yaw angle with respect to the array, and Ω is the rotational speed of the source. $t(k')$ indicates the emission time considered. θ_j and R_j define the location of the grid point j with respect to the centre of the grid at the initial time sample and are calculated for a two-dimensional grid as

$$\theta_j = \arctan\left(\frac{y_j(0)}{x_j(0)}\right) \tag{3.7}$$

$$R_j = \sqrt{x_j(0)^2 + y_j(0)^2}. \tag{3.8}$$

The time delay from grid point location $\boldsymbol{\xi}_{j,k'}$ to receiver location $\boldsymbol{x}_n$, $\Delta t_{j,n,k'}$, is calculated as

$$\Delta t_{j,n,k'} = \frac{||\boldsymbol{\xi}_{j,k'} - \boldsymbol{x}_n||}{c}. \tag{3.9}$$

Subsequently, the emitted pressure signal can be reconstructed for grid point j per sample k' by selecting the received pressure for mic n at time $t(k') + \Delta t_{j,n,k'}$. Once all

samples have been considered, the reconstructed signal is summed and further processed to an OSPL as described in Section 3.2.1.

3.2.3. CONVENTIONAL FREQUENCY DOMAIN BEAMFORMING

Conventional beamforming can also be implemented in the frequency domain, known as Conventional Frequency Domain Beamforming (CFDB). CFDB is computationally more efficient than CTDB and allows for focusing on specific frequencies rather than overall levels. However, it retains the limitations of CTDB regarding spatial resolution and sidelobe levels.

To adapt the time domain method to the frequency domain, the Fourier Transform is applied to the received pressures. This results in a pressure vector per frequency, expressed as:

$$\boldsymbol{P}_{\text{meas}}(f) = \begin{pmatrix} P_1(f) \\ \vdots \\ P_{N_{\text{mic}}}(f) \end{pmatrix} \tag{3.10}$$

where $P_n(f)$ is the element of a single microphone, and N_{mic} is the total number of microphones in the array. For a single monopole sound source at a specific frequency, the received pressure from Equation 3.10 can be described as

$$\boldsymbol{P} = s\boldsymbol{g} \tag{3.11}$$

where s is the source amplitude at a specific frequency, and $\boldsymbol{g}$ is the steering vector that models the propagation effects from the source to the microphones. The steering vector consists of two components: (1) the attenuation of amplitude due to spherical spreading, and (2) the phase delay relative to the phase of the signal at emission time. For a monopole stationary source located at $\boldsymbol{\xi}_j$ and a microphone at $\boldsymbol{x}_n$, the elements of the steering vector are given by:

$$g_n(\boldsymbol{\xi}_j, f) = \frac{1}{||\boldsymbol{\xi}_j - \boldsymbol{x}_n||} e^{-2\pi i f \Delta t_{j,n}} \tag{3.12}$$

for frequency f, where $\Delta t_{j,n}$ reflects the time delay between source and receiver calculated as $\Delta t_{j,n} = \frac{||\boldsymbol{\xi}_j - \boldsymbol{x}_n||}{c}$. This steering vector formulation follows the approach described in formulation IV of Sarradj [131], which implicitly normalises for the number of microphones and optimises for the best estimate of both location and strength.

It is also possible to identify a rectilinearly moving source in CFDB when $\Delta t_{j,n}$ is calculated for every time sample k' to include source movement as

$$\Delta t_{n,j,k'} = \frac{-(\boldsymbol{\xi}_{j,k'} - \boldsymbol{x}_n) \cdot \boldsymbol{M} + \sqrt{\left((\boldsymbol{\xi}_{j,k'} - \boldsymbol{x}_n) \cdot \boldsymbol{M}\right)^2 + \|\boldsymbol{\xi}_{j,k'} - \boldsymbol{x}_n\|^2 \beta^2}}{c\beta^2} \tag{3.13}$$

where $\boldsymbol{M}$ is the Mach vector and $\beta = \sqrt{1 - \|\boldsymbol{M}\|^2}$ [132]. In this case, g_n has to be corrected for $\sqrt{\left((\boldsymbol{\xi}_{j,k'} - \boldsymbol{x}_n) \cdot \boldsymbol{M}\right)^2 + \|\boldsymbol{\xi}_{j,k} - \boldsymbol{x}_n\|^2 \beta^2}$ as distance instead of $||\boldsymbol{\xi}_j - \boldsymbol{x}_n||$. Note that for $\boldsymbol{M} = [0, 0, 0]$ this equation simplifies to Equation 3.9.

The steering vector can alternatively be seen as the pressure amplitudes at the microphones for a sound source with unit strength at the grid point $\boldsymbol{\xi}_j$. This definition is used to reconstruct the source map and find the original strength of the source at grid point j. The final step of CFDB to arrive at the source amplitude, is the result of the least-squares optimisation between the measured pressures on all microphones from Equation 3.10 and the pressures modelled on all microphones according to Equation 3.11.

The solution for s_j is usually denoted as the autopower (A) of grid point j as

$$A(\boldsymbol{\xi}_j, f) = \frac{1}{2}\frac{\boldsymbol{g}_j^*(f)\boldsymbol{P}_{\text{meas}}(f)\boldsymbol{P}_{\text{meas}}^*(f)\boldsymbol{g}_j(f)}{||\boldsymbol{g}_j(f)||^4} \tag{3.14}$$

with * denoting the complex conjugate transpose. When the grid point $\boldsymbol{\xi}_j$ is near the true source location, the modelled steering vectors closely match the phase pattern across the microphone array, resulting in the inner product of vector $\boldsymbol{g}_j$ with vector $\boldsymbol{P}_{\text{meas}}$ approaching s_j. The combination of the steering vector formulation and the normalisation to the fourth power result in A_j being the true source autopower, with no additional corrections required.

Note that some formulations use the Cross Spectral Matrix (CSM) $\boldsymbol{C}$ which equals

$$\boldsymbol{C}_{\text{meas}}(f) = \frac{1}{2}\langle \boldsymbol{P}_{\text{meas}}(f)\boldsymbol{P}_{\text{meas}}^*(f)\rangle \tag{3.15}$$

in which $\langle\rangle$ indicates the ensemble average over time. In this dissertation the ensemble average is omitted as all sources are moving, thus an ensemble average does not accurately portray the source's sound emission.

3.2.4. IMPROVED SOURCE IDENTIFICATION METHODS

While CFDB is robust, it suffers from limited spatial resolution as well as high sidelobe levels which both hamper source identification. Therefore, several acoustic imaging methods have been developed to improve source identification. These methods can be divided in deconvolution methods and inverse methods. Deconvolution methods improve source maps by post-processing the CFDB results, while inverse methods account for all sound sources and potential interactions simultaneously and solve an inverse problem.

Comparison studies and benchmark studies have assessed the performance of a number of popular source identification methods, such as, but not limited to, Functional Beamforming, CLEAN-SC, DAMAS, and Generalised Inverse Beamforming [133–136]. Some methods take into account source coherence or directionality of the source. The accuracy and computational effort of these methods vary and none of the methods outperforms the others on all benchmark cases, and therefore a trade-off should be made depending on the use-case. This trade-off should consider at least the number of sources [136], the signal-to-noise ratio [133], and the source coherence [135].

The methods that have been analysed in previous studies, generally use a pre-defined search grid. This requires information on the approximate location of the source, especially when a two-dimensional grid is defined as is commonly done. Recent studies showed that it is possible instead to approach source identification as an optimisation problem which allows for a grid-free search in a bounded space [137]. The potential of

grid-free searches is interesting for noise source identification on aircraft flyovers where the exact distance between aircraft and array may not be known [42]. Therefore, this dissertation investigated the use of global optimisation for source identification, while leaving aside the grid-based methods.

3.2.5. GLOBAL OPTIMISATION

Global Optimisation (GO) approaches source identification as a grid-free search, whereas the acoustic imaging methods discussed previously perform an exhaustive search over predefined potential source locations. Besides the advantage of a broader, less user-guided search, GO can incorporate more unknowns into its cost function than only source location and strength.

GO directs the search towards the optimum using a cost function that evaluates estimates of the search parameters. The cost function is minimised by iteratively updating values of the unknown parameters. Notable global optimisation methods include simulated annealing [138, 139], genetic algorithms [140, 141], and ant colony algorithms [142, 143]. Among these, Differential Evolution (DE), a type of genetic algorithm, has shown success in experiments involving the localisation of acoustic sources [137, 144].

In brief, DE is an optimisation algorithm based on Darwinian principles, where individuals with advantageous traits are more likely to pass those traits to the next generation, thereby enhancing the species' overall adaptation and fitness. In the context of this thesis, the traits of individuals can include acoustic parameters such as source strength, source location, and speed of sound. The "fitness of the species" corresponds to the quality of source identification. In both nature and the algorithm, traits are passed to the next generation by combining genes from an original member with those from a partner member, introducing some random mutations to diversify the gene pool. "Survival of the fittest" determines whether a descendant is more fit than its predecessor, allowing it to continue to the next generation. This process is further elaborated in the following paragraphs, with acoustic source identification used as an example.

The set of potential values for the unknown parameters, hereafter referred to as *search parameters*, constitutes the candidate solution member. In the context of acoustic source identification, these parameters encompass the source location coordinates (x, y, z) and the source autopower s^2. The Sound Pressure Level (SPL) can easily be derived from the autopower as $10\log_{10}\left(\frac{0.5s^2}{p_{\text{ref}}^2}\right)$. For a single source scenario, a candidate solution member contains four search parameters, denoted as $\boldsymbol{m} = (x, y, z, s^2)$. In cases involving K_{src} sources, the candidate solution member expands accordingly. In the specific instance of an experimental case featuring three sources, the candidate solution member is represented as $\boldsymbol{m} = [\boldsymbol{m}_{k=1}, \boldsymbol{m}_{k=2}, \boldsymbol{m}_{k=3}]$.

The initial population of candidate solutions is randomly generated within predefined search boundaries. To iteratively minimise the energy function, the candidate solutions undergo updates via DE. This approach aligns with Darwin's Evolution Theorem, where natural selection occurs over multiple generations based on the fitness of a population member. The updated candidate solution members, termed descendants $\boldsymbol{d}$, are derived from an original population member $\boldsymbol{m}$ in conjunction with a partner popula-

tion member $\boldsymbol{s}$. The partner population mirrors the original population in size, where population size is defined as q, and is formed through a combination of original population members. A partner population member is formulated as:

$$\boldsymbol{s}_{\gamma,r_1} = \boldsymbol{m}_{\gamma,r_2} + F(\boldsymbol{m}_{\gamma,r_3} - \boldsymbol{m}_{\gamma,r_4}), \tag{3.16}$$

where γ denotes the generation and r signifies the population member index. The partner population comprises members from the same generation γ but different original members r, ensuring mutual exclusivity. The partner member is thus created by the values of an original member and F times the difference between two other original members. The multiplication factor F dictates the degree of dissimilarity between the partner member and the first original member, with a larger F generating greater exploration of the search space and vice versa.

The crossover between a current population member $\boldsymbol{m}$ and a partner population member $\boldsymbol{s}$ occurs per search parameter, based on a uniform crossover realisation b to a predefined probability p_c. The parameters of the descendant $\boldsymbol{d}$ for u, indicating the parameter number ranging from 1 to the number of search parameters, are

$$d_{\gamma,r,u} = \begin{cases} m_{\gamma,r,u} \text{ if } b \geq p_c \\ s_{\gamma,r,u} \text{ if } b < p_c \end{cases} \tag{3.17}$$

thus a larger p_c results in more exploitation (of the partner population) and vice versa. The population of descendants is evaluated based on the energy function. Descendants with lower energy compared to the original population member are included in the next generation, and vice versa. Options for energy functions are further specified in Section 3.2.5.

This iterative process repeats for a finite number of generations N_{gen} to ensure convergence. The outcomes contribute to the analysis of the energy landscape, with a focus on escaping the local optima. Multiple independent runs (N_{runs}) are conducted, to ensure finding the most optimal outcome. The performance of the algorithm is thus influenced by the *setting parameters* encompassing q, F, p_c, N_{gen}, and N_{runs}. These parameters together determine the number of forward calculations needed to achieve conversion, where N_{forward} is defined as

$$N_{\text{forward}} = q N_{\text{gen}} N_{\text{runs}}. \tag{3.18}$$

Importantly, the number of forward calculations is independent of the number of search parameters, allowing for a comparison with the calculations required in acoustic imaging methods such as CFDB, where it depends on the number of grid points.

ENERGY FUNCTIONS

Beamforming methods employ a (least-squares) cost function to determine the source level at predefined grid points. A high level indicates a good match and hence a local or global optimum. In contrast, Global Optimisation (GO) uses a cost function to assess whether it has reached an optimum for the estimated search parameters. This cost function is not a direct output but is typically defined to minimise an error, i.e., in this

dissertation, the error between a modelled and a measured pressure field. For source identification, two main cost functions are used: the Bartlett equation and the CSM equation. The Bartlett equation closely resembles the beamforming equation, while the CSM equation incorporates more source information and can potentially address some limitations of beamforming, such as the presence of multiple sources and the spatial resolution limit [137].

The energy function in this dissertation is based on the latter, i.e., minimising the difference between the measured CSM and the modelled CSM. This function utilises the phase and amplitude information present in the CSM. Since a CSM can be deconstructed into individual CSMs for each incoherent source, such as in CLEAN-SC [145], this energy function can account for the simultaneous presence of multiple sources by adding them in the modelling process.

A modelled pressure vector at the microphone can be constructed according to Equation 3.11 with the information present in $\boldsymbol{m}$. The source amplitude s can be used directly, while the steering vector is constructed with Equation 3.12 in which $\boldsymbol{\xi}_j$ is replaced by the (x, y, z) of $\boldsymbol{m}$. When multiple incoherent sources are present, the CSM is modelled for all sources K_{src} separately and then summed to obtain $\boldsymbol{C}_{\text{mod}}$ as

$$\boldsymbol{C}_{\text{mod}}(\boldsymbol{m}, f) = \sum_{k=1}^{K_{\text{src}}} \frac{1}{2} \boldsymbol{P}_{\text{mod}}(\boldsymbol{m}_k, f) \boldsymbol{P}^*_{\text{mod}}(\boldsymbol{m}_k, f). \tag{3.19}$$

The energy of a solution, E_{CSM}, is finally computed as

$$E_{\text{CSM}}(\boldsymbol{m}, f) = \sum_{\text{elements of CSM}} |\boldsymbol{C}_{\text{mod}}(\boldsymbol{m}, f) - \boldsymbol{C}_{\text{meas}}(f)|^2. \tag{3.20}$$

SENSITIVITY ANALYSIS FOR SETTING PARAMETERS

The DE algorithm's search settings vary across different publications, reflecting the diversity of applications and available computational resources [137, 146–148]. Typically, a lower F value reduces the exploration capability within the search space, necessitating a larger population size q if the number of generations N_{gen} remains unchanged. This, however, increases the number of forward calculations and thus the computational cost. Similarly, a lower p_c diminishes the exploitation of promising search parameters in the partner population. Hence, achieving an optimal balance between F and p_c is crucial for a given population size and number of generations.

This balance can be found through a sensitivity analysis at the start of the research. The most complex case for which the true solution is known, should be evaluated with different combinations of q, F, and p_c for a high value of N_{gen}. The final energy of the best run, i.e., the one with the lowest final energy, per combination of search parameters is then evaluated, along with the N_{gen} at which the search converged. If multiple combinations of search parameters result in convergence, the least computationally expensive solution should be chosen. Additionally, N_{gen} can be adjusted to a lower number if the solution converged sufficiently early.

4

Sound quality aspects

The loudest noise in the world,
is silence.

Thelonious Monk

Sound levels are not representative of the human perception of sound. The human perception is influenced by the contribution of different frequencies, the presence of tonal content, and the presence of fluctuations in level or frequency. This is captured in so-called sound quality metrics. The sound quality metrics can be combined to form a prediction of psychoacoustic annoyance. This chapter covers the sound quality metrics, some psychoacoustic annoyance models, and lastly touches upon psychoacoustic experimental design which is used to validate annoyance models.

Although traditional acoustic source identification methods primarily focus on the level and location of a source, Sound Quality Metrics (SQMs) can also aid in assessing a noise source. For instance, a vacuum cleaner is identifiable by its roughness, while a helicopter is characterised by the impulsive noise generated by blade vortex interaction.

Six commonly used sound quality metrics are loudness (N), sharpness (S), roughness (R), fluctuation strength (FS), tonality (K), and impulsiveness (I) [149, 150]. These metrics are often combined into a single metric called psychoacoustic annoyance (PA), which aims to reflect the annoyance perceived in listening experiments [130]. The human ear is not equally sensitive to all these metrics, as indicated by the Just Noticeable Difference (JND) values for the models that are used in this dissertation in Table 4.1 [130, 150]. For example, a change in loudness is perceptible at a 7% difference, whereas other metrics require a larger variation to be noticeable. It should be noted that, to the best of the author's knowledge, no JND tests have been conducted for impulsiveness, as it remains a relatively unexplored sound quality metric. Figure 4.1 shows the expected importance of individual SQMs towards perceived annoyance, where red indicates relatively the strongest importance and green the lowest importance.

Table 4.1: Range and Just-Noticeable Differences per major SQM, for which impulsiveness is excluded as these have not yet been defined in literature [22, 150, 151].

SQM Dimension (symbol)	**Model**	**Range (unit)**	**JND (%)**
Loudness (N)	ISO532-1:2017 [152]	0 - 120 (sone)	$\Delta N = 7\%$
Tonality (K)	Aures [153]	0 - 1 (t.u.)	$\Delta K = 10\%$
Sharpness (S)	DIN 45692:2009 [154]	0 - 10 (acum)	$\Delta S = 10\%$
Roughness (R)	Daniel & Weber [155]	0 - 3.2 (asper)	$\Delta R = 17\%$
Fluctuation Strength (FS)	Osses [156]	0 - 3 (vacil)	$\Delta FS = 10\%$

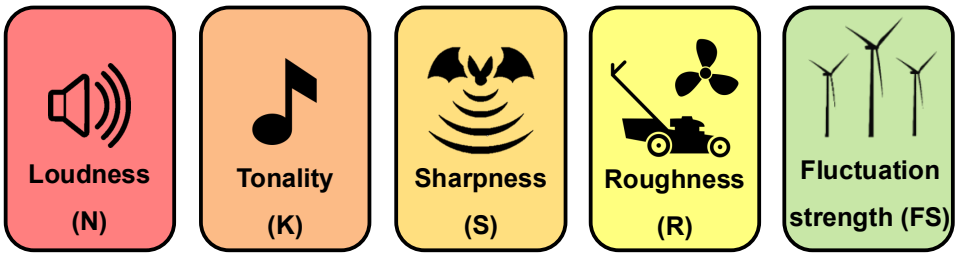

Figure 4.1: Relative importance in perceived annoyance for the most studied SQMs. Left (red) indicates more importance and right (green) indicates less importance. Graphical representation courtesy of Roberto Merino-Martínez.

SQMs are typically presented as a 5th percentile value, which represents the value exceeded in 5% of the time samples. This should not be confused with the 95th percentile, which is *not* reached in 5% of the time.

While there are a few models available for each metric, only the ones that have been used in this dissertation are described in the following sections. In this dissertation, the

SQMs have been computed with the use of the Sound Quality Analysis Toolbox (SQAT) V1.1 [22].

4.1. CRITICAL BANDS

The human hearing system can be modelled as a filter bank with overlapping frequency-dependent bandpass filters, known as critical bands [130]. Sounds within the same critical band cannot be perceived separately, a phenomenon known as masking, thus one sound can mask another if they share the same band.

Masking can occur in both the time and frequency domains, affecting both broadband and tonal sounds. Post-masking is stronger than pre-masking, meaning a masker remains effective even after it ceases. Post-masking can last up to 200 ms, whereas pre-masking only affects the 20 ms before the masker begins [130]. Generally, a masker more effectively masks higher frequencies than lower ones. Additionally, white noise is a more effective masker than tonal noise, even at levels significantly lower than the source of interest.

The Critical Band Width (CBW) can be approximated as

$$\mathrm{CBW}(f) = \begin{cases} 100, & \text{if } f < 500 \text{ Hz} \\ 0.2f, & \text{otherwise} \end{cases} \tag{4.1}$$

where f is the frequency of interest. The CBW is used to calculate some of the SQMs discussed in the following sections.

4.2. LOUDNESS

Loudness refers to the subjective perception of sound level, which can be expressed on a logarithmic scale as phon or on a linear scale as sone, with a 1 kHz tone at 120 dB corresponding to 120 phon or 256 sone [152]. Loudness depends on the frequencies present, the signal duration, and the level at each frequency. For broadband noise, spectral density is crucial, as lower spectral densities over a wider bandwidth can achieve the same loudness due to integration across critical bands. Figure 4.2 indicates this effect; while both signals have the same OSPL, the loudness is different due to the difference in spectral density.

Loudness (N) is calculated according to ISO 532-1:2017 [152]. All measurements in this dissertation were conducted in a free-field environment, so corrections for diffuse fields are not applied, although they could be in between step 5 and 6 if necessary. The signals in this research are time-varying, so the full approach is detailed below. For stationary signals, steps 1 (splitting into 2 ms intervals), 7, and 9 can be omitted. The steps for loudness are:

1. Decompose the input signal (SPL or time-pressure) into 28 one-third octave bands per 2 ms snapshot.

2. Smooth the one-third octave bands with third-order low-pass filters.

3. Construct critical band levels (L_{CB}) by applying corrections to the one-third octave bands.

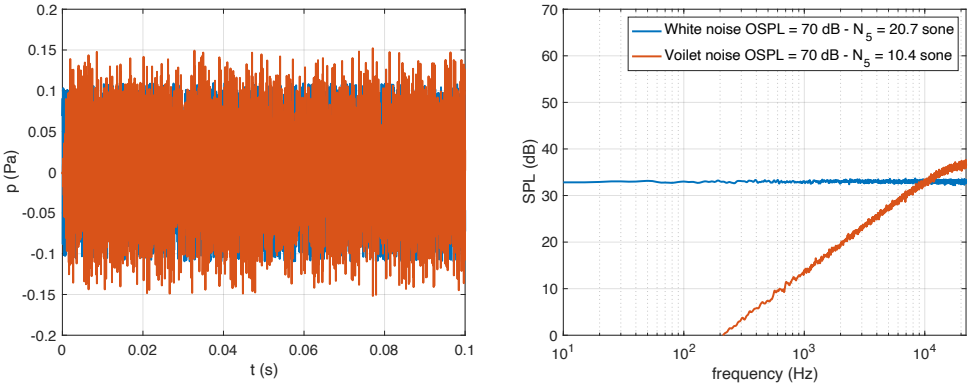

Figure 4.2: Example for loudness with the time-domain and frequency-domain content of a white noise signal and a violet noise signal with equal OSPL, but different power spectral density where violet noise has more high frequency content in comparison to white noise.

4. Combine lower frequency bands, resulting in 20 critical bands.
5. Apply the ear's transmission characteristics a_0 as $L_{CB} - a_0$.
6. Calculate core specific loudness N'_c for each critical band z_C at each time step t, where $LCB > L_{TQ}$, as

$$N'_c(t, z_C) = \left(0.0635 \cdot 10^{0.025 L_{TQ}}\right)\left(\left(0.75 + 0.25 \cdot 10^{0.1(L_{CB} - L_{TQ})}\right)^{0.25} - 1\right) \tag{4.2}$$

with L_{TQ} denoting the threshold in quiet.

7. Account for the nonlinear temporal decay of the human ear through an electrical circuit analogy.
8. Convert $N'_c(t, z_C)$ to 24 unmasked critical bands using conversion tables, resulting in unmasked specific loudness $N'(t, z_C)$.
9. Account for pre-masking and post-masking using first-order low-pass filters.
10. Compute total loudness by integrating $N'(t, z_C)$ over the critical bands as:

$$N(t) = \int_0^{24} N'(t, z_C) dz_C \tag{4.3}$$

4.3. TONALITY

Tonality (K) measures the perceived strength of tones within a sound, on a scale from 0 to 1 for Aures' model [153]. This metric is significant as higher tonality is generally perceived as more annoying, even at the same sound pressure level as a broadband signal [19, 130]. Examples include a flute's tone or noise from the cavities in A320 landing gear [67]. Figure 4.3 shows a white noise signal and a 1 kHz tone. Both signals have an OSPL of 70 dB, but their tonality is diametrically opposed.

The unmasked tonality, as described in Aures' model, is computed as [153]

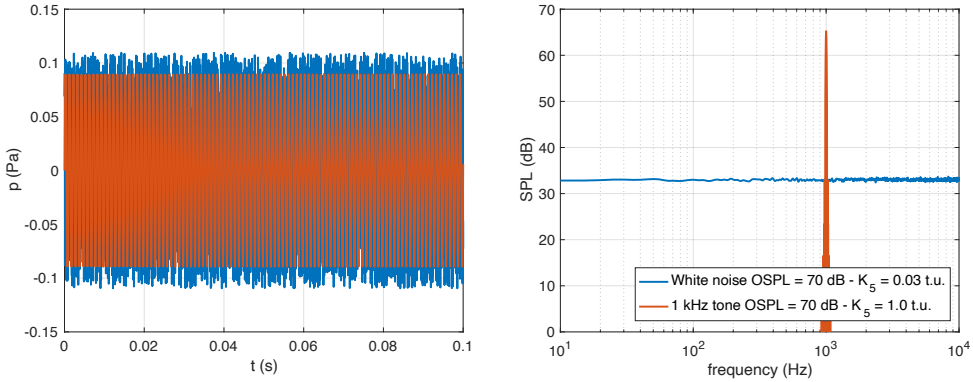

Figure 4.3: Example of the time-domain and frequency-domain of a white noise signal and a 1 kHz tone with equal OSPL.

1. Compute the narrowband spectrum of the signal in sample blocks of 80 or 160 ms.

2. Identify peaks in the spectrum that protrude by more than 7 dB from surrounding frequencies or critical bands.

3. Compute the SPL excess ΔL per tone i to identify the aurally relevant, i.e., unmasked and audible, tones

$$\Delta L_{i'} = L_{i'} - 10\log_{10}\left(\left(\sum_{k_t \neq i'}^{n_{\text{tones}}} A_{Ek_t}(f_{i'})\right)^2 + E_{Gr}(f_{i'}) + E_{HS}(f_{i'})\right) \tag{4.4}$$

where i' is the index of the tonal component, k_t represents the k_t^{th} tone, and n_{tones} the number of tones. A_{Ek_t} accounts for mutual masking of tonal components based on excitation level L_{Ek_t}. E_{Gr} provides masking of broadband noise in a 1 Bark band around the tone, and E_{HS} represents the threshold of hearing.

4. Using the SPL excess, in combination with tonal frequency and bandwidth, calculate the tonal weighting W_T as

$$W_T = \sqrt{\sum_{i'=1}^{n_{\text{tones}}} \left(w_1(\Delta z_{C,i'})\, w_2(f_{C,i'})\, w_3(\Delta L_{i'})\right)^{2/0.29}} \tag{4.5}$$

with weighting functions w_n for tonal bandwidth, tonal frequency, and SPL excess, respectively.

5. Compute the loudness weighting W_{Gr} representing the tones-removed signal as

$$W_{Gr} = 1 - \frac{N_{Gr}}{N} \tag{4.6}$$

where N_{Gr} is the loudness without tonal components, and N the output of Equation 4.3.

6. Calculate the tonality K as

$$K = C_T W_T^{0.29} W_{Gr}^{0.79} \tag{4.7}$$

with $C_T = 1.11$ for this work, based on a tonality calibration signal.

4.4. SHARPNESS

Sharpness quantifies the proportion of high-frequency content relative to the overall content of a signal [157]. A typical example of sharpness is the screeching sound produced by a microphone feedback loop during testing or speaking. Figure 4.4 indicates the sharpness of two signals with equal OSPL but different high frequency content.

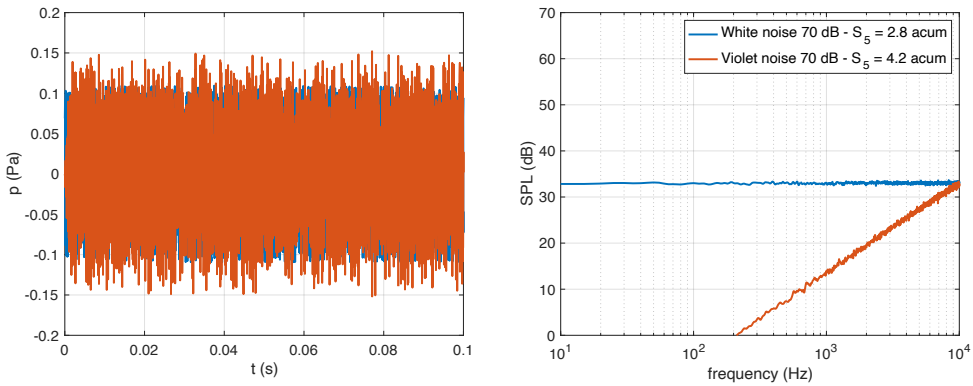

Figure 4.4: Example for sharpness with the time-domain and frequency-domain content of a white noise signal and a violet noise signal with equal OSPL, but different power spectral density where violet noise has more high frequency content in comparison to white noise.

Sharpness (S) is defined in DIN 45692:2009 [154] and measures the ratio of weighted loudness to total loudness, with increased weighting for loudness at $z_C \geq 15.8$ Bark, corresponding to 3054 Hz. The following steps can also be applied to a time-varying signal, although for simplicity, this is not detailed here.

1. Compute specific loudness $N'(z_C)$ according to ISO 532-1:2007.

2. Calculate the weighting function per critical band z_C as

$$g(z_C) = \begin{cases} 1, & \text{if } z_C < 15.8 \text{ Bark.} \\ 0.15e^{0.42(z_C - 15.8)} + 0.85, & \text{if } z_C \geq 15.8 \text{ Bark.} \end{cases} \tag{4.8}$$

3. Calculate total sharpness, with $C_S = 0.11$ as

$$S = C_S \frac{\int_0^{24} N'(z_C) g(z_C) z_C \, dz_C}{N}. \tag{4.9}$$

4.5. ROUGHNESS

Roughness (R) represents the perception of fluctuating loudness in sounds, whether caused by amplitude or frequency modulation, with relatively fast modulation frequencies. Roughness peaks at a 70 Hz modulation frequency and is negligible below modulations of 10 Hz and above 500 Hz modulation [155]. Generally, roughness is perceived maximum between 15 Hz and 300 Hz modulation frequencies, as these modulations occur too rapidly for the human ear to discern separately. Examples of rough sounds include an electric razor or a chainsaw. Figure 4.5 indicates what happens to the roughness level when a white noise signal is amplitude modulated with a modulation frequency of 70 Hz.

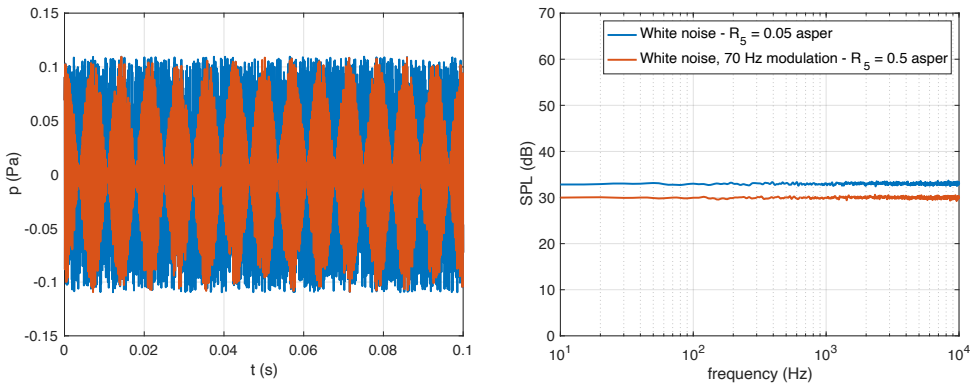

Figure 4.5: Example of the time-domain and frequency-domain of a white noise signal and a modulated white noise signal. The modulation frequency is 70 Hz, which results in high roughness values.

Amplitude modulation involves periodic increases and decreases in sound level, akin to turning the volume up and down. Frequency modulation, often resulting from the interaction of multiple tones in the signal, can cause constructive or destructive interference. For frequency modulation to occur, two frequencies should typically be within the same critical band [130].

Roughness is calculated according to Daniel & Weber's model which is a modified version of Aures' model designed to more accurately capture JNDs [155]. The steps are:

1. Divide the input signal into blocks of 0.2 s, and transform each block into the frequency domain.

2. Convert the blocks into 47 overlapping excitation patterns $e_{0,R,i}(t)$, each with a 1 Bark bandwidth, simulating the basilar membrane.

3. Apply weighting to each excitation pattern $e_{0,R,i}$ in the frequency domain to model the band-pass characteristic for the modulation frequency f_{mod}, resulting in $e_{R,i}(t)$.

4. Estimate the generalised modulation depth $m^*_{R,i}$ for each pattern using

$$m^*_{R,i} = \frac{\text{rms}(e_{R,i}(t))}{\overline{e_{0,R,i}(t)}}. \tag{4.10}$$

5. Calculate the specific roughness (R') as

$$R'_i = C_R \left(g_R (z_{C,i} m^*_{R,i} k_{i-2} k_i \right)^2 \tag{4.11}$$

where $C_R = 0.5$, k_i is the cross-correlation between $e_i(t)$ and $e_{i+2}(t)$, k_{i-2} is the cross-correlation between $e_{i-2}(t)$ and $e_i(t)$, and g_R is a weighting factor for the carrier frequency.

6. Calculate total roughness R by integrating over all excitation patterns, with $\Delta z_C = 0.5$, using

$$R = \Delta z_C \sum_{i=1}^{47} R'_i. \tag{4.12}$$

4

4.6. FLUCTUATION STRENGTH

Fluctuation Strength (FS) measures the perception of slow fluctuations in amplitude or frequency, reaching its peak at a 4 Hz modulation frequency and is negligible below modulations of 0.25 Hz and above 32 Hz [130]. Examples of sounds with strong FS include the test alarm in the Netherlands (first Monday of the month at 12:00), which has noticeable loudness fluctuations, and the swooshing of wind turbine blades when standing directly underneath them. Figure 4.6 indicates what happens to the fluctuation strength when a white noise signal is amplitude modulated with a modulation frequency of 4 Hz.

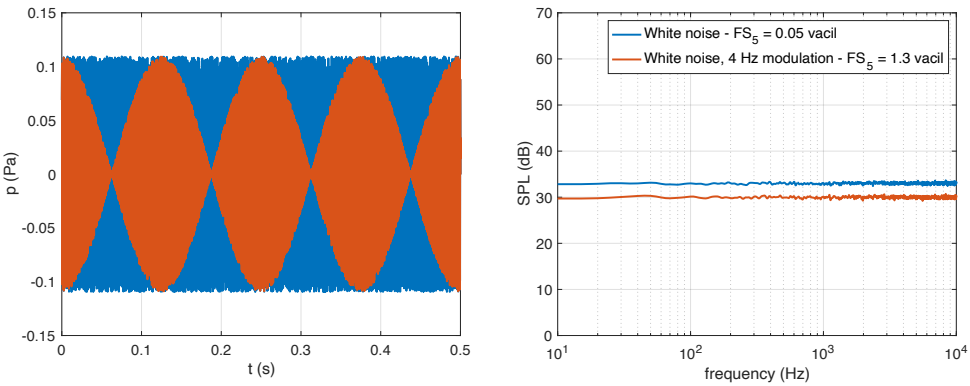

Figure 4.6: Example of the time-domain and frequency-domain of a white noise signal and a modulated white noise signal. The modulation frequency is 4 Hz, which results in high fluctuation strength values.

The FS model used in this dissertation, adapted from Osses [156], follows these steps:

1. Divide the input signal into blocks of 2 s with 90% overlap in the frequency domain.

2. Transform these blocks into 47 overlapping excitation patterns $e_{0,FS,i}(t)$, resembling the basilar membrane, with bandwidths of 1 Bark.

3. Weight each excitation pattern $e_{0,FS,i}$ in the frequency domain to model the bandpass characteristic for the modulation frequency f_{mod}, resulting in $e_{FS,i}(t)$.

4. Estimate a generalised modulation depth $m^*_{FS,i}$ per pattern as

$$m^*_{FS,i} = \frac{\mathrm{rms}(e_{FS,i}(t))}{\overline{e_{0,FS,i}(t)}}. \tag{4.13}$$

5. Define the specific fluctuation strength (FS') as

$$FS'_i = C_{FS}\left(g_{FS}(z_{C,i})(m^*_{FS,i})^{p_m}|k_{i-2}k_i|^{p_k}\right) \tag{4.14}$$

where $C_R = 0.498$, $p_m = p_k = 1.7$, k_i is the cross-correlation between $e_i(t)$ and $e_{i+2}(t)$, k_{i-2} is the cross-correlation between $e_{i-2}(t)$ and $e_i(t)$, and g_{FS} is a weighting factor per carrier frequency.

6. Calculate the total FS by integrating over all excitation patterns, with $\Delta z_C = 0.5$, as

$$FS = \Delta z_C \sum_{i=1}^{47} FS'_i. \tag{4.15}$$

4.7. IMPULSIVENESS

Impulsive noise and roughness or fluctuation noise may appear similar since all involve fluctuations over time. However, impulsiveness is characterised by sudden, strong loudness peaks that do not gradually fade in or out like amplitude modulations [158]. Impulses can be generated either as tonal or broadband sounds. Figure 4.7 shows a white noise signal and an impulsive signal, in this case of a recording of a person typing on a typewriter.

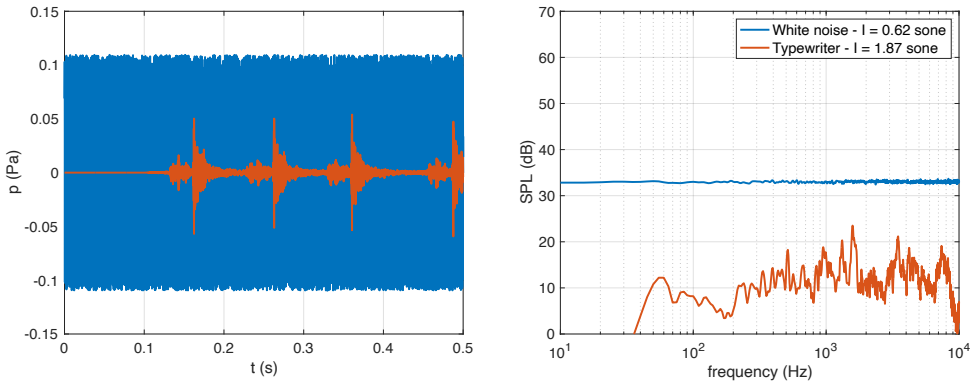

Figure 4.7: Example of the time-domain and frequency-domain of a white noise signal and typewriter noise as impulsive sound.

Several models exist for computing impulsiveness noise, including an ISO standard for IT-related impulsive sounds. However, the ISO standard model has limitations, such as failing to capture the effect of the number of impulsive events or the rapid decay of impulsive noise [159]. Therefore, a time-varying loudness-based measure was suggested by Willemsen and Rao to overcome the limitations. The steps for calculating impulsiveness are as follows [159]:

1. Compute the instantaneous time-varying loudness according to Section 4.2.

2. Determine the baseline loudness level $N_b(t)$ at each time step t as N_{95} for a 1-second interval centred around t of the instantaneous loudness $N(t)$.

3. Calculate the instantaneous impulsiveness $I(t)$ as $N(t) - N_b(t)$.

4. Calculate total impulsiveness I as the average over all T time samples as

$$I = \frac{1}{T}\sum_{t=1}^{T} I(t). \tag{4.16}$$

The final step provides the average impulsiveness over the signal length, effectively reflecting the fraction of time during which impulses are present. More pulses or longer pulses increase the number of samples with impulses, thereby increasing I. This measure does not include frequency weighting, though implicitly loudness accounts for the ear's sensitivity to different frequencies.

4.8. PSYCHOACOUSTIC ANNOYANCE FACTOR

All the previously discussed metrics can be integrated into a single annoyance measure: the Psychoacoustic Annoyance (PA) factor. This metric provides a scale for interpreting annoyance, thereby facilitating a straightforward comparison between different sound samples. In listening experiments, the PA factor normally performs better as a predictor of reported annoyance than conventional metrics such as the A-weighted OSPL (OASPL), Effective Perceived Noise Level (EPNL), or Perceived Noise Level Tone-corrected (PNLT)[160, 161].

Most PA models use weighting factors that account for the influence of each metric while controlling for loudness, as loudness can confound annoyance assessments [130]. The factors w_S, which integrates sharpness and loudness, and w_{FR}, which combines roughness and fluctuation strength, are computed in the same way for most suggested models.

For $S_5 > 1.75$ acum the combination factor is computed as

$$w_S = 0.25(S_5 - 1.75)\log_{10}(N_5 + 10). \tag{4.17}$$

If S_5 is below 1.75 acum, then $w_S = 0$. Loudness amplifies this combination factor: as loudness increases, w_S increases. However, the logarithmic nature of the subfunction means that increases in loudness have a particularly strong effect in low loudness regions ($N_5 < 80$ sone).

For w_{FR}, the combination incorporates not only roughness and fluctuation strength but also includes a reciprocal effect of loudness. This means that as loudness increases, the impact of roughness (R) and fluctuation strength (FS) is diminished. w_{FR} is computed as

$$w_{FR} = \frac{2.18}{N_5^{0.4}}(0.4FS_5 + 0.6R_5). \tag{4.18}$$

Zwicker's PA model combines the four metrics (N, S, FS, R) to calculate the total PA [130]. In this equation, loudness is used as a multiplier for the other factors, thus emphasising its impact. The equation is expressed as:

$$PA = N_5\left(1+\sqrt{w_S^2+w_{FR}^2}\right). \tag{4.19}$$

Following Zwicker's PA factor, researchers tried to better align the PA with perceived annoyance from listening tests. Many studies concluded that incorporating tonality effects would make the metric more representative [20, 149, 162]. In More's revised version, the tonality factor w_T accounts for both loudness and tonality as [20]

$$w_T = \left(1-e^{-0.29N_5}\right)\left(1-e^{-5.49K_5}\right), \tag{4.20}$$

where a higher value of K_5 increases w_T. Due to the asymptotic nature of the subfunctions, the loudness factor reaches a value of 0.99 already at $N_5 = 15.9$ sone. Consequently, More includes w_T in the equation for PA, while additionally changing the weights of the factors, as [20]

$$PA = N_5\left(1+\sqrt{-0.16+11.48w_S^2+0.84w_{FR}^2+1.25w_T^2}\right). \tag{4.21}$$

More places greater emphasis on w_S compared to w_{FR}, in contrast to Zwicker's original equation. In 2016, Di et al. [162] provided another method to compute tonality, as

$$w_T = \frac{6.41}{N_5^{0.52}}K_5 \tag{4.22}$$

which reduces the tonality weighting factor for the same K_5 compared to More. It is included in the Zwicker's PA model with the same weighting as the other combination factors as [162]

$$PA = N_5\left(1+\sqrt{w_S^2+w_{FR}^2+w_T^2}\right). \tag{4.23}$$

For propeller noise there is a new PA model defined by Torija et al. [149], which includes a weighting factor for impulsiveness as

$$w_I = \frac{0.075I_5}{N_5^{-1.334}}. \tag{4.24}$$

The denominator of w_I includes N_5 raised to a negative power, meaning w_I can be expressed as a multiplication of impulsiveness and loudness. This formulation indicates that impulsiveness is weighted more heavily as loudness increases. The factor w_I is included in PA as

$$PA = N_5\left(1+\sqrt{103.08+339.49w_S^2+121.88w_{FR}^2+77.20w_T^2+29.29w_I^2}\right) \tag{4.25}$$

where w_S and w_{FR} are modelled according to Zwicker, and w_T is modelled according to More. Unfortunately, the precise calculation method of I for use in Torija et al.'s

model is not easily traceable. Hence, this dissertation uses the PA factor proposed by Willemsen and Rao to assess the impact of impulsiveness. Their model is based directly on percentile values, rather than weighting factors as seen in the previous models [159]. They suggest

$$PA = 27.73 + 1.24I + 0.86N_5S_{50} + 1.81R_5, \tag{4.26}$$

where I is the impulsiveness metric of Section 4.7, and the other metrics are different percentile values of the other SQMs. Notably, this model differs from others by excluding FS and incorporating sharpness using the 50th percentile rather than the 5th. This approach might yield similar results to the adjustment of S_5 in Equation 4.17. Additionally, unlike other models where loudness is adjusted for in the weighting factors, this PA model does not account for loudness adjustments across the metrics.

4.9. CONSIDERATIONS IN PSYCHOACOUSTIC EXPERIMENTAL DESIGN

Psychoacoustic, or listening, experiments involve exposing participants to various sounds and posing questions about the samples. The questions can include identifying tones within noise, comparing different sounds, or rating annoyance levels, depending on the research goals. In this dissertation, listening experiments are used to rate annoyance of aircraft flyovers in Chapter 9. These experiments were conducted in the PsychoAcoustic LIstening LAboratory (PALILA) of Delft University of Technology. The acoustic characterisation of PALILA is described in Appendix A.

Conducting these experiments presents challenges due to the non-linear nature of human perception and potential confounding factors. Key confounders include loudness, reverberation, hysteresis, and echoic memory [163]. Additionally, the duration of sound samples, test sequences, and order of the samples can affect results due to learning effects or fatigue [164]. Participants' backgrounds can also introduce biases [165].

Loudness can significantly affect perceptions, particularly with tonal sounds. To control for this, experiments should either present tones at multiple loudness levels or control for loudness, with the latter being more common to reduce the number of required samples [19, 163].

Reverberation can impact the perception of sounds typically experienced in free-field conditions, such as aircraft noise. To mitigate this, an anechoic room and over-ear headphones are commonly used. Larger anechoic rooms are preferable as they can more accurately simulate free-field conditions, even for moving sources [166].

Hysteresis, where a system does not immediately return to its original state after excitation, can also affect results. For example, participants might gradually become more annoyed or fatigued, leading to more negative ratings over time. To address this, sound samples should be short, breaks should be included between samples and blocks, and the sample order has to be randomised to average out effects across participants [167].

Echoic memory, lasting for two to four seconds, can influence results when sound samples follow each other closely and thus mask each other [168]. To reduce masking effects, breaks should be scheduled. Additionally randomised tones to clear participants' echoic memory between samples can be used.

Finally, participants' backgrounds can impact results. While it is challenging to quantify and eliminate this bias, a large, diverse sample population that forms a good representation of society with different ages, sexes, backgrounds, demographics, and opinions can help average out these effects [165]. Participants should also be able to disclose any biases related to their proximity to sound sources, economic interests, or attitudes toward specific sounds. This can provide useful insights, even if biases cannot be entirely removed.

5

Assessment of Global Optimisation for Source Identification [1]

In theory, theory and practice are the same.
In practice, they are not.

Albert Einstein

The previous chapter showed that many of the beamforming algorithms suffer from a spatial resolution limitation, also known as the Rayleigh limit. Additionally, many methods need a two-dimensional predefined scan grid to find a source and cannot explicitly account for the presence of multiple sources. In this chapter, the method of Global Optimisation with Differential Evolution is explored as means to overcome the limitations. An experiment with three incoherent speakers in an anechoic room proved that this method can accurately determine the three-dimensional location and the respective sound level of each individual source. In addition, super-resolution is achieved beyond half the Rayleigh resolution limit.

[1] This chapter is an extended version of a paper published in JASA Express Letters [169] and a paper presented at BeBeC 2022 [134]. The dataset is published in the 4TU Research Data repository [170].

5.1. INTRODUCTION

Recent studies by the European Union under the Environmental Noise Directive and the World Health Organization show that a large part of the European population is exposed to noise levels that can be harmful for physical and mental health [2, 3, 171]. Noise exposure can lead to annoyance, hypertension, sleep disturbance, hearing impairment, decreased performance, and ultimately coronary artery diseases [4, 23]. Thus, it is essential to reduce noise levels, which requires accurate knowledge of the location and individual contributions of all noise sources within a system.

To localise and quantify noise sources, phased microphone arrays are typically used. The pressures emitted by a complex sound source can be measured by the microphones in the array and then imaged with a beamforming method. The most well-known method is Conventional Frequency Domain Beamforming (CFDB), see also Section 3.2.3 [41]. Although robust and easy to implement, CFDB suffers from high sidelobe levels and limited spatial resolution [114, 119, 172]. Moreover, CFDB requires an exhaustive search of source locations within a scanning grid. Given the predominant use of planar arrays and their poor resolution in the depth direction, normally two-dimensional scan grids are placed parallel to the array plane [173, 174]. Also, CFDB assumes that a single monopole source is present per grid point, potentially causing an overestimation of the source amplitude when other sources are present elsewhere [175].

Over the past years, a multitude of research was invested in a vast range of acoustic imaging methods to overcome these limitations [133]. Most methods are based on enhancing the CFDB source map through deconvolution, examples of which include DAMAS [176] and CLEAN methods [120, 145, 177]. Modifications to improve the CFDB algorithm also exist, such as Functional Beamforming [178, 179] and Orthogonal Beamforming [180]. This chapter, however, approaches the localisation and quantification of acoustic sources as a Global Optimisation (GO) problem [137].

By using the GO approach, the use of a scan grid is not necessary and a search in three-dimensional (3D) space can be initiated. As was shown in previous research, this approach can be used to determine the location of multiple sources simultaneously, but also determine propagation parameters of the medium such as the sound speed [137, 144, 146–148]. In previous research, simulations of a single point source and multiple point sources were analysed. Additionally, a single speaker in an anechoic room at a single frequency was used to test the algorithm. GO was even applied on an airfoil measurement in an aeroacoustic wind tunnel, although it was concluded that the energy function would have to be changed from a point source to a distributed line source [147].

These cases proved the ability of the algorithm to correctly identify sound sources by explicitly accounting for the simultaneous presence of multiple sources in simulations. However, for the case with multiple sources, all sources had the same normal distance to the array. In reality, sources might be located at different normal distances from the array. Therefore, this research compares the ability to find multiple sources at the same normal distance and at different normal distances, in order to assess whether GO with Differential Evolution (DE) is able to locate real sound sources in a 3D space. Additionally, this research investigates the ability of DE to separate sources below the Rayleigh resolution limit in a multi-source environment.

This chapter is organized as follows: the experimental setup used is described in

Section 5.2 and this section also discusses the optimal settings for DE that were used for this specific experiment. The results and discussion of DE applied to the experimental case are presented in Section 5.3 for the CSM energy function introduced in Section 3.2.5. Section 5.4 presents results for adapted versions of the energy function for broadband sources and for asynchronous measurements. Section 5.5 compares the performance of the proposed method to that of CFDB. Lastly, Section 5.6 contains the conclusions of this research.

5.2. EXPERIMENTAL SETUP

For the experiment, the anechoic chamber of the Faculty of Applied Sciences at Delft University of Technology was used. The room has inner dimensions 8 m by 8 m by 8 m and is covered with 1 m long glass wool wedges, thus its outer dimensions are 10 m by 10 m by 10 m. The chamber is entirely decoupled from the building and has its own support, creating a fully vibration- and (virtually) sound-free room. There is no structural floor present, but there is a wire net on which a rigid floor can be installed if necessary. To set up the equipment for the experiment, a small grid was placed as floor to support the tripod of the microphone array. The sound sources were placed on a separate support system that did not need a rigid floor.

The acoustic measurements were recorded with a CAE Systems Bionic-M microphone array of 1 m in diameter, consisting of 112 MEMS digital microphones. Each microphone was calibrated for phase and amplitude over the full frequency range. The microphone distribution is shown on the left of Figure 5.1. Three microphones were ill-performing and those were taken out of the analysis and hence are not present in the overview. The sound sources were placed in front of the array, on a wooden bar. As sound sources, three Visaton FRWS 5 speakers were used [181]. These speakers were coupled to an amplifier with white noise signals as input, which were generated in Matlab. Each of the speakers had its own input signal, to create incoherent signals. All speakers were set at the same overall sound pressure level of 60 dBA measured at 1 m in front of the speaker baffle at the start of the measurement campaign. An amplitude degradation of source 1 was found throughout the campaign. The combination of three speakers in a 3D domain aims to simulate a complex noise source where multiple closely-spaced elements cause noise.

The reference system is defined from the centre of the microphone array. The bar with the three speakers is located in the xz-plane, thus all speakers have the same y-coordinate of 0 m. One speaker is placed exactly opposite of the centre of the microphone array at a distance of 2.32 m, i.e., $(x, y, z) = (0, 0, 2.32)$. This is speaker 2 (S2), which is the middle speaker. Speaker 1 (S1) is located in negative x-direction at x = -0.3 m and speaker 3 (S3) is located in positive x-direction at x = 0.5 m. S1 and S3 can be moved in z-direction to create two different test cases: (1) all sources at the same z-distance at z = 2.32 m, and (2) all sources at different z-distance for which S1 was moved 10 cm towards the array, to z = 2.22 m, while S3 was moved 20 cm forward to z = 2.12 m. See Figure 5.1 for a top view of the experimental setup with the speaker numbering. Note that for all frequencies above 796 Hz, the array is in the far-field according to the Fresnel distance [182]. Generally, this makes it more difficult to search for z, the normal distance between the microphone and source.

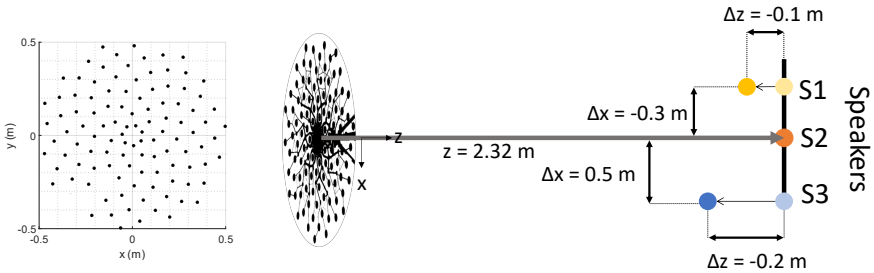

Figure 5.1: (Left) The microphone array distribution as seen from behind. (Right) Top view of the speakers with respect to the microphone array in the anechoic room of Delft University of Technology. The speakers are indicated by dots, with lighter shades for the first position of S1 and S3. Their second position, a darker shade, is set relative to the z-location of S2 to generate out of plane positions.

5

The microphone array is connected to a data acquisition system with a sampling frequency of 48 kHz. From the 15 s of measured signal, a part of 3 s is selected. This part is subdivided into time blocks of 2048 samples (0.043 s) which are averaged over 70 time blocks in the CSM. Thus, the resulting frequency resolution is 23.4 Hz. The results in this chapter are presented for frequencies from 100 Hz to 6000 Hz in steps of two times the frequency resolution to save computational cost.

5.2.1. CHOICE OF OPTIMAL DE SETTINGS

The settings for the DE algorithm vary per publication due to the variety of applications and also the computational budget available [137, 146–148]. In general, decreasing F means a decreased exploration of the search space and therefore a need for a larger population size q when N_{gen} is kept constant. This would however lead to an increase in forward calculations and hence computational cost. The same logic can be applied for decreasing p_c which decreases the exploitation of promising search parameters of the partner population. Thus, an optimal balance between F and p_c should be found for a certain population size and number of generations.

For this chapter an analysis was performed to assess the energy of the final solution as a function of F and p_c for a baseline case. The baseline case is the most complicated case used, which has three different sources in a 3D domain, i.e., case 2 . The case was analysed only at $f = 4992$ Hz for $N_{\text{gen}} = 600$ and $N_{\text{runs}} = 5$. At this frequency, it is possible to recognize the sources separately with CFDB and the image is not corrupted with a high level of sidelobes and thus it is expected that DE will converge well. Two possibilities for the population size, i.e., $q = 64$ and $q = 128$, were considered. The multiplication factor F was increased from 0.2 to 1 in steps of 0.2, while the crossover probability p_c was increased from 0.45 to 0.85 in steps of 0.1. The search was initiated in a 3D space with bounds for x from -2 m to 2 m, for y from -2 m to 2 m, for z from 0 m to 4 m, and for s^2 from 0 Pa^2 to 0.5 Pa^2. These boundaries are used throughout the whole research.

The final energy of the best run, i.e., having the lowest final energy, per combination of search parameters was evaluated. $q = 128$ reached the lowest energy for $F = 0.4$ and $p_c = 0.55$. $q = 64$ has a minimum energy for $F = 0.6$ and $p_c = 0.75$. Although us-

ing $q = 128$ results in a slightly lower energy, it requires more forward calculations than $q = 64$. As both solutions converged, the least computationally expensive solution was chosen. Thus, the final DE setting parameters are $q = 64$, $F = 0.6$, and $p_c = 0.75$. All runs converged to the same final solution.

5.3. APPLICATION ON MULTI-SOURCE CASE

Before the more complex multi-source cases were analysed, the sound emissions of each speaker were analysed individually. This analysis provides an insight in the performance of DE on the experiments which can help in understanding the results of the multi-source cases. The single source analysis is only described here briefly. The case resulted in a perfect match for x and y, and an accurate estimation of the source spectrum. However, an overestimation is present for z over a wide range of frequencies. This overestimation has a maximum around $f = 4008$ Hz of 24 cm, but reduces to 4 cm for $f \geq 7195$ Hz. In this experiment it was not possible to determine whether this offset for z is an effect of the algorithm, the directionality of the source, or perhaps an artifact of the microphone array or other experimental errors. As this offset is already present for the single source results, it was taken into account for the multi-source cases.

5.3.1. SOURCES AT SAME NORMAL DISTANCE

The first multi-source case is the case with the three speakers placed at the same z distance. The results, presented in Figure 5.2, are shown solely for the run resulting in the lowest energy function value with the colours defining the results from different speakers: S1 is yellow, S2 is orange, and S3 is blue. The solid black horizontal lines indicate the true location, while the Rayleigh resolution limit is indicated by the solid vertical gray line. The latter represents the minimum frequency (3236 Hz) at which the two closest spaced sources, i.e., S1 and S2, are separable in a CFDB source map at $z \leq 2.32$ m [118]. In the results for z the true location is indicated, as well as the z estimated by DE for the single source analysis to determine whether multi-source cases find the same offset. For the source amplitude the reference lines were determined by the average SPL in dB measured on the array for a single speaker, which is transferred back to the source by correcting for the spherical spreading. Additionally, the predicted spectra are energetically summed and presented in black and compared with the total measured SPL, corrected to $z = 2.32$ m.

The results in Figure 5.2 show that DE is able to overcome the Rayleigh resolution limit. The x and y location of each sound source are correctly determined for $f \geq 1523$ Hz and $f \geq 1148$ Hz respectively, which correspond to roughly one-half and one-third of the Rayleigh resolution frequency of 3236 Hz. Figure 5.2 also shows that S1 is the weakest source for most frequencies, while S2 and S3 are of comparable strength. Note that although y is the same for all speakers, it does not simplify the search for DE as it still has to find three individual source positions that are not linked to each other. The results for z show similarities with the single speaker results in terms of offset from the true values. All three locations are only found at a similar z for $f \geq 2508$ Hz. The results for SPL show that the individual spectra are determined quite well. However, the total spectrum is slightly overestimated which can be explained from the overestimation of z.

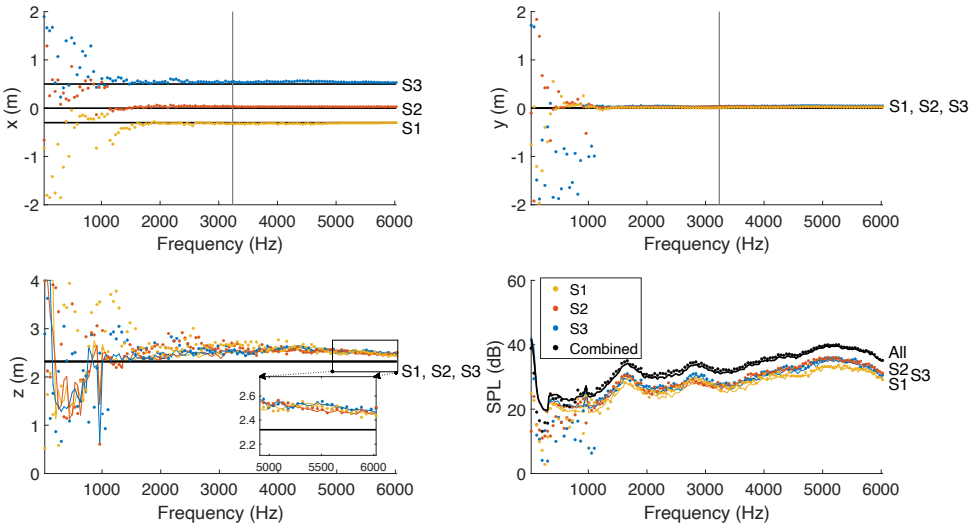

Figure 5.2: Estimated location (x, y, z) and SPL for each speaker per frequency for the case with the same normal distance z. The gray vertical line represents the Rayleigh resolution limit, while the black horizontal lines represent the true source coordinates. For z the coloured lines indicate the values of a single source search, while for SPL the coloured lines indicate the measured SPL in a single source measurement. S1 is yellow, S2 is orange, S3 is blue.

The average offset for $f \geq 1523$ Hz per search parameter is also presented in Table 5.1. The values μ are calculated as modelled value minus true value per parameter and consecutively averaged over the frequency range considered. Thus a positive μ represents an overestimation. The frequency range was chosen as $f \geq 1523$ Hz, because this is the minimum frequency at which both x and y are accurately found. Including offsets for lower frequencies would increase μ and not represent the offset trend well.

Table 5.1: Mean offset between the modelled parameter value and true parameter value for $f \geq 1523$ Hz. For the same z case the mean offset of total ΔSPL is 0.709 dB. For the different z case the mean offset of total ΔSPL is 0.315 dB.

	Same z			Different z		
	S1	S2	S3	S1	S2	S3
$\mu_{\Delta x}$ (m)	-0.016	0.032	0.045	-0.027	0.003	0.022
$\mu_{\Delta y}$ (m)	0.017	0.029	0.042	0.026	0.039	0.039
$\mu_{\Delta z}$ (m)	0.269	0.253	0.229	0.262	0.237	0.167
$\mu_{\Delta \text{SPL}}$ (dB)	0.730	0.413	0.668	0.970	0.133	0.527

Thus, DE with the CSM energy function is successful in quantifying individual sources even under the Rayleigh resolution limit, which is not possible with other energy functions. This is due to the capability of the CSM energy function to account for multiple sources in the model.

This case has already proven two main advantages of DE over CFDB: (1) its ability to

localise sources under the Rayleigh resolution limit, and (2) its ability to correctly quantify individual sources when multiple sources are present.

5.3.2. SOURCES AT DIFFERENT NORMAL DISTANCES

The next case presented in this chapter has three out-of-plane sources as presented in Figure 5.1. The Rayleigh frequency used is the same, although now the distance to the source varies per speaker, yet $z = 2.32$ m is the worst case scenario. The results for this case are shown in Figure 5.3. Note that the total measured SPL is still corrected with $z = 2.32$ m, as it is not possible to correct the combined measured spectrum for individual distances.

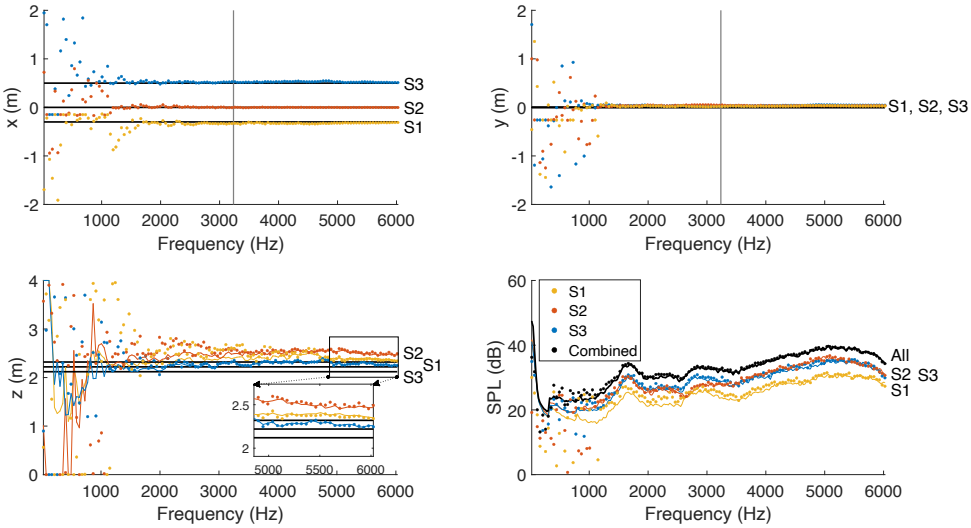

Figure 5.3: Estimated location (x, y, z) and SPL for each speaker per frequency for the case with different normal distances. The gray vertical line represents the Rayleigh resolution limit, while the black horizontal lines represent the true source coordinates. For z the coloured lines indicate the values of a single source search, while for SPL the coloured lines indicate the measured SPL in a single source measurement. S1 is yellow, S2 is orange, S3 is blue.

Again, DE is able to localise the three different sources correctly in x and y below the Rayleigh resolution limit, and it does so for $f \geq 1523$ Hz and $f \geq 1242$ Hz respectively. These new limitations correspond to roughly half the Rayleigh resolution frequency of 3236 Hz. The algorithm has more difficulty finding the correct z locations for the three sources, especially for S1 which is the weakest source. Whereas the two stronger sources already show a constant trend for z for $f \geq 3023$ Hz, this happens only at 4992 Hz for the weakest source (S1). For all three, z is overestimated with the same offset as the single speaker cases, however the relative Δz between the three sources is correct for high frequencies. This overestimation of z results in the same offset for the SPL as was seen for the previous case. Table 5.1 presents the average offset for $f \geq 1523$ Hz per search parameter.

This case proves that DE is also able to find the relative z-distances between sources

at higher frequencies, but that there still is an offset present in the absolute values for z. In the controlled environment used in this research, the offset of a single source can be used to correct for this. However this can be a problem in uncontrolled environments.

5.3.3. SOURCES WITH DIFFERENT LEVELS

For small differences in level, GO is still able to approximately find the source location of a weaker source, however it tends to overestimate the source strength, see Figure 5.3. Unknown source environments likely contain sources with a larger difference in strength. Therefore a test case was proposed where S2 remained at the original strength of 60 dB, while S1 was reduced to 48 dB and S3 was reduced to 54 dB. A 6 dB reduction corresponds to halving the acoustic pressure of the source, so for S1 only a quarter of the original pressure remained. This is a large contrast, but for aerospace applications this is not uncommon [41, 42, 45].

The results of this analysis are presented in Figure 5.4. The locations of the stronger two speakers (S2 and S3) are found correctly, with only slightly more difficulty for S3. However, the location of S1 is not properly identified in x and certainly not in z. The overestimation in z is also reflected in the overestimation in SPL for S1. This leads to a small overestimation for the total measured SPL.

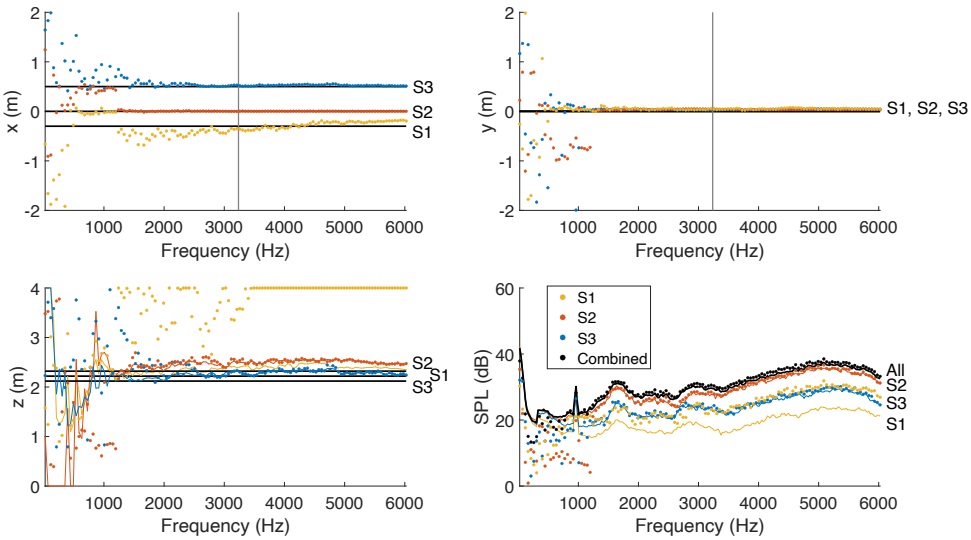

Figure 5.4: Estimated location (x, y, z) and SPL for each speaker per frequency for the case with different normal distances and different levels per speaker. The gray vertical line represents the Rayleigh resolution limit, while the black horizontal lines represent the true source coordinates. For z the coloured lines indicate the values of a single source search, while for SPL the coloured lines indicate the measured SPL in a single source measurement. S1 is yellow, S2 is orange, S3 is blue.

To verify that this is the best solution GO can reach without limitations from the settings, the convergence of the solution over the 600 generations was checked. The solution converged in roughly 350 generations, hence adding extra generations would not improve the results. Thus it is concluded that for a complex acoustic environment with

a difference of more than 6 dB between source levels, the weakest source might not be identified accurately.

5.4. ENERGY FUNCTION ADAPTATIONS FOR COMPLEX SOURCE ENVIRONMENTS

A common method to improve clarity in the beamform map is to apply incoherent summation over a range of frequencies which is especially useful for broadband sources. Another method to improve source localisation with conventional beamforming is the use of asynchronous measurements. Both approaches are considered here and are applied to the second case (Section 5.3.2). The energy function from previous sections was adapted to analyse potential performance improvements. Section 5.4.1 uses an energy function for multiple frequencies. Section 5.4.2 uses an energy function that combines asynchronous measurements.

5.4.1. ENERGY FUNCTION FOR BROADBAND SOURCES

In different beamforming techniques, the use of incoherent addition of the source map over multiple frequencies is used to obtain clean the source map. This is based on the principle that the location of the sidelobes is different for each frequency, but the source remains at the same location. By adding incoherently the source maps of different frequencies, the strength of the mainlobe is amplified with respect to the sidelobes and hence a more clean map appears. For energy functions based on the beamforming output, this can help escape local maxima (sidelobes). The energy function is therefore adapted to sum over the result per frequency, while accounting for a varying SPL per frequency, as

$$E_{\text{CSM,freqs}}(\boldsymbol{m}, f_{\text{range}}) = \sum_{f_{range}} \sum_{\text{elements of CSM}} |\boldsymbol{C}_{\text{mod}}(\boldsymbol{m}_{\text{freq}}, f) - \boldsymbol{C}_{\text{meas}}(f)|^2. \tag{5.1}$$

$\boldsymbol{m}_{\text{freq}}$ contains the source location and the source autopower for the frequency selected. If there is one source which is analysed at three different frequencies, then the candidate solution member $\boldsymbol{m}$ can be described as $\boldsymbol{m} = (x_1, y_1, z_1, s^2_{1,\text{freq }1}, s^2_{1,\text{freq }2}, s^2_{1,\text{freq }3})$.

This adapted energy function was applied to the case presented earlier, with different normal distances between the sources. A comparison was made between the single frequency analysis at 4992 Hz and a multi-frequency analysis that incorporated frequencies 4992 Hz to 5085 Hz. To compensate for the increased number of search variables, N_{gen} was increased to 1000 generations. Table 5.2 shows the results of both methods.

Unfortunately this adaptation to the energy function does not improve the source identification.

5.4.2. ENERGY FUNCTION FOR ASYNCHRONOUS MEASUREMENTS

With well-established beamforming techniques, 3D imaging can be achieved by extending the exhaustive grid search from a 2D grid to a 3D grid, i.e., not placing the grid at a certain scan distance. However, with only a single view, this method is limited by the limited resolution in the direction perpendicular to the array. Therefore, several studies

Table 5.2: Comparison between the final results of the single frequency and multiple frequency analyses. The multi-frequency case had 1000 generations and converged in around 800 generations. The single frequency method converged at around 300 out of 600 generations. The offsets are calculated as modelled value minus true value, at f = 4992 Hz with a Δf = 23.4 Hz. The multi-frequency case also considered the 9 frequencies above this.

	Single frequency				Multi-frequency			
	Δx (m)	Δy (m)	Δz (m)	ΔSPL (dB)	Δx (m)	Δy (m)	Δz (m)	ΔSPL (dB)
S1	-0.023	0.03	0.17	1.20	-0.029	0.04	0.21	1.61
S2	0	0.03	0.19	-1.33	0	0.04	0.29	-0.61
S3	0.027	0.05	0.16	0.57	0.03	0.05	0.18	1.01

have proposed the use of 3D arrays or asynchronous measurements from different angles [134, 183]. These methods, although computationally heavy due to the large grid, show that adding an extra dimension in the microphone array improves the localisation results.

5

The use of multiple views that are measured asynchronously was also tested on GO to potentially improve the results in z. To this end, the energy function was adapted to identify a source that is at the same location for all views, but has different source powers per view to account for source directionality differences. If there is one source that is measured from three different viewing angles, then the candidate solution member $\boldsymbol{m}$ can be described as $\boldsymbol{m} = (x_1, y_1, z_1, s^2_{1,\text{view }1}, s^2_{1,\text{view }2}, s^2_{1,\text{view }3})$. This can be expanded to multiple sources. The energy function is adapted to $E_{\text{CSM,views}}$ as

$$E_{\text{CSM,views}}(\boldsymbol{m}, f) = \sum_{\text{views}} \sum_{\text{elements of CSM}} |\boldsymbol{C}_{\text{mod}}(\boldsymbol{m}_{\text{view}}, f) - \boldsymbol{C}_{\text{meas,view}}(f)|^2. \tag{5.2}$$

where $\boldsymbol{m}_{\text{view}}$ is the original $\boldsymbol{m}$ with (x, y, z) corrected for the viewing angle, and s^2 selected to the viewing angle. $\boldsymbol{C}_{\text{meas,view}}$ is the measured CSM corresponding to a specific view.

Using the same settings as before, does not result in proper source localisation or sound level estimate (front view) as can be seen in Figure 5.5. Especially S1, the weakest source, is not identified correctly. This is mostly due to the fact that convergence was not reached within 600 generations. This is potentially due to the extra source strength parameters for different views that GO had to search for.

Table 5.3: Comparison between the final results of the single view and multiple view analyses. The multi-view case has 1000 generations and converged around 800 generations. The single view converged at around 300 out of 600 generations. The offsets are calculated as modelled value minus true value, at f = 4992 Hz with a Δf = 23.4 Hz. The front view SPL is taken for the multi-view case.

	Single view				Multi-view			
	Δx (m)	Δy (m)	Δz (m)	ΔSPL (dB)	Δx (m)	Δy (m)	Δz (m)	ΔSPL (dB)
S1	-0.023	0.03	0.17	1.20	-0.027	0.03	0.21	1.56
S2	0	0.03	0.19	-1.33	0	0.03	0.21	-0.93
S3	0.027	0.05	0.16	0.57	0.029	0.05	0.17	0.91

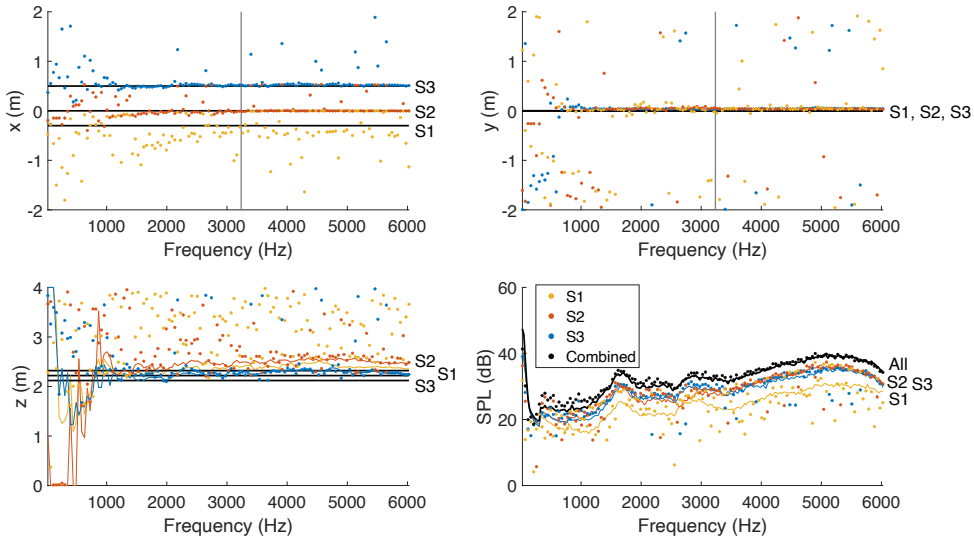

Figure 5.5: Estimated location (x, y, z) and SPL for each speaker per frequency for the case with different normal distances. This is for the algorithm with the combined views. The gray vertical line represents the Rayleigh resolution limit, while the black horizontal lines represent the true source coordinates. For z the coloured lines indicate the values of a single source search, while for SPL the coloured lines indicate the measured SPL in a single source measurement. The SPL is that of the front view of the speaker. S1 is yellow, S2 is orange, S3 is blue.

By increasing the number of generations from 600 to 1000, convergence is achieved around 800 generations when applying the algorithm for $f = 4992$ Hz. Interestingly, the final results for this frequency are not better than those for the single view, as can be seen in Table 5.3. This might be due to the directionality of the speakers, which were found to be resembling a dipole. The source identification for the side views may be hampered by this.

5.5. PERFORMANCE WITH RESPECT TO OTHER IMAGING METHOD

A comparison was made between DE and CFDB, to provide a first indication of the performance of DE. CFDB was applied to the case with different z for a frequency of 4992 Hz with a Δf of 23.4 Hz, as a comparison is only fair well above the Rayleigh resolution limit which CFDB suffers from. For this case 3D beamforming has to be applied to find the different z and thus a 3D grid of potential source locations was specified with the same boundaries as DE and with a grid step size of 1 cm. This results in 64,481,302 grid points, whereas the necessary forward calculations for DE are 192,000 for 5 runs. It is challenging to compare CFDB and DE in computational time since CFDB requires the calculation of a scan grid. This step is time consuming, however the grid can be reused for every frequency. On the other hand, if DE has well-evaluated setting parameters and thus converges, a single run equals one CFDB source map. To give the reader an initial indication, DE took 179 s for a single run and CFDB took 309 s for a single frequency on

a DELL (Round Rock, TX) Precision Tower 5810 x64-based personal computer (PC), with a 4-core Intel (Santa Clara, CA) Xeon central processing unit (CPU) E5-1620 at 3.50 GHz with 64 GB RAM.

Table 5.4 shows the offsets per method per source calculated as modelled value from CFDB or DE minus the true value. The offsets found with DE are generally slightly lower, hence indicating a more accurate result which holds for any frequency above the Rayleigh resolution limit of 3236 Hz. Especially for z DE shows an increased accuracy. For y both methods show a similar offset of 3 or 4 cm, which is most likely caused by measurement inaccuracies due to the non-rigid floor in the anechoic room.

Table 5.4: Offsets found by 3D CFDB for each of the sources in the case with different z compared to the offsets found by DE at the same frequency. The offsets are calculated as modelled value minus true value, at f = 4992 Hz with a Δf = 23.4 Hz.

	CFDB				DE			
	Δx (m)	Δy (m)	Δz (m)	ΔSPL (dB)	Δx (m)	Δy (m)	Δz (m)	ΔSPL (dB)
S1	-0.02	0.04	0.20	1.30	-0.023	0.03	0.17	1.20
S2	0	0.04	0.28	-0.24	0	0.03	0.19	-1.33
S3	0.03	0.05	0.20	1.10	0.027	0.05	0.16	0.57

5

DE was also compared to a set of three-dimensional acoustic imaging methods that used asynchronous measurements [134]. These imaging methods were applied on the measurement per view angle, after which a combined source map was constructed by using the geometric mean of the separate source maps. For CFDB, adding additional views improved the source localisation above the frequency corresponding to the Rayleigh resolution limit, but the quantification was hampered likely due to directionality effects of the sources. The quantification for DE with a single viewpoint remains of comparable accuracy as that of CFDB with a single view measurement, and the localisation is slightly better than CFDB with three asynchronous measurements.

5.6. CONCLUSIONS AND OUTLOOK

In this research the applicability of Differential Evolution (DE) with the Cross-Spectral Matrix (CSM) energy function as Global Optimisation method to identify multiple acoustic sources was investigated. Additionally, the analysis was used to assess the identification of sources below the Rayleigh resolution limit and simultaneously find sources that are at different normal distances to the planar microphone array.

The algorithm was applied to an experimental case with three speakers, which emitted incoherent white noise, in an anechoic room. For the first case, the three speakers had the same normal distance z to the array. DE was able to accurately localise the speakers in x and y, but overestimated z with 15 cm with respect to the true distance of 2.32 m. This offset however is comparable to the offset when DE was applied for a single source. The x, y, and Sound Pressure Level (SPL) were correctly determined even under the Rayleigh resolution limit, i.e., the spatial resolution was improved by approximately a factor two with respect to Conventional Beamforming.

For the second case, the speakers were located at different normal distances to the

microphone array. Again, DE was able to accurately localise the speakers in x and y, with a two times better spatial resolution than conventional acoustic imaging methods. The SPL is also determined accurately, however with an overestimation for the weakest source. This offset can be explained by the overestimation that DE found in z. Again, the algorithm had difficulty determining z for each source, especially at low frequencies for the weakest source. However, for higher frequencies the final solution was stable and the three sources were found at the correct distances with respect to each other.

The method also was applied to a case where the source levels vary. The case has one dominant source and two sources at -6 dB and -12 dB from the level of the main source respectively. Such a situation can occur in unknown source environments such as aircraft noise measurements, where various source components play a role. DE was able to accurately identify the source at -6 dB, but was unable to identify the source at -12 dB in terms of z and level.

Two improvements for source localisation that are commonly applied for beamforming algorithms were also applied to DE by using an adapted energy function. The first improvement was the use of multiple frequencies to identify a single source location, which can be useful for broadband sources to escape local maxima. The second improvement was the use of asynchronous measurements at various view angles which were hypothesised to improve the localisation in z. However, both adaptations did not improve results compared to the original implementation at a single frequency with a single view.

Compared to other acoustic imaging methods, even when they employ combined results of asynchronous measurements, DE is better in localisation in x and y and provides more accurate source level estimates. Additionally, DE requires less forward calculations for a single frequency than three-dimensional acoustic imaging methods to find source locations with a high accuracy, as for CFDB the grid step should be reduced to do so while DE can search grid free.

The advantages of DE with the CSM energy function as presented in this research are fourfold: (1) it is able to accurately quantify individual sources in a multi-source environment, (2) it is able to localise and quantify sources even under the frequency corresponding to the Rayleigh resolution limit, (3) it is able to find the respective normal distances between sources in a 3D space with a planar array, and lastly, (4) it is able to achieve a high localisation accuracy without a fine predefined 3D scan grid thereby reducing computational costs.

6

Noise emissions of taxibotted versus conventional taxiing operations [1]

The most important single ingredient in the formula of success is knowing how to get along with people.

Theodore Roosevelt

This chapter is the first of three chapters in which the signal processing and acoustic imaging methods of the theory chapter (Chapter 3) are applied to a complex source. The source is a pilot-controlled hybrid-electric aircraft-towing vehicle called TaxiBot. The TaxiBot is expected to reduce fuel-burning emissions during the taxiing phase, but it is unknown what the effect of its noise emissions are on ground workers. Therefore, noise measurements during operational testing of the TaxiBot were performed and compared to noise measurements on conventional taxiing aircraft. The results indicate that the taxibotted operation is more silent, especially while approaching the observer. At 90°, side view during pass-by, a taxibotted pass-by produces 7.1 dBA less than conventional two-engine taxiing.

[1] This chapter is a revised and extended version of a paper presented at Inter-Noise 2021 [184]. The dataset is published in the 4TU Research Data repository [185].

6.1. INTRODUCTION

Aircraft noise nuisance is not only relevant for communities around airports, but also for airport ground workers. These ground workers are often exposed to high noise levels when aircraft are starting their engines, are taxiing, or are taking off. Especially in the vicinity of ground workers, this noise may cause severe nuisance and even hearing loss in the long term [186, 187]. Usually, it is not possible to measure aircraft noise levels per aircraft as there are high background noise levels and a high number of operations, leaving no safe location for researchers and equipment. However, the COVID-19 pandemic created a unique opportunity at Amsterdam Airport Schiphol. During the pandemic, the airport turned silent due to lower numbers of operations. This resulted in an ideal test ground for a noise assessment of taxiing aircraft. Royal Schiphol Group was investigating the use of a so-called TaxiBot, a hybrid-electric pilot-controlled aircraft push-back and towing vehicle, to reduce the fuel burn emissions during taxiing operations [188]. The TaxiBot is designed by Israel Aerospace Industries and Teleflex Lionel-Dupont (TLD). The pandemic created an opportunity to assess the operational changes and the reduced fuel consumption, and also the noise levels of a taxibotted aircraft versus a conventional taxiing aircraft. Previous studies were performed to assess the noise levels of taxiing aircraft [189, 190], and even a first study comparing taxibotted versus taxiing aircraft was performed in the past [191]. However, these studies were carried out with one or multiple uncoupled single microphones. In the current study, a microphone array is used which provides additional insight into the different noise sources that contribute to the noise levels.

The chapter is organised as follows: Section 6.2 describes the experiment setup used at Amsterdam Airport Schiphol. The results of the noise measurements are described in Section 6.3. The potential impact of the noise emissions on surroundings is discussed in Section 6.4. Section 6.5 contains the conclusion of this research.

6.2. EXPERIMENT SETUP

The noise measurements are recorded when the taxibotted or taxiing aircraft is passing by a microphone array. The TaxiBot-aircraft combination is shown in Figure 6.1. The TaxiBot is a towing vehicle, therefore the aircraft engines remain turned off during the transfer to and from the runway. However, the Auxiliary Power Unit (APU) is turned on to power the aircraft systems. The TaxiBot itself is powered by a combination of diesel and electric engines. For conventional two-engine taxiing aircraft, the APU is turned off and both engines are turned on.

The microphone array used is the Bionic M-112 array by CAE [192]. This array consists of 112 omnidirectional digital microphones with an optical camera in the centre, see the left side of Figure 5.1. Each microphone was calibrated for phase and amplitude over the full frequency range. The array aperture is 1 m and the full setup can be mounted on a tripod. With an additional dB meter the OASPL at the array was recorded for validation of the measurements.

The microphones are connected to a data acquisition system with a sampling frequency of 48 kHz. The microphone array is also equipped with an optical camera with a frame rate of approximately 56 frames/s. In addition to the measurements, data was

Figure 6.1: TaxiBot towing a B737-800 at Amsterdam Airport Schiphol. The CAE Bionic M-112 array is visible on the right side.

gathered on the aircraft and engine type. Also GPS logs of the TaxiBot and aircraft were gathered. The TaxiBot transponder is located on the TaxiBot cabin, while the aircraft transponder is located slightly behind the cockpit. The GPS data had to be smoothed and fitted with a polynomial to take out the irregularity and small offsets present in the data. See Figure 6.2a for the effect of post-processing the longitudinal and lateral distance with respect to the array.

Several measurement campaigns were performed, which started with taxibotted operations on a platform at Amsterdam Airport Schiphol, see the overview in Figure 6.2b with the platform outlined in red. At this location, the microphone array had to be positioned within the red clearance lines for ground workers. On this platform, three different manoeuvres were recorded for three different array locations (L): pass by (L1), a turn ending away from the array (L2), and a turn starting towards the array (L3) when the taxibotted aircraft was driving pattern 1 (P1). These turns are measured to be able to construct a full directionality plot from the noise measurements at the 0° and 180° poles. On the side of the platform, another test was performed with the array at location L4 and the taxibotted aircraft passing by along P2. This last location allowed for a symmetry check between the noise on the right and left side of the aircraft. The sides are defined in the taxiing direction, i.e., the left side is measured when the aircraft passes by from right to left and vice versa. At every location at least three measurements were recorded, which were repeated for two measurement days with two airlines. During all repeat measurements the pilots tried to follow the same path at the same velocity.

The noise measurements of taxiing aircraft are all recorded for aircraft that are returning to the gates after landing. These manoeuvres are planned by air traffic control and thus strategic locations around Schiphol had to be chosen. The chosen locations depended on the runway in use for landing, the availability of taxiways, and the vicinity of other runways. The taxiing aircraft were measured on two separate days, where on the first day a pass-by location along the taxiway to the Polderbaan of Amsterdam Airport Schiphol was chosen, see Figure 6.2c. This location is further from the gates and thus hardly suffers from background noise. At this location 19 aircraft were measured, of which one B737-700 and three B737-800 aircraft.

On the second day of taxiing measurements, the aircraft had to pass through turns

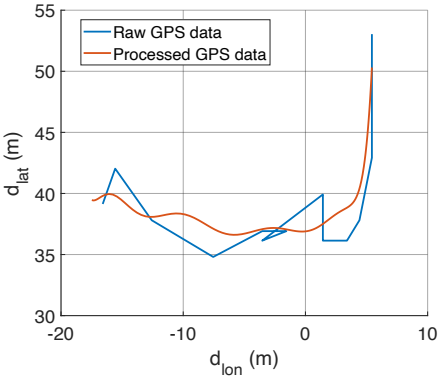

(a) Raw GPS data versus fitted and smoothed data.

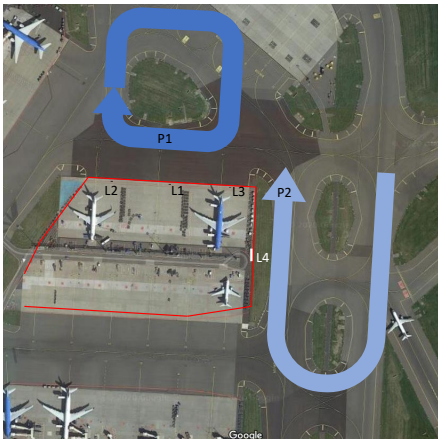

(b) Platform with 4 microphone locations for taxibotted manoeuvres.

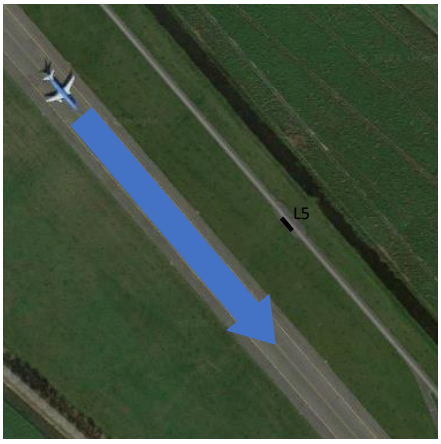

(c) The taxiway towards/from the Polderbaan for taxiing manoeuvres.

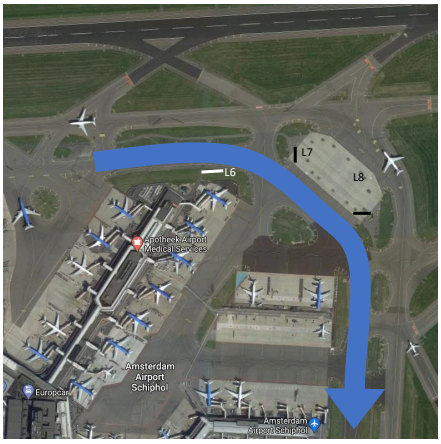

(d) Holding zone with 3 measurement locations for taxiing manoeuvres.

Figure 6.2: Schematic overview of the measurement locations at Amsterdam Airport Schiphol.

to approach or depart perpendicular to the array as was done for L2 and L3 with the TaxiBot. However, there were no suitable 90° turns at the airport. Therefore the locations in Figure 6.2d was chosen. This still allows for a perpendicular approach and departure with respect to the array. Location L6 was chosen to assess the noise symmetry. The right side of the aircraft was measured here and the left side was measured at the Polderbaan. At L6 two measurements of a B737-700 were recorded. At L7 three measurements of the B737-700 were recorded and at L8 two measurements were recorded.

The OASPL was computed on 0.125 s intervals, including a correction for spherical spreading and atmospheric attenuation [193] to the source position. Background levels below 30 dB are removed to prevent amplification in propagation corrections. Welch's spectral estimation method was used for the 0.125 s snapshot with averaging of Hanning

weighted blocks of 2048 samples, with zeropadding of 2048 samples, and an overlap of 50%. The data was recorded at a sampling frequency of 48 kHz. The beamforming maps were based on 2048 samples, with Hanning weighting on the window and zeropadding with a factor two. The source-receiver distance for acoustic imaging was computed with the Haversine equation between the GPS coordinate of the microphone array and the nose of the aircraft or TaxiBot [194]. The acoustic imaging method used here is CFDB, see Section 3.2.3, with the assumption of a non-moving source.

For a pass-by the emission angles for Figure 6.4 are calculated from the GPS data as the angle between the taxi path and the array to the aircraft nose position line. However, the emission angle of the aircraft or TaxiBot during a turn is not necessarily the same as the taxi path due to the object turn angle. Therefore, video footage of one measurement per microphone location is analysed. By determining the projected length of the object versus its real length, the emission angle is calculated. It was assumed that all measurements at the same location have the same relation with the emission angle as the aircraft follow a similar path. Thus a unique relation is assumed between aircraft location and emission angle.

6.3. NOISE EMISSION COMPARISON OF TAXIBOTTED AND TAXIING OPERATIONS

The results first focus on an overall comparison between taxibotted and conventional two-engine taxiing noise measurements in Section 6.3.1. After that, the sources of taxibotted and taxiing operations are investigated in Section 6.3.2 and 6.3.3 respectively. Lastly, a deeper investigation into a specific noise source is presented in Section 6.3.4.

6.3.1. COMPARISON OF TAXIBOTTED AND CONVENTIONAL TAXIING MEASUREMENTS

Figure 6.3 presents the OASPL at the source location for a selected taxibotted and conventional taxiing pass-by. The OASPL is presented against normalised time, where $t = 0$ indicates the time when the aircraft nose is at the centre of the optical camera, to better indicate the impact of a pass-by. The start and end time of the selection represent the time the aircraft or TaxiBot enters (negative time) or leaves the optical camera (positive time). A taxiing aircraft travels faster and the distance to the taxiway was larger. The latter implies that the aircraft was visible for longer, as the field of view is larger for distances further away, but this is counteracted by the faster taxiing velocity.

For the taxiing aircraft two areas of increased noise are visible. The first one is caused by the forward propagating noise from the fan and compressor. The second one is caused by the aftward propagating noise from the fan exhaust, turbine, and combustor noise [45, 191]. The minimum is when the engines are in front of the observer. At the moment of pass-by, i.e., at normalised time 0 s, the difference in source level between the taxibotted and conventional taxiing operation is 7.1 dBA. Shortly after pass-by, this is reduced to a minimum difference of 3.6 dBA. The reason for the increase in noise of the taxibotted aircraft after pass-by is that the APU then becomes present in the noise profile.

The directionality for the taxiing aircraft that was visible in Figure 6.3 is confirmed by the directionality plot in Figure 6.4 with the peak of the combustor noise around 120°.

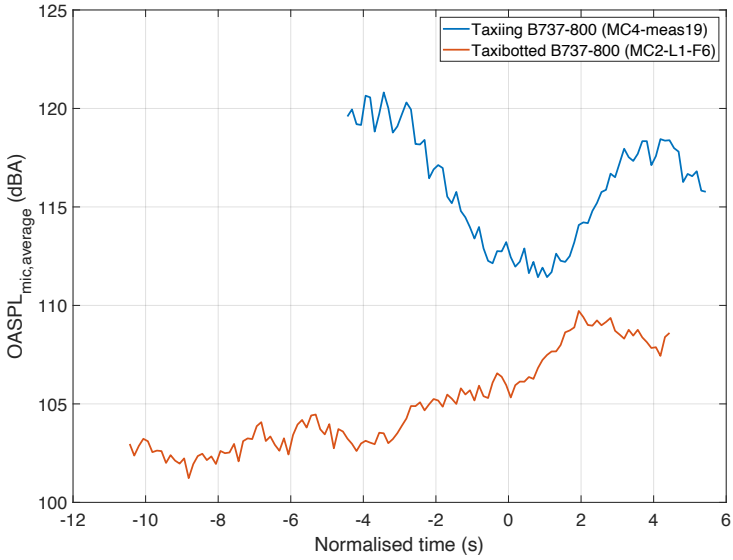

Figure 6.3: OASPL at the source position as a function of normalised time for a taxibotted B737-800 pass-by and a conventional two-engine taxiing B737-800 pass-by. At 0 s the aircraft nose is exactly opposite the receiver.

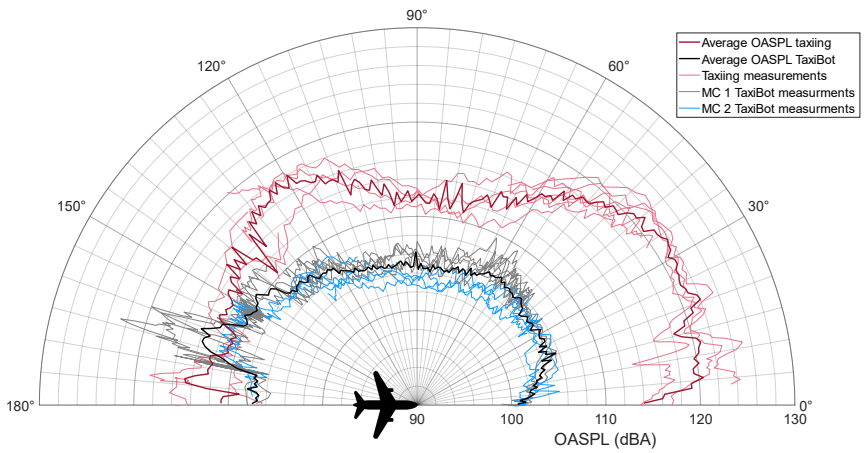

Figure 6.4: OASPL directionality plot at source location for a taxibotted B737-800 on two measurement campaigns (MC1 and MC2) and conventional taxiing with a B737-700 or B737-800.

The variance in the measurements (see different thin lines) can be explained by the different taxiing speeds which varied from 37 to 55 km/h. Besides the generally reduced and more constant levels for the TaxiBot, it also appears that the TaxiBot is especially silent in the forward turning arc from 0° to 20°, i.e., when the TaxiBot is driving towards the observer. As expected, the TaxiBot combination is loudest in the rearward arc from

150° to 180° where noise from the APU is present. For these angles, the taxibotted noise levels can exceed the levels of taxiing procedures.

However, there is a possibility of overestimation of the source levels. The level measured by the microphones is corrected to the source level by taking into account the distance between the array and the GPS receiver, which is at the nose of the TaxiBot. Therefore, to obtain more accurate levels in Figure 6.4 a better prediction of the sources and their respective distances is necessary.

There is also the limitation that the taxibotted measurements were performed with an empty aircraft, while the taxiing aircraft were inbound flights and thus had payload. Additionally, the taxibotted operations are performed at lower velocities than the taxiing operations. However, the operators of the TaxiBot indicated that the diesel engine of the TaxiBot always operates on the same setting, and thus likely the same noise level, to drive the electric engine regardless of its velocity.

The directionality plot in Figure 6.4 only represents the left side of the aircraft or taxibotted aircraft as the measurements were performed on the left side mostly. For the TaxiBot itself, previous research shows that the noise is symmetrical, i.e., receivers on the left and right side measure the same levels [191]. Furthermore, all the taxiing measurements that were taken on the Polderbaan (60° to 120° part) were from two-engine taxiing aircraft as here the engines are cooled down. However, at the corner locations it is not always clear whether single- or two-engine taxiing was performed. This is difficult to check as the engines are turning idle and this information is also not available to the researchers. It is estimated that 40% of the inbound flights uses single-engine taxiing [188], where the APU is assumed to be running. The exact impact of single-engine taxiing on noise levels is unknown.

6.3.2. SOURCE IDENTIFICATION ON A TAXIBOTTED PASS-BY

Firstly, the spectrogram of a single, exemplary, taxibotted aircraft pass-by is analysed. The spectrogram shows dominant tones that often can be attributed to a single source. For the spectrogram in Figure 6.5 of a taxibotted B737-800, the TaxiBot-aircraft combination is visible on the optical camera from 34 to 49 s.

Primarily in the low frequency region up to 3 kHz noise is generated and a tone can be identified around 2.5 kHz. Furthermore, two tones can be identified around 8.6 and 8.9 kHz. By applying CFDB to the data, the sources of these tones were identified. The scan plane is placed parallel to the microphone array at the GPS distance to the TaxiBot which is 30 m. The lower source map in Figure 6.5 shows the CFDB map for the tone of 2.5 kHz. This tone is generated at the diesel engine location of the TaxiBot. The noise source around 8.5 to 9 kHz appears to be located around the wheels of the main landing gear of the B737-800, see the upper source map in Figure 6.5. Although this tone is apparent in the spectrogram for each measurement, it cannot be said with certainty what is causing this source as there are multiple systems active at this location, for example the air conditioning packs, the wheels, and the hydraulic pumps in the landing gear bay area. From beamforming analysis at different time slots, it was found that the source moves along with the main landing gear.

A few pass-by measurements on the right side of the taxibotted aircraft were analysed. They show a strong pattern of harmonic tones in the spectrogram, see Figure 6.6.

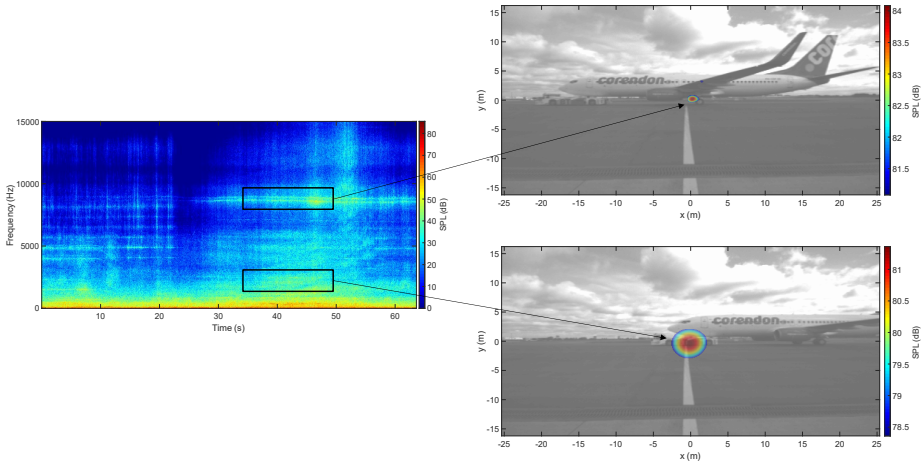

Figure 6.5: Spectrogram of a taxibotted B737-800 pass-by at microphone level. The receiver is on the left side of the aircraft. The taxibotted aircraft is visible from 34 to 49 s. Two CFDB source maps are presented at the tone of 2.5 kHz at $t = 42.25$ s and from 8.5 to 9 kHz at $t = 45.69$ s. The scan grid is placed at a distance of 30 m.

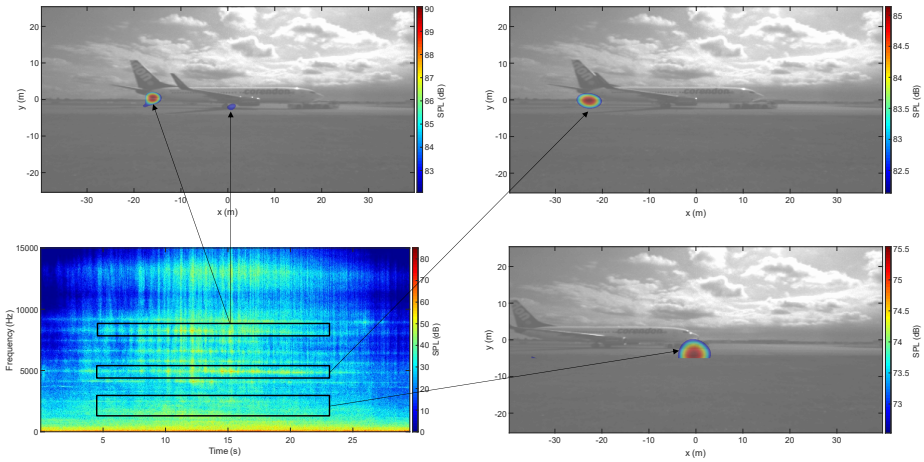

Figure 6.6: Spectrogram of a taxibotted B737-800 pass-by, receiver on the right side of the aircraft, microphone level. The taxibotted aircraft is visible from 4 to 23 s. The CFDB source map of tone 2502 Hz at $t = 11.9$ s is shown in the lower right corner. The CFDB source map of a tone at 4945 Hz at $t = 14$ s is shown in the upper right corner. The CFDB source map on the upper left corner represents 8.5 to 9 kHz at $t = 14.9$ s. All source maps are constructed at a distance of 47 m.

This may indicate that the TaxiBot-aircraft combination is not noise symmetrical. CFDB is applied to one of the tones at 4.95 kHz and the source that is found is located around the APU inlet of the B737-800. The same frequencies that were selected on the left side are investigated for the right side as well. This shows again that the TaxiBot diesel engine is present at 2.5 kHz. Between 8.5 and 9 kHz a noise source around the main landing

gear is present, however, at these frequencies the noise source at the APU inlet is also found. The APU inlet for the B737-800 is located only on the right side of the aircraft. However, it is important to note that this behaviour on the right side was not present with a B737-700 of another airline during a taxibotted pass-by.

6.3.3. SOURCE IDENTIFICATION ON A TAXIING PASS-BY

For taxiing B737-800 aircraft during pass-by, a tone can be identified at 5.33 kHz as can be seen in the spectrogram in Figure 6.7. This tone is attributed to the engine as is visible in the CFDB source map of 5.33 kHz and could be a higher harmonic of the Blade Passage Frequency (BPF). The CFDB map shows that the source is located on the back of the engine. Analysis of CFDB maps at other time blocks, which are not shown here, shows that the source is localised on the front of the engine as the aircraft approaches the array. The source is located at the back of the engine as the aircraft departs from the array. This is as expected from the directionality of the engine noise. At lower frequencies, just after pass-by, a strong increase in noise level is visible. The CFDB source map for 1 to 2.5 kHz shows that this is caused by the engine.

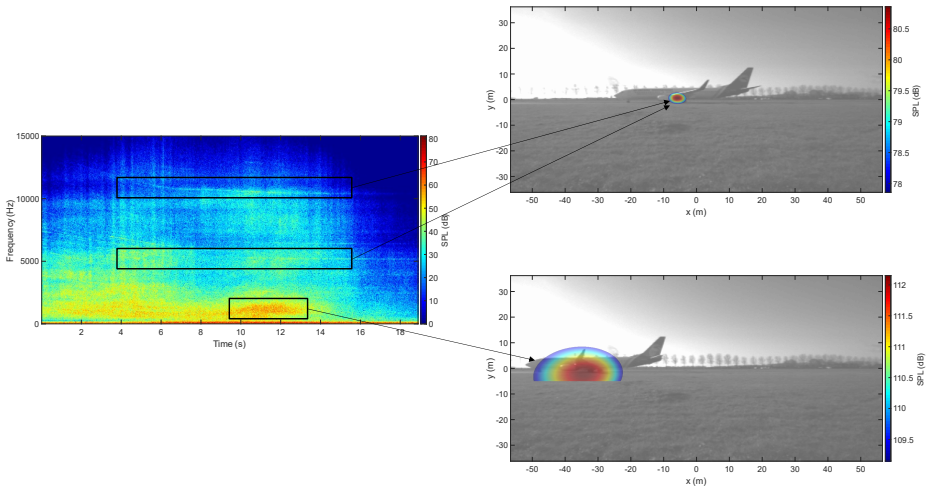

Figure 6.7: Spectrogram of a taxiing B737-800 pass-by. The aircraft is visible from 3 to 14 s. CFDB source map at 5.33 kHz for a conventional taxiing B737-800 pass-by at $t = 9.2$ s. Additionally a CFDB source map after pass-by for 1 to 2.5 kHz at $t = 11$ s. The scan grid is placed at a distance of 67 m.

In addition to measurements on the left side of a taxiing aircraft, also the right side was measured to assess the noise symmetry. The spectrogram showed the same behaviour on the right side as on the left side. This can also be seen from the directionality plot in Figure 6.8 which shows similar levels at similar angles.

6.3.4. NOISE SOURCE AROUND THE LANDING GEAR

The noise source that was found around the main landing gear was investigated by analysing data of a B737-800 of another airline which was towed solely by a towing vehicle, i.e., not

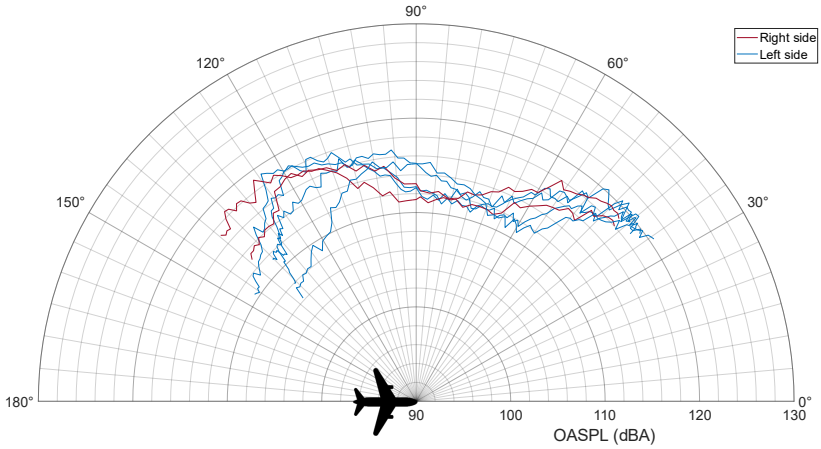

Figure 6.8: Directionality comparison of the source levels on the left and right side of a taxiing B737-800.

the TaxiBot. In these measurements, the tone around 8.5 to 9 kHz was not apparent, see the spectrogram Figure 6.9. However, this still does not give clarity regarding the source as, f.e., the airconditioning settings cannot be checked in retrospect.

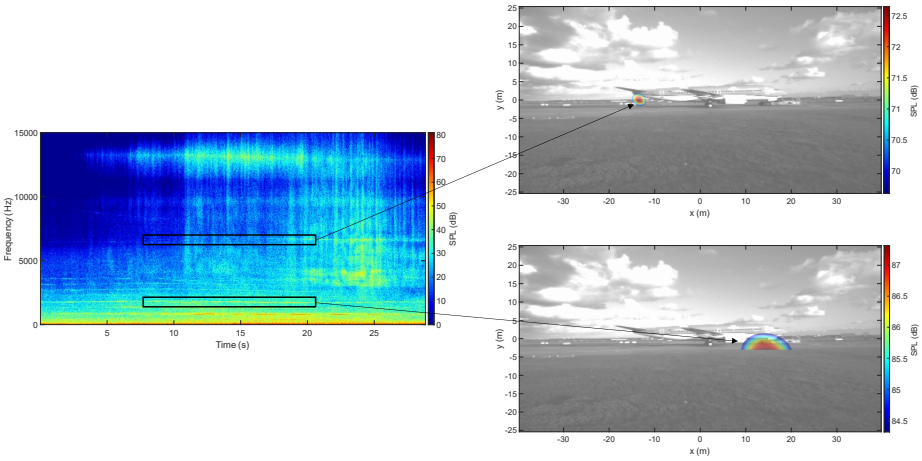

Figure 6.9: Spectrogram of a B737-700 towed by a regular towing vehicle. The aircraft is visible from 8 to 21 s. A CFDB map of the tone at 1.8 kHz is shown below and a CFDB map of the from 6.6 to 6.8 kHz is shown above. Both are constructed at $t = 17$ s. The scan grid is placed at a distance of 47 m.

What can also be noted from this towing experiment, is that the strong tonality that was visible in the spectrogram in Figure 6.6 is not present here, even though the pilot was specifically asked to open the APU inlet for this measurement. Measurements with a closed APU inlet also do not show the previously present tonality. Lastly, the 1.8 kHz

tone was found to originate from the towing vehicle's engine.

6.4. IMPACT OF NOISE EMISSIONS ON SURROUNDINGS

Even with the limitations and necessary assumptions, the research is still valuable to assess the noise level impact on ground workers. The results presented in this paper are compared to the European Union noise standards and limits to protect workers against hearing loss [187]. The limits are defined as A-weighted daily noise exposure limits for three different action levels: (1) provide protection, (2) mandatory protection, (3) maximum level (reduce noise). The daily exposure limit is calculated as the time-weighted average for an eight hour workday. For an airport, the exposure to noise depends on the number of operations on a day and is thus not comparable to the single event measurements presented in this research. Therefore the maximum daily exposure limit is converted to an equivalent level for one minute exposure time.

The maximum daily exposure limit is 87 dBA for an eight hour day but is 113 dBA for a single minute [195]. The 113 dBA level is compared to the source level OASPL as found in Figure 6.4. For the taxibotted operations, the 113 dBA level is only exceeded around 160°. The taxiing operations exceed this level for most emission angles (at the source). However, the ground workers are located at a distance from the source. Thus the OASPL will be reduced by a spherical spreading correction of $20\log_{10}(\text{distance})$ to reach the at-ear levels, where the distance is measured between the worker and the aircraft. Therefore the taxiing and taxibotted operations are deemed safe in terms of noise for ground workers. However, the significant noise reduction of taxibotted operations can still aid the ground workers and reduce their long-term risks and nuisance.

Propagating the source levels even further to the neighbouring communities results in levels below the general background noise. The closest houses to a runway or taxiway are at a distance of 1500 m, therefore only spherical spreading would already reduce the levels by 63.5 dB. That means that the taxiing or taxibotted manoeuvrers hardly impact the airport noise contours in comparison to a take-off or engine warm up.

6.5. CONCLUSIONS AND OUTLOOK

In this chapter, a comparison of noise measurements on a taxibotted operation and a taxiing operation was presented for measurements taken on Amsterdam Airport Schiphol. These measurements were performed with a microphone array to be able to analyse the noise sources present for both types of taxiing by applying Conventional Beamforming to the data. For the taxibotted operations, the diesel engine of the TaxiBot is present at the lower frequencies and produces a tone at 2.5 kHz. Additionally, during taxibotted operations the APU needs to be turned on to provide for the onboard electrical systems. The APU is the main source of noise when the rear part of the aircraft passes by. Lastly, a source was present between 8.5 to 9 kHz with a strong tonality. The source was located around the main landing gear, however the exact origin remains unknown.

For the taxiing operations, the engines are turned on but the APU is turned off. The main noise source for these operations is the engine which produces tones at harmonics of the blade passage frequency. Especially at 5.33 kHz a strong harmonic is present. The engines also have a strong directionality effect caused by the fan and compressor propa-

gating more forward and the fan exhaust, turbine, and combustor propagating aftward.

In addition to noise source identification, an Overall A-weighted Sound Pressure Level (OASPL) directionality plot at source location was constructed. For this, the data was corrected for background noise levels, distance to the receiver, and atmospheric attenuation. The emission angle was determined based on the GPS coordinates and video footage, and is defined between the taxi path and the array-to-aircraft-nose position line. It is observed that at angles from 0° to 150° around the aircraft, the taxibotted operation has a lower A-weighted noise level than the taxiing operation. Specifically at the front of the aircraft, the TaxiBot has significantly lower noise levels. From 150° to 180° the APU noise dominates the noise levels of the taxibotted operation and here the taxibotted operation can have a higher OASPL than a conventional taxiing operation. The difference in source level at 90°, when an observer sees the side of the aircraft, is 7.1 dBA which is a significant reduction for the taxibotted operation.

The results show that introducing the TaxiBot to replace conventional engine taxiing operations, will substantially reduce the noise level at the airport. This will significantly reduce noise nuisance and risks of hearing loss for ground workers.

7

Noise emissions and annoyance of the Skymaster for different propellers [1]

Never quit. Never give up. Fly it to the end.

Chuck Aaron

While the previous chapter focused on more sustainable taxiing methods, this chapter focuses on a propeller aircraft that could potentially be fuelled by a more sustainable power source. For electric aircraft, the annoyance is largely unknown but research by NASA in the early 1970s suggests that propeller noise is deemed more annoying than turbofan aircraft noise. This chapter presents an experimental investigation of the noise emissions and annoyance of the Cessna Skymaster, which is a push-pull propeller aircraft with space for six people. Several methods have been applied to engine run-up and flyover measurements of the aircraft to find noise emissions and annoyance, including directionality assessment, spectra, spectrograms, and annoyance metrics. The propeller was the dominant noise source in all flight modes, with the number of propeller blades influencing the perceived noise annoyance.

[1] The dataset is published in the 4TU Research Data repository [196].

7.1. INTRODUCTION

Over the past decade, the interest in propeller-driven aircraft has increased as they can have a higher fuel efficiency on short-distance flights [197]. Additionally, propeller aircraft can be retrofitted with an electric engine [198]. However, propeller aircraft are considered to have a high noise annoyance [33, 34, 199]. Therefore, research into the noise emissions of propeller aircraft is necessary. Learnings from general aviation can be used for commercial aircraft in later stages.

The Cessna Skymaster was acquired by the Dutch Electric Aviation Centre Teuge (DEAC) consortium to assess the impact of retrofitting an electric engine [200]. The Cessna Skymaster is an interesting testbed for this as it has a push-pull propeller configuration, in which one of the engines can be replaced by an electric engine. Ultimately, the goal of the research was to assess the noise emissions and annoyance of the Skymaster pre- and post-retrofit of the electric engine, which can aid in understanding the noise impact of electric aviation. The electric engine selected needs a 3-bladed propeller, and therefore the noise had to be assessed at three different stages: (1) in the original configuration with 2-bladed propellers, (2) with the original engine, but with 3-bladed propellers, (3) with an electric engine and 3-bladed propellers. Unfortunately, the instalment of the electric engine was postponed until after the duration of this PhD, and therefore only the first steps of the noise assessment were performed.

The difference between 2-bladed and 3-bladed propellers on the same aircraft is interesting to research, as 3-bladed propellers are expected to reduce noise emissions due to the reduced loading per blade and, in some cases, the 3-bladed propeller can have a smaller size which potentially reduces thickness noise through reduced tip speeds [201]. As the remainder of the aircraft stays the same, the impact of a different propeller on the noise levels can be researched more easily. The advantage of performing noise measurements in operational conditions over wind tunnel experiments is the full-scale size with realistic inflow conditions.

The aim of this research is to identify the different noise sources on the Cessna Skymaster to establish a good baseline for noise studies when the engines and propellers are changed. Additionally, the measurements with the Skymaster are used to find a method to decompose the measured spectrum for rotating and non-moving sources. This can be useful to validate noise prediction models with measurements of full-scale objects at operational conditions. The propeller change allowed to research the impact on noise emissions as well as noise annoyance when 2-bladed propellers are replaced with 3-bladed propellers to test the hypothesis that 3-bladed propellers are more silent.

This chapter first explains the measurement campaign at Teuge International Airport, for ground and flyover measurements, in Section 7.2. Following that, the noise emissions and the noise sources of the ground measurements and the flyover measurements are presented in Section 7.3. Next, the noise annoyance of the flyover measurement is discussed in Section 7.4 and lastly the chapter is concluded.

7.2. MEASUREMENT CAMPAIGNS

The Cessna Skymaster is a push-pull configuration aircraft, providing centreline thrust which prevents yawing in case of engine failure. The Skymaster is known for its char-

acteristic sound which is mainly caused by the rear propeller turning through turbulent air from the front propeller convected over the airframe [202]. The airframe has a high-wing configuration, two booms extending to the vertical and horizontal stabilisers, and retractable tricycle landing gear. Furthermore, the Skymaster has a wing flap system with four settings ranging from "no flaps" to "full flaps" at 25° [203].

Figure 7.1: Photo of the DEAC Skymaster in flight at Teuge International Airport. Courtesy of Remco de Wit.

Over the course of several measurement campaigns, two groups of measurements were recorded: (1) ground measurements, and (2) flyover measurements. Note that both types of measurements were performed for the Skymaster with the 2-bladed and the 3-bladed propellers installed. The front propeller is a right-hand tractor, the rear propeller a left-hand pusher. The 2-bladed propeller is a wooden propeller with a diameter of 193 cm, specifically a McCauley D2AF34C301/(L)76CTA-0, for "constant speed, feather". The 3-bladed propeller is type MTV-12-D-C-F/CF(LD)192-119a, which is a natural composite propeller with a diameter of 192 cm, for "constant speed, feather".

The engines installed on the Skymaster are Continental IO-360-C air-cooled flat-six-piston engines, i.e., six horizontally opposed four-stroke cylinders on the same crankshaft [204]. To cool the engines, the Skymaster has two cowl flaps for the front and two for the rear engine.

7.2.1. GROUND MEASUREMENTS

The goal of the ground experiments is to find a method to separate propeller noise from other noise sources to validate noise prediction models for individual components. This is easier to test in this simplified case where there is no forward velocity component involved.

During the ground measurements the aircraft was located on the engine run-up location (Taxiway Charlie at Teuge International Airport, see Figure 8.3) and the front engine was turned on while the rear engine was turned off. The front propeller was measured at different angles with respect to the propeller plane. Figure 7.2 shows how these measurements were performed. The measurements were performed with a 112 MEMS-microphone array from CAE with a sampling frequency of 48 kHz, see Section 6.2 for more information [192]. Generally 4096 samples were used for spectra.

The array centre aligned with the rotation centre of the propeller. The propeller ran

at 2000 RPM, which resulted in an exhaust firing frequency of 100 Hz ($\frac{N_{\text{cylinders}}\text{RPM}}{60N_{\text{stroke}}/2}$) and a shaft frequency of 33.3 Hz. The BPF for the 2-bladed propeller type was 66.7 Hz, and for the 3-bladed type this was 100 Hz which inconveniently aligns with the exhaust firing frequency.

Figure 7.2: Photo during the measurements of the front engine run-up.

The engine run-up measurements were recorded at seven positions for directionality. Both propellers turn counter-clockwise from the perspective of the array. Note that the propellers are contra-rotating when perceived from position F4 in Figure 7.3. The distance to the propeller hub was kept constant at 5 m to ensure far-field measurements [2]. Figure 7.3 shows the angles at which the engine run-up was measured. For the measurements of the front propeller, the blade is going down at position F6 and turning upwards at position F2. For the measurements at the rear propeller, the blade goes down at R2 and turns upward at R6.

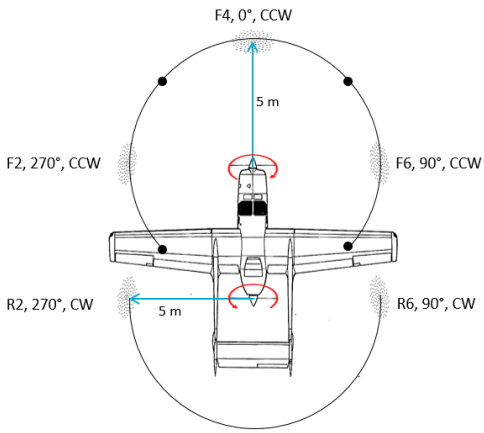

Figure 7.3: Measurement positions of the array and corresponding directionality angles of the engine run-up measurement. The propeller rotation direction is indicated by the red arrow.

[2] The acoustic far-field limit for propellers is defined as (1) greater than one propeller diameter away from the tip, or (2) a distance larger than the dominant wavelength (of the BPF).

7.2.2. FLYOVER MEASUREMENTS

The aim of the flyover measurements was to identify the contributions of different noise sources, such as the landing gear and high-lift devices. The flyover measurements were performed at two locations at Teuge International Airport, i.e., the extended areas on either side of the runway. The exact location is determined by the runway direction, which is dependent on the wind direction on the day of measurements.

For the measurements, several flyovers over a 64-analog microphone array were recorded at a sampling frequency of 50 kHz. This research only used the data from a single microphone, so details on the array are omitted here. The overhead spectra and spectrograms shown in the results were computed with 4096 samples, a zero-padding factor 2, and 50% overlap for spectrograms. In this time snapshot the aircraft moves roughly 4 m, yet no correction was applied to compensate for the movement.

The equipment was placed under the take-off path such that pilots could make a go-around over the entire length of the runway to stabilise the flight parameters before passing over the array. As a diverse set of measurements was recorded, the chapter will refer to "propeller type" to indicate whether 2-bladed or 3-bladed propellers were used, and to "operating condition" or "condition" to indicate the airframe settings and usage of engines.

Six operating conditions were defined in which the airframe and engine settings were varied, and each condition was measured for three individual flyovers. See Table 7.1 for the settings per operating condition. The altitude, speed, and engine RPM were kept constant by the pilots for all measurements. The flight parameters were agreed to be an altitude of 30 ft, an engine RPM of 2200 for both engines, and a flight speed of 104 kts based on the maximum flap extension speed defined in the type certificate data sheet [205]. When turning idle, the engine RPM reduced to 1600-1800. For 2200 RPM the tip Mach number was 0.65, and with a flight speed of 104 kts the advance ratio was 0.76 for a 1.92 m diameter propeller. In this research, the RPM and the advance ratio were kept constant between the measurements of the 2-bladed and the 3-bladed propeller. This might not be a fair comparison as an increased number of blades might allow for a lower RPM at the same flight speed to obtain the same thrust [201]. However, it is easier to compare cases with the same RPM and velocity rather than the same thrust.

The recorded flight parameters differed slightly from the intended, due to pilot manual input and aircraft responses to meteorological changes. Only condition 5 could not be flown at 104 kts, but was flown around 90 kts for safety. For the 3-bladed propeller type, the pilots were not able to safely fly condition 1 at 30 ft and hence diverted to roughly 60 ft. This is accounted for in the noise emission and noise annoyance analysis.

True determination of the flight parameters which are needed for further analysis, was done by matching the GPS location of the array with the GPS locations of the aircraft and reading out the recorded flight instruments. The resulting parameters are presented in Figure 7.4 to show the variability over the flights.

Operating condition	Short name	Landing gear	Cowl flaps	Flaps	Engines
C1	LG down	Down	Open	Up	Both
C2	Clean	Up	Close	Up	Both
C3	Flaps down	Up	Open	1/3rd	Both
C4	Dirty	Down	Open	1/3rd	Both
C5	Front engine	Up	Close	Up	Front only
C6	Rear engine	Up	Close	Up	Rear only

Table 7.1: Settings of the airframe and engines during the Skymaster flying measurements per propeller type. Every condition was repeated three times. All flights were performed at a speed of 104 kts, altitude of 30 ft, and an engine RPM of 2200.

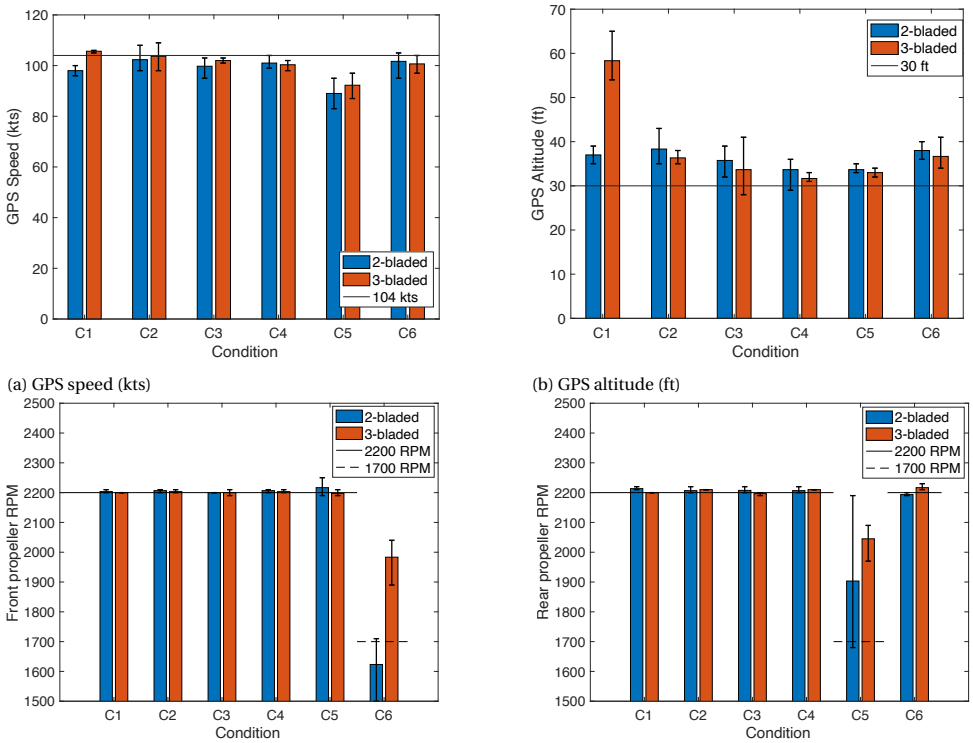

(a) GPS speed (kts)

(b) GPS altitude (ft)

(c) RPM of front propeller

(d) RPM of rear propeller

Figure 7.4: Flight parameters for each of the operating conditions as recorded from the flight instruments. The bars indicate the average level with a spread on top indicating the range over the three measurements per operating condition.

7.3. NOISE EMISSION COMPARISON OF THE 2-BLADED AND 3-BLADED PROPELLERS

For the noise emissions, the ground and flyover measurements are discussed separately, but each type of measurement includes the results for the 2-bladed and the 3-bladed

propeller. The aim for ground measurements is to investigate if rotating sources, i.e., propeller, and ground sources, such as the engine and airframe, can be separated through the use of different beamforming methods. The analysis of the flyover measurements on the other hand aids in understanding the impact of different noise sources on the aircraft which cannot be assessed in ground measurements.

7.3.1. GROUND MEASUREMENTS

The goal of the ground measurements is to investigate the possibility of separating the different types of noise sources of a propeller aircraft by the combined use of Rotating Source Identifier (ROSI) and Conventional Time-Domain Beamforming (CTDB). However, prior to acoustic imaging, the general directionality of the propellers is investigated and the propellers are compared. The directionality and spectra at interesting observation angles can provide an indication of the sources present in the acoustic source maps.

Firstly, the Overall Sound Pressure Level (OSPL) is calculated at all measurement positions for intervals of 0.5 s, for which the variability in time is presented with an error bar. The results for the front propeller are presented in Figure 7.5a. There is no clear pattern visible between the 2-bladed and 3-bladed propeller yet, therefore the normalised OSPL with respect to the measurement at 0° is presented in Figure 7.5b. Again no shared pattern is visible between the 2-bladed and 3-bladed propeller, but both have an increased OSPL at the side where the propeller blade turns upward in comparison to the downward turning blade.

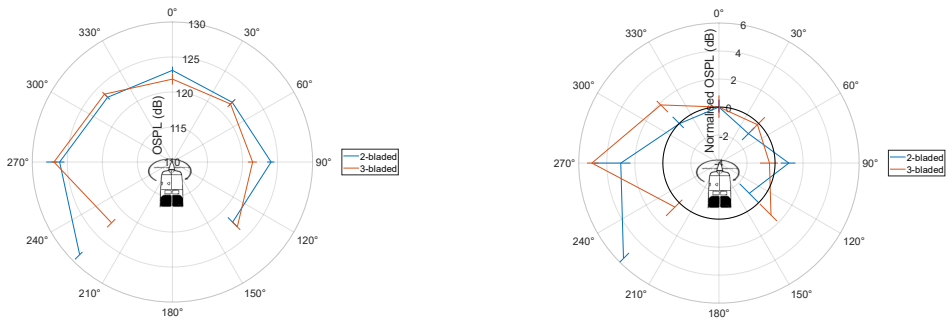

(a) OSPL

(b) Normalised OSPL w.r.t. 0°

Figure 7.5: Directionality of engine during ground measurements. The errorbars indicate the spread over time snapshots of 0.1 s in a total measurement of 10 s.

An increase in unsteady loading noise was expected for ground measurements, as the blade moves through the ground boundary layer and the recirculated air thereby experiencing loading fluctuations. The difference between the 90° and 270° measurements can be caused by ground vortices that are different on both sides, as well as through convective amplification, or differences in the ground reflection.

The differences between the OSPL at different angles are caused by the different sources that play a role at a specific angle. It can be worthwhile to look at the spectra

to see different tonal or broadband effects there. This also could give an indication of the frequency range on which to perform source identification through acoustic imaging. The spectra of 0°, 90°, 270° for a ground run-up at 2000 RPM are depicted in Figure 7.6 per propeller type. The spectra contain a double marking for the x-axis: below the graph the x-axis indicates the frequencies and at the top of the graph the axis indicates multiples of the BPF. The difference between the 90° and 270° sides in OSPL as seen earlier can now be explained by the difference in strength of the BPF as well as stronger harmonics above the eighth order although they hardly play a role in the OSPL due to their low SPL compared to the BPF level.

From the spectra it is evident that above the seventh harmonic the tones are stronger for the 0° measurement than for the side measurements. This indicates a strong presence of unsteady loading noise as this affects mostly higher harmonics and, additionally, steady loading noise should not be present on the propeller axis (0°). Furthermore, the spectra for both propeller types showed a significant difference in tonality between the 90° measurement angle and the other measurement angles, where the 90° measurement contains fewer tones.

The spectrum for the 2-bladed propeller shows clearly the BPF and its harmonics, but also the engine tone (100 Hz) is present in the spectrum. When the harmonic of the BPF and the harmonic of the engine align in frequency, it is not possible from this spectrum to identify the separate contributions. This becomes even more difficult for the spectrum of the 3-bladed propeller where the BPF and engine tone frequency, and hence all harmonics, are equal. Therefore, the spectra are rather analysed for tones that do not coincide with the BPF and its harmonics.

Interestingly, the spectrum for the 3-bladed propeller for the 90° and 270° measurements angles at 150 Hz and 250 Hz indicates tonal content, which does not correspond with an integer multiple of the BPF and does not occur for the 0° angle measurement. To verify whether this is a propeller effect, the spectra of the rear propeller are also analysed. Figure 7.7 shows both the spectra of the front and rear measurement at 90° and 270°. The rear measurements lack the tone at 150 and 250 Hz. That would indicate that the tones are caused by installation effects or other sources which are only present at the front part of the aircraft. Unfortunately, the spatial resolution according to the Rayleigh limit as defined in Chapter 3, is too low at 150 and 250 Hz to locate the source, thus further spectral analysis was performed.

Tonal content at 150 Hz and 250 Hz is also present for the 2-bladed propeller type, but it is less clear in the spectrum in Figure 7.6a. If the tones were an effect of the rotating propeller than their frequencies would have to be different for the 2-bladed and 3-bladed propeller type, thus the engine components could be the source of noise.

A further inspection of the spectrum shows that there are also tones present at 350 Hz and 450 Hz. The tones are not harmonics of each other, but could be harmonics of a tone at 50 Hz which is (albeit at low level) present in Figure 7.6b for 90° and 270° measurements. 50 Hz is half the exhaust firing frequency. For the front engine, the three cylinders on the left side of the engine are connected to a pipe which exits on the left side, just behind the nose landing gear, while the cylinders on the right side are connected to a pipe exiting on the right side. Thus, for these pipes on either side of the plane the exhaust firing frequency is 50 Hz, while in total the exhaust firing frequency is 100 Hz.

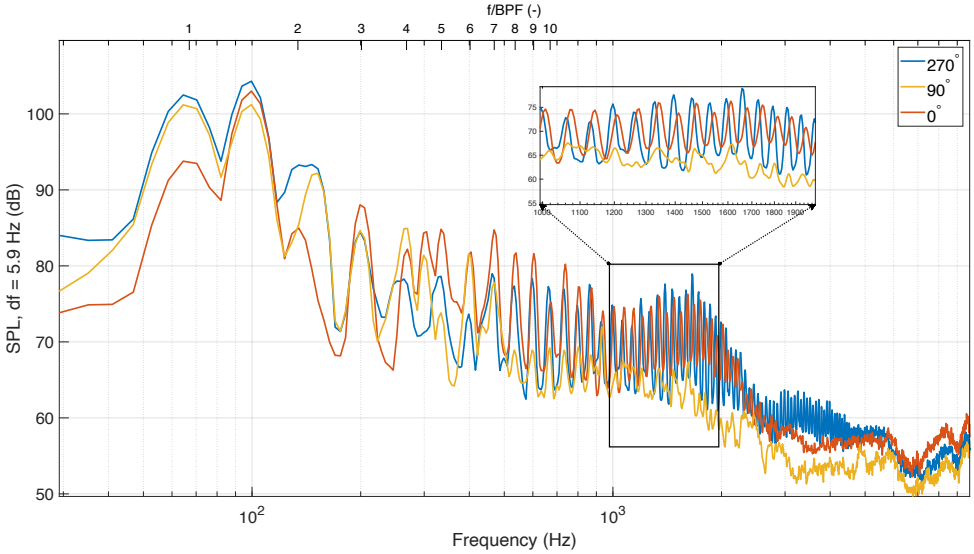

(a) 2-bladed

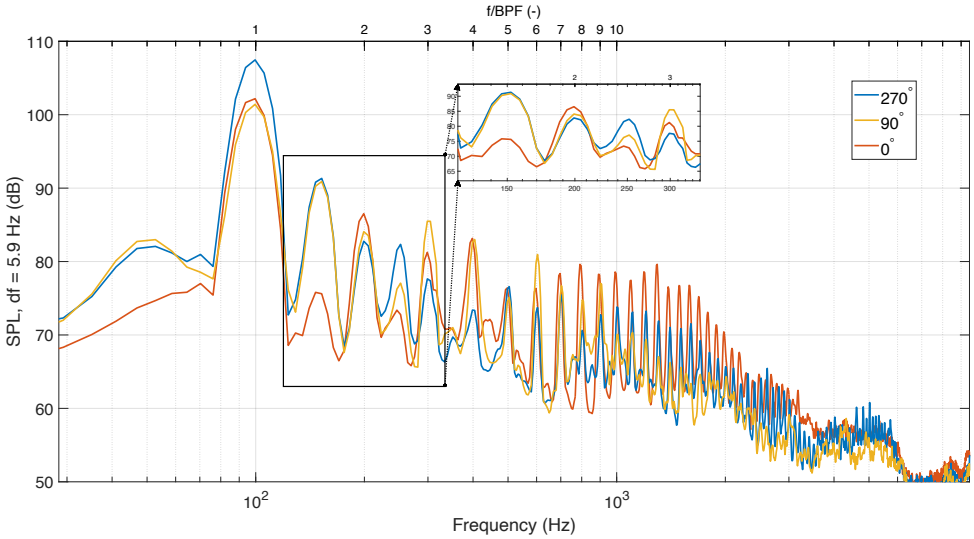

(b) 3-bladed

Figure 7.6: Spectra at different angles per propeller type. The x-axis is defined in terms of frequency below the graph and in harmonics of the BPF above the graph.

For the rear engine all cylinders are connected to the same exhaust pipe and therefore this tone is not present in the rear measurements [3].

The spectra indicate a range of frequencies that are interesting to investigate for

[3] The engine lay-out and the coupling of exhaust pipes to cylinders was analysed by the aircraft technicians Fred den Toom and Menno Klaassen during an engine overhaul.

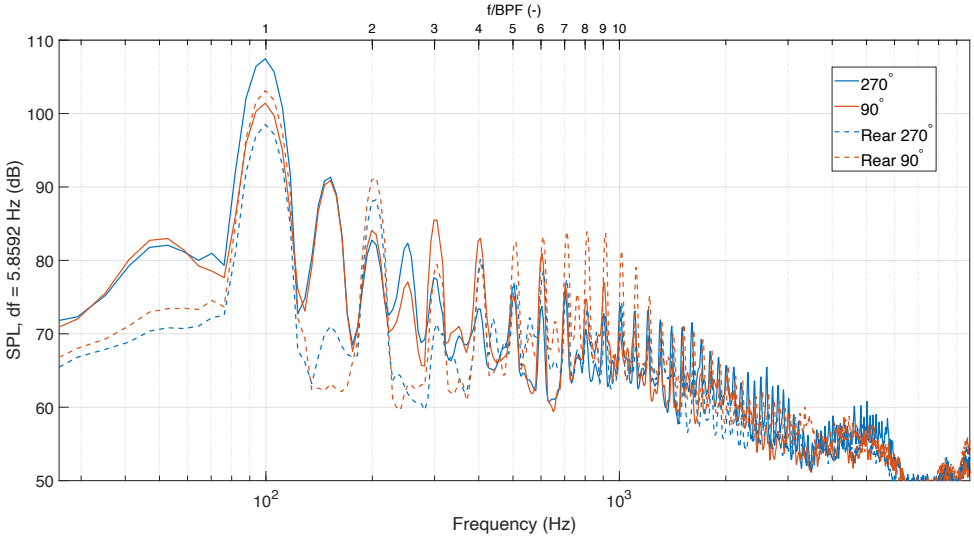

Figure 7.7: Spectra of the 3-bladed propeller measurements at the sides of the front and rear propeller.

source decomposition, but unfortunately the spatial resolution is only sufficient above 1000 Hz for proper source separation in the propeller plane (for the 3-bladed propeller the lower limit is 1500 Hz). Therefore, the focus was shifted to the higher frequencies. First, the 1000 to 2000 Hz region for the 2-bladed propeller is analysed with CTDB to identify any non-moving sources at different angles, see Figure 7.8.

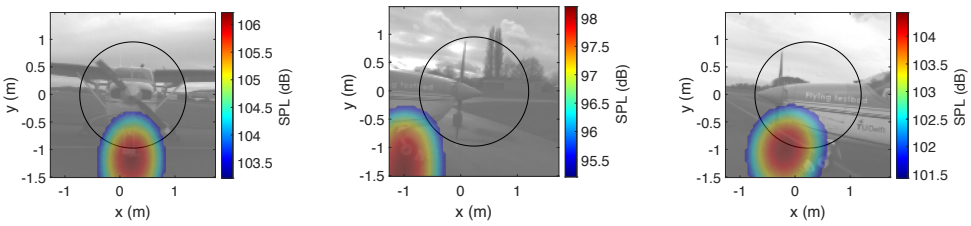

(a) 0° - F4

(b) 90° - F6 - down-going side

(c) 270° - F2 - up-going side

Figure 7.8: CTDB for 2-bladed propeller type ground measurements. Note that the maximum level is different for each figure.

From the CTDB source maps it seems that the source for the 90° observer angle appears around the landing gear, which could be the exhaust which was described earlier, while for 270° the source is slightly forward, closer to the propeller plane in general. The blade is turning downward at 90° angle, and turning up at 270° angle, so perhaps the effect of the boundary layer ingestion at 270° is causing a stronger noise source, and additionally the convective amplification could play a part here with higher amplification for the up-going blade. For the front (0°) measurement, the source is found around the ground location. This could be a ground reflection but potentially also the effect of the

cyclostationary source of the landing gear that is excited as the blades pass by [206]. It is unlikely to be a propeller noise source solely, as that would have appeared in CTDB as a ring of sources in the propeller plane (see simulation results in Section 3.2.2).

For the further separation of non-moving and rotating sources, only the front plane measurements are used, as the side planes are significantly hampered by convective amplification effects. Two acoustic imaging methods, CTDB and ROSI, were applied to two frequency regions per propeller type. The first region starts at the lower resolution limit and ends at the frequency for which tones are no longer present. This upper limit is 2500 Hz for the 2-bladed type, i.e., roughly 37 harmonics were present, and the limit is 3500 Hz for the 3-bladed type (35 harmonics). Note that harmonics of the engine tone were no longer present at the seventh harmonic (700 Hz) and higher frequencies. The second frequency region includes the broadband noise content and ends at 6000 Hz for both propeller types.

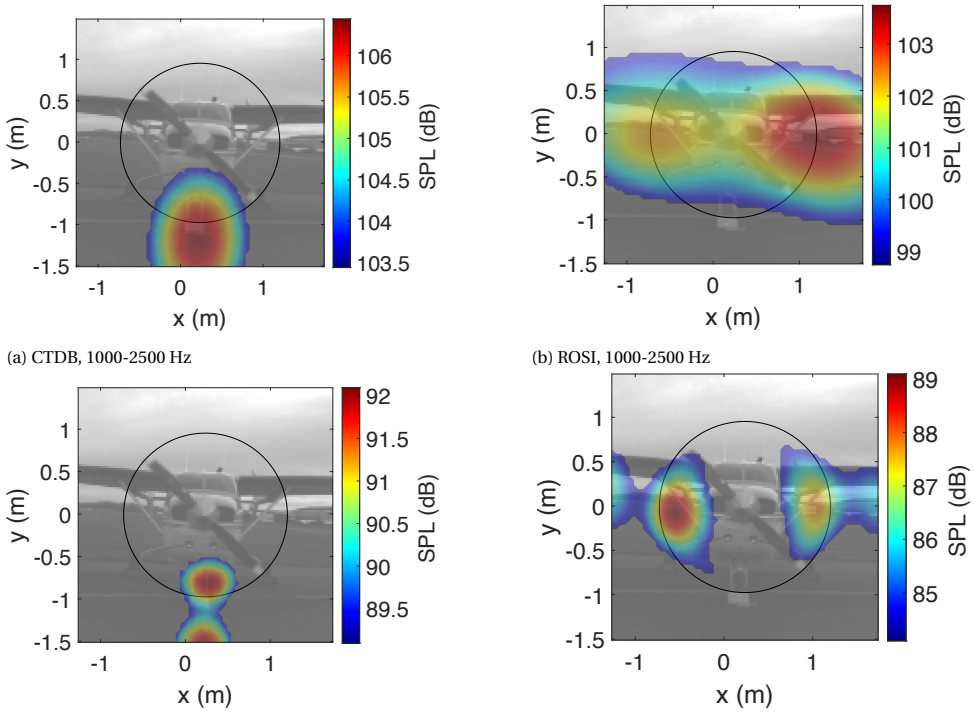

(a) CTDB, 1000-2500 Hz

(b) ROSI, 1000-2500 Hz

(c) CTDB, 2500-6000 Hz

(d) ROSI, 2500-6000 Hz

Figure 7.9: Acoustic imaging maps for the 2-bladed propeller type on the region where tones are still dominant, up to 2500 Hz, and the region where no tones are present (lower row). Note that the lower bound of 1000 Hz represents the frequency at which the two propeller blades can be perceived separately according to the Rayleigh spatial resolution criterion. Note that the maximum level in each source map is different.

The acoustic source maps for the 2-bladed propeller type are presented in Figure 7.9, where the left column contains CTDB source maps and the right column contains ROSI source maps, with the lower frequency range on top and the higher frequency range at

the bottom. The CTDB source maps show a strong source at the bottom of the propeller plane. It is not certain whether this is still an effect of the exhaust or a cyclostationary source. For the higher frequency range a ground reflection is visible in the source maps. For the ROSI source maps, it appears as if one blade is stronger than the other, however analysing a full rotation at different starting times shows that the dominant blade is not always the same, see Figure 7.10. The variations could be caused, for example, by an asymmetrical wind gust on the propeller plane.

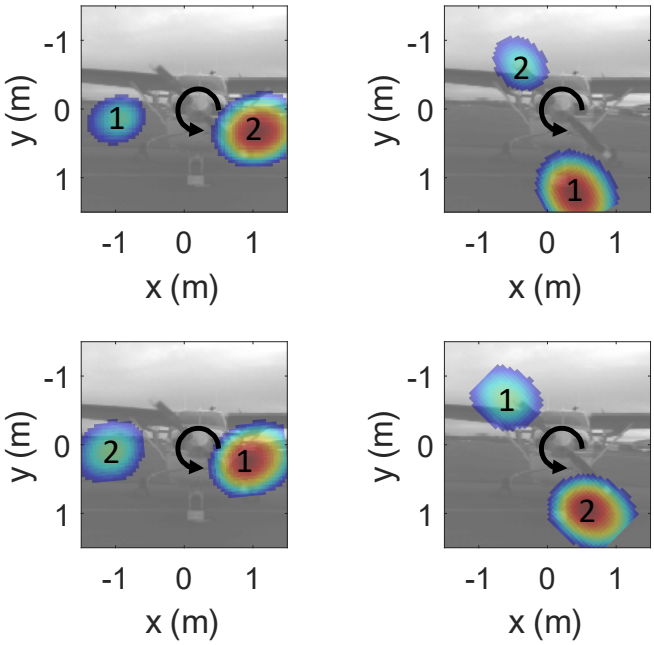

Figure 7.10: ROSI acoustic source maps for a full rotation, started at different times.

The acoustic source maps for the 3-bladed propeller type are presented in Figure 7.11. In the lower frequency range ROSI identifies the three blades separately, at a position that is roughly in the middle of the lobes in the source map of the higher frequency range. It is not clear what is causing this spread. For the non-moving sources in the higher frequency range no ground reflection is present within the dynamic range. However, two sources are present in the lower part of the propeller plane. This source is not present at all time stamps. ROSI also does not clearly indicate sources at that frequency range.

While this section showed that the total measured pressure can be separated in non-moving and rotating sources by using CTDB and ROSI simultaneously, it also showed that the engine can hamper spectrum decomposition. Additionally, cyclostationary sources may be present for ground measurements that are potentially not present during flyover measurements. Therefore, it is advised to be careful with measurements of propellers

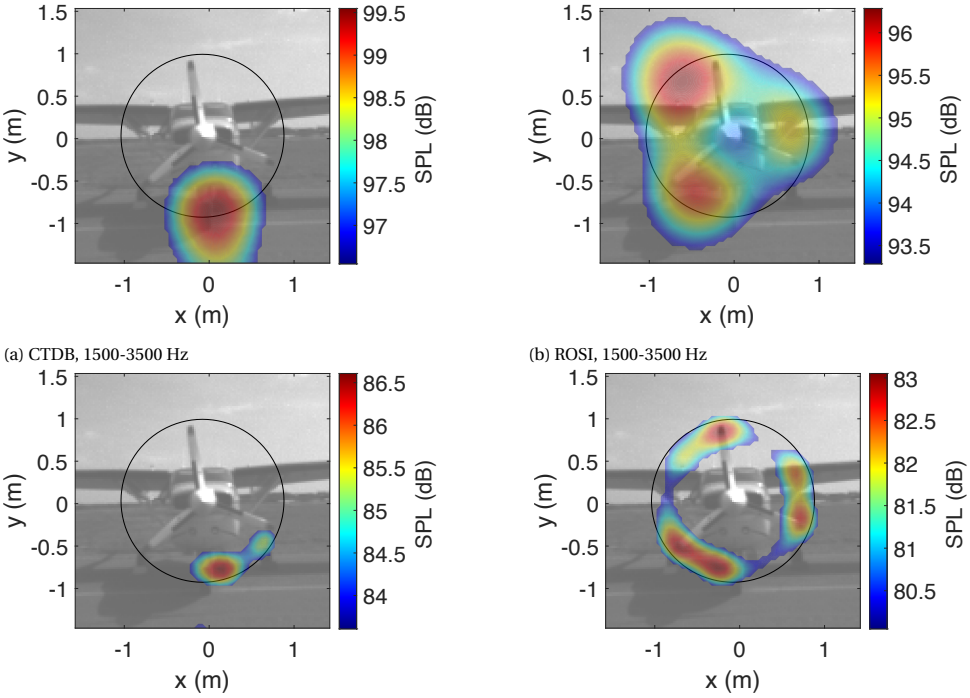

(a) CTDB, 1500-3500 Hz

(b) ROSI, 1500-3500 Hz

(c) CTDB, 3500-6000 Hz

(d) ROSI, 3500-6000 Hz

Figure 7.11: Acoustic imaging maps for the 3-bladed propeller type on the region where tones are still dominant, up to 3500 Hz, and the region where no tones are present. Note that the lower bound of 1500 Hz represents the frequency at which the three propeller blades can be perceived separately according to the Rayleigh spatial resolution criterion. Note that the maximum level in each source map is different.

close to the ground, especially for single microphone measurements where no source decomposition can be made.

7.3.2. FLYOVER MEASUREMENTS

The goal of this part was to identify the noise sources that are present during a flyover, as this is the condition which impacts communities most. The variety of conditions, specified in Table 7.1 as C1 through C6, allows for a separation of noise sources beyond the propeller noise through a comparison of the spectra overhead. The overhead spectra were corrected for the distance between source and receiver and averaged over all repetitions, see Figure 7.12. Note that for operating condition C5 and C6, only one of the propellers has a RPM of 2200, while the other propeller ran idle which unfortunately resulted in a wide range of RPMs (see Figure 7.4). This can cause interference effects and instabilities, as well as shifted propeller tones which result in an inaccurately averaged spectrum. Therefore, only conditions C1 up to and including C4 are shown here.

From the spectra, it is clear that the aircraft emits a strong tone at the BPF for all operating conditions. For the 2-bladed propeller type, the BPF is 73.3 Hz and the engine tone is 110 Hz. It is interesting to note that the BPF and its first harmonic, at 73 Hz

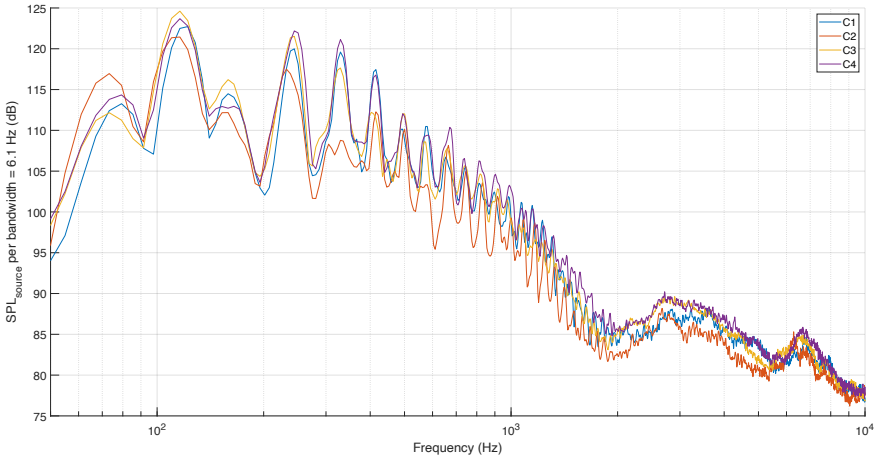

(a) 2-bladed

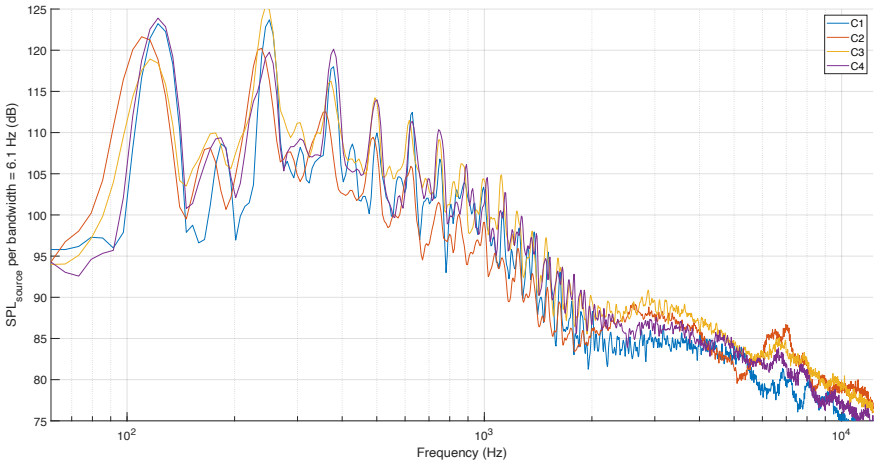

(b) 3-bladed

Figure 7.12: Spectra averaged over all flights per operating condition, for the conditions where both engines were used.

and 146 Hz respectively, have a level at least 10 dB lower than the first couple of engine tones. The engine tone thus strongly influences the noise emissions. However, for C2 the harmonics of the engine tones are not present at 330 Hz and 550 Hz. The only difference that C2 consistently has with the other conditions is the closed cowl flaps which may have specifically reduced these tones.

When comparing the operating conditions, it seems that C2 is the most silent over the spectrum, especially above 500 Hz where the baseline level (excluding the peaks) is up to 5 dB lower. The other conditions tend to have a higher broadband baseline level in this frequency range, although these frequencies still are dominated mostly by tones. For most of the spectrum C4 is slightly higher than the other conditions.

Only for the 2-bladed propeller type it is possible to study the harmonics of the engine and the propeller tones separately. The tones above 1000 Hz are perfect harmonics of the BPF of 73 Hz, i.e., above the 15th harmonic. Below 1000 Hz, sometimes the tones do not align clearly with a harmonic, which may partially be influenced by the presence of a strong engine tone close to a propeller harmonic. Yet, sometimes the tone does not match an integer multiple of either the engine or the propeller, such as 415 Hz. It is not clear where the tone originates from, but the level is roughly 6 dB higher for C1 and C4, compared to C2 and C3. These conditions, C1 and C4, have the landing gear down which could have caused a tone. However, the lower level tone at C2 and C3 could not be explained by the landing gear.

For the 3-bladed propeller type, the BPF and the engine tone are at the same frequency, and hence it is not possible to make a distinction between these contributions in terms of relative strength. Interestingly, there is a tone present around 170 Hz for almost all conditions, which is not related to an integer multiple of the BPF or the engine tone. However, it is the third harmonic of the firing exhaust frequency of three cylinders, thus hinting at the same source as found for the ground measurements; the exhaust from one side of the front engine.

When comparing the conditions for the 3-bladed propeller type, it is again clear that the spectrum of C2 lies lower than the others in the tonal range from 300 Hz to 1500 Hz, but in contrast to the 2-bladed propeller type the broadband noise above 2000 Hz is not necessarily the lowest for C2. C1 also shows slightly different behaviour, with a tone at 430 Hz where other conditions show no tones. While this tone is clearly lower than the propeller and engine tones, it lies well above the broadband levels and therefore is interesting. Its source remains unknown.

The overhead spectra indicate that the 3-bladed propeller type has higher levels for the tonal content, which could be due to the alignment of the BPF with the engine tone. It thus has fewer tones in the spectrum, but the ones that are present are stronger. In the following section the impact of this on annoyance is discussed.

So far the analysis focused on the overhead time, but it is worthwhile to look at the entire flyover to see whether an overhead spectrum is representative of what is perceived on ground. A spectrogram can show directionality effects for example when a source is only perceived before or after the overhead position. It is not feasible to show all spectrograms of every flight and every condition, therefore the dirty configuration (C4) is depicted here as generally the overhead spectra are similar for different conditions but the dirty configuration has most potential of showing other sources.

Figure 7.13 shows a spectrogram for both the 2-bladed propeller type and the 3-bladed propeller type in dirty configuration (C4). The spectrograms indicate that the spectrum at overhead position was a good indicator for the sources present during an entire flyover as only tonal content at harmonics of the BPF and engine show up. It also shows clearly that the tones below 100 Hz exist for a long duration, which might be causing significant annoyance.

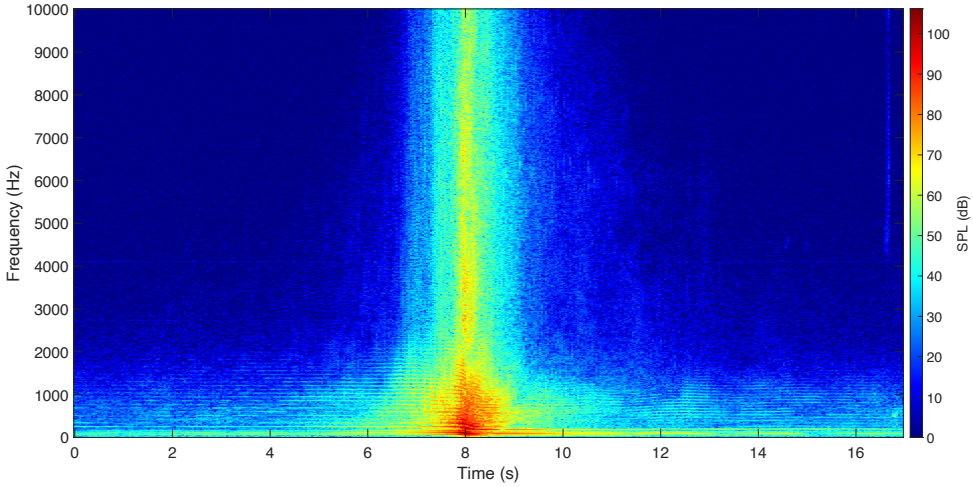

(a) 2-bladed

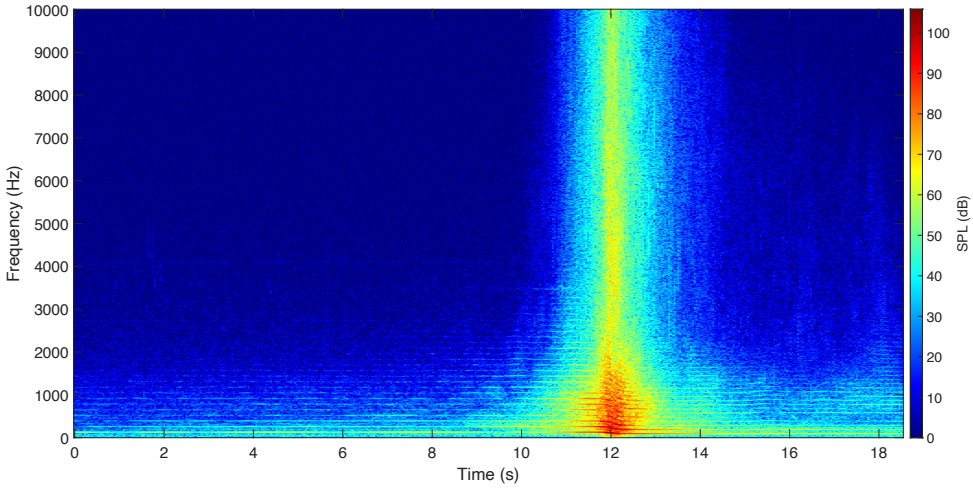

(b) 3-bladed

Figure 7.13: Spectrogram of a single flyover for C4 (dirty configuration)

7.4. NOISE ANNOYANCE COMPARISON OF THE 2-BLADED AND 3-BLADED PROPELLERS

The impact of changing from a 2-bladed propeller to a 3-bladed propeller has been investigated here in terms of annoyance over the full recording. To achieve a more fair comparison, all flights have been normalised to a height of 30 ft with a spherical correction for the overhead altitude, which is commonly applied in psychoacoustic research [67, 207]. Note that this correction does not take into account the varying flight velocities, varying RPMs, and variations in flight paths.

The conventional metrics of maximum OASPL and SEL over the duration of the flight,

see Figure 7.14, show that the 3-bladed propeller type has higher levels for most operating conditions, excluding the first condition for $OASPL_{max}$. Even though the values were corrected to a reference height, the difference could be caused by the slightly higher RPM levels for the 2-bladed propeller type. The integrated levels over time, called Sound Exposure Level (SEL), also show that the 3-bladed propeller flights have higher levels.

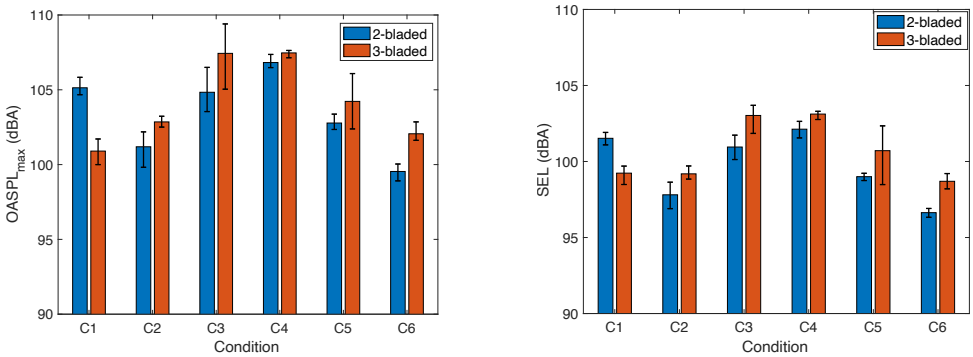

(a) OASPL

(b) SEL

Figure 7.14: Conventional sound metrics, corrected for an altitude of 30 ft.

However, these increased noise levels do not reflect the received complaints from the neighbourhood during the measurements which indicated "still loud, but less annoying sound" [4]. Of course, it is not possible to derive conclusions from that, as the weather conditions on the measurements days were not the same and the operational conditions may differ between the recorded measurements and the moment above the community, but it is nevertheless interesting to analyse what could cause this difference. Therefore, the sound quality metrics (SQMs) have been calculated, and their results are indicated in Figure 7.15.

Firstly, the comparison between 2-bladed and 3-bladed propeller types was made, for all conditions. This comparison is made based on the individual SQMs in Figure 7.15. The spread of the metric over the three flights is indicated by the black bar, while the Just Noticeable Difference (JND) of the average value is indicated by the gray bar. If a value is outside of the JND line, i.e., below or above the caps, then that value is noticeably different from the average (top of a bar). Thus a JND spread smaller than the data spread indicates that there is a noticeable difference between the flights. The caps of the JND line also can be used to compare the values of the 2-bladed and the 3-bladed propeller types. While the following comparison may provide initial insights, the small sample size (three flights) poses a risk of misinterpretation.

The loudness levels show that the 3-bladed propeller is louder for most conditions, but the difference is only noticeable for certain conditions. For C1, the 2-bladed propeller had loudness differences between the flights that are noticeable already. Even

[4] Teuge International Airport receives noise complaints on a regular basis for the Cessna Skymaster. The Skymaster measurements with the 2-bladed propeller and the 3-bladed propeller happened two days apart. Some complaints during the 3-bladed measurements mentioned a difference in reference to the 2-bladed propeller measurements.

though the flights were normalised for height, the altitude throughout the recording could still have varied and thus play a part in the spread that was found.

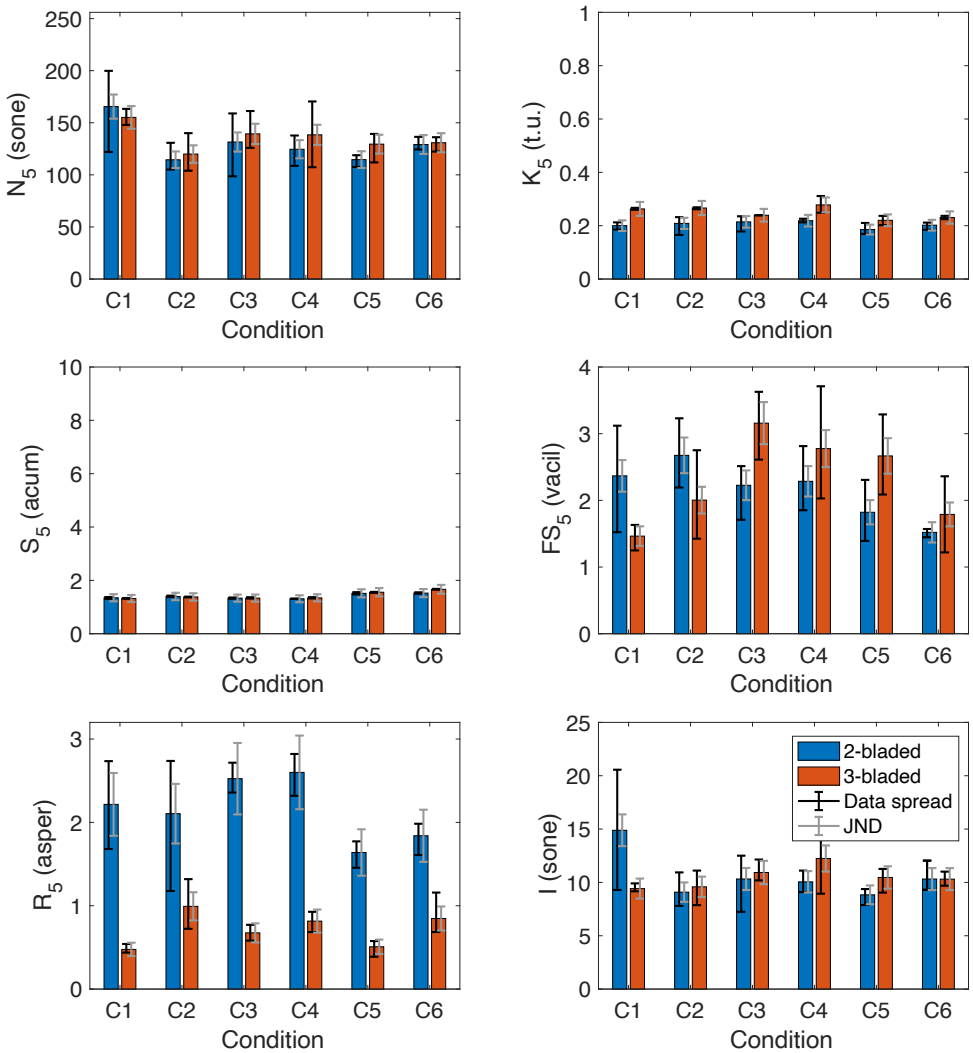

Figure 7.15: Sound quality metrics for all flight conditions, normalised to a height of 30 ft. The black bars indicate the average level with a spread on top indicating the range over the three measurements per condition. The y-axis limits have been defined on the range limits reported in Table 4.1, however, for Loudness the threshold of pain is the upper limit, while for Impulsiveness there was no limit, and for FS the limit had to be increased to 4 vacil.

For tonality the 3-bladed propeller flyovers were noticeably higher than the 2-bladed propeller flyovers, according to their reported JND values. This could be caused by the higher BPF, resulting also in harmonics of higher frequency, which occur more in the audible range. Additionally, for the 3-bladed type the tones of the propeller and the engine

align, which means the spectrum exhibits fewer tones but of stronger level which might result in a higher tonality. For sharpness, low values are reported with only unnoticeable differences between the two propeller types, which indicates sharpness is dominated by the airframe.

Fluctuation strength behaves interestingly, with a noticeable difference between all flights, but for some conditions it is higher for 2-bladed propellers and for the other conditions it is higher for the 3-bladed propellers. Fluctuation strength values are high as the unit range is 0-3 vacil, but also have a large spread, which indicates strong slow modulations are present for the flyovers in general.

In terms of fast modulations, the roughness metric shows consistently and noticeably lower values for the 3-bladed propeller than the 2-bladed propeller. This is attributed to the BPF which gives frequent amplitude modulations due to convective amplification when the blade passes closer to the receiver on the downward angles. This modulation for a 3-bladed propeller happens at 110 Hz (the BPF), while for the 2-bladed propeller it happened at 73 Hz, thus the modulation frequency shifts out of the maximum region for roughness for the 3-bladed propeller, thereby reducing the metric. Combining these findings with the anecdotal reduction in complaints and perceived annoyance of bystanders, could indicate that roughness noise is an important metric in perceived annoyance.

Lastly, impulsiveness is higher for the 3-bladed propellers than the 2-bladed propellers, except for C1. For C1 this could be caused by the higher loudness levels of the 2-bladed propeller flights, which influence the loudness-based impulsiveness metric. A JND of 10% is indicated, in line with the JND for most metrics, but this has not yet been proven in listening experiments. This spread merely is to show that most conditions have rather comparable levels between the two propeller types.

The total Psychoacoustic Annoyance (PA) was also assessed according to various models, for which the results are shown in Figure 7.16. Di and Zwicker tend to predict lower annoyance for the 3-bladed propeller type, while Willemsen's model predicts more similar annoyance between the two propeller types. Willemsen's model takes into account roughness and impulsiveness, and omits tonality, yet it does not account for the confounding factor loudness which could explain its differences with respect to the Di and Zwicker models which are very similar, with Di including tonality additionally. Interestingly, the Di and Zwicker models predict a reduced annoyance for the 3-bladed propeller, whereas the conventional metrics (OASPL and SEL) indicated higher levels.

Apart from looking at the differences between propellers, it is interesting to compare the clean configuration (C2) to the other conditions where engine settings and airframe configuration options were altered. For loudness, the clean condition (C2) is perceived least loud, even if just a single propeller is used. For C5 this is especially interesting as it also has a lower aircraft speed, which had to be reduced for safety reasons, which was expected to result in lower loudness levels.

For all other factors there is no clear pattern between the conditions that is consistent for both propeller types, even though the differences may be noticeable. For example, comparing the clean condition (C2) with the fully dirty condition (C4), then C4 does give more broadband noise resulting in a higher loudness. C4 was also expected to result

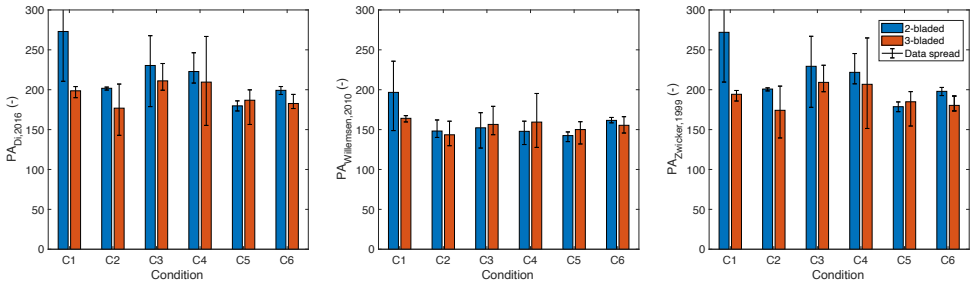

Figure 7.16: Results of several models for the PA metrics. The bars indicate the average level with a spread on top indicating the range over the three measurements per condition.

in more high frequency content resulting in higher sharpness but that is not the case. Adding only the landing gear (C1) or the flaps (C3), both with open cowl flaps which may cause more noise with respect to the clean condition, gives hardly lower sharpness values, but does increase loudness. Other metrics showed no clear pattern that is shared by the 2-bladed and the 3-bladed propeller.

The conditions where only one of the propellers is providing power and the other is turning idle, do provide a lower tonality and lower roughness noise than C2, regardless of the propeller type, but the effect of these lower metrics on the total PA is limited due to their higher loudness levels.

In general, for all PA models, the clean condition results in the lowest annoyance, and turning one propeller to idle can reduce the annoyance, but not below the level of a clean configuration with two operational propellers. The 3-bladed propeller reduces the roughness noticeably at a limited increase of loudness which in total results in a lower PA for Di et al. and Zwicker et al. models. However, for Willemsen's model the 3-bladed propeller has a higher PA value, thus it is suggested to perform listening experiments to find the most representative PA model.

7.5. CONCLUSIONS AND OUTLOOK

The aim of this chapter was to get a better understanding of the noise sources of the Cessna Skymaster as it transitioned from 2-bladed propellers to 3-bladed propellers. This understanding and baseline assessment can help when the noise of the Skymaster is researched after changing to an electric engine.

The aircraft proved to be difficult to understand in terms of noise due to its push-pull centre line aligned propellers and atypical airframe structure with tail booms and a rear propeller that experiences inflow turbulence. Additionally, the exhaust firing frequency aligning with the Blade Passage Frequency (BPF) of the 3-bladed propeller caused difficulties in noise assessment.

This chapter found that measurements on the ground are difficult to interpret due to the addition of cyclostationary sources or noise sources arising from ground vortices, which are generally absent during flight. While applying Rotating Source Identifier (ROSI) and Conventional Time-Domain Beamforming (CTDB) to measurements can aid in identifying all sources, the levels might still not be representative.

The flyover measurements indicated that the noise is dominated by the propeller and potentially some engine exhaust noise, while airframe components such as landing gear and flaps hardly play any role in noise emissions and annoyance. This is an interesting finding for the future when the electric engine will be installed, which will hopefully reduce the noise emissions further.

Lastly, the noise annoyance analysis showed, while only a limited number of samples could be used, that roughness noise is strongly dependent on the BPF and thus on the RPM and number of blades. In this study, the roughness was lower for the 3-bladed propeller. By reducing the roughness noise, some models also indicate that the psychoacoustic annoyance could be lower. Listening experiments will have to confirm whether a reduced roughness truly reduces perceived annoyance, when all other metrics are kept constant. Yet, this change in RPM and number of blades is an important parameter in reducing noise annoyance of propeller aircraft.

In this study, two psychoacoustic annoyance models that are commonly used, predicted a reduced annoyance for the 3-bladed propeller flyovers, while conventional metrics indicate larger values for the 3-bladed propeller. Listening experiments can also confirm if the modelled annoyance or conventional metrics is a better indicator of annoyance.

8

Propeller noise model validation for a Pipistrel Velis Electro [1]

We tend to overestimate the effect of a technology in the short run, and underestimate the effect in the long run.

Roy Amara

The previous chapter concluded that a push-pull propeller aircraft represents a complex noise source with numerous unknown interactions. Therefore, the single-propeller electric aircraft, Pipistrel Velis Electro from E-flight Academy, was selected to conduct the analysis initially intended for the Skymaster. ROSI and CB were employed to separate rotating and non-moving noise sources in ground run-up measurements. Subsequently, in-flight measurements of this aircraft were used to validate a propeller tonal noise prediction model, the Helix-tool. Validation was successful for the first harmonic tones, however improvements could be achieved by incorporating non-axial inflow effects into the Helix-tool. Ultimately, a thoroughly validated and accurate propeller noise prediction model could support the design of quieter aircraft.

[1] This chapter is a revised version of papers presented at BeBeC 2022 [208] and AIAA 2024 [209]. The dataset is published in the 4TU Research Data repository [210].

8.1. INTRODUCTION

Recently, the first fully-electric aircraft was certified for flight. Although the Pipistrel Velis Electro is still the only one certified [211], many companies announced the launch of a propeller-driven electric aircraft. Propeller-driven aircraft are known to cause significant noise annoyance, which is predicted to only increase with more propeller (electric) aircraft in service [33, 34]. Therefore it is important to investigate and ultimately reduce the noise production of propeller-driven aircraft. Some studies have investigated whether electric propeller aircraft produce less noise than their piston-engine counterpart through a reduction of engine noise [35, 36], but it is unclear whether the engine was the dominant noise source and thus whether an electric engine provides a sufficient noise reduction. Therefore additional studies in reducing propeller-driven aircraft noise are ongoing, with a focus on redesigning the propeller instead to reduce propeller tonal noise [212]. The aim of this chapter is to understand the various noise sources of the (electric) Pipistrel Velis aircraft and how these sources can be predicted accurately, while the next chapter (Chapter 9) aims to understand the annoyance of the Pipistrel Velis.

To reduce the noise emissions and annoyance of propeller-driven aircraft, the noise sources need to be analysed, and their contribution reduced during the design process of a new propeller aircraft. The noise emissions of the Pipistrel Velis were found to be dominated by propeller tonal noise [209]. Therefore this chapter applies a focus on semi-empirical prediction models for propeller tonal noise, and in specific the Helix-tool [96]. The Helix-tool is an implementation of Hanson's helicoidal surface theory, based in the frequency domain, which has proven to be among the most simple yet accurate for far-field tonal noise of propellers [213–215]. The model was validated with wind-tunnel data in the past, but still has to be validated with full-scale propellers in operating conditions which means a comparison with data of a propeller aircraft [216, 217].

The measurements on full-scale models however include other aircraft noise sources and potential interaction effects that need to be separated from the propeller noise. Thus, this chapter first investigates the possibility to separate rotating and non-moving noise sources by applying two acoustic imaging methods on the same measurement of an aircraft on the ground. This allows for filtering in the spatial, velocity, and frequency domain [132].

The measured spectrum is then compared to predictions of the Helix-tool, both in frequency content through the spectrum at overhead position as well as the polar directivity predicted during a flyover. Finding the limitations of the Helix-tool can aid in understanding when or how to apply the tool for propeller noise predictions. Ultimately this can aid in reducing propeller noise in the design phase.

This chapter is entirely centred on noise measurements of the Pipistrel Velis aircraft, which are explained in Section 8.2. Section 8.3 analyses the noise measurements with the aircraft on the ground to obtain first insights in the acoustic sources on the aircraft, as also indicated in Chapter 7. The measurements are used to validate the Helix-tool, a propeller tonal noise prediction model. The model as well as the validation are treated in Section 8.4. The chapter closes off with a conclusion and recommendations.

8.2. MEASUREMENT CAMPAIGNS

The experiments for this chapter were performed on a Pipistrel Velis Electro stationed at Teuge International Airport, the Netherlands. This aircraft is the first certified electric aircraft [211]. It is a two-seater aircraft with a single engine-propeller combination. The electric engine drives a three-bladed fixed-pitch propeller with a diameter of 1.64 m. It has tricycle landing gear which are non-retractable.

8.2.1. GROUND MEASUREMENTS

Ground measurements were performed to obtain a source decomposition of the rotating sources from the non-moving sources. This is a repetition of the attempt for the Skymaster, but applied to a simpler case where the engine is expected to be less intrusive. The measurements took place at Taxiway Charlie (see Figure 8.3) with the setup shown in Figure 8.1.

Figure 8.1: Setup engine run-up with the microphone array aligned with the propeller rotation centre.

The microphone array that is visible on the right side is a CAE Systems Bionic M-112 array [192]. It was placed 5 m in front of the aircraft nose, which is in the far-field of the propeller [2]. The system contains 112 MEMS digital microphones spread over seven microphone arms and achieves a sampling rate of 48 kHz. Additionally, a small optical camera was placed in the centre of the array.

In addition to the microphone specifics, the aircraft operational conditions are a necessary input for Rotating Source Identifier (ROSI). These can be extracted from the cockpit dashboard, of which a screenshot from GoPro footage is shown in Figure 8.2. Additionally, the rotation direction of the propeller is required. For the Pipistrel Velis Electro,

[2] The acoustic far-field limit for propellers is defined as (1) greater than one propeller diameter away from the tip, or (2) a distance larger than the dominant wavelength (of the BPF) [62].

this is clockwise as seen from the pilot, i.e. ,counter-clockwise as seen from the array. The propeller is rotating at 2020 RPM for the snapshot considered. This means the rotation frequency is 33.5 Hz and the BPF is 100.5 Hz. In the time selected for the snapshots considered with Conventional Frequency-Domain Beamforming (CFDB) and ROSI, the propeller rotates roughly 5.7 times.

Figure 8.2: GoPro photo of the cockpit instruments at the time of the measurement.

8.2.2. FLYOVER MEASUREMENTS

To validate the Helix-tool under operational conditions, besides the validations done previously on wind-tunnel measurements, measurements of the Pipistrel Velis in forward flight were used. Measurements during flyovers, take-offs, or landings can provide information about the different noise sources on the aircraft during operation. This is generally considered to be a more realistic scenario than a wind-tunnel, albeit more difficult to control all flight parameters.

This propeller-driven aircraft has an electric engine and little airframe components. High fidelity CFD simulations performed by Yunus et al. [209] for solely the propeller provided a sufficient match to the tonal components as well as the broadband levels, compared to measured noise of the entire aircraft in the same operational conditions. Hence leading to the conclusion that the Pipistrel Velis propeller aircraft with fixed-pitch can be seen as a “flying propeller” for modelling purposes. Potential deviations of the assumption of no airframe noise will become apparent in tonal and broadband characteristics that cannot be linked to propeller tones. It is however unknown if the electric engine has any noise contribution specifically.

For these flyover measurements, two locations were used which were dependent on the wind direction on the measurement day. Figure 8.3 indicates the flight direction with the corresponding location of the array, represented by a dot, in the same colour. Both locations were used to record flyovers on two separate days. For the Pipistrel Velis three take-offs and three flyovers were recorded in total.

The flight characteristics are presented in Table 8.1 and the derived parameters in Table 8.2. From these flight parameters it can be concluded that the tip Mach speed is not nearing sonic for any case, which means that loading noise is expected to be the

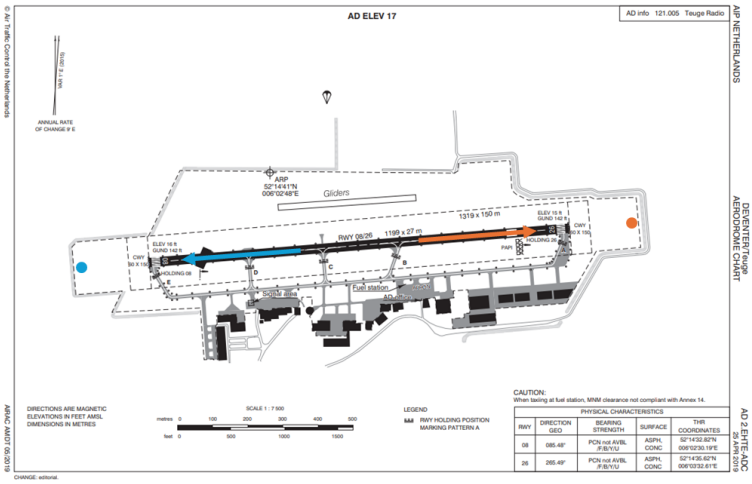

Figure 8.3: Teuge International Airport Aerodrome chart with indications of the flyover locations: the arrow indicates the flight direction and the dot in corresponding colour represents the array location.

dominant noise source [62].

Table 8.1: Flight parameters for each flyover recording according to the data recorded inside the cockpit.

Measurements	**Altitude** [a] **(m)**	**Velocity (m/s)**	**BPF (Hz)**	**Power (kW)**
Data Source	Altimeter/GPS	GPS	Cockpit display	Cockpit display
Take-off 1	76.2	31.0	2430	68
Take-off 2	39.6	36.8	2460	66
Take-off 3	42.8	36.1	2440	65
Flyover 1	8.9	35.7	2000	20
Flyover 2	8.3	35.9	2100	25
Flyover 3	12.2	41.7	2520	64

[a] Flyover 1 and 2 had unclear GoPro footage of the cockpit display, thus GPS data was used. For the other flights the cockpit data and GPS were compared, but take-off 2 and 3 had strong fluctuations in GPS data and thus were deemed insufficient.

8.2.3. 3D SCANS OF PROPELLER

The propeller geometry is not readily available, and therefore the geometry was acquired through 3D scans of the propeller blades. The scans were performed with a FaroBlu HD laser in combination with a FARO Quantum E 3.5m 7-axis arm for a high degree of mobility. The accuracy of the scanner is 25µm with a scan rate of 300 frames per second, each including 2000 points, with a point cloud as output.

The point cloud was post-processed through the commercial software of the scanner

Table 8.2: Relevant derived metrics for propeller noise based on the flight parameters.

Measurements	BPF (Hz)	Advance ratio (-)	M_{tip} (-)
Take-off 1	121	0.47	0.61
Take-off 2	123	0.55	0.62
Take-off 3	122	0.54	0.62
Flyover 1	100	0.65	0.51
Flyover 2	105	0.63	0.52
Flyover 3	128	0.61	0.64

first, where a smoothing and outlier check was performed. The point cloud is used to create a 3D surface on which several sections are defined for aerofoil coordinate files, as well as the distributions for thickness-to-chord, blade pitch angle, and chord-to-diameter.

8.3. DECOMPOSITION OF NOISE SOURCES DURING GROUND MEASUREMENTS

In Section 7.3.1, which researched the decomposition of noise sources of the Skymaster by using ROSI and CB jointly, it proved to be difficult to capture all sources. Therefore, the method was applied to ground measurements of the Pipistrel Velis, as this aircraft is expected to have less engine noise sources and thus has a lower number of different non-moving noise sources present.

A few interesting frequency bands were analysed with ROSI and CFDB. Figure 8.4 presents incoherently summed CFDB results and ROSI results with a bandpass filter on the time-domain signal for three frequency ranges. The methods can be compared side by side for difference in source velocity domain or top to bottom for differences in spatial and frequency domain. Note that all the maximum levels were added in the caption for each figure in Figure 8.4 for easy comparison. The dynamic range for all images equals 3 dB.

What stands out from the CFDB results is that the lower right source is dominating the beamforming levels. From the simulation in Figure 3.10 it was expected that a ring of increased levels would be present when applying CFDB to rotating sources, but this only happens for higher frequency ranges (see Figure 8.4e) where the source strength of the blades increases relative to the source strength of the non-moving source from Figure 8.4a. Thus, the lower right source has to be a source at a fixed position which could be due to flow recirculation along the nose landing gear which is excited every blade passing or by a blade passing through the ground vortices. In other research the noise source arising from an interaction of the pressure field of a rotating source with a non-moving source is called a cyclostationary noise source [206]. Additionally, the ground reflection of the non-moving source is visible.

When considering the acoustic imaging results of ROSI, it is important to observe the levels in the source map. First a comparison with the CFDB images is made. For the lower two frequency ranges, the non-moving source has a higher maximum level but for the highest frequency range (Figures 8.4e and 8.4f) the rotating sources were stronger. When comparing all ROSI images for the different frequency bands, it appears that one

blade can be stronger or weaker than the others at different frequency ranges. For example, the rightmost blade is the strongest for 6.1 to 6.6 kHz, but this is not true for 2.1 to 2.6 kHz.

Interestingly, adding the contributions of the three blades in ROSI images yields roughly the same level as the source in the CFDB map. This might indicate a cyclostationary source as described in the PhD thesis of Jekosch [206] where ROSI shows the same source as CFDB but now distributed over the blades.

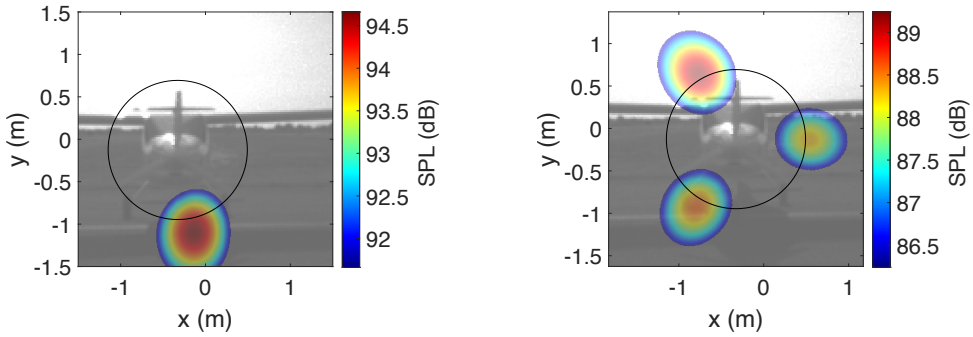

(a) CFDB 2.1 to 2.6 kHz, SPL_{max} = 94.7 dB

(b) ROSI 2.1 to 2.6 kHz, SPL_{max} = 89.3 dB

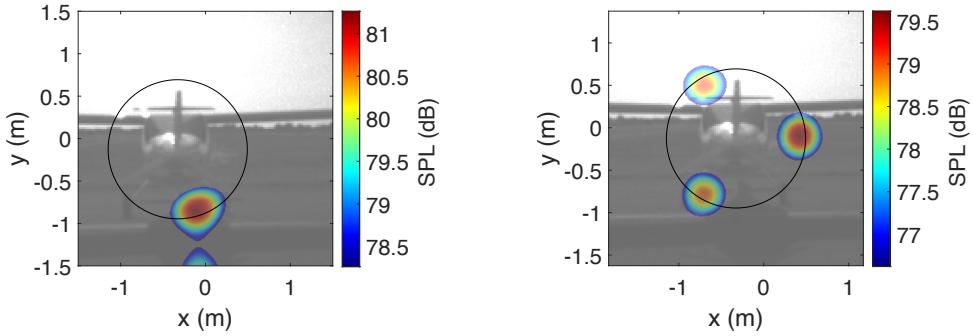

(c) CFDB 3.6 to 4.1 kHz, SPL_{max} = 81.2 dB

(d) ROSI 3.6 to 4.1 kHz, SPL_{max} = 79.6 dB

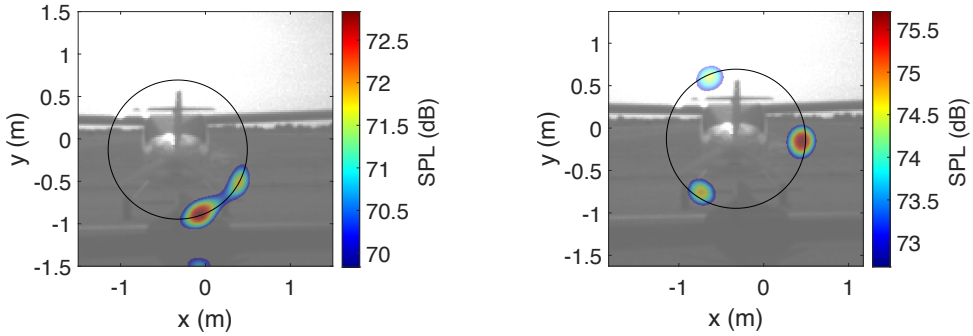

(e) CFDB 6.1 to 6.6 kHz, SPL_{max} = 72.8 dB

(f) ROSI 6.1 to 6.6 kHz, SPL_{max} = 75.8 dB

Figure 8.4: Comparing CFDB and bandpass filtered ROSI on different frequency ranges. The colourbar represents the total level over the selected frequency band. The colourbar has a dynamic range of 3 dB for all images.

By extracting the reconstructed pressures at the source locations (at maximum level), the individual source contributions are found. The numbering of the blades is indicated in Figure 8.5a, which is the position of the blades at the start of the measurement. The reconstructed pressure signal is depicted in Figure 8.5 and shows a pressure maximum for each of the blades per rotation, rather than a constant level. This position corresponds to approximately the position of a blade close to the ground, like blade 2 in Figure 8.5a, where it is expected that the noise levels are higher due to ground reflections or ground recirculation causing unsteady loading.

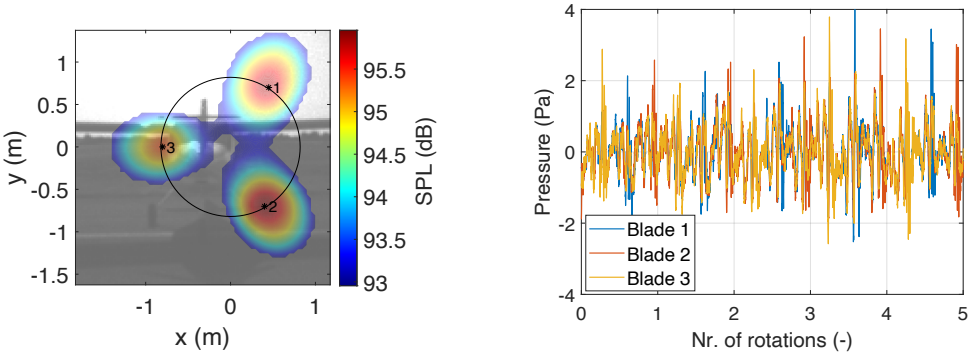

(a) Identified blades

(b) Pressure signal over multiple rotations

Figure 8.5: Reconstructed pressure signals from ROSI sources for the Pipistrel Velis non-moving measurement per blade.

The analysis of the sources through CB and ROSI simultaneously as is done here, can be interesting for future research as a method. Especially the reconstructed pressure signal from ROSI proved useful to confirm that there are sources present around the ground location, and that the levels portrayed on the blades in the acoustic maps are not only the blade sources. However, these measurements themselves may not be useful as a basis for understanding flyover noise sources due to the additional noise sources around the ground.

8.4. VALIDATION OF A TONAL PROPELLER NOISE PREDICTION MODEL

The model that is investigated in this chapter is based on a frequency domain method which generally eases the computation of propeller tonal noise [101]. The method is Hanson's helicoidal surface theory which predicts the tonal components including the effects of thickness noise, steady loading noise during forward flight of a propeller aircraft, and corrections for blade sweep [96]. In this research the far-field model was used, of which the model implementation is described first. The validation of the model on measurements of a Pipistrel Velis is described next. Also a brief explanation of the model improvements for take-off flights and non-axial inflow are presented here, along with their validation.

8.4.1. HELIX PROPELLER NOISE MODEL

The Helix noise prediction tool that was used in this work, is based on Hanson's far-field noise prediction model for axial inflow for which the equations are stated in Chapter 2. It computes the thickness and loading noise of a propeller separately and combines this to the predicted pressure field at a specified microphone location. To acquire the inputs for the model equations, an extensive set of parameters is needed, part of which are derived from the propeller shape and a part of which are derived via the airfoil data in combination with operational flight data. The aerodynamic data is a necessary input for the acoustic formulation.

The thickness noise can be computed with as inputs just the propeller blade shape, discretized into several aerofoil sections along the span, the forward velocity, and the propeller RPM. The local velocities are calculated for each airfoil section, after which these are used to compute non-dimensional wavenumbers. The chordwise thickness distribution per section is normalized which allows to compute the thickness source term. Separately, the Bessel function is computed for every radial section and harmonic number. The thickness source term and the Bessel function are fed into the integral of the volume displacement component P_{Vm} from Equation 2.4. The components are integrated over all radial sections to the total thickness noise component in Fourier components which can be used in Equation 2.2. The flowchart of this process is presented in Figure 8.6.

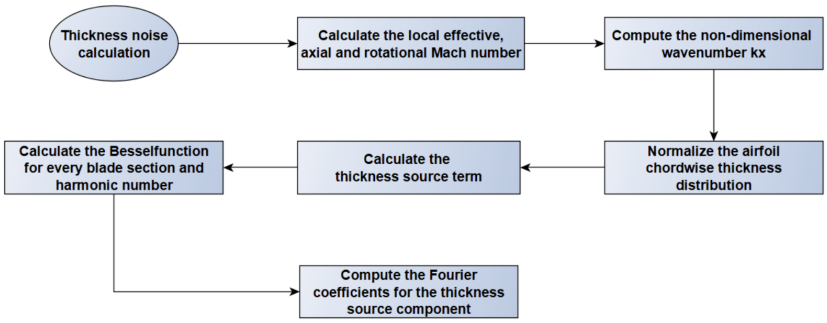

Figure 8.6: Flowchart of the computation of thickness noise in the Helix-tool (adapted from Haddaoui [218]).

For the loading noise the lift and drag forces on the local blade sections have to be determined. For a rotating blade section, this requires two consecutive steps: (1) determine 2D aerodynamic characteristics of the blade, and (2) define the 2D characteristics in the advance direction, i.e., correct for the induced effects of the propeller. Note that the pitch of the propeller blades in this research is fixed, which significantly simplifies the use of prediction models as pitch is an input for blade loading. For variable pitch propellers such as the Pipistrel Virus, it is difficult to measure the pitch at any given moment during the flight, and therefore other aircraft are less suited for the validation of propeller noise prediction models.

XFOIL [219] is used to obtain the 2D characteristics of each blade section, such as the

sectional lift and drag coefficients. XROTOR [220] computes the induced velocity components and local angle of attack through an iterative approach based predominantly on the chord-to-radius ratio local blade pitch angle as well as the propeller geometry. These components are used to shift the previously calculated characteristics in the advance direction. After the shift, non-dimensional wavenumbers are calculated and then the chordwise lift and drag distribution per section are defined. With these inputs the source loading term is computed. Separately, the Bessel function is computed and all components are combined in Equations 2.6 and 2.7 and integrated over the radial sections, resulting in the lift and drag noise components, respectively P_{Lm} and P_{Dm}. The flowchart of this process is presented in Figure 8.7.

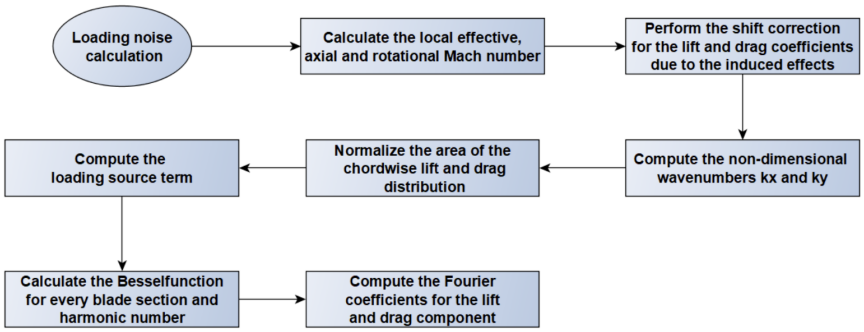

Figure 8.7: Flowchart of the computation of loading noise in the Helix-tool (adapted from Haddaoui [218]).

The source Fourier components for thickness, lift, and drag can then be added and used in the Fourier Series of Equation 2.2 to compute the time-pressure signal at an observer location. The individual source components can also be analysed, by simply omitting the sum of components and using P_{mB} equal to a single source contribution. This can aid in understanding when or where thickness or loading noise is dominant.

8.4.2. VALIDATION OF SPECTRA AT OVERHEAD POSITION

At the overhead position, the tonal components were expected to be dominant and hence the validity of the Helix-tool to model tonal components is assessed at this position first [217, 221]. Figure 8.8 shows the spectra as predicted by the Helix-tool at the microphone location as well as the measured spectra at overhead position (snapshot of 0.08 s). For the prediction, 10 harmonics were considered, and level flight with axial inflow was assumed in all cases.

For flyover 1 and flyover 2 the propeller RPM was lowest of all flights, which indicated a higher advance ratio and thus lower loading, which resulted in less strong tonal peaks in the overhead spectrum compared to flyover 3 and the take-offs [218]. Yet, the first two harmonics which were dominant in level were modelled accurately with an offset of at most 1.8 dB. For flyover 3 the first two harmonics frequencies correspond well, although with an offset of 4.1 dB for the first harmonic, but for the higher harmonics the tonal peak in the measurements is shifted slightly away from an integer multiple of the BPF. Higher

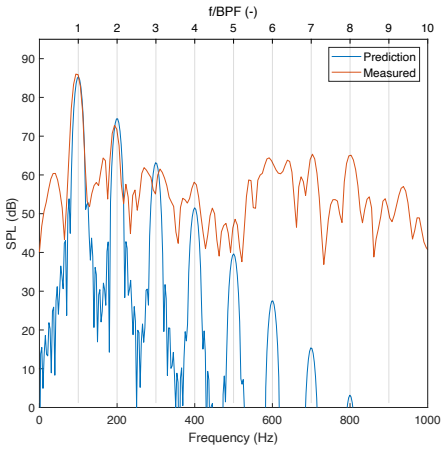

(a) Flyover 1

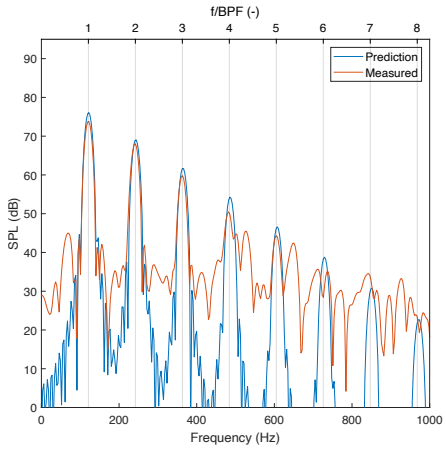

(b) Take-off 1

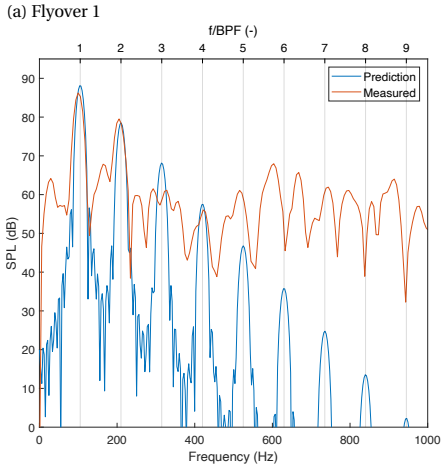

(c) Flyover 2

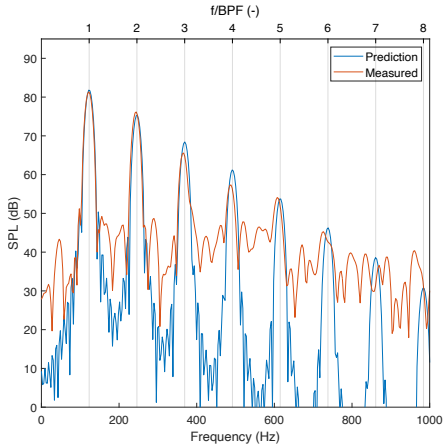

(d) Take-off 2

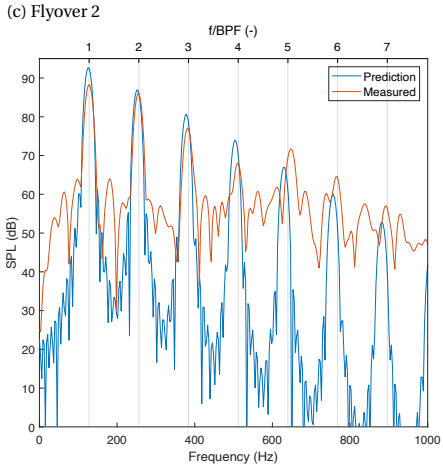

(e) Flyover 3

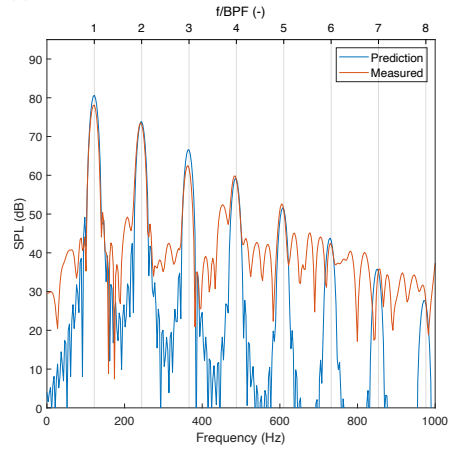

(f) Take-off 3

Figure 8.8: Comparison of Helix-tool output, at the middle microphone, versus measured spectra at microphone level.

harmonics were underprecited by the model, which could be due to underprediction of higher order harmonics due to the strong dampening in the Bessel functions [217]. Furthermore, the first four tones were overpredicted in level. It is not clear why this is the case, although a sensitivity analysis indicated a strong sensitivity to flight speed V_x when the advance ratio was kept constant and RPM was allowed to vary [222]. The analysis showed that an overprediciton of V_x resulted in an overprediction of SPL at all harmonics. However, the cockpit display showed a velocity around 40.5 m/s instead of the values in Table 8.1 but this only reduced levels with 0.1 dB and does not resolve the shift in higher frequencies.

For the take-off cases, the Helix-tool is able to capture the first and second harmonic accurately with an offset of at most 2.5 dB, while it sometimes overpredicts the third and fourth harmonic similarly to the flyover 3 case. The higher harmonics (≥5) were not represented well by the Helix-tool for take-off 1 and 2 which might be due to the periodic changes in the blade loading [209]. However, including these unsteadiness effects should rather result in (even higher) model predictions at high harmonics thus increasing the overprediction. The measured spectra do not show tonal components above the seventh harmonic for take-off so it could be that the discrepancy is caused by the presence of other sources or by propeller interaction and installation effects.

In general, this validation shows that the Helix-tool is capable of accurately predicting the first few tonal components when the first harmonics are dominating the OSPL. Take-off operations were better predicted by the Helix-tool than flyover operations, as the tonal components are relatively stronger than the broadband level. At higher harmonics, the model decays too strongly compared to the flyover measurements. This can be attributed to periodic unsteady loading which manifests at higher harmonics [223]. For take-offs it was expected that the model underpredicts higher harmonics as it does not account for the periodic loading effect of non-axial inflow, but this is not apparent in the measurements presented here.

8.4.3. POLAR DIRECTIONALITY DURING FLYOVER

Aside from the validation of Helix at the overhead position through the spectrum, its prediction capability at other polar angles was also validated. Figure 8.9 shows that the forward arc ($\theta < 90°$) is dominated by thickness noise, whereas lift noise is the strongest term in the aftward arc ($\theta > 120°$). The maximum is located at the overhead position $\theta = 90°$.

Figure 8.10 shows the total model prediction versus the measured total OSPL for the flyovers with the Pipistrel Velis. As the Helix-tool is not capable of including a climb angle and non-axial inflow, which causes differences in the source-receiver distance and thus the polar angle, this type of validation is not performed for take-offs.

For flyover 1 and 2 the measured levels were within 3 dB of the modelled levels (underpredicted for flyover 2 and overpredicted for flyover 1). For flyover 3 the predictions in the aftward arc (around 120°) showed deviations up to 5 dB. It is unclear what causes this offset as the GPS data shows hardly any variation in velocity or altitude. It is expected that the Helix-tool is not able to predict forward and aftward angles, as tonal noise is dominant in the propeller plane, i.e., at 90°, and the model would need to be extended with broadband components for other angles. Some studies found that the model was

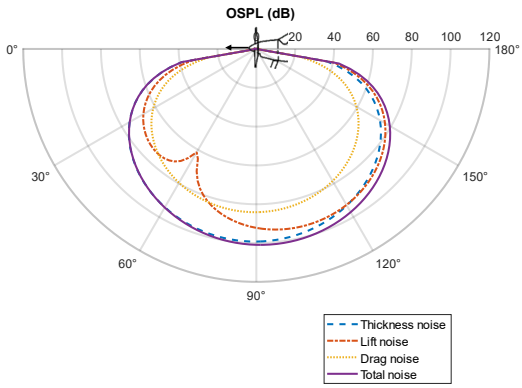

Figure 8.9: Helix-tool prediction of the different tonal source components for various polar angles for flyover 3.

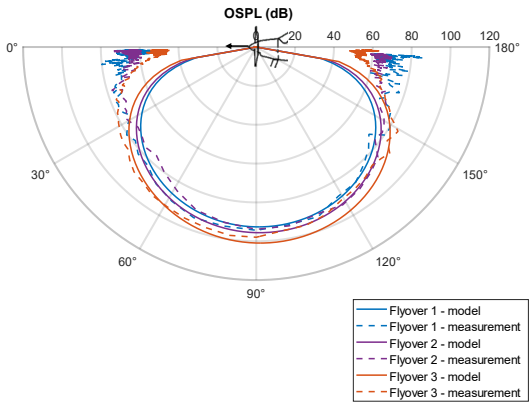

Figure 8.10: Polar directionality for measurements (dashed line) versus model (solid line).

not capable of predicting the loading component in the forward arc ($\theta < 90°$) accurately, where destructive interference of their lobes is present, but the thickness noise is far more dominant here for this propeller model (and RPM) hence this issue does not seem present [217].

It might be worth investigating whether the differences between model and measurement at various polar angles are caused by the broadband noise or by specific harmonic components in the spectra.

8.4.4. INFLUENCE OF SHAFT ANGLE OF ATTACK ON NOISE PREDICTIONS

The Helix-tool from the previous sections does not include a correction for the angle of attack of the shaft propeller (α_{shaft}), while this may have a large impact on the loading

noise especially in take-off. Especially higher harmonics of the propeller tonal noise are sensitive to a non-axial inflow [100, 209]. The helicoidal surface theory developed by Hanson, and applied in the previous section, was later extended to take into account the non-axial inflow through incorporating the α_{shaft} in the source-receiver angle θ and the flow induction angle ϕ [100]. This could improve the results of the Helix-tool.

To this end, LOPNOR [209] was developed which uses as basis the Hanson's formulation of [100] in combination with a BEMT-procedure which defines the propeller sectional lift and drag and replaces the need of XROTOR used in the Helix-tool. Results of LOPNOR and the Helix-tool for $\alpha_{\text{shaft}} = 0°$ were thus expected to be the same. The results of LOPNOR for take-off 1 up to and including 3 and flyover 3 are presented in Figure 8.11. Case 1, the flyover, shows that the high fidelity model (HF) based on CFD simulations, matches well with the measurements for broadband levels up to 5 times the BPF, but overestimates the level of the 3rd and 4th harmonic. LOPNOR matches HF for the first four harmonics, with >5 dB underpredictions for higher harmonics. Thus LOPNOR was deemed a valid method to predict tonal propeller noise.

However, for cases with non-axial inflow, LOPNOR with the α_{shaft} correction is able to better capture the higher harmonics thereby reducing its underprediction with the remaining discrepancy accredited to unsteady loading which is not modelled in this formulation. For the first four harmonics, the prediction is only slightly changed, with generally higher levels than for the axial-inflow assumption, thus increasing the overprediction at the third and fourth harmonic.

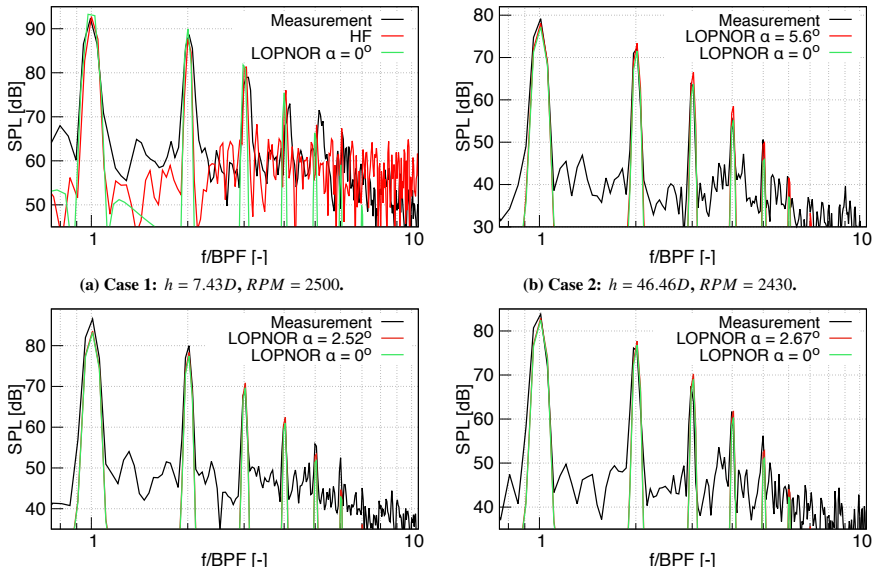

(a) Case 1: $h = 7.43D$, $RPM = 2500$.

(b) Case 2: $h = 46.46D$, $RPM = 2430$.

(c) Case 3: $h = 24.16D$, $RPM = 2460$.

(d) Case 4: $h = 26.07D$, $RPM = 2440$.

Figure 8.11: Noise spectra of LOPNOR for take-off 1, 2, 3, and flyover 3 from Table 8.1, in comparison with the measured spectra at overhead position. Figure from [209].

If the Helix-tool were to incorporate the non-axial inflow, it is expected to yield im-

proved predictions at higher harmonics as well. Yet, the inclusion of unsteady loading and broadband noise should also be considered.

8.5. CONCLUSIONS AND OUTLOOK

The Pipistrel Velis Electro aircraft has as primary noise source the propeller according to a comparison between computational fluid dynamics simulations and measurements. This aircraft thus is valuable for validating propeller noise prediction models to aid in quieter propeller designs.

Measurements confirm that the propeller's first few Blade Passage Frequency (BPF) harmonics dominate the noise spectrum. Some additional sources were present in conventional frequency-domain beamforming source maps such as ground reflection and potentially a form of flow recirculation with nose landing gear interaction. Rotating Source Identifier (ROSI) source maps clearly identify the three propeller blades, however the levels are not correct. The ROSI source maps presented here are averaged over a rotation, which includes the excitation of a cyclostationary source and thereby increases the levels beyond the blade levels. It is not clear if these sources are also present in flight as then the interaction with the ground boundary layer and ground vortices is removed, but a cyclostationary source around the fixed landing gear might still arise.

Three flyover and three take-off measurements were used to validate the Helix-tool, showing a tone prediction offset of 4.1 dB for flyovers and 2.5 dB for take-offs for the first two harmonics. However, the higher harmonics were less accurate, likely due to the model's limitations. Including non-axial inflow in the model improved predictions at higher harmonics for take-off flights. Polar directionality results were mixed, with two flyovers showing some consistency in the aftward arc but variable accuracy across cases for the forward arc. This could be due to the contribution of non-tonal noise sources, also around the propeller axis.

In summary, the Helix-tool can predict propeller noise effectively, with higher accuracy at the first few harmonics, when other sources and installation effects are minimal, and the flow is axial. Further studies on directionality with more flights or a validation per harmonic could improve the understanding of these results. Adding non-axial inflow to the Helix-tool would allow for more comprehensive flight operation predictions which could be used for auralisation of propeller noise. This could aid in achieving the overall goal of designing aircraft for lower noise annoyance, while the validation and definition of use cases of the Helix-tool alone are already aiding in designing for lower noise emissions.

9

PSYCHOACOUSTIC ANNOYANCE OF ELECTRIC PROPELLER AIRCRAFT [1]

A theory may be so rich in descriptive possibilities
that it can be made to fit any data.

Phillip Johnson-Laird

In previous chapters, the sound source location and level were established for various sources. However, Chapter 7 already showed that the sound level does not fully represent the human perception, which is more accurately captured through several sound quality metrics. This chapter explores this topic further by studying sound quality metrics as well as reported annoyance in listening experiments for the Pipistrel Virus and its electric-counterpart the Pipistrel Velis Electro. The aim is to understand whether replacing conventional aircraft by electric aircraft reduces the noise annoyance around airports. This research found that the Pipistrel Velis Electro had a predicted annoyance reduction of 50%. Listening experiments confirmed a reduced annoyance, but indicated a reduction of 33%.

[1] This chapter is an extended version of a paper presented at ICSV 30 [224]. The dataset is published in the 4TU Research Data repository [210, 225].

9.1. INTRODUCTION

The aviation sector contributes significantly to greenhouse gas emissions through burning fossil fuels in jet engines. While engines are becoming more fuel efficient, the increase in number of flights worldwide partially counteracts the reduction in emissions, which affects the climate [226]. Therefore, the industry is looking for alternative propulsion methods beside the ever continuing quest of increasing engine efficiency.

Alternative propulsion methods include, but are not limited to, hydrogen fuel cells, hydrogen combustion, and electric motors drawing from batteries. Many concepts that use one of these methods make use of propellers as they can be more efficient on the short to mid-range operations [201]. Additionally, propellers can be connected to any type of motor, hence providing the possibility to research different propulsion methods.

While some research found that the electric motor will hardly contribute to the total noise level, due to its limited noise production, this does not mean that the noise level of a propeller-driven aircraft is lower automatically [35, 36]. This would be an analogy to electric cars, that are more silent than cars with combustion engines [227]. Yet, this claim omits the influence of the propeller itself which might be dominant over the combustion engine. In addition, conventional sound metrics often fall short in explaining human auditory perception [149]. Perception is an important contributor in successful adoption of these new aircraft types as communities are fighting for stricter noise regulations.

Therefore, the research presented in this chapter focuses on noise emissions and annoyance of electric propeller-driven aircraft in comparison to a combustion engine counterpart. In essence, it aims to answer the question *"If you would fly an electric aircraft the same as its non-electric counterpart, would there be a difference in noise annoyance?"* The aircraft investigated here are the two-seater Pipistrel Virus and its direct (electrical) replacement the Pipistrel Velis Electro, which is the first-certified electric aircraft.

The characteristics of the Pipistrel Virus and the Pipistrel Velis Electro are described in Section 9.2. The procedure of the listening experiments is extensively described in Section 9.3. Then the measurements are compared through spectral analysis and conventional metrics in Section 9.4 to understand the sound signal, and subsequently the sound quality metrics are reported in Section 9.5. The results of the listening experiments are reported in Section 9.6, where the predicted annoyance is compared with the measured annoyance. These steps contribute to the ultimate goal of assessing the community impact of replacing combustion engine aircraft with electric aircraft in terms of noise.

9.2. CHARACTERISTICS OF PIPISTREL VELIS AND VIRUS

The research objects for this study are two propeller-driven aircraft manufactured by Pipistrel. The combustion engine aircraft is the Pipistrel Virus SW121 and the electrical version is the Pipistrel Velis Electro SW128 as seen in Figures 9.1a and 9.1b respectively.

Table 9.1 presents the aircraft parameters from the Type Certificate Data Sheet (TCDS) from EASA. Both aircraft fall under the same TCDS category, as Pipistrel launched the Velis and Virus as sub-models within aircraft type SW 121. Both aircraft have nearly identical airframes as can be derived from the dimensions, in combination with the photos.

(a) Pipistrel Virus

(b) Pipistrel Velis Electro

Figure 9.1: Photos of the exact aircraft used in the current study. Photo courtesy: E-flight Academy.

Table 9.1: Technical characteristics of the two Pipistrel aircraft under study, obtained from EASA TCDS and Pipistrel manufacturing data [211, 228, 229].

Aircraft name	**Pipistrel Virus**	**Pipistrel Velis**
Aircraft type	SW 121	SW 121
Aircraft model	SW 121	SW 128
Engine type	Rotax 912 S3	E-811 / 268MVLC
Propeller type	MTV-33-1-A/170-200	Pipistrel P-812 / 164-F3A
Nr. of propeller blades (-)	2	3
Propeller diameter (m)	1.70 (CW)	1.64 (CW)
Propeller pitch	constant-speed	fixed-pitch
MTOW[a] (kg)	600	600
Payload weight (kg)	229	172
Nr. of seats (-)	2	2
Wingspan (m)	10.70	10.71
Length (m)	6.45	6.47
Height (m)	2.06	2.08
Flap deflections (deg)	-5, 0, 9, 19	0, 8, 19
Landing gear	fixed tricycle	fixed tricycle
V_{NO} (kts, indicated air speed)[b]	120	98
Max. climb rate (m/s)	5.33	3.3
Max. continuous power (kW)	69/5500 RPM	49.2/2350 RPM
Service ceiling (ft)	18,000	12,000
Endurance (time)	5h 33 min [c]	50 min [d]
Noise certification $L_{A,max}$ (dBA)	70	60

[a]Maximum Take-off Weight
[b]NO: normal operation, maximum structural cruising speed
[c]at 4000 ft., 65% power (+30 min reserve)
[d]plus Visual Flight Rules (VFR) reserve

The Maximum Take-Off Weight (MTOW) is identical too. The weight differences from the motor, propeller, and fuel/battery are compensated in the maximum payload weight

which is lower for the Velis than the Virus. Another airframe component, the landing gear, is registered as a fixed tricycle for both types, however, the photos of the aircraft types show that the Virus has fixed covers around the landing gear. While these covers add weight to the plane, they also provide drag reduction during flight.

The main differences between the aircraft types are the engine and propeller types. The propeller differences could explain differences in the noise profile, as propellers with more blades typically provide more thrust, or for a given thrust there is lower loading per blade. An increased number of blades also increases the Blade Passing Frequency (BPF).

The noise certification value was determined by measurements during take-off according to ICAO Annex 16, Volume I, edition 8, amendment 12, chapter 10.4b [230]. This is the certification standard for propeller-driven vehicles with a MTOW of 8618 kg at most. For this type of aircraft, the measurement was recorded under the take-off flight path at 2500 m from the start of take-off roll, while operating at maximum take-off power. While the ICAO noise certification standard can be assumed to provide maximum noise levels, it does not represent a relevant comparison for noise annoyance for two reasons: (1) conventional metrics are not necessarily indicative of annoyance, and (2) communities are not necessarily under the take-off path but could be situated under a cruise path instead. Therefore, flyover measurements are performed during cruise flight which are extensively analysed for a broader range of metrics.

Table 9.2: Flight parameters for each flyover recording. $L_{A,eq}$ calibrated and scaled to maximum allowable levels for listening experiments.

Flyover	h (m)	V (m/s)	RPM (-)	BPF (Hz)	P (kW)	$L_{A,eq}$ (dBA)
Virus 1	7.6	39.2	2200-2600	unclear	unknown	55.9
Virus 2	10.2	41.6	2550	85	unclear	51.4
Virus 3	6.4	37.8	2550	85	unclear	51.4
Velis 1	8.9	35.7	2000	100	20	40.9
Velis 2	8.3	35.9	2100	105	25	41.7
Velis 3	12.2	41.7	2560	128	64	47.3

The flyover measurements were already described in Section 8.2 for the Velis and for the Virus the same procedure was followed, with the same altitude and flight velocity, but RPM was allowed to vary. Thus the Mach tip number and the advance ratio are different between the Velis and the Virus measurements, but the required thrust for these flights should be roughly equal due to the identical aircraft design.

The measurements are recorded on the airport perimeter, for low altitude flights to improve the signal to noise ratio. However, one study indicates that these types of measurements may lead to a different trend compared to flyovers above a community for large airports [67]. While the spectral shape indeed can be different due to atmospheric attenuation over larger distances, it is expected that this effect is limited for the flyovers considered here as the spectrum is dominated by low frequency tones.

The flight parameters of the Velis and the Virus flyovers are presented in Table 9.2. As these measurements were used in a concurrent listening experiment, they were calibrated and scaled according to maximum allowable levels for listening experiments ($L_{\mathrm{A,max}}$ = 80 dBA). All results presented in this chapter, are based on the calibrated and

scaled sound files.

9.3. LISTENING EXPERIMENTS

The listening experiments were performed in the Psychoacoustic Listening Laboratory (PALILA) of Delft University of Technology. The psychoacoustic lab is named after the Hawaiian honeycreeper bird palila. The acoustic characterisation of the room is specified in Appendix A [166]. The specifics of the listening experiment performed for this study are described here, with first a description of the user interface to listen to sound files and answer corresponding questions, then a description of the sound stimuli, and lastly some information about the participants.

9.3.1. GRAPHICAL USER INTERFACE (GUI)

Participants recorded their subjective responses to the sounds using a Python-based graphical user interface (GUI) for listening experiments [231]. They could use both the laptop touchscreen and a mouse to click on the desired answers. In the current experiments, four different blocks of sound samples were considered, out of which only the third one is discussed in this chapter.

A standard questionnaire at the start of the experiments collected demographic data to compile population statistics, such as age, gender identity, level of education, and employment status. There were additional questions to gauge the hearing health of the participants. Overall hearing health was self-assessed by participants on a five-point scale from *poor* to *excellent*. Participants were also asked about potential past accidents that may have affected their hearing, the use of hearing aids, and the regular use of hearing protection. Participants then indicated whether they suffered from an ear disease and/or a cold. Lastly, general well-being and tiredness were also self-assessed using yes/no questions. The full list of the questions used and the possible answers can be found in the open-source GitHub repository of the GUI [231].

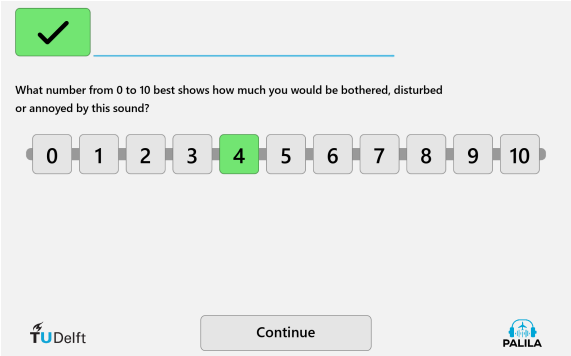

Figure 9.2: Example of the graphical user interface (GUI) employed in the listening experiment.

The sound sample block considered in this study was introduced to the participants as follows: *"The next part of this survey inquires about the annoyance of aircraft, both electric and non-electric. This block contains 12 questions. While listening, imagine that*

this is the sound situation in your garden." Participants then listened to each sound sample only once and answered the following question *"'hat number from 0 to 10 best shows how much you would be bothered, disturbed, or annoyed by this sound?"* using an ICBEN 11-point scale from 0 (*not at all*) through 10 (*extremely*), see Figure 9.2.

9.3.2. SOUND STIMULI

All the sound stimuli considered in the listening experiments correspond to audio files of the flyovers explained in Section 9.2. These recordings were reduced to a 5 s sample centred at the overhead position with respect to the microphone array. The order of reproduction of the stimuli was randomised per participant to minimise learning effects. Each sound stimulus was presented twice (also in randomised order) to assess the consistency and repeatability of the responses of the participants.

After the sound stimuli the participants had to answer a few questions to test the attitude and exposure of participants towards (sustainable) aviation. The answers can provide insight into potential biases that may influence the reported annoyance ratings. Regarding exposure to aviation noise participants were asked *"Do you hear aircraft passing over your house on a daily basis due to close proximity to an airport?"* and if they answered "Yes" they has to answer *"What best describes the size of the airport?"*. The attitude towards aviation was tested with *"What is your general attitude towards aviation?"*, and specifically tested for electric aviation with *"Do you think it is likely that you can board an electric aircraft for your holiday trip in 2035?"*.

9.3.3. PARTICIPANTS

The listening experiment included a total of 57 participants, comprising 38 men, 17 women, and two individuals identifying as *other* gender. The average age of the participants was 27 years with a standard deviation of 10.4 years. The age distribution per gender is depicted in Figure 9.3a. In each boxplot, the central horizontal line denotes the median values, the edges of the box are the 25th, and the 75th percentiles, and the whiskers extend to the most extreme data points. The outliers are plotted as +.

Regarding the level of education, 23 participants had a high school diploma as their highest level of education, while the rest held various degrees, such as BSc, MSc, and PhD. The subject group included 35 students, 20 people employed for wages, and two self-employed individuals. Amongst the *employed for wages* group, some individuals worked at Delft University of Technology, resulting in a total 46 participants being either employees or students of this university. Of the remaining participants, three were employed by other companies, three were students/employees at partner universities, and five had no affiliation with TU Delft.

The overall health of the group was considered good, and only eight participants reported a mild cold (1 – 2 on a scale from 0 to 5). Five participants reported feeling tired at the start of the experiment. The self-reported hearing level of the participants was high, with 13 indicating *excellent*, 27 indicating *very good*, and 17 indicating *good*. None of the participants had ear diseases or wore hearing aids, although one had had a hearing accident in the past, and four experienced tinnitus currently. Three participants regularly used hearing protection for work or for attending concerts.

Figure 9.3b shows the difference in rated annoyance for a participant between the

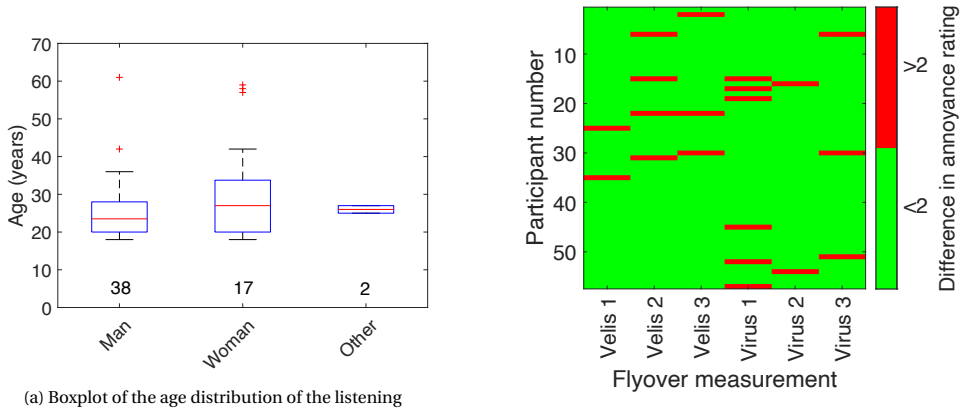

(a) Boxplot of the age distribution of the listening experiment participants grouped per gender.

(b) Difference in rating per participant

Figure 9.3: (a) Boxplot of the age distribution of the listening experiment participants grouped per gender. In each boxplot, the diamond marker denotes the mean value, the central horizontal line denotes the median values, the edges of the box are the 25th, and the 75th percentiles, and the whiskers extend to the most extreme data points. The outliers are plotted individually as circles. (b) Matrix showing the difference in rating per participant for a repeated sound file.

first and second time that a given sound file was rated. In general, the differences between the responses for all repeated sounds were below 2 points in 94% of the cases ($n_{\text{participants}} \cdot n_{\text{flyovers}}$), which is deemed as acceptable. Therefore, all 57 participants were considered in the psychoacoustic analysis henceforth. For further analysis, the annoyance ratings of the two repetitions of a sound file per flyover measurement were averaged to a single annoyance rating per flyover per participant.

9.3.4. EXPERIMENTAL PROCEDURE

The individual participants were welcomed and shortly briefed about the characteristics of the listening experiment. They were requested to read and sign an informed consent form, which was previously approved by the Human Research Ethics Committee from the Delft University of Technology (form number 3599).

The participants were then taken to PALILA where they were familiarized with the GUI and explained how to conduct the listening experiment and how to record their answers. After the experiment was completed, they completed a post-experiment questionnaire and received a €10 voucher as a reward for their time and participation.

On average, the mean time required to complete the whole listening experiment was 25 min and 15 s, with a standard deviation of 2 min and 48 sec.

9.4. CONVENTIONAL SOUND ANALYSIS

The aircraft were flown in the same manner, yet, not all flight parameters are exactly the same. When assessed in terms of altitude and velocity, Table 9.2 shows that the Velis 1 and Velis 2 flights are more similar, and that the Virus 1 and Virus 3 flights are more similar. However, the $L_{A,eq}$ shows a difference of 4.5 dBA. Additionally, a large difference in RPM is seen and consequently the BPF varies between the aircraft types. This is due

to the difference in the number of propeller blades and the RPM necessary for the same thrust with different propeller designs. Note that the altitude level was not corrected for in the audio files, as scaling was already applied on the maximum level.

The spectrograms of the Virus and Velis in Figure 9.4 were constructed with a Hanning window of 4096 samples, 50% overlap, and zero-padding of 4096 samples, for a signal with a 48 kHz sampling frequency. The spectrograms show three differences: (1) the Velis spectrograms show a tone at 4500 Hz, (2) the Virus spectrograms show a larger contribution of higher frequencies, and (3) the Virus spectrograms show more tones below 500 Hz.

As the spectrograms in Figure 9.4 do not provide a clear view of the lower frequencies, where propeller noise is dominant, Figure 9.5 provides the spectrograms and overhead spectra from 0 to 1500 Hz. Clearly, the Pipistrel Virus spectra contain more tones in the lower frequencies which can be attributed to the propeller, the exhaust firing frequency, and a combination of the two tones. Interestingly, the Virus spectrogram also shows more broadband acoustic energy which is mostly present at overhead positions. This broadband noise has a limited presence in the forward and aftward flight arc, while the propeller tones are present in the spectrogram for a longer period of time. The harmonics of the firing exhaust tone which are present in between the harmonics of the BPF, at roughly 135 Hz and 200 Hz, have limited presence and are mostly detected around the overhead position. These tones thus have a strong directionality.

9.5. SOUND QUALITY METRICS OF THE FLYOVERS

Figure 9.6 shows the Sound Quality Metrics (SQMs), as explained in Chapter 4, for each sound sample as computed by Sound Quality Analysis Toolbox (SQAT) V1.1 [22, 150]. The Virus and Velis are compared based on the Just Noticeable Differences (JND) reported as a percentage change for each SQM in [22]. Here, the Virus aircraft is taken as the reference situation for the analysis of JNDs.

In general, the first flyover with Virus (Virus 1) is fairly different from the second and third flyover (Virus 2 and Virus 3) on all metrics except for sharpness. It is unclear from the flight parameters and the spectrogram why this is exactly the case, although in general, the noise levels of Virus flyover 1 are higher as also seen in Table 9.2. Higher levels increase the N_5 characteristic. For FS_5 and R_5 the increase might not be explained by level differences.

Figure 9.6 shows that the loudness of the Virus is higher, as could be expected from the higher $L_{A,eq}$ for the Virus aircraft. The JND for loudness is 7%, so the difference is noticeable. Mostly the lower frequencies cause this behaviour, as the equal-loudness contours converge at lower frequencies, meaning that the same ΔSPL can have a larger impact on loudness at low frequencies than at higher frequencies.

Another metric that shows noticeable differences is the tonality, for which the JND is 10%. The Velis has a reduced tonality which might have been expected from the reduced number of tones at frequencies below 500 Hz. However, the tone at 4500 Hz for the Velis spectrograms in Figure 9.4, which is not present for the Virus, seems to make no difference.

The difference in loudness and tonality can be attributed to a change in engine as well as a change in propeller, resulting in different thickness and loading noise. Unfortu-

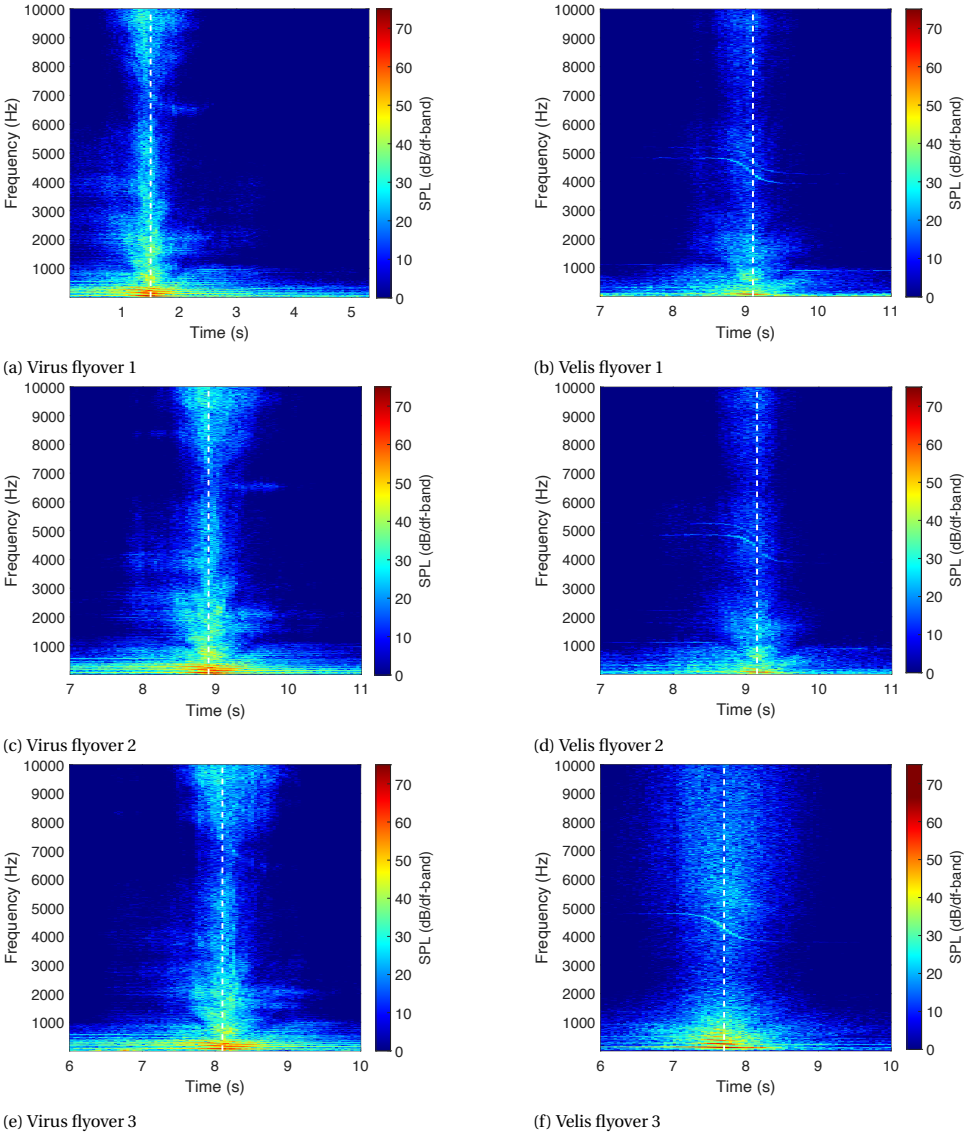

(a) Virus flyover 1

(b) Velis flyover 1

(c) Virus flyover 2

(d) Velis flyover 2

(e) Virus flyover 3

(f) Velis flyover 3

Figure 9.4: Spectrograms of the flyovers, with the left column the Virus flyovers and the right column the Velis flyovers. All spectrograms have a colour scale of 0 to 75 dB for a spectral bandwidth of 5.85 Hz. The overhead time is indicated with a white dashed line.

nately, these effects are hard to separate in this study. Yet, the absence of exhaust firing frequencies for the Pipistrel Velis is already important to reduce these metrics specifically.

The sharpness attribute is similar and relatively low for both aircraft types. As propeller and engine noise show up in the lower frequency range, the airframe is expected

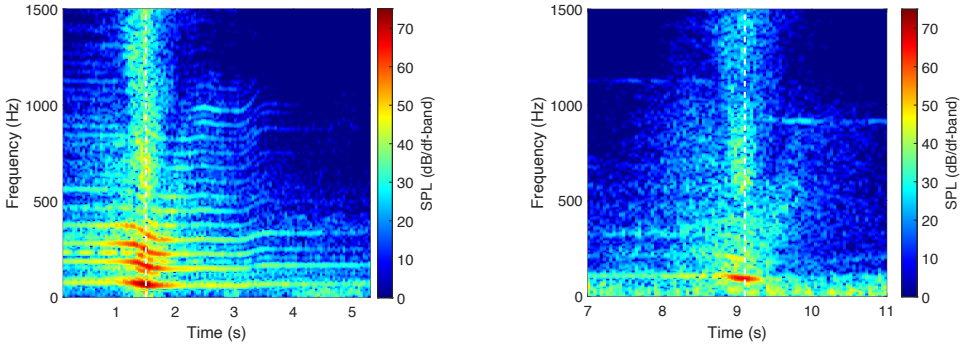

(a) Virus flyover 1

(b) Velis flyover 1

Figure 9.5: Zoom in on the 0 to 1500 Hz frequency range of the spectrograms of Virus and Velis, to see harmonics and engine tones. The colour scale spans 0 to 75 dB for all spectrograms. The bandwidth in the spectra is 5.85 Hz.

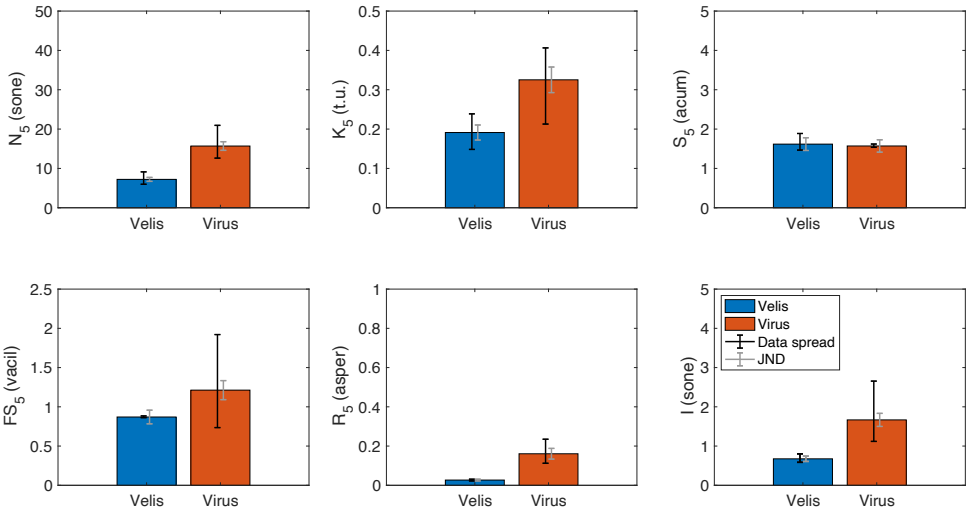

Figure 9.6: Bar charts with the average SQM value per metric and the data spread over the three flyovers for Velis and Virus separately. The JND is indicated with the gray spread.

to be the main contributor to the higher frequency acoustic content. As the airframe is the same for both aircraft, this difference is expected to be limited which results in the same sharpness value.

For FS_5, the JND requires a 20% change between the old and new situation, which is not the case if Virus 1 is excluded. The roughness values are small, but the differences are noticeable as the change is more than 17% between the Virus and Velis flyovers. The difference is due to the change in BPF, as the BPF indicates the amplitude modulations due to a blade passing closer to an observer (per rotation) during flyover. The BPF thus indicates the modulation frequency in this case. Roughness has its maximum at a mod-

ulation frequency of 70 Hz, and hence the Virus with a BPF of 85 Hz causes stronger roughness than the Velis with a BPF larger than 100 Hz.

There is no JND value for impulsiveness yet, but the difference is roughly 50% which is expected to be noticeable. The impulsiveness for the Velis flyovers is lower, although neither of the spectrograms shows impulsive noise. As the impulsiveness metric by Willemsen et al. is strongly linked to loudness, the difference in loudness could influence the results.

Lastly, Figure 9.7 shows the Psychoacoustic Annoyance (PA) values for different PA models. All models for PA show a lower annoyance level for the Velis flyovers than for the Virus flyovers. Most PA models predict that a flyover with the Velis results in only 50% of the PA of a Virus flyover. However, the annoyance difference for the model of Willemsen between the Virus and Velis flyovers is much smaller. This might be due to the reduced correction for the impact of loudness through its linear rather than logistic model. It cannot be attributed to the omission of tonality, as that is also missing in Zwicker's model which represents similar values as Di and More, which do include tonality.

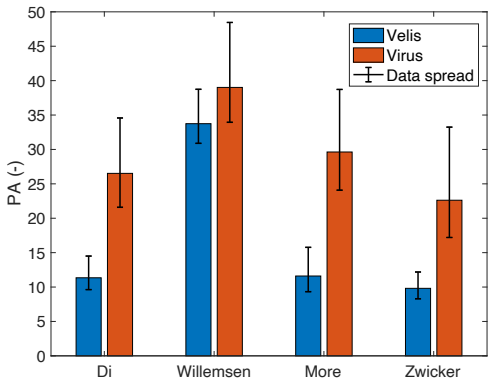

Figure 9.7: Bar charts with the average PA value per model and the data spread over the three flyovers for Velis and Virus separately.

9.6. COMPARISON OF PREDICTED WITH EXPERIENCED ANNOYANCE

The analysis based on psychoacoustic models predicted that Velis flyovers would be half as annoying as Virus flyovers for most models. Listening experiments were conducted to validate these predictions. Figure 9.8 illustrates the rated annoyance per flyover, with boxplots showing the distribution, with the median indicated in red, and black markers indicating the mean annoyance.

The rated annoyance of Velis flyovers was consistently lower than that of Virus flyovers in terms of both mean and median ratings. The averaged rated annoyance for Velis flyovers was 33% lower than for the average of Virus flyovers. Although the observed reduction was smaller than the predicted 50% difference, a substantial reduction was present. Unfortunately, the sample set of flyovers is too limited to study which SQM and

PA model best predict the reported annoyance, but this could be interesting for future work.

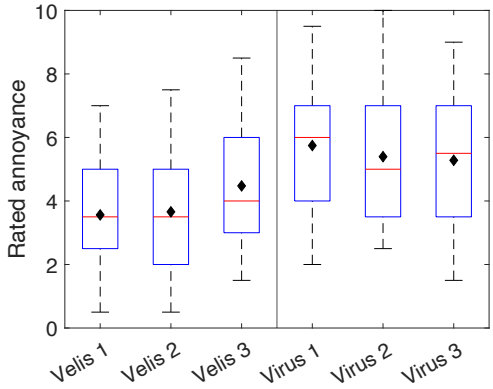

Figure 9.8: Listening experiment rated annoyance per flyover, where the diamond marker indicates the mean of the data set.

The flyovers were not directly comparable, due to variations in the flight parameters. However, it is still interesting to assess whether the mean rated annoyance of every Velis flyover is lower than the mean rated annoyance of every Virus flyover in order to establish the annoyance impact of an electric counterpart aircraft. Therefore, a two-tailed paired t-test was performed between all combinations of the Velis flyovers with the Virus flyovers. In all cases it was found that the difference between the means is significant, and thus that the population mean of the Velis flyover is less than the population mean of the Virus flyover. The highest p-value is the combination of the rated annoyance of Velis 3 with Virus 3 which is $1.5 \cdot 10^{-6}$, which is significant for a significance value of 0.05. A statistical power analysis showed that a power of 0.95 is reached for 30 participants on a paired t-test between the rated annoyance of Velis 3 and Virus 3. Thus, this study has sufficient participants to analyse the perceived annoyance difference.

The results clearly indicate that Velis flyovers were rated as less annoying than Virus flyovers. However, to explore potential attitude biases in the ratings, the bias was analysed by comparing the difference in rated annoyance between Virus and Velis flyovers across participant answer groups for the questions posed in Section 9.3.2. The results are presented in Figure 9.9 per question.

Approximately a quarter of the participant group reported hearing flyovers daily, primarily from major airports such as Amsterdam Schiphol, Eindhoven, or Rotterdam-The Hague. Overall, the group exhibited a positive attitude towards aviation, with only 25% expressing a neutral or negative perspective. Regarding the likelihood of boarding an electric aircraft by 2035, 30% considered it unlikely, while 60% believed it was plausible but potentially later than 2035.

No clear trend was visible across the four questions. The group sizes were too small to conduct simple statistical tests between group means, as this would introduce a small-sample bias. It would be interesting to explore how these potential biases manifest in a larger participant group, perhaps in future experiments.

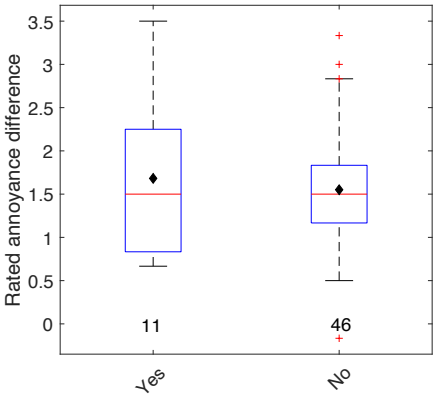

(a) Do you daily hear aircraft passing over your house?

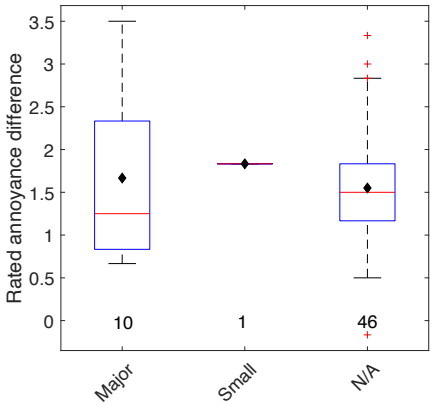

(b) What best describes the size of the airport?

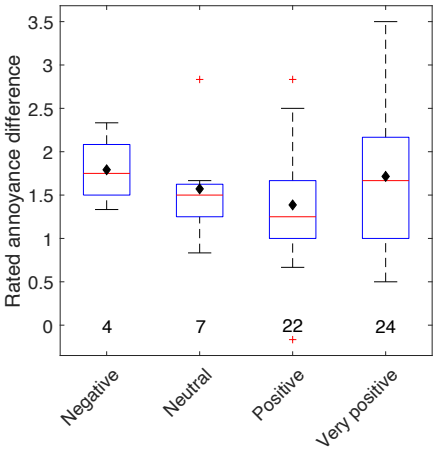

(c) What is your general attitude towards aviation?

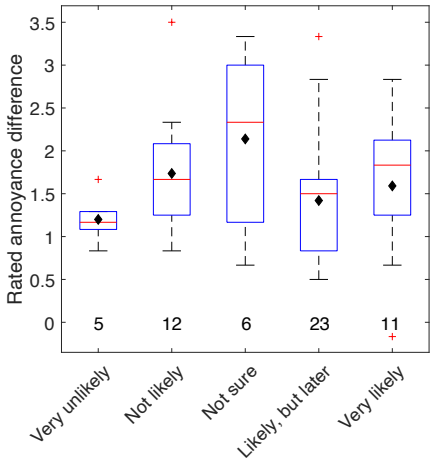

(d) Do you think it is likely that you can board an electric aircraft for your holiday trip in 2035?

Figure 9.9: Rated difference in annoyance rating per group from the bias test (Virus - Velis). The boxplot indicates the distribution of the results and the marker indicates the mean of the group.

9

9.7. CONCLUSIONS AND OUTLOOK

The results of this research show that the Pipistrel Velis Electro has lower noise emissions during flyover than the Pipistrel Virus (combustion engine). The Velis especially has less strong tonal noise related to the Blade Passage Frequency (BPF). The sound quality metrics indicate similar trends, with a noticeable difference in loudness, tonality, and impulsiveness. In general, the Pipistrel aircraft have little roughness and fluctuation strength, and equal levels of sharpness. The difference in roughness however is also noticeable. The psychoacoustic annoyance is predicted to be 50% lower for the Velis flyovers than the Virus flyovers.

The reported annoyance showed a 30% difference, confirming that Velis flyovers are perceived as less annoying than Virus flyovers. This addresses the question posed in the

introduction, specifically for the Pipistrel aircraft: *"If you would fly an electric aircraft the same as its non-electric counterpart, would there be a difference in noise annoyance?"*. The results indicate that the answer is yes; electric aircraft would result in lower noise annoyance. This conclusion likely extends to other electric aircraft, due to the absence of strong combustion engine tones at low frequencies which influence the loudness and tonality metrics.

As this experiment contained only six flyovers, it is recommended to expand future listening experiments to a larger set of flyovers to study the correlations between sound quality metrics and reported annoyance. This could aid in finding a reliable method of estimating noise annoyance during early aircraft design stages.

10

Conclusion and Outlook

For after all what is man in nature?
A nothing in relation to infinity,
all in relation to nothing,
a central point between nothing and all,
and infinitely far from understanding either.

Blaise Pascal

This chapter ties all chapters together: it reflects on the research objectives and their relevance to the overarching goal of lowering noise annoyance for truly sustainable aviation. First, the chapter provides the conclusions of this dissertation per objective. After that, it provides recommendations for further research.

The motivation for this dissertation was formed around the need for truly sustainable aviation, which encompasses climate, air quality, and noise emissions. Only truly sustainable aviation will be accepted by society and thus succeed. The field of sustainable aviation however contains limited operational examples. These were only investigated for noise emissions upon certification which does not accurately capture the annoyance. Additionally, it is more effective to analyse the impact of noise emissions and noise annoyance during the design phase rather than at the final design. Therefore this research focused on measurements of these few operational examples to improve understanding of noise emissions and annoyance which should be incorporated in earlier design phases in the future. This was captured in the thesis' objective: *to identify noise sources and validate noise prediction models to improve the assessment of noise emissions and annoyance in sustainable aviation systems.*

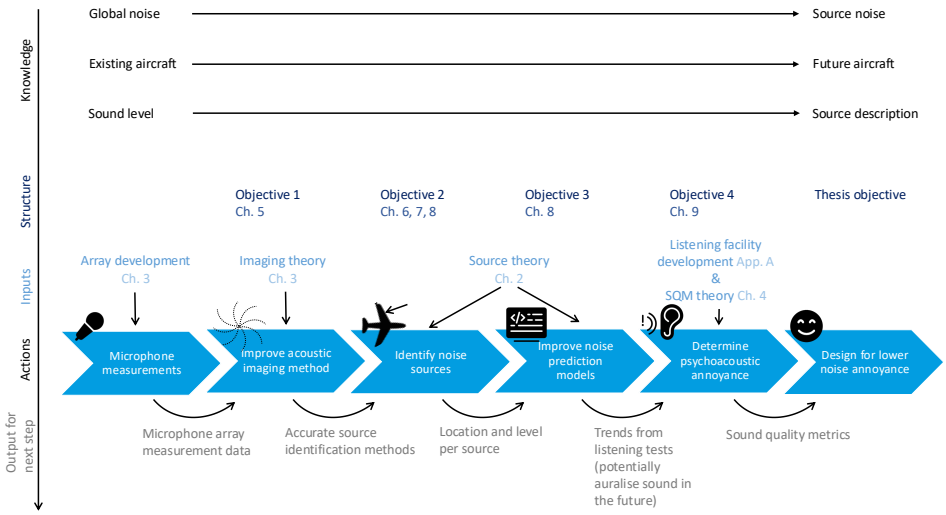

Figure 10.1: Outline of the thesis as presented in the introduction of this dissertation.

The main objective was divided into four sub-objectives, each linking to a different step of the research outline. Figure 10.1 revisits the outline to provide an overview of which objective links to which chapter. The conclusion per objective is provided in Section 10.1, with recommendations linked to specific objectives in Section 10.2.

10.1. REFLECTION ON OBJECTIVES

The main objective was divided into four sub-objectives that were researched in consecutive order:

1. **Improve acoustic imaging methods to identify in three-dimensional space, the location and level of a noise source.**
   To identify acoustic sources in three-dimensional space it is possible to use conventional imaging techniques for a set of asynchronous measurements, however

this is computationally expensive as it requires an exhaustive search of all potential source locations in a three-dimensional grid. Therefore, Chapter 5 approached the search as a Global Optimisation (GO) problem with the use of a Differential Evolution learning method and an energy function based on the difference between the Cross-Spectral Matrix of measurement data and of predicted sources. This method was applied to a case with three-dimensionally spaced sources in an anechoic room, measured with a planar array. It outperformed conventional methods in terms of accuracy in identifying individual sources in a three-dimensional multi-source environment. The method is capable of identifying sources accurately below the commonly assumed resolution limit. Additionally it has reduced the computational expense due to its grid free search. Future research should include the application of GO on a less controlled environment, to study its performance on a lower signal-to-noise case.

2. **Use acoustic imaging methods on microphone array measurements of sustainable aviation systems during normal operations to identify their noise sources.** The acoustic imaging methods from Chapter 3 were applied on three different aviation systems, of which one was a TaxiBot and two were propeller aircraft, i.e., the Cessna Skymaster and the Pipistrel Velis Electro.

   - **TaxiBot** (Chapter 6)
     The TaxiBot is a hybrid-electric taxiing robot which was operationally tested at Amsterdam Schiphol Airport to reduce climate emissions during taxiing operations. Noise emissions were measured for the TaxiBot operations and regular taxiing operations to assess the impact of noise levels on ground workers and surrounding communities. The acoustic sources identified for the TaxiBot were restricted to the TaxiBot engine, an unidentified source around the landing gear, and the Auxiliary Power Unit (APU) of the aircraft. For conventional taxiing the noise is dominated by the aircraft engines, and the APU is turned off. TaxiBot operations can reduce upto 7 dB of noise at the source during a pass-by, but the APU hampers any potential noise reduction of the TaxiBot in the aftward polar arc. It is worthwhile to compare single-engine taxiing to TaxiBot operations to find a preferred method in terms of noise and climate emissions.

   - **Cessna Skymaster** (Chapter 7)
     The Cessna Skymaster will be altered in steps to a hybrid-electric aircraft by changing the 2-bladed to 3-bladed propellers, and later changing the front engine to an electric engine. So far, the noise impact of the first stage was researched. The spectra show clear tones at the Blade Passage Frequency (BPF) and its higher harmonics, and for the 2-bladed propeller the firing exhaust tones of the engine are identifiable too. However, for the 3-bladed propeller the firing exhaust frequency aligns with the BPF. Therefore an attempt was made to decompose the measured signal in the engine source and the propeller sources through applying Conventional Beamforming (CB) and Rotating Source Identifier (ROSI) jointly. The source maps showed the presence of

a stationary source around the landing gear, which could be a cyclostationary source or a noise source arising from ground vortices. These source levels might thus not be representative of in-flight propeller noise levels.

After analysing the flyover spectra with various airframe configurations, it was argued that the propeller sources were dominant during operations. Hence, no acoustic imaging was applied to these flyover cases.

However, these flyover measurements were used to analyse the psychoacoustic annoyance of the different propeller types. The 3-bladed propellers were found to be less annoying according to psychoacoustic models, likely due to the reduced roughness noise while loudness increased slightly for the 3-bladed propeller.

- **Pipistrel Velis Electro** (Chapter 8)
  In the first part of Chapter 8, ROSI and CB are applied to stationary noise measurements of the Pipistrel Velis Electro to decompose the measured signal in rotating sources and stationary sources. The acoustic imaging maps showed a clear separation of the sources above the frequency corresponding to the Rayleigh resolution limit, with a rotating source at each blade tip and a stationary source just above the ground around the nose landing gear. The latter might be a cyclostationary source, that is also spread out over the blades in the ROSI acoustic map. The absence of a combustion engine did not aid in the separation of sources.

  It is therefore concluded that on-ground measurements should be carefully analysed as there are additional noise sources present. Single microphone measurements to analyse these types of operations should be avoided as they cannot separate between the contributions of various sources.

  The levels in a ROSI source map cannot be trusted when a cylostationary source is present. Therefore, applying CB is necessary to identify if a stationary source is present and the reconstructed pressure signal from ROSI can indicate whether it is a cyclostationary source by an indication of an excitation per blade per rotation.

3. **Use the identified noise sources of propellers to validate a propeller noise prediction model.**
   The second part of Chapter 8 used the flyover measurements from the Pipistrel Velis Electro to validate a propeller noise prediction tool. The Pipistrel Velis Electro acts as “flying propeller” and therefore allowed for validating without having to decompose spectra into propeller and non-propeller sources. The propeller noise prediction model used is the Helix-tool which models the thickness and steady loading noise of a propeller under axial inflow according to Hanson’s formulation, but omits the broadband noise. Prediction models are generally validated through single component measurements in a wind-tunnel, but the Pipistrel Velis Electro noise measurements allowed for a validation at full-scale at operating conditions. The model was able to predict the tones at a maximum overprediction of 4.1 dB for flyovers and 2.5 dB for take-offs for the first two harmonics when the aircraft was

at overhead position. Higher harmonics were underestimated by the model, as it excludes unsteady loading. Including non-axial inflow for take-off measurements improved the predictions at higher harmonics. The overall levels in terms of polar directivity were predicted with deviations up to 5 dB per polar angle, including both underpredictions and overpredictions. Incorporating unsteady loading and a broadband noise model could reduce the discrepancies.

4. **Perform listening experiments with the propeller noise measurements to assess the psychoacoustic annoyance of electric propeller aircraft.**
Measurements of the Pipistrel Virus and its electric counterpart, the Pipistrel Velis Electro, were used to establish the difference in annoyance during flyovers in Chapter 9. These aircraft are marketed as direct replacements of each other in terms of flying. The measurements were performed at a consistent altitude and velocity for both aircraft types. While the Pipistrel Velis is considered a flying propeller, the Pipistrel Virus spectra contained tones of the combustion engine which increased its tonality slightly. Additionally, the higher sound levels of the tones resulted in a higher loudness for the Virus, which was twice that of the Velis. The Virus' roughness was also higher due to a BPF close to the modulation frequency causing maximum roughness. All of these factors contributed to a 50% higher psychoacoustic annoyance prediction for the Virus compared to the Velis. Listening experiments concluded that the Virus indeed was perceived more annoying, yet the difference was reduced to 30%. Thus, replacing all Pipistrel Virus flights with Pipistrel Velis flights will reduce the noise pollution around airports.

   Besides the difference in engine, the increased number of blades in combination with the decreased RPM, and hence the decreased blade loading for the Velis, likely resulted in lower noise emissions and annoyance. The relation between the Sound Quality Metrics (SQMs) and the perceived annoyance can be found when more flyovers of different aircraft at different operating conditions and for different design parameters, are analysed in listening experiments.

The results of the individual sub-objectives aid in reflecting on the main objective, yet more cross-objective learnings can be exploited in the future. For example, extensive validation of a propeller noise model requires validation against various aircraft which might include other noise sources than those of the Pipistrel Velis. This would require the use of advanced acoustic imaging techniques to separate sources, as was attempted in sub-objective 1 and 2.

Furthermore, auralisation results of noise prediction models should be assessed in listening experiments side-by-side to real recordings to understand their effectiveness at representing a source. This could necessitate further research in auralisation methods, but also in improved source modelling. Improved noise prediction models can be used to study noise annoyance rather than requiring a full-scale model of the aircraft for listening experiments.

However, an important limitation is that subjective annoyance does not necessarily align with physiological impact. Individuals may not report annoyance even when aircraft noise contributes to measurable bodily stress responses. Thus, future research should include physiological monitoring (e.g., heart rate variability) to capture subcon-

scious or long-term health effects of aircraft noise exposure. This is particularly relevant as sustainable aviation systems might reduce noise emissions and perceived annoyance potentially without eliminating health risks.

A part of the limitations mentioned here, can be addressed with future research for which specific steps are addressed in the next section. Addressing these recommendations will bring the field closer to the goal of truly sustainable aviation with limited impact on planet, people, and profit.

10.2. RECOMMENDATIONS FOR FUTURE RESEARCH

Based on the objectives, some recommendations for future research are provided.

- This thesis proved the advantage of GO methods to identify noise sources over conventional imaging algorithms in controlled environments with high Signal-to-Noise Ratio (SNR). However, its applicability in measurements where the SNR is lower still has to be researched. Especially in flyover measurements, its super-resolution and grid-free search capabilities can be useful. Therefore it is suggested to apply GO to aircraft in landing when they are close to the ground and thus have high SNR.

- The TaxiBot operations were more silent than two-engine taxiing operations, however to fulfil airports' aims to reduce climate emissions during taxi operations it can be useful to assess single-engine taxiing operations as well. The added benefit may be shielding of noise for observers on the opposite side of the aircraft. This case should be compared to the emissions, both in terms of climate and noise, to the hybrid-electric TaxiBot, while taking into account the need for an engine test run at the start of the runway for a taxibotted operation.

- Propeller noise prediction models such as the Helix-tool used in this research already show a good agreement for the first few harmonics, but their usefulness in designing for lower noise annoyance has to be improved through the following steps:

    1. Include a broadband noise model to improve the prediction at higher frequencies where the tonal content is lower;
    2. Include the effects of unsteady loading, beginning by modelling for non-axial inflow;
    3. Validate the Helix-tool with measurements in operational conditions on a larger variety of propellers;
    4. Include the prediction of SQMs based on the auralisation output of the Helix-tool;
    5. Validate the auralisation and annoyance prediction of Helix versus the sound samples of measurements in listening experiments.

- SQMs were found to be useful in predicting noise annoyance. It would be interesting to extend acoustic imaging maps to produce sound quality maps as output. This gives a good visual insight in the relevance of sources for the public.

- Initial listening experiments showed a similar trend as psychological acoustic prediction models for propeller-driven aircraft noise measurements, but the data set was too limited for correlations. Thus the data set has to be extended to a larger set of flyovers as well as a larger variety of propeller noise measurements to find correlations with design parameters and understand better which metric specifically impacts annoyance.
- Listening experiments should include physiological monitoring to achieve a better understanding of long-term health effects of aircraft noise exposure. This can be a combined research effort between engineering and social sciences.

A

Acoustic characterisation of a listening room [1]

If I have seen further,
it is by standing on the shoulders of giants.

Isaac Newton

Pyschoacoustic metrics are often based on empirically established models from listening tests with a group of participants. These listening tests are performed in special anechoic rooms with low background noise to reduce the distractions and influences of uncontrolled other sounds. Delft University of Technology recently acquired its own listening room, called PALILA. This chapter covers the acoustic characterisation of the room in terms of background noise, reverberation time, free-field conditions, and transmission losses of the walls.

[1] This chapter is a revised version of a paper presented at ICSV 2023 [166].

A

A.1. INTRODUCTION

As per the World Health Organization (WHO) [2], noise pollution ranks as the second-largest environmental health threat following air pollution. Beyond causing annoyance, [232], prolonged exposure to excessive noise leads to severe and often irreversible health effects, including hearing impairments, sleeping disturbances [233], and cardiovascular ailments [234]. Notably, an increasing number of industrial stakeholders, such as manufacturers of electric vehicles [235] and household appliances [236, 237], are now placing special emphasis on the acoustic characteristics of their products. Aircraft and wind turbines, due to their complexity, the large populations they affect, and the anticipated growth in these industries, are particularly noteworthy as critical noise sources [41, 226, 238].

Despite the critical significance of noise emissions, they are frequently underestimated and relegated to a secondary role in traditional design processes. The acoustic impact of devices, such as aircraft or wind turbines, is typically assessed during certification and subsequent enforcement of environmental noise regulations. However, these procedures rely on conventional, physics-based sound metrics based on the sound pressure level L_p, which have faced criticism [239] for their failure to account for essential sound aspects in the human auditory sensitivity, including tonality [153], sharpness [157], and amplitude modulations [155] among others. Consequently, these conventional metrics often prove inadequate in accurately modelling noise-induced annoyance. Recent research [19, 22, 151, 162, 240, 241] advocates for the integration of novel sound quality metrics (SQMs) based on human perception into comprehensive psychoacoustic metrics [150], offering a more precise representation of noise annoyance.

To firmly establish these novel SQMs as a more precise alternative for assessing noise annoyance compared to current methods, it is essential to conduct psychoacoustic listening experiments [19, 162, 242–247]. Given the notable perceptual differences in the sound signatures of the different noise sources aforementioned (aircraft, wind turbines, household applications, etc.), it becomes imperative to empirically determine whether any proposed noise-annoyance prediction model for a certain noise source is extendable and also reliably applicable to others. For conducting psychoacoustic listening experiments, dedicated research facilities with appropriate acoustic conditions (low background noise and, ideally, an anechoic environment) and suitable audio equipment are necessary. Several research institutions and universities have established such listening laboratories, including the AuraLab from EMPA [244], the Small Anechoic Chamber [248], the Exterior Effects Room (EER) [249], and the Interior Effects Room (IER) [250] at the NASA Langley Research Center, the MobiLab from RWTH Aachen [251], and the Listening Room at the University of Salford [252]. An overview of their main characteristics is provided in Table A.3 in Section A.3.5. Despite the existing facilities and the growing interest in the field of psychoacoustics, there is a lack of literature regarding the design, development, and characterisation of new and affordable listening laboratories.

This manuscript presents the development and acoustic characterisation of the recently-established PsychoAcoustic LIstening LAboratory (PALILA) at Delft University of Technology (TU Delft), as depicted in Figure A.1. The motivation for this chapter is to describe the main design guidelines of a high-quality, yet affordable, listening facility to promote the expansion of psychoacoustics studies and perception-induced design ap-

Figure A.1: Example of a listening experiment inside PALILA.

proaches.

The primary mission of this facility is to conduct empirical investigations concerning the human perception of aeroacoustic noise sources, including aircraft, drones, or wind turbines. PALILA is also well-suited for the study of other sound sources, such as household appliances and ground vehicles. This laboratory is a valuable addition to the ongoing acoustic research at TU Delft, complementing the anechoic (A-tunnel) [253] and low-turbulence (LTT) wind-tunnel [254] facilities, and the anechoic chamber [169, 177] of which the acoustic parameters are also included in Table A.3. The overarching objective is to explore the societal impact of these noise sources, identify the main factors contributing to noise annoyance, and ultimately develop more accurate noise-annoyance prediction models compared to current methods. These enhanced models would be of paramount importance for improving the enforcement of environmental noise regulations and enabling the perception-induced design of future low-noise-annoyance devices.

The chapter is structured as follows. Section A.2 provides an in-depth exploration of PALILA, detailing its main structural components, acoustic attributes, and a comprehensive equipment overview. Section A.3 delves into the acoustic characterisation experiments and their corresponding findings. Finally, Section A.4 summarises the primary conclusions drawn from this study.

A.2. FACILITY DESCRIPTION

This section outlines the hardware and software of the facility.

A.2.1. STRUCTURAL COMPONENTS AND SOUND-ABSORBING ELEMENTS

The design of PALILA follows the box-in-a-box concept, which features a quiet, soundproof booth situated within a dedicated room at the Aerospace Engineering faculty of TU Delft. The interior layout of PALILA, which includes the space occupied by the acoustic-

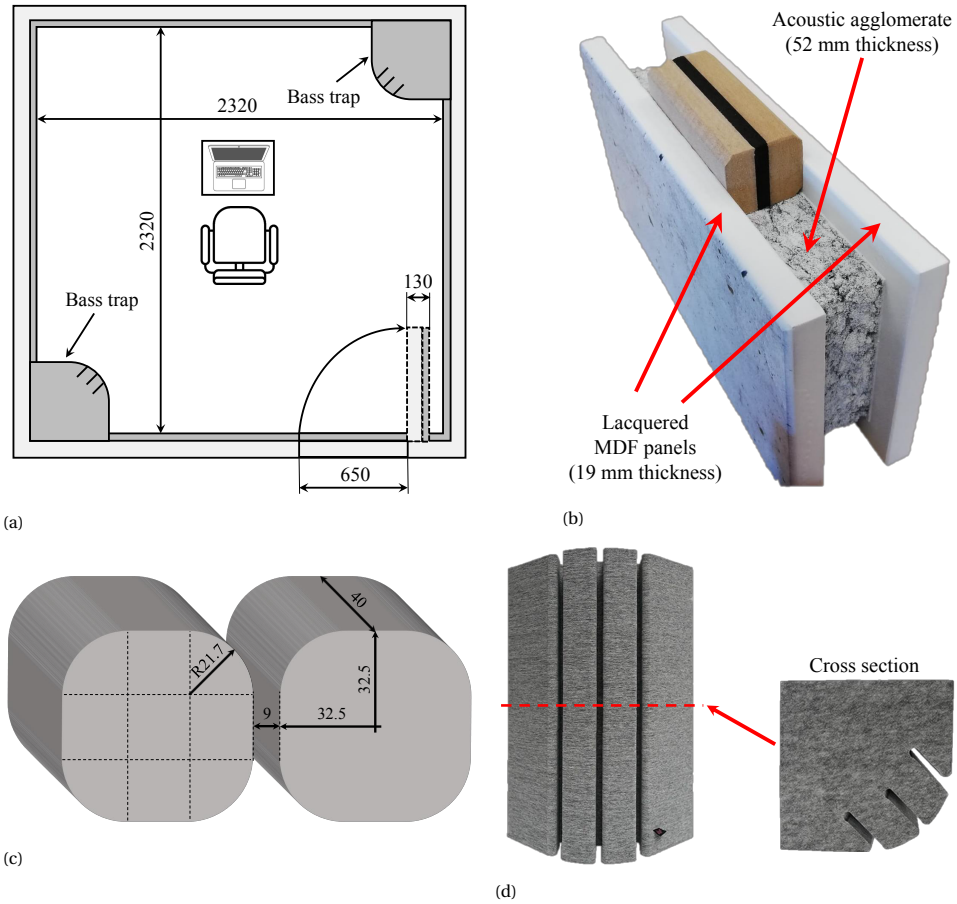

Figure A.2: (a) Top view of the listening laboratory (the light gray areas denote the wall bricks, whereas the darker gray areas indicate the acoustic absorbing foam panels), (b) cross-sectional view of a wall brick, (c) detail of the acoustic-absorbing foam panels, and (d) detail of the bass trap with the cross-sectional view. Dimensions expressed in millimetres.

absorbing padding on the walls and ceiling, is a square floor plan of 2.32 m in length, 2.32 m in width, and a height of 2.04 m, as depicted in Figure A.2a. The outer dimensions of the booth are 2.58 m in length, 2.58 m in width, and 2.28 m in height.

Table A.1 provides an overview of the main characteristics of the sound-absorbing components within PALILA, including the materials, the absorption (as transmission loss TL or as weighted sound absorption coefficient α_w), and the expected effective frequency range. The parameter α_w is a single-number frequency-independent value estimated following the procedure explained in the ISO 11654:1997 standard [255] and is used to classify sound absorbers into different classes.

Table A.1: Overview of the sound-absorbing components within PALILA indicating their material, sound absorption capabilities (transmission loss (TL) and weighted sound absorption coefficient α_w), and effective frequency range.

Component	Material	Absorption	Effective freq. range
Wall bricks	MDF (panels)	TL = 45 dB	Above 200 Hz
	Polyurethane foam (core)	-	-
Foam panels	Recycled PET	$\alpha_w = 0.6$	Above 500 Hz
Bass traps	Recycled PET	$\alpha_w = 0.6$	160 Hz - 500 Hz
Floor carpet	PA6 IMPREL	$\alpha_w = 0.15$	-
Floor filling	Polyester wool	$\alpha_w = 0.85$	Above 500 Hz
Ceiling filling	Melamine	$\alpha_w = 0.75$	Above 500 Hz

The booth (manufactured by the company *StudioBricks* [256]) is constructed using modular wall bricks with a thickness of 90 mm. These bricks employ a double-wall sandwich structure, featuring two outer panels made of lacquered medium-density fibreboard (MDF), each measuring 19 mm in thickness. Within this structure, there is a core made of acoustic-absorbing agglomerated polyurethane foam and fibres, which is 52 mm thick and crafted from recycled denim and upholstery, see Figure A.2b. All three layers within the wall bricks are glued together using vinyl acetate homopolymer.

The laboratory's entrance is a 650-mm-wide door that opens inward, as shown in Figure A.2a, and is constructed from the same materials as the modular wall bricks (Figure A.2b). The door is equipped with a special sealing system to guarantee optimal sound insulation from the outside.

Both the ceiling and floor employ the same sandwich structure as depicted in Figure A.2b. The entire booth is connected to the exterior room's floor through a vibration-damping system, and the space beneath the floor is filled with *Akotherm Basic D40/50* sound-absorbing foam [257] to prevent the occurrence of any potential cavity resonance. This filling consists of foam panels with dimensions of 1200 mm × 1000 mm × 50 mm with a density of 40 kg/m^3.

To mitigate acoustic reflections within PALILA, the entirety of the interior walls and ceiling, and approximately 20% of the floor (parts which are not used for walking) are covered with acoustic-absorbing foam panels of A-B-C-D classification level, as illustrated in Figure A.1. This configuration provides a nearly-anechoic and quiet environ-

ment for the calibration of acoustic equipment, see section A.3.3. The foam panels belong to the Eco45 model [258] and are crafted from recycled PET (polyethylene terephthalate) bottles converted into felt-like fibers and shaped into rounded square forms. The squares have a side that is 65 mm long and rounded corners with a 21.7-mm radius (i.e. one-third of the side). The thickness of the foam panels is 40 mm, as depicted in Figure A.2c. They are arranged with a 9-mm gap between two neighbouring panels, ensuring an effective absorption of mid-to-high-frequency sounds. The material density is 25 kg/m^3.

To reduce the impact of low-frequency sound reflections, two sets of bass traps [259] were placed in diagonally opposite corners, adjacent to the corner where the door is situated, as shown in Figures A.2a and A.2d. Each bass trap module measures 450 mm in length, 450 mm in width, and 620 mm in height, featuring three vertical cut-outs that create a wedge-like structure, as depicted in the cross-section shown in Figure A.2d. To effectively cover most of the room's interior height, a set of three bass trap modules was employed per corner to reach a total height of 1.86 m.

Additionally, concealed behind the foam panels, the ceiling is covered with a 50-mm-thick layer of *Flamex Facet* acoustic-absorbing foam, weighing 475 g/m^2. Within the booth, the floor is covered with a finely woven and dense loop pile carpet, specifically designed for sound absorption from the Master collection of *Arc Edition* [260]. The carpet has a thickness of 5 mm, with a surface density of 1490 g/m^2.

Furthermore, the laboratory is equipped with a quiet ventilation system, 2 LED lamps, and a cable tunnel that serves to provide power outlets and an Ethernet connection inside PALILA. The entire laboratory setup fully complies with the required fire and safety regulations. The modular design of the wall, ceiling, and floor structures allows for convenient disassembly if needed, and subsequent reassembly at an alternative location.

A.2.2. AUDIO EQUIPMENT DESCRIPTION

PALILA features an audio reproduction system comprising a dedicated *Dell Latitude 7420* laptop (equipped with an *Intel® Core^{TM} i5-1145G7 vPro®* processor and 16 GB of RAM). This laptop is connected to a set of *Sony WH-1000XM4* [261] over-ear, closed-back headphones via a universal audio jack connector. These headphones enable binaural hearing and are equipped with a 40-mm diameter dome-type driver unit. They deliver a frequency response spanning from 4 Hz to 40 kHz and a sensitivity of 105 dB/mW at 1 kHz. Despite not using the noise-cancelling capabilities of these headphones, they provide an average attenuation of the A-weighted background noise of approximately 6.9 dBA.

Although an alternative design featuring an array of loudspeakers, similar to setups in other listening laboratories [244, 249, 250, 252, 262], was considered, it was determined that the limited inner dimensions of the booth (as depicted in Figure A.2a) would hinder the accurate reproduction of sounds below approximately 300 Hz due to near-field acoustic phenomena. Given the significance of low-frequency components in various application scenarios of interest, such as wind turbines, propeller-driven aircraft, drones, and others, it was decided that the use of headphones provided a more practical and effective solution.

The precision of sound reproduction of the combined system of the laptop and head-

phones requires meticulous calibration. It is essential to account for the transfer function between the audio input and the actual sound being reproduced to ensure that the participants experience the precise desired audio signals. To calibrate the whole audio reproduction system, a G.R.A.S. 45BB-14 KEMAR head and torso simulator [263] was employed, see Figure A.3a. This specialised device closely resembles the acoustic impedance of the human ear and is designed specifically for high-frequency (above 10 kHz) testing of both ear- and headphones, and it fully complies with the requirements of ANSI S3.36/ASA58 [264] and IEC 60318-7 [265] standards. The simulator incorporates two built-in *G.R.A.S. 40A0* half-inch pre-polarized pressure microphones [266] and includes two anthropometric pinnae made of silicone 25 Shore OO hardness, which closely mimic the properties of a real human ear. The design of this device is based on the worldwide average human male and female head and torso dimensions [263]. The sensitivity of the simulator is -38.5 dB ref 1 V/Pa ±2 dB at 250 Hz and from 10 Hz to 20 kHz the transfer impedance is within ±2.2 dB.

A.2.3. AUDIO EQUIPMENT CALIBRATION

The experimental setup employed for the calibration of the audio equipment is depicted in the schematic of Figure A.3a. The calibration experiments were conducted in the A-tunnel facility [253]. Different audio signals were played on the laptop via the headphones and recorded via the KEMAR connected to a data acquisition system (DAS) consisting of a *National Instruments* (NI) *PXIe-4499* sound and vibration module with 24 bits resolution controlled by a NI *RMC-8354* computer via NI *PXIe-8370* board. The two recorded audio signals (left and right ears) by the KEMAR are sent to the DAS via two 10-m long *G.R.A.S. AA00228* SMB-BNC coaxial cables [267].

Two types of synthetic sound signals were employed for the calibration procedure:

- A broadband white noise signal with a flat spectrum within the frequency range of interest (20 Hz to 20 kHz).
- Pure tones at a single frequency corresponding to the centres of the 31 one-third-octave bands between 20 Hz and 20 kHz.

The white noise signal was employed to calculate the transfer functions for the sound pressure level L_p within the frequency range of interest for each ear. Figure A.3b depicts these functions as offsets between the measured and expected L_p values $\Delta L_\mathrm{p}(f) = L_\mathrm{p,measured}(f) - L_\mathrm{p,input}(f)$. Hence, positive ΔL_p values correspond to higher sound outputs than desired and vice versa. The offsets for the left ear are relatively low ($\Delta L_\mathrm{p} \leq 5$ dB) between 30 Hz and 2500 Hz, whereas those for the right ear show higher offsets below 200 Hz. For frequencies outside of that range, the offsets reach values up to −25 dB. The absolute offset averaged over the whole frequency range considered $\varepsilon = \overline{|\Delta L_\mathrm{p}|}$, i.e., the average $\mathscr{L}^1$ norm of the differences, was approximately 5 dB for both ears, see Figure A.3b. These offsets are corrected for in the reproduction of sound in listening experiments via sound equalisation within the graphical user interface, see Section A.2.4.

The pure tones enabled the evaluation of the phase ($\Delta\phi$) and time (Δt) delays between the left and right ear signals measured. These delays are depicted, respectively, in Figures A.3c and A.3d. In general, all phase delays $\Delta\phi = \phi_\mathrm{left} - \phi_\mathrm{right}$ are between ±45°

(except for 12.5 kHz). The time delays between both signals presented in Figure A.3d are below 6 ms for frequencies higher than 20 Hz and are negligible for frequencies higher than 300 Hz. Such offsets are not considered perceivable for listening experiments.

Lastly, to assess the variability in the sound levels that participants may experience due to small differences in the placement of the headphones and fitting around their heads, five different recordings were performed for the same white noise signal after removing the headphones from the KEMAR and placing them back again. The standard deviations σ in the recorded spectra for each ear are depicted in Figure A.3e. For most of the frequency range of interest, the standard deviations are below 1 dB for the left ear and below 2 dB for the right ear. The standard deviations for the overall L_p values are 0.18 dB and 0.29 dB and for the A-weighted overall L_p values are 0.33 dBA and 0.31 dBA, for the left and right ear, respectively. These differences are considered negligible and barely perceivable by the human ear.

A.2.4. GRAPHICAL USER INTERFACE AND EXPERIMENTAL PROCEDURE

Using the current setup in PALILA, participants in psychoacoustic listening experiments would first receive an explanation about the practical details of the experiment from the corresponding researcher and then sign an informed consent form allowing their responses to be stored and used for research. Afterward, they would sit on a chair placed in the centre of the booth and input their subjective opinion after listening to each sound stimulus using a graphical user interface (GUI) on the laptop on the table in front of them, see Figure A.1. The GUI employed has been developed in-house using MATLAB and it can be tailored depending on the specific requirements of the corresponding listening experiment.

A typical GUI version includes an introductory questionnaire to collect basic personal information from the participant for demographic analysis and bias evaluation, as well as detecting potential hearing impairments or health conditions that may affect the results, see an example in Figure A.4a. Such information is anonymized for general data protection regulation (GDPR) reasons to prevent potential data leaks, following the guidelines of the Human Research Ethics Centre (HREC) of TU Delft.

After completing that questionnaire, the actual listening experiment begins, in which the participant will listen to different stimuli and then express their subjective opinion regarding (typically) annoyance, see Figure A.4b. A usual question [19] asked to the participants in such an experiment would be: "*Imagine that you are at home and hearing the noise; what number from 0 to 10 best shows how much you are bothered, disturbed, or annoyed by the noise?*". Following the recommendations of the ISO 15666:2021 standard [268], a similar question can also be answered in a non-numerical way with the following answers: "*Not at all*", "*Slightly*", "*Moderately*", "*Very*", and "*Extremely*". Usually, the reproduction order of the sound stimuli is (partly) randomised to compensate for potential learning effects, and the same stimulus is normally played twice throughout the experiment to evaluate the self-consistency of the answers of each participant.

Once the listening experiment is concluded, participants normally fill up a closing questionnaire regarding, for example, their attitude towards the noise source under study (e.g. aircraft, wind turbines, etc). This is performed after the experiment to avoid potential biases in the answers.

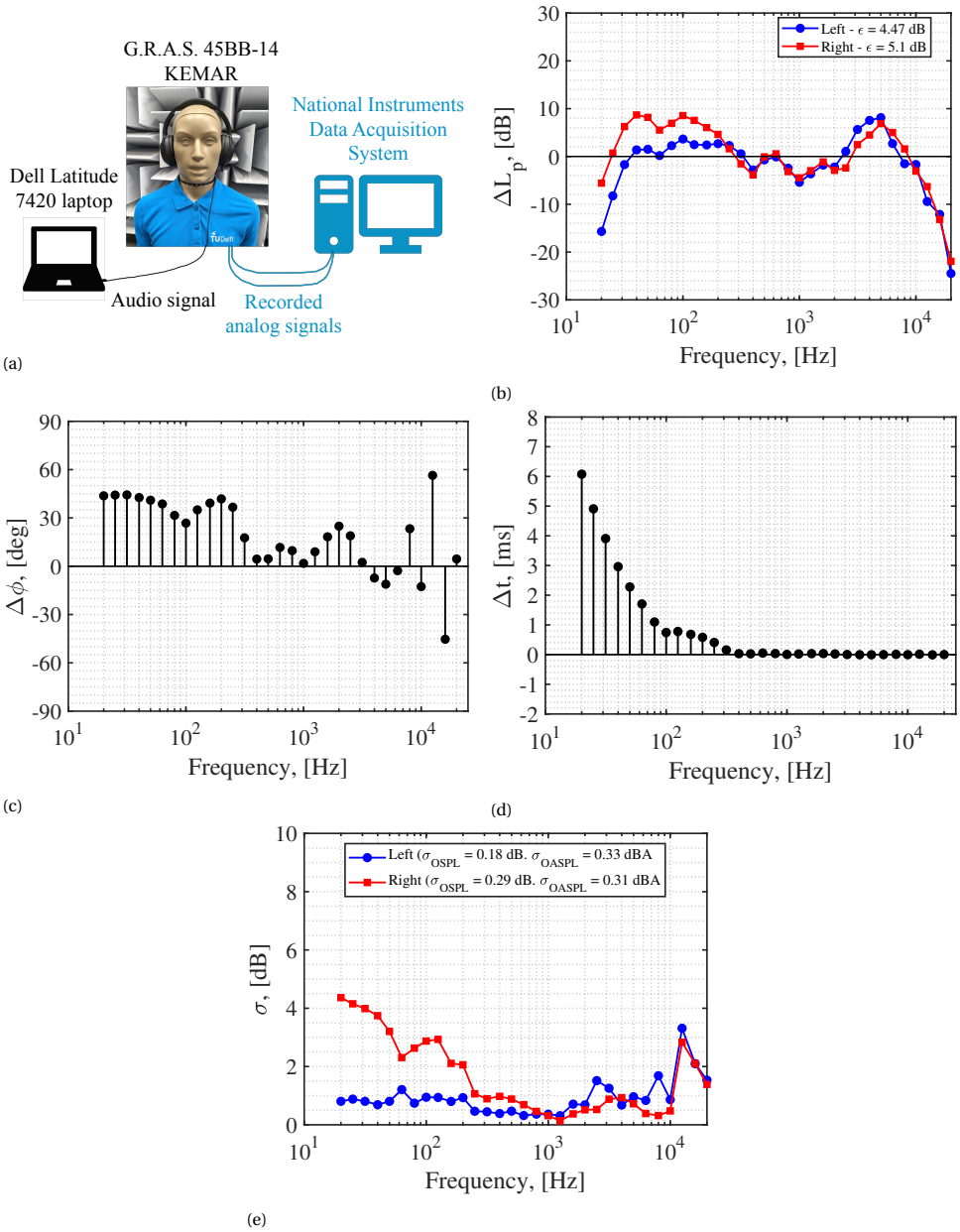

Figure A.3: (a) Schematic of the experimental setup employed for the audio equipment calibration. (b) Transfer function for L_p between input and output for each headphone audio signal. (c) Phase and (d) time delays between left and right audio signals in the headphones. (e) Standard deviations of the output signals for the same input audio signal after repeatedly placing the headphones in the KEMAR five times. All results are presented as one-third-octave bands.

A

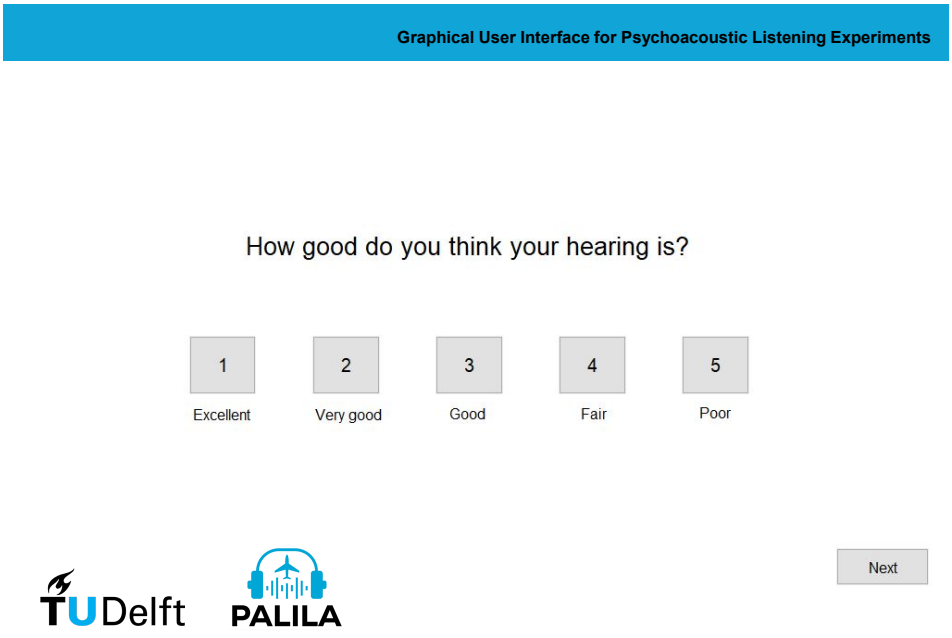

(a)

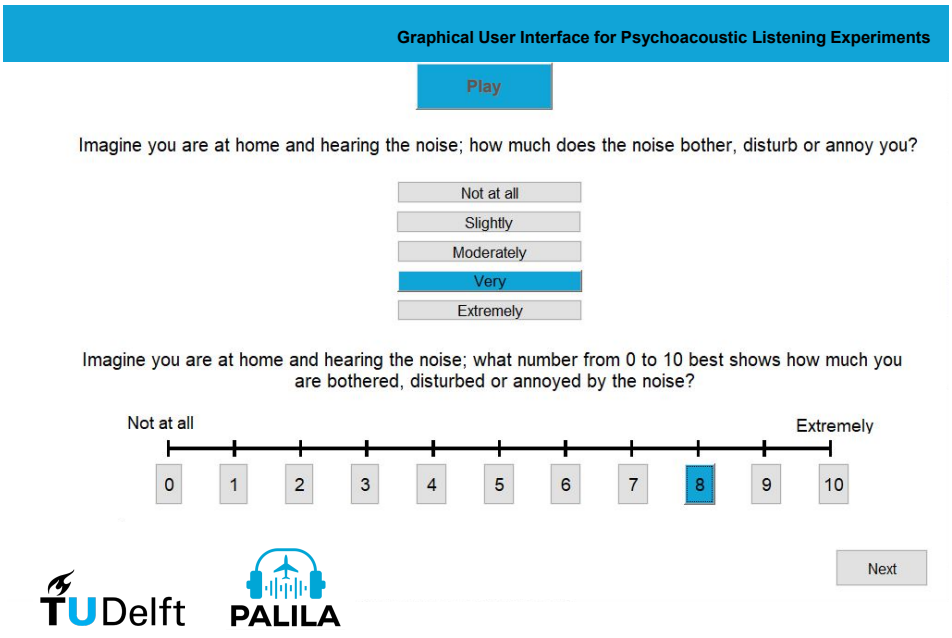

(b)

Figure A.4: Example screens from the graphical user interface (GUI) employed for listening experiments in PALILA: (a) Introductory questionnaire, and (b) example listening experiment with responses recorded.

Lastly, the participant is debriefed by the responsible researcher and receives monetary compensation for their time (usually a voucher between 10 and 20 euro, depending on the duration of the experiment (typically between 30 and 60 minutes).

A.3. ACOUSTIC CHARACTERISATION

This section presents the acoustic characterisation experiments and their corresponding results. The acoustic recordings were performed using a Brüel & Kjær (B&K) 2250-G4 Sound Level Meter (SLM)/Analyser [269] equipped with a B&K 4189 half-inch pre-polarized free-field microphone. This device was calibrated externally and additionally verified with a B&K 4226 Multifunction Acoustic Calibrator [127]. To measure the background noise within PALILA (as outlined in section A.3.1), the B&K 4189 microphone [270] of the SLM was replaced by a specialised system for very-low-level sound measurements, consisting of a B&K 4179 condenser microphone [271] coupled with a B&K 2669-L microphone preamplifier [272]. Such a system was employed because previously reported background noise levels [166] overlapped with the noise floor of the B&K 4189 microphone. All sound recordings lasted 15 s and were performed with a 24-bit resolution and a sampling frequency of 48 kHz.

To assess the free-field sound propagation, a Visaton FRWS 5-8 ohm speaker [181] was employed as a sound source. This device was equipped with an amplifier and emitted broadband noise. The speaker has a baffle diameter of 45 mm, an effective piston area of 12 cm^2, a maximum power of 3 W, and a frequency response ranging from 150 Hz to 20 kHz. For the evaluation of the transmission loss of the walls (as detailed in Section A.3.4), a JBL Flip 5 [273] Bluetooth speaker was employed instead, due to its superior low-frequency performance, extending down to 65 Hz and a higher maximum power of 20 W, compared to the Visaton FRWS 5-8 ohm speaker previously employed in [166].

A.3.1. BACKGROUND NOISE LEVELS

The background noise levels inside PALILA were measured with the door closed and the SLM positioned in the centre of the facility and at a height of 1 m. During the recordings, the lighting was on and the person taking the measurements was also inside quietly. The frequency spectrum was estimated using Welch's method [274] with time blocks of 1 s (i.e. 48,000 samples) with Hanning windowing with a 50% overlap. Hence, the frequency resolution was 1 Hz.

The measured sound pressure levels L_p are presented in Figure A.5a as narrowband spectra (with $\Delta f = 1$ Hz) and one-third-octave frequency band spectra. In general, these measurements reveal that the noise levels are very low and exhibit a broadband character.

For reference, the threshold of human hearing (in one-third-octave frequency bands) according to the ISO 226:2003 norm [275] is also included in Figure A.5. The measured background noise is below the threshold of human hearing for the whole spectrum. The equivalent, overall A-weighted sound pressure level $L_{p,A,eq}$ measured by the SLM averaged during 15 s was 13.4 dBA. The typical noise floor of the B&K 4179 condenser microphone is also plotted for reference, and the measured noise levels between 1 kHZ and 2 kHz and between 10 kHz and 20 kHz are very close to this measurement limit.

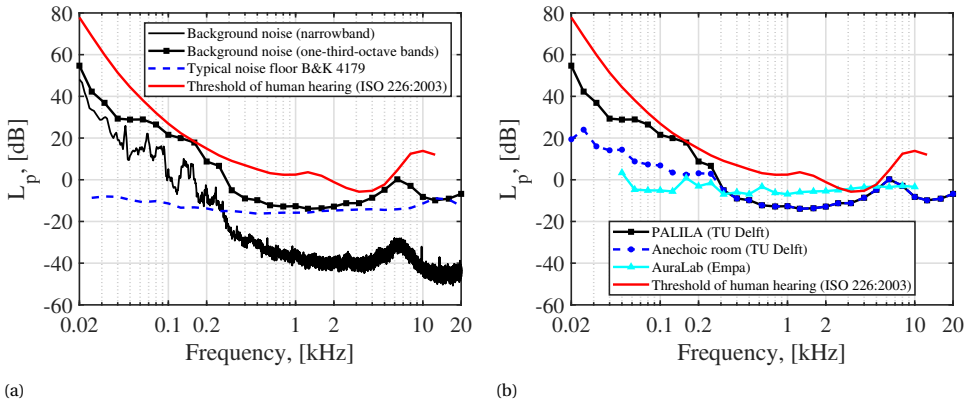

Figure A.5: (a) Background noise levels measured inside PALILA and threshold of human hearing, denoted as a red solid line. (b) Comparison of the background noise levels of PALILA with other similar facilities.

For comparison, Figure A.5b depicts the background noise one-third-octave frequency band spectra of two similar listening facilities: the anechoic room of the Applied Sciences faculty of TU Delft [169, 177] and the AuraLab facility of Empa [276]. More details on both facilities are included in Table A.3 in Section A.3.5. It should be noted that, due to the aforementioned limitation of the noise floor of the B&K 4189 microphone used for the measurement, the background noise levels of the anechoic room of TU Delft for frequencies higher than 315 Hz, were assumed to be the same as those recorded within PALILA with the low-noise B&K 4179 microphone. In general, the background noise levels of the three facilities follow a similar trend and remain below the threshold of human hearing [275].

Overall, the measured noise levels are deemed sufficiently low to not contaminate or interfere with psychoacoustic listening experiments. Moreover, as aforementioned, the headphones used during listening experiments provide an average A-weighted sound attenuation of 6.9 dBA.

A.3.2. REVERBERATION TIME

The reverberation time T_{60} within the laboratory was determined through the recording of six consecutive claps, which were generated approximately at the central point of the room and measured with the SLM placed at a distance of 1 m. These measurements were conducted with the laboratory door closed and the room was devoid of any furniture, such as the chair, laptop, or laptop table.

The reverberation time is traditionally defined in the time domain, but it can also be characterized in the frequency domain (e.g. decay rates per one-third-octave frequency band) [277, 278]. In this particular case, the claps served as a suitable approximation for broadband percussions, effectively exciting the frequencies within the range of interest from 250 Hz to 20 kHz. The choice of the lower frequency boundary is influenced by the characteristics of the acoustic-absorbing foam panels, see Figure A.2c.

To perform the frequency analysis, Welch's method was employed again, but this

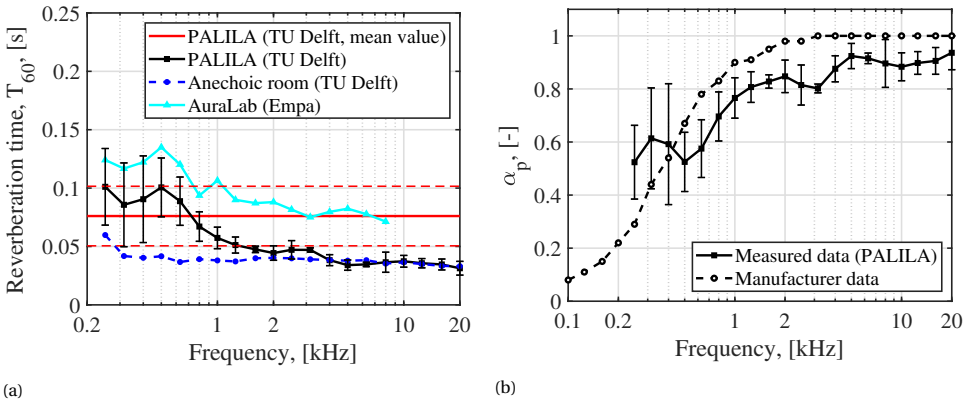

Figure A.6: (a) Reverberation time (T_{60}) measured inside PALILA compared with other similar facilities. (b) Comparison of the estimated sound absorption coefficient (α_p) of the acoustic-absorbing foam panels with the data provided by the manufacturer. Error bars denote the standard deviations.

time with considerably shorter time blocks of 20 ms to enhance the time resolution, enabling a more precise capture of the percussions, while maintaining an adequate frequency resolution of $\Delta f = 50$ Hz.

For each clap, the value of T_{60} was estimated as the time it took the increase in sound pressure level L_p above the background noise (typically reaching approximately 100 dB due to the percussion) to decay by 60 dB. Time interpolation down to 1 ms was employed to define more accurately the time required for the 60 dB decay.

The estimated reverberation times, both in the time and frequency domains, within one-third-octave frequency bands, are depicted in Figure A.6a. The mean T_{60} value in the time domain averaged over the six claps is 0.076 s ± 0.01 s (standard deviation, illustrated as dashed red lines in Figure A.6a). The same figure also contains the mean reverberation times per one-third-octave frequency band, along with their respective standard deviations represented as error bars. For comparison purposes, the reverberation times of the anechoic room of TU Delft and AuraLab of Empa, are also presented. The three facilities present similar values and behaviours.

In general, all the mean T_{60} values in the frequency range of interest are below 0.1 s (even below 0.05 s for frequencies higher than 1600 Hz), making PALILA belong to the acoustically *dead-space* category according to the ISO 3382 norm [278].

The estimated T_{60} in the frequency domain can be employed to estimate the sound absorption coefficient α_p as a function of frequency of the acoustic-absorbing foam panels as these cover most of the internal surfaces of the laboratory. As such, this approach provides a useful check of the α_p values claimed by the manufacturers. PALILA is a relatively small room (it has a volume of 11 m^3) and the expected absorption coefficients are relatively high, hence, Eyring's formula is employed since it is the more appropriate approach compared to Sabine's law for these conditions [277]. The influence of the bass traps and carpet was accounted for in the calculations using the absorption coefficients reported in Table A.1.

The estimated α_p values are presented in Figure A.6b together with the data pro-

vided by the manufacturer. Both curves present a similar trend and show an acceptable agreement, although for most of the frequency range, the estimated α_p are consistently lower than those determined by the manufacturer. These discrepancies could be due to small deviations in the assumed absorption coefficients of the other sound-absorbing elements in the room, i.e. bass traps and carpet, included in these α_p calculations. It was observed, however, that the bass traps have a negligible effect on the agreement.

A.3.3. FREE-FIELD PROPAGATION ASSESSMENT

An important feature of anechoic rooms is the region of space in which the inverse square law spreading [277] holds, i.e. where the free-field sound propagation conditions are present without significant sound reflections of the walls, floor, or ceiling. To calculate the expected L_p value at a distance r from the sound source in the free field, one can use the following expression which assumes omnidirectional spherical spreading of sound:

$$L_\mathrm{p}(r) = L_\mathrm{p}(r_0) - 20\log\left(\frac{r}{r_0}\right), \tag{A.1}$$

where r_0 represents a reference distance from the source, typically set at 1 m. It is worth noting that the impact of atmospheric sound absorption is neglected in this equation due to the relatively small distances considered.

The measured deviation from the expected free-field decay ΔL_p can be calculated for every distance r using the following equation

$$\Delta L_\mathrm{p} = L_\mathrm{p,exp} - L_\mathrm{p,ref}, \tag{A.2}$$

where $L_\mathrm{p,exp}$ and $L_\mathrm{p,ref}$ are the measured and modelled (using Equation A.1) sound pressure levels, respectively.

The maximum allowable ΔL_p values per one-third-octave frequency band for an anechoic room are given by the ISO 3745 [279] standard, see Table A.2.

Table A.2: Maximum allowable difference between measured and modelled free-field L_p for an anechoic room depending on the frequency range according to the ISO 3745 [279] standard.

One-third-octave-band centre frequency f, [Hz]	Allowable ΔL_p, [dB]
$f \leq 630$	± 1.5
$800 \leq f \leq 5000$	± 1
$f \geq 6300$	± 1.5

To assess the free-field conditions of PALILA a simple setup was employed (see Figure A.7a) consisting of:

- The Visaton FRWS 5-8 ohm speaker [181] positioned on a tripod 1 m high situated close to the bass trap opposite to the door with the speaker's baffle oriented towards the centre of the booth. This position represents the worst-case scenario for

placing a potential sound source because the sound reflections are strongest close to the corners. The speaker consistently reproduced the same white noise signal for each measurement. The door was kept closed for all measurements.

- The B&K 2250-G4 SLM aligned with the centre of the baffle of the speaker and directly facing it. For each measurement, the SLM was moved 0.2 m away from the speaker, traversing the room diagonally, starting from an initial distance of 1 m until a distance of 2 m, see Figure A.7a.

The measured ΔL_p values for each one-third-octave frequency band of interest in relation to the distance from the source r are presented in Figure A.7. The maximum allowable discrepancies, as outlined in Table A.2, are represented as horizontal red dashed lines.

The free-field propagation characteristics for low frequencies (Figure A.7b) only hold for certain frequency bands for distances to the source up to about 1.4 m (except for the 630 Hz band). The results improve for the middle (Figure A.7c) and, especially, for high (Figure A.7d) frequencies. In general, for frequencies exceeding 1600 Hz, free-field propagation conditions remain applicable for the majority of the distances considered. An exception arises for the largest distance of 2 m, where the reflections from the corner opposite to the speaker are expected to contaminate the measurements.

A.3.4. TRANSMISSION LOSS OF THE WALLS

The room hosting PALILA is located in a relatively quiet office corridor, devoid of significant noise sources. Nonetheless, to maintain a quiet environment to conduct psychoacoustic listening experiments and acoustic measurements, any potential external noise sources need to be effectively attenuated. On the other hand, it is also required to mitigate the transmission of any potential sound generated within PALILA to the exterior to prevent disturbances in the adjacent offices. Hence, an important criterion for acoustic characterisation pertains to quantifying the transmission loss (TL) of the booth's walls and door.

The experimental setup entailed placing the JBL Flip 5 [273] Bluetooth speaker outside of the booth mounted on a 1-m high tripod, oriented towards the boot's door, and emitting white noise with an overall L_p of roughly 68 dB. This process was conducted first with the door open and then with the door closed, see Figure A.8a. Within the booth, the SLM was positioned at a height of 1 m and situated 1 m away from the speaker. Both measurements employed the same sound signal, and the sound levels within PALILA were measured using the SLM. The TL for each one-third-octave frequency band can then be estimated by subtracting the sound spectrum measured with the door closed from that measured with the door open.

The obtained results are depicted in Figure A.8b compared with the TL data provided by the manufacturer [256] for a similar booth of smaller dimensions. Whereas there are some disparities, both curves exhibit comparable trends and values, demonstrating that the manufacturer's data can serve as a reference even for different design configurations. Below 63 Hz, the TL performance drops considerably reaching values below 10 dB.

The weighted average TL value provided by the manufacturer, in accordance with the ISO 717-1 [280] standard, is 45 dB. This value is considered adequate for mitigating

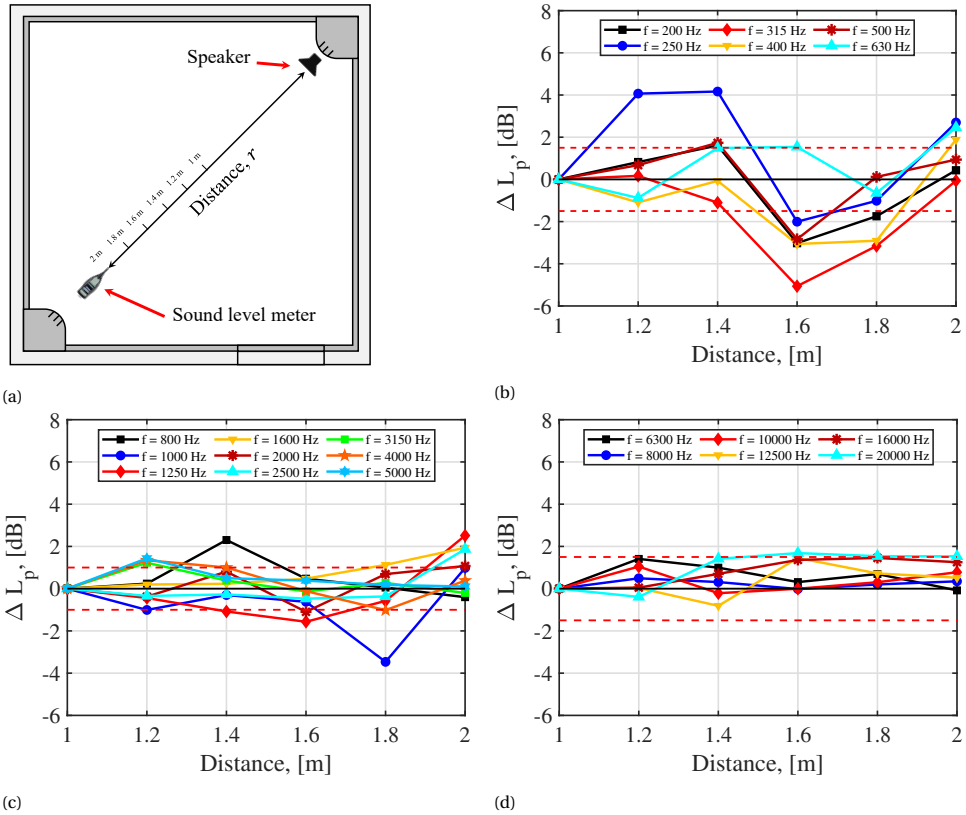

Figure A.7: (a) Experimental setup for characterizing the free-field propagation within PALILA. Deviations from the expected free-field decay due to spherical spreading with respect to the distance to the sound source for (b) low frequencies, (c) middle frequencies, and (d) high frequencies. The tolerances according to the ISO 3745 [279] standard are represented as dashed red lines.

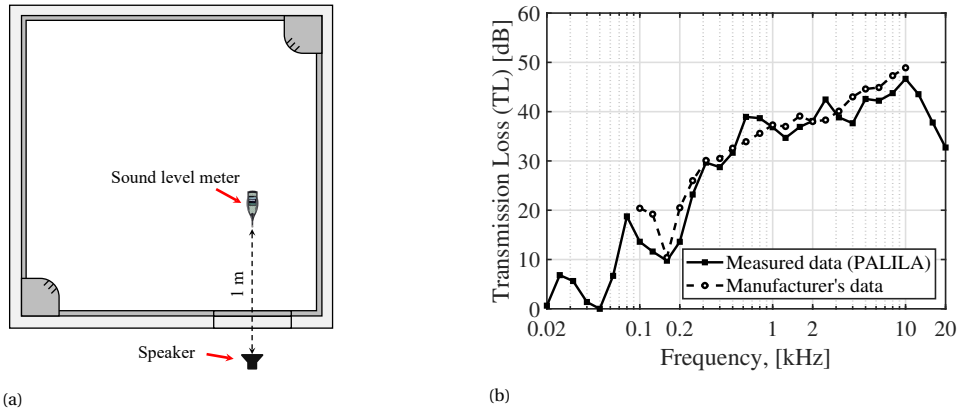

Figure A.8: (a) Experimental setup for characterizing the transmission losses of the wall and door for an observer inside the booth. (b) Comparison of the measured transmission loss (TL) with the data provided by the manufacturer.

potential external noise sources. It is worth noting that the gypsum wall and door of the room (outside the booth) would provide some additional transmission loss in practice.

A.3.5. COMPARISON WITH OTHER LISTENING LABORATORIES

In this section, the performance of PALILA is compared with other renowned laboratories dedicated to psychoacoustic research. These facilities encompass the AuraLab from EMPA [244], the Small Anechoic Chamber [248] from the NASA Langley Research Center, the MobiLab from RWTH Aachen [251], and the Listening Room at the University of Salford [252]. For additional reference, the two primary acoustic laboratories within TU Delft (the anechoic room of the Applied Sciences faculty [169, 177] and the A-tunnel [253]) are also included in this comparative assessment.

Table A.3 provides an overview of the key attributes of these facilities, including their dimensions, overall A-weighted background noise level $L_{p,A}$, and reverberation time T_{60}. PALILA presents one of the shortest reverberation times, with only the anechoic room of TU Delft featuring a lower value, and a very low background noise level. Hence, this new laboratory is well positioned with respect to existing similar research facilities.

A.4. CONCLUSIONS

This manuscript explains the design, calibration, and acoustic characterisation of the recently commissioned PsychoAcoustic LIstening LAboratory (PALILA) at Delft University of Technology. This facility consists of a soundproof room with very low background noise levels (even below the human hearing threshold across the whole audible frequency spectrum). With a reverberation time of 0.08 s, PALILA is categorized as an *acoustically dead-space*. The acoustic-absorbing foam panels covering walls, ceiling, and part of the floor, in conjunction with the sound-absorbing carpet, provide free-field sound propagation for frequencies higher than 1600 Hz. Furthermore, the box-in-box configuration, featuring double-layer walls, provides robust sound isolation capabilities, atten-

Table A.3: Comparison of the dimensions, overall A-weighted background noise levels ($L_{p,A}$), and reverberation times (T_{60}) of other (psycho)acoustic laboratories worldwide reported in the literature [169, 177, 244, 248, 251–253] with those of PALILA.

Facility	L × W × H [m × m × m]	Volume [m^3]	$L_{p,A}$ [dBA]	T_{60} [s]
AuraLab (EMPA)	5 × 4.5 × 3.34	74	7	0.11[a]
Small Anechoic Chamber (NASA)	3.7 × 2.5 × 2.1	20	15	-
MobiLab (RWTH Aachen)	2.4 × 1.82 × 1.77	7.5	-	0.2[a]
Listening Room (University of Salford)	6.6 × 5.8 × 2.8	107	5.7	0.27[a]
A-tunnel, without flow (TU Delft)	6.4 × 6.4 × 3.2	131	29	0.22
Anechoic room (TU Delft)	8 × 8 × 8	512	5.5[b]	0.03
PALILA (TU Delft)	**2.32 × 2.32 × 2.04**	**11**	**13.4**	**0.08**

[a] This T_{60} value corresponds to the middle frequencies.
[b] Includes a correction for the noise floor of the measurement equipment, see Section A.3.1.

uating potential external sound sources by up to 45 dB.

The calibration procedure of the audio equipment employed as well as the experimental procedure during listening experiments (e.g. the use of a graphical user interface) is also explained in detail for reference.

Overall, PALILA is considered a suitable quiet environment to conduct high-quality psychoacoustic listening experiments, offering acoustic performance on par with established research facilities of a similar nature. Its modular, relatively simple, and cost-effective design holds the potential to facilitate the establishment of analogous laboratories for a broader spectrum of researchers, thereby promoting the advancement of psychoacoustic listening experiments.

PALILA's primary focus is the evaluation of human perception, particularly in terms of short-term noise annoyance induced by diverse noise sources. Looking forward, there are initiatives to augment the laboratory's capabilities by integrating a virtual reality reproduction system. This enhancement will enable the assessment not only of auditory but also visual factors influencing annoyance, especially in the context of devices like drones or wind turbines [281, 282]. This future trajectory aligns with the concept of the Virtual Community Noise Simulator (VCNS) [283] developed by the Netherlands Aerospace Centre (NLR).

BIBLIOGRAPHY

[1] WHO Regional Office for Europe and JRC European Commission, *Burden of disease from environmental noise: Quantification of healthy life years lost in Europe*, Tech. Rep. (World Health Organization, 2011).

[2] WHO Regional Office for Europe, *International Journal of Environmental Research and Public Health*, Tech. Rep. 8 (World Health Organization, 2018).

[3] European Environmental Agency, *Environmental noise in Europe - 2020*, Tech. Rep. (European Environment Agency, Copenhagen, 2020).

[4] O. Hänninen, A. B. Knol, M. Jantunen, T. A. Lim, A. Conrad, M. Rappolder, P. Carrer, A. C. Fanetti, R. Kim, J. Buekers, R. Torfs, I. Iavarone, T. Classen, C. Hornberg, and O. C. Mekel, *Environmental burden of disease in Europe: assessing nine risk factors in six countries,* Environmental health perspectives **122**, 439–446 (2014).

[5] World Health Organization, *Uptake and impact of the WHO Environmental noise guidelines for the European Region Experiences from Member States*, Tech. Rep. (World Health Organization Regional Office for Europe, 2023).

[6] B. Kärcher, *Formation and radiative forcing of contrail cirrus,* Nature Communications 2018 9:1 **9**, 1–17 (2018).

[7] V. Grewe, S. Matthes, and K. Dahlmann, *The contribution of aviation NOx emissions to climate change: are we ignoring methodological flaws?* Environmental Research Letters **14**, 121003 (2019).

[8] D. S. Lee, D. W. Fahey, A. Skowron, M. R. Allen, U. Burkhardt, Q. Chen, S. J. Doherty, S. Freeman, P. M. Forster, J. Fuglestvedt, A. Gettelman, R. R. De León, L. L. Lim, M. T. Lund, R. J. Millar, B. Owen, J. E. Penner, G. Pitari, M. J. Prather, R. Sausen, and L. J. Wilcox, *The contribution of global aviation to anthropogenic climate forcing for 2000 to 2018,* Atmospheric Environment **244**, 117834 (2021).

[9] J. Faber and L. Van Wijngaarden, *Moet de luchtvaart groeien om onze welvaart te behouden?*, Tech. Rep. (CE Delft, 2019).

[10] IATA, *20-Year Air Passenger Forecast*, Tech. Rep. (IATA, Montreal, 2017).

[11] S. Gössling and A. Humpe, *The global scale, distribution and growth of aviation: Implications for climate change,* Global Environmental Change **65**, 102194 (2020).

[12] L. Hopkinson and S. Cairns, *Elite Status: global inequalities in flying*, Tech. Rep. (Possible charity, 2021).

[13] T. Rucinski, A. Ringstrom, and M. Green, *Airlines scramble to overcome polluter stigma as 'flight shame' movement grows,* (Accessed 25 May 2023).

[14] IPSOS, *A New World Disorder? Navigating a Polycrisis*, Tech. Rep. (IPSOS, 2023).

[15] IEA, *Aviation and shipping - net zero emissions guide*, Tech. Rep. (IEA, 2023).

[16] Maricopa Community Colleges, *Creating a Culture of Sustainability,* (Accessed 24 May 2023).

[17] A. K. Sahai, M. Snellen, D. G. Simons, and E. Stumpf, *Aircraft design optimization for lowering community noise exposure based on annoyance metrics,* Journal of Aircraft **54**, 2257–2269 (2017).

[18] S. Kephalopoulos, M. Paviotti, F. Anfosso-Lédée, D. Van Maercke, S. Shilton, and N. Jones, *Advances in the development of common noise assessment methods in Europe: The CNOSSOS-EU framework for strategic environmental noise mapping,* Science of The Total Environment **482-483**, 400–410 (2014).

[19] R. Merino-Martínez, R. Pieren, and B. Schäffer, *Holistic approach to wind turbine noise: From blade trailing-edge modifications to annoyance estimation,* Renewable and Sustainable Energy Reviews **148**, 111285 (2021).

[20] S. More, *Aircraft Noise Characteristics and Metrics*, Ph.D. thesis, Purdue University, West Lafayette, Indiana (2010).

[21] A. Vieira, M. Snellen, and D. G. Simons, *Experimental assessment of sound quality metrics for takeoff and landing aircraft,* AIAA Journal **59**, 240–249 (2021).

[22] G. F. Greco, R. Merino-Martínez, A. Osses, and S. C. Langer, *SQAT: a MATLAB-based toolbox for quantitative sound quality analysis,* in *InterNoise 23* (Chiba, Greater Tokyo, Japan, 2023).

[23] J. L. Peters, C. D. Zevitas, S. Redline, A. Hastings, N. Sizov, J. E. Hart, J. I. Levy, C. J. Roof, and G. A. Wellenius, *Aviation Noise and Cardiovascular Health in the United States: a Review of the Evidence and Recommendations for Research Direction,* Current Epidemiology Reports **5**, 140–152 (2018).

[24] S. Benz, J. Kuhlmann, S. Jeram, S. Bartels, B. Ohlenforst, and D. Schreckenberg, *Impact of Aircraft Noise on Health,* in *Aviation Noise Impact Management*, edited by L. Leylekian, A. Covrig, and A. Maximova (Springer International Publishing, 2022) pp. 173–195.

[25] S. Stansfeld, S. Hygge, C. Clark, and T. Alfred, *Night time aircraft noise exposure and children's cognitive performance,* Noise & health **12**, 255–262 (2010).

[26] N. Kranjec, S. Benz, N. E. Burtea, P. Hooper, R. Hudson, S. Jeram, J. Kuhlman, F. Rajé, and D. Schreckenberg, *ANIMA D2.3 - Recommendations on noise and health*, Tech. Rep. (ANIMA Project, 2019).

[27] J. E. Dekkers and J. W. van der Straaten, *Monetary valuation of aircraft noise: A hedonic analysis around Amsterdam airport,* Ecological Economics **68**, 2850–2858 (2009).

[28] A. Vieira, M. Snellen, and D. G. Simons, *Assessment of engine noise shielding by the wings of current turbofan aircraft,* in *24th International Congress on Sound and Vibration, ICSV 2017* (London, 2017).

[29] European Commission Directorate-General for Research and Innovation, *Fly the Green Deal - Europe's Vision for Sustainable Aviation*, Tech. Rep. (Publications Office of the European Union, 2022).

[30] Rolls-Royce, *Section 1. Design,* in *The Jet Engine* (Wiley, 2015) 5th ed., Chap. 1.

[31] Delft University of Technology, *1,44 miljoen subsidie voor Smart Rotors-project,* (Accessed 24 April 2024).

[32] Clean Aviation Joint Undertaking, *Strategic Research and Innovation Agenda 2024*, Tech. Rep. (Clean Aviation Joint Undertaking, 2024).

[33] D. A. I. Mccurdy, C. A. I. Powell, and N. I. Si, *Nasa Technical Memorandum*, Tech. Rep. (NASA, 1981).

[34] Civil Aviation Authority, *Emerging Aircraft Technologies and their potential noise impacts*, Tech. Rep. (Civil Aviation Authority, 2019).

[35] M. Y. Pereda Albarrán, M. Kreimeier, W. Enders, and E. Stumpf, *Noise evaluation of battery powered small aircraft,* CEAS Aeronautical Journal **11**, 125–135 (2020).

[36] D. L. Huff, B. S. Henderson, and E. Envia, *Motor Noise for Electric Powered Aircraft,* in *22nd AIAA/CEAS Aeroacoustics Conference* (Lyon, France, 2016) pp. 1–12.

[37] P. Aragão, *Airbus A320-214,* (Accessed 2 February 2025).

[38] A. van Beem, *Fokker 70 KLM cityhopper,* (Accessed 2 February 2025).

[39] A4Aviation, *Velis Electro - First Electric Certified Aircraft,* (Accessed 29 April 2023).

[40] DLR, *Design for a hybrid-electric aircraft with distributed propulsion units,* (Accessed 2 February 2025).

[41] R. Merino-Martínez, *Microphone arrays for imaging of aerospace noise sources*, Ph.D. thesis, Delft University of Technology (2018).

[42] A. Vieira, B. von den Hoff, M. Snellen, and D. G. Simons, *Comparison of Semi-Empirical Noise Models with Flyover Measurements of Operating Aircraft,* Journal of Aircraft **59**, 1574–1587 (2022).

[43] R. Merino-Martínez, S. J. Heblij, D. H. Bergmans, M. Snellen, and D. G. Simons, *Improving aircraft noise predictions considering fan rotational speed,* Journal of Aircraft **56**, 284–294 (2019).

[44] S. K. Lele and J. W. Nichols, *A second golden age of aeroacoustics?* Philosophical Transactions of the Royal Society A: Mathematical, Physical and Engineering Sciences **372** (2014).

[45] E.-L. Bertsch, *Noise Prediction within Conceptual Aircraft Design*, Ph.D. thesis, Technischen Universität Carolo-Wilhelmina (2013).

[46] C. Zellmann, *Development of an Aircraft Noise Emission Model Accounting for Flight Parameters*, Ph.D. thesis, Technical University of Berlin (2017).

[47] L. Bertsch and P. Krammer, *PANAM - a noise prediction tool for conceptual aircraft design*, Tech. Rep. (German Aerospace Center (DLR), 2008).

[48] C. Zellmann, J. M. Wunderli, and B. Schäffer, *SonAIR - Data acquisition for a next generation aircraft noise simulation model,* in *INTER-NOISE 2013: Noise Control for Quality of Life*, Vol. 1 (Innsbruck, 2013) pp. 842–850.

[49] W. E. Zorumski, *Aircraft Noise Prediction Program Theoretical Manual - Part 1*, Tech. Rep. (NASA, Langley Research Center, 1982).

[50] J. L. Thomas and R. J. Hansman, *Framework for analyzing aircraft community noise impacts of advanced operational flight procedures,* Journal of Aircraft **56**, 1407–1417 (2019).

[51] M. Lugten, *Assessing the influence of street canyon shape on aircraft noise: results from measurements in courtyards near Amsterdam Schiphol Airport,* InterNoise 2022 (2022).

[52] DeNoize, *DeNoize testing window technology to reduce noise nuisance in homes,* (Accessed 25 May 2023).

[53] I. Tsionis, *Make Some Noise Schiphol: A study on a parametric architectural strategy for the design of aircraft noise abatement landscape elements within cities*, MSc. thesis, Delft University of Technology (2020).

[54] L. Bertsch, D. G. Simons, and M. Snellen, *Aircraft Noise: The major sources, modelling capabilities, and reduction possibilities*, Tech. Rep. (German Aerospace Centre, 2015).

[55] A. Vieira, M. Snellen, and D. G. Simons, *Assessing the shielding of engine noise by the wings for current aircraft using model predictions and measurements,* The Journal of the Acoustical Society of America **143**, 388 (2018).

[56] M. Arntzen, T. A. van Veen, H. G. Visser, and D. G. Simons, *Aircraft noise simulation for a virtual reality environment,* in *17th AIAA/CEAS Aeroacoustics Conference 2011 (32nd AIAA Aeroacoustics Conference)*, June (Portland, Oregon, 2011) pp. 5–8.

[57] D. Casalino, F. Diozzi, R. Sannino, and A. Paonessa, *Aircraft noise reduction technologies: A bibliographic review,* Aerospace Science and Technology **12**, 1–17 (2008).

[58] S. Pietrzko and R. Bütikofer, *FLULA - Swiss aircraft noise prediction program,* in *Acoustics 2002 - Innovation in Acoustics and Vibration* (Adelaide, Australia, 2002).

[59] P. Malbéqui, Y. Rozenberg, and J. Bulté, *Aircraft noise prediction in the IESTA program*, Tech. Rep. (ONERA, 2009).

[60] M. Lighthill, *On sound generated aerodynamically I. General theory,* Proceedings of the Royal Society of London. Series A. Mathematical and Physical Sciences **211**, 564–587 (1952).

[61] N. Curle, *The influence of solid boundaries upon aerodynamic sound,* Proceedings of the Royal Society of London. Series A. Mathematical and Physical Sciences **231**, 505–514 (1955).

[62] J. E. Marte and D. W. Kurtz, *Review of Aerodynamic Noise From Propellers, Rotors, and Lift Fans*, Tech. Rep. (NASA, 1970).

[63] D. A. Russell, J. P. Titlow, and Y.-J. Bemmen, *Acoustic monopoles, dipoles, and quadrupoles: An experiment revisited,* American Journal of Physics **67**, 660–664 (1999).

[64] R. Merino-Martínez, J. Kennedy, and G. J. Bennett, *Experimental study of realistic low–noise technologies applied to a full–scale nose landing gear,* Aerospace Science and Technology **113**, 106705 (2021).

[65] W. Dobrzynski, L. C. Chow, P. Guion, and D. Shiells, *A European study on landing gear airframe noise sources,* in *6th AIAA/CEAS Aeroacoustics Conference and Exhibit* (Lahaina, 2000).

[66] H. H. Heller and W. M. Dobrzynski, *Sound Radiation from Aircraft Wheel-Well/Landing-Gear Configurations,* Journal of Aircraft **14**, 768–774 (1977).

[67] R. Merino-Martinez, I. Besnea, B. von den Hoff, and M. Snellen, *Psychoacoustic Analysis of the Noise Emissions from the Airbus A320 Aircraft Family and its Nose Landing Gear System,* in *30th AIAA/CEAS Aeroacoustics Conference (2024)* (Rome, 2024).

[68] M. R. Fink, *Noise component method for airframe noise,* in *4th Aeroacoustics Conference* (Atlanta, 1977).

[69] Y. Guo, *Empirical Prediction of Aircraft Landing Gear Noise*, Tech. Rep. (NASA, 2005).

[70] G. J. Bennett, E. Neri, and J. Kennedy, *Noise characterization of a full-scale nose landing gear,* Journal of Aircraft **55**, 2476–2490 (2018).

[71] K. Zhao, P. Okolo, E. Neri, P. Chen, J. Kennedy, and G. J. Bennett, *Noise reduction technologies for aircraft landing gear-A bibliographic review,* Progress in Aerospace Sciences **112**, 100589 (2020).

[72] T. F. Brooks, D. S. Pope, and M. A. Marcolini, *Airfoil self-noise and prediction*, Tech. Rep. (NASA, 1989).

[73] S. Luesutthiviboon, *Assessing and improving trailing-edge noise reduction technologies for industrial wind-turbine applications*, Ph.D. thesis, Delft University of Technology (2022).

[74] T. J. Mueller, *Aeroacoustic measurements*, edited by T. Mueller (Springer, 2002).

[75] R. K. Amiet, *Noise due to turbulent flow past a trailing edge,* Journal of Sound and Vibration **47**, 387–393 (1976).

[76] M. P. Sanders, C. H. Venner, and L. D. de Santana, *Slat noise measurements in open-jet, hard-wall and hybrid wind tunnel test sections,* Journal of Sound and Vibration **546**, 117420 (2023).

[77] M. Murayama, K. Yamamoto, M. Kohzai, T. Hirai, Y. Ueno, K. Isotani, and K. Hayashi, *Aircraft Noise Reduction Study on Inboard Slat-Tip Region,* in *AIAA AVIATION Forum 2023* (San Diego, 2023).

[78] M. Arntzen, *Aircraft noise calculation and synthesis in a non-standard atmosphere*, Ph.D. thesis, Delft University of Technology (2014).

[79] V. Jazarević and B. Rašuo, *Numerical Calculation of Aerodynamic Noise Generated from an Aircraft in Low Mach Number Flight,* in *BAIL 2016*, Vol. 120 (Springer Verlag, 2017) pp. 113–127.

[80] W. E. Zorumski, *Aircraft Noise Prediction Program Theoretical Manual - Part 2*, Tech. Rep. (NASA, Langley Research Center, 1982).

[81] X. Gloerfelt, C. Bogey, and C. Bailly, *Cavity noise,* in *In VKI Lecture Series: Aerodynamic Noise from Wall-Bounded Flows* (Cambridge University Press, 2009).

[82] K. K. Ahuja and J. Mendoza, *Effects of cavity dimensions, boundary layer, and temperature on cavity noise with emphasis on benchmark data to validate computational aeroacoustic codes*, Tech. Rep. (NASA, 1995).

[83] D. Rockwell and E. Naudascher, *Review-Self-Sustaining Oscillations of Flow Past Cavities,* Journal of Fluids Engineering **100**, 152–165 (1978).

[84] R. Merino-Martinez and M. Snellen, *Implementation of tonal cavity noise estimations in landing gear noise prediction models,* in *AIAA Aviation 2020 Forum* (Virtual event, 2020) pp. 1–19.

[85] I. E. Treager, *Aircraft Gas Turbine Engine Technology*, 3rd ed. (McGraw-Hill Education, 1978).

[86] R. Victoria Petrescu, R. Aversa, B. Akash, R. Bucinell, A. Apicella, and F. Ion Tiberiu Petrescu, *Modern Propulsions for Aerospace-A Review,* Journal of Aircraft and Spacecraft Technology **1**, 1–8 (2017).

[87] M. F. Heidmann, *Interim prediction method for fan and compressor source noise*, Tech. Rep. (NASA, 1975).

[88] M. G. Jones, W. R. Watson, D. M. Nark, B. M. Howerton, and M. C. Brown, *A Review of Acoustic Liner Experimental Characterization at NASA Langley*, Tech. Rep. (NASA, 2020).

[89] A. P. Dowling and Y. Mahmoudi, *Combustion noise,* Proceedings of the Combustion Institute **35**, 65–100 (2015).

[90] P. Y. Ho and V. L. Doyle, *Combustion noise prediction update,* in *5th Aeroacoustics Conference* (1979).

[91] A. K. Sahai, *Consideration of Aircraft Noise Annoyance during Conceptual Aircraft Design*, Ph.D. thesis, RWTH Aachen (2016).

[92] J. R. Stone, D. E. Groesbeck, and C. L. Zola, *Conventional profile coaxial jet noise prediction,* AIAA Journal **21**, 336–342 (2012).

[93] C. Tam, K. Viswanathan, K. Ahuja, and J. Panda, *The sources of jet noise: experimental evidence,* Journal of Fluid Mechanics **615**, 253–292 (2008).

[94] C. K. Tam and L. Auriault, *Jet Mixing Noise from Fine-Scale Turbulence,* AIAA Journal **37**, 145–153 (1999).

[95] T. Raef, A. A. Elzahaby, M. K. Khalil, and E. Armed, *Enhancement of propulsion performance through jet noise reduction technologies: a review,* in *The International Conference on Applied Mechanics and Mechanical Engineering*, 16th International Conference on Applied Mechanics and Mechanical Engineering. (2014) pp. 1–24.

[96] D. B. Hanson, *Helicoidal Surface Theory for Harmonic Noise of Propellers in the Far Field,* AIAA Journal **18**, 1213–1220 (1980).

[97] D. B. Hanson, *Compressible Helicoidal Surface Theory for Propeller Aerodynamics and Noise,* AIAA Journal **21**, 881–889 (1983).

[98] S. Glegg and W. Devenport, *Open rotor noise,* in *Aeroacoustics of Low Mach Number Flows* (Academic Press, 2017) Chap. 16, pp. 399–436.

[99] D. Casalino, *Analytical and numerical methods in vortex-body aeroacoustics,* Ph.D. thesis, Politechnico di Torino and l'École Centrale de Lyon (2002).

[100] D. B. Hanson, *Noise Radiation of Propeller Loading Sources with Angular Inflow,* in *AIAA 13th Aeroacoustics Conference* (Tallahassee, Florida, 1990).

[101] B. Magliozzi, D. B. Hanson, and R. K. Amiet, *Propeller and propfan noise,* in *Aeroacoustics of Flight -Vehicles: Theory and- Practice, Volume 1: Noise sources* (NASA, 1991) 1st ed.

[102] T. F. Brooks, M. A. Marcolini, and D. S. Pope, *Airfoil trailing-edge flow measurements,* AIAA Journal **24** (1986).

[103] T. Sinnige, D. Ragni, A. M. Malgoezar, G. Eitelberg, and L. L. Veldhuis, *APIAN-INF: an aerodynamic and aeroacoustic investigation of pylon-interaction effects for pusher propellers,* CEAS Aeronautical Journal **9**, 291–306 (2018).

[104] L. Rego, D. Ragni, F. Avallone, D. Casalino, R. Zamponi, and C. Schram, *Jet-installation noise reduction with flow-permeable materials,* Journal of Sound and Vibration **498**, 115959 (2021).

[105] G. F. Greco, *A computational investigation of jet-plate interaction noise using a Lattice-Boltzmann based method*, Ph.D. thesis, Technische Universität Braunschweig (2018).

[106] A. Vieira, M. Snellen, A. M. N. Malgoezar, R. Merino-Martinez, and D. G. Simons, *Analysis of shielding of propeller noise using beamforming and predictions,* The Journal of the Acoustical Society of America **146**, 1085 (2019).

[107] M. Van Ieperen, *Noise Prediction of the Flying V*, MSc. thesis, Delft University of Technology (2021).

[108] R. C. Johnson, *MEMS Mics Taking Over,* (Accessed 30 August 2024).

[109] Y. Yasuno and Y. Riko, *A chronological review of production and applications of electret condenser microphone for consumer use,* in *8th International Symposium on Electrets, ISE 1994 - Proceedings* (Institute of Electrical and Electronics Engineers Inc., 1994) pp. 943–948.

[110] G. M. Sessler and J. E. West, *The electret microphone,* IEEE Transactions on Broadcast and Television Receivers **BTR-10**, 73–76 (1964).

[111] B. Rose, *Comparing MEMS and Electret Condenser Microphones,* (Accessed 4 September 2024).

[112] P. Malcovati and A. Baschirotto, *The Evolution of Integrated Interfaces for MEMS Microphones,* Micromachines **9** (2018).

[113] R. Merino-Martínez, M. P. Sanders, L. C. Caldas, F. Avallone, D. Ragni, L. D. de Santana, M. Snellen, and D. G. Simons, *Comparison between analog and digital microphone phased arrays for aeroacoustic measurements,* in *2018 AIAA/CEAS Aeroacoustics Conference* (Atlanta, Georgia, 2018) pp. 1–17.

[114] Z. Prime and C. Doolan, *A comparison of popular beamforming arrays,* in *Acoustics 2013: Science, Technology and Amenity*, November (Victor Harbor, 2013) pp. 151–157.

[115] S. Luesutthiviboon, *Design of an Optimized Acoustic Array for Aero-acoustic Research in an Open-jet Anechoic Wind Tunnel*, MSc. thesis, Delft University of Technology (2017).

[116] J. Ocker and S. Tilgner, *The porsche wind tunnel microphone array system,* in *Aachen Acoustics Colloquium* (Aachen, 2015) pp. 135–151.

[117] B. D. Steinberg, *Principles of aperture and array system design: including random and adaptive arrays* (Wiley, 1976) p. 356.

[118] F. R. S. Lord Rayleigh, *XXXI. Investigations in optics, with special reference to the spectroscope,* The London, Edinburgh, and Dublin Philosophical Magazine and Journal of Science **8**, 261–274 (1879).

[119] J. Benesty, J. Chen, and Y. Huang, *Microphone array signal processing,* Springer Topics in Signal Processing **1**, 1–240 (2008).

[120] S. Luesutthiviboon, A. M. N. Malgoezar, R. Merino-Martinez, M. Snellen, P. Sijtsma, and D. G. Simons, *Enhanced HR-CLEAN-SC for resolving multiple closely spaced sound sources,* International Journal of Aeroacoustics **18**, 392–413 (2019).

[121] A. Malgoezar, M. Snellen, P. Sijtsma, and D. G. Simons, *Improving Beamforming By Optimization of Acoustic Array Microphone Positions,* in *BeBeC* (2016) pp. 1–24.

[122] E. Sarradj, *A generic approach to synthesize optimal array microphone arrangements,* in *BeBeC* (Berlin, 2016).

[123] L. Carneiro, A. Berry, and T. Padois, *Optimization methodology of microphone arrays for environmental source localization using the generalized cross-correlation,* in *BeBeC* (Berlin, 2018).

[124] R. P. Sallen and E. L. Key, *A practical method of designing RC active filters,* IRE Transactions on Circuit Theory **2**, 74–85 (1995).

[125] A. Lauterbach, K. Ehrenfried, L. Koop, and S. Loose, *Procedure for the accurate phase calibration of a microphone array,* in *15th AIAA/CEAS Aeroacoustics Conference (* (Miami, 2009).

[126] HBK, *Pistonphone Calibrator | Type 4228,* (Accessed 20 March 2024).

[127] HBK, *Type 4226 - Multifunction acoustic calibrator,* (Accessed 8 April 2024).

[128] HBK, *Microphone Phase Match Calibration System,* (Accessed 20 March 2024).

[129] G. Wade, *A History of Acoustic Imaging,* in *Proceedings of the Fifteenth International Symposium*, Vol. 15 (Springer, Boston, MA, 1986) pp. 1–28.

[130] H. Fastl and E. Zwicker, *Psychoacoustics: Facts and Models* (Springer Berlin Heidelberg, 2007) pp. 1–463.

[131] E. Sarradj, *Three-dimensional acoustic source mapping with different beamforming steering vector formulations,* Advances in Acoustics and Vibration **2012** (2012), 10.1155/2012/292695.

[132] P. Sijtsma, *Beamforming on moving sources*, Tech. Rep. May (Netherlands Aerospace Centre, 2007).

[133] R. Merino-Martínez, P. Sijtsma, M. Snellen, T. Ahlefeldt, J. Antoni, C. Bahr, D. Blacodon, D. Ernst, A. Finez, S. Funke, T. Geyer, S. Haxter, G. Herold, X. Huang, W. Humphreys, Q. Leclère, A. Malgoezar, U. Michel, T. Padois, A. Pereira, C. Picard, E. Sarradj, H. Siller, D. Simons, and C. Spehr, *A review of acoustic imaging methods using phased microphone arrays,* CEAS Aeronautical Journal, Special Issue "Aircraft Noise Generation and Assessment" **10**, 197–230 (2019).

[134] R. Merino-Martínez, B. Von Den Hoff, D. Morata, and M. Snellen, *Three-dimensional acoustic imaging using asynchronous microphone array measurements,* in *9th Berlin Beamforming Conference* (Berlin, 2022).

[135] Q. Leclère, A. Pereira, C. Bailly, J. Antoni, and C. Picard, *A unified formalism for acoustic imaging based on microphone array measurements,* International Journal of Aeroacoustics **16**, 431–456 (2017).

[136] E. Sarradj, G. Herold, and S. Jekosch, *Array methods: which one is the best?* in *Proceedings of BeBec 2018* (Berlin, 2018) pp. 1–12.

[137] A. M. N. Malgoezar, M. Snellen, R. Merino-Martinez, D. G. Simons, and P. Sijtsma, *On the use of global optimization methods for acoustic source mapping,* The Journal of the Acoustical Society of America **141**, 453–465 (2017).

[138] C. E. Lindsay and N. Ross Chapman, *Matched Field inversion for Geoacousutic Model Parameters Using Adaptive Simulated Annealing,* IEEE Journal of Oceanic Engineering **18**, 224–231 (1993).

[139] S. Kirkpatrick, C. D. Gelatt, and M. P. Vecchi, *Optimization by Simulated Annealing,* Science **220**, 671–680 (1983).

[140] P. Gerstoft, *Inversion of seismoacoustic data using genetic algorithms and a posteriori probability distributions,* Journal of the Acoustical Society of America **95**, 770–782 (1994).

[141] J. Grefenstette, *Optimization of Control Parameters for Genetic Algorithms,* IEEE Transactions on Systems, Man, and Cybernetics **16**, 122–128 (1986).

[142] M. Dorigo, V. Maniezzo, and A. Colorni, *Ant system: Optimization by a colony of cooperating agents,* IEEE Transactions on Systems, Man, and Cybernetics, Part B: Cybernetics **26**, 29–41 (1996).

[143] M. Dorigo, G. Di Caro, and L. M. Gambardella, *Ant algorithms for discrete optimization,* Artificial Life **5**, 137–172 (1999).

[144] P. Kumar and M. Pant, *Noisy source recognition in multi noise plants by differential evolution,* Proceedings of the 2013 IEEE Symposium on Swarm Intelligence, SIS 2013 - 2013 IEEE Symposium Series on Computational Intelligence, SSCI 2013 , 271–275 (2013).

[145] P. Sijtsma, *CLEAN based on spatial source coherence*, Tech. Rep. (National Aerospace Laboratory NLR, 2007).

[146] E. Sarradj, G. Herold, P. Sijtsma, R. M. Martinez, A. Malgoezar, M. Snellen, T. F. Geyer, C. J. Bahr, R. Porteous, D. J. Moreau, and C. J. Doolan, *A microphone array method benchmarking exercise using synthesized input data,* in *23rd AIAA/CEAS Aeroacoustics Conference, 2017* (Denver, 2017).

[147] R. Merino-Martínez, G. Herold, M. Snellen, and R. P. Dougherty, *Assessment and comparison of the performance of functional projection beamforming for aeroacoustic measurements,* in *8th Berlin Beamforming Conferece* (Berlin, 2020).

[148] M. Snellen and D. G. Simons, *An assessment of the performance of global optimization methods for geo-acoustic inversion,* Journal of Computational Acoustics **16**, 199–223 (2008).

[149] A. J. Torija, Z. Li, and P. Chaitanya, *Psychoacoustic modelling of rotor noise,* The Journal of the Acoustical Society of America **151**, 1804 (2022).

[150] Greco; Gil Felix, Merino-Martínez; Roberto, and Osses; Alejandro, *SQAT: a sound quality analysis toolbox for MATLAB - Version 1.1,* (2024).

[151] A. Osses, G. F. Greco, and R. Merino-Martínez, *Considerations for the perceptual evaluation of steady-state and time-varying sounds using psychoacoustic metrics,* in *10th Forum Acusticum* (Turin, Italy, 2023).

[152] International Standardization Organization, *ISO 532-1:2017(en), Acoustics — Methods for calculating loudness — Part 1: Zwicker method,* (2017).

[153] W. Aures, *Procedure for calculating the sensory euphony of arbitrary sound signal. In German: Berechnungsverfahren für den sensorischen Wohlklang beliebiger Schallsignale,* Acustica **59**, 130–141 (1985).

[154] Deutsches Institut für Normung, *DIN 45692 - 2009-08*, Tech. Rep. (DIN, 2009).

[155] P. Daniel and R. Weber, *Psychoacoustical Roughness: Implementation of an Optimized Model,* Acta Acoustica united with Acustica **83**, 113–123 (1997).

[156] A. Osses Vecchi, R. García León, and A. Kohlrausch, *Modelling the sensation of fluctuation strength,* in *Proceedings of Meetings on Acoustics* (2016) pp. 1–8.

[157] G. von Bismarck, *Sharpness as an attribute of the timbre of steady sounds,* Acustica **30**, 159–172 (1974).

[158] International Organization for Standardization, *ISO 7779:2018 - Acoustics — Measurement of airborne noise emitted by information technology and telecommunications equipment*, Tech. Rep. (International Organization for Standardization, 2018).

[159] A. M. Willemsen and M. D. Rao, *Characterization of sound quality of impulsive sounds using loudness based metric,* in *20th International Congress on Acoustics* (Sydney, 2010).

[160] A. Vieira, U. Mehmood, R. Merino-Martínez, M. Snellen, and D. G. Simons, *Variability of sound quality metrics for different aircraft types during landing and take-off,* in *25th AIAA/CEAS Aeroacoustics Conference, 2019* (American Institute of Aeronautics and Astronautics Inc, AIAA, Delft, the Netherlands, 2019).

[161] R. Merino-Martínez, R. M. Yupa-Villanueva, B. Von den Hoff, and J. Pockelé, *Human response to the flyover noise of different types of drones recorded in field measurements,* in *Quiet Drones* (Manchester, 2024).

[162] G. Q. Di, X. W. Chen, K. Song, B. Zhou, and C. M. Pei, *Improvement of Zwicker's psychoacoustic annoyance model aiming at tonal noises,* Applied Acoustics **105**, 164–170 (2016).

[163] D. J. Levitin, *Experimental Design in Psychoacoustic Research,* in *Music, Cognition and Computerized Sound: An Introduction to Psychoacoustics.* (M.I.T. Press, 1999) Chap. 23.

[164] D. Schwarz, G. Lemaître, M. Aramaki, and R. Kronland-Martinet, *Effects of Test Duration in Subjective Listening Tests,* in *International Computer Music Conference (ICMC)* (Utrecht, 2016) pp. 515–519.

[165] M. A. Alamir, K. L. Hansen, B. Zajamsek, and P. Catcheside, *Subjective responses to wind farm noise: A review of laboratory listening test methods,* Renewable and Sustainable Energy Reviews **114**, 109317 (2019).

[166] R. Merino-Martínez, B. Von Den Hoff, and D. G. Simons, *Design and acoustic characterization of a psychoacoustic listening facility,* in *ICSV29* (Prague, 2023).

[167] C. Chambers and D. Pressnitzer, *Perceptual hysteresis in the judgment of auditory pitch shift,* Attention, perception & psychophysics **76**, 1271–1279 (2014).

[168] M. Thaut, *Musical echoic memory training (MEM),* in *Handbook of Neurologic Music Therapy* (Oxford University Press, 2014) Chap. 25.

[169] B. von den Hoff, R. Merino-Martínez, D. G. Simons, and M. Snellen, *Using global optimization methods for three-dimensional localization and quantification of incoherent acoustic sources,* JASA Express Letters **2** (2022).

[170] B. Von den Hoff, R. Merion-Martínez, M. Snellen, and D. G. Simons, *Data underlying the publication "Using global optimization methods for three-dimensional localization and quantification of incoherent acoustic sources",* (2025).

[171] WHO Regional Office for Europe, *Environmental Noise Guidelines for the European Region*, Tech. Rep. (World Health Organization, Copenhagen, 2018).

[172] P. Sijtsma, *Experimental techniques for identification and characterisation of noise sources*, Tech. Rep. NLR-TP-2004-165 (Royal Netherlands Aerospace Centre, 2004).

[173] S. Oerlemans, *Detection of aeroacoustic sound sources on aircraft and wind turbines*, Ph.D. thesis, University of Twente, Enschede (2009).

[174] Y. Zhou, V. Valeau, J. Marchal, F. Ollivier, and R. Marchiano, *Three-dimensional identification of flow-induced noise sources with a tunnel-shaped array of MEMS microphones,* Journal of Sound and Vibration **482**, 1–20 (2020).

[175] R. P. Dougherty, *Functional Beamforming,* in *5th Berlin Beamforming Conference* (Berlin, 2014).

[176] T. F. Brooks and W. M. Humphreys, *A deconvolution approach for the mapping of acoustic sources (DAMAS) determined from phased microphone arrays,* Journal of Sound and Vibration **294**, 856–879 (2006).

[177] P. Sijtsma, R. Merino-Martinez, A. Malgoezar, and M. Snellen, *High-Resolution CLEAN-SC: theory and experimental validation,* International Journal of Aeroacoustics **16**, 274–298 (2017).

[178] R. Merino-Martínez, M. Snellen, and D. G. Simons, *Functional beamforming applied to imaging of flyover noise on landing aircraft,* Journal of Aircraft **53**, 1830–1843 (2016).

[179] R. P. Dougherty, *Determining Spectra of Aeroacoustic Sources from Microphone Array Data,* in *25th AIAA/CEAS Aeroacoustics Conference, Delft, The Netherlands* (Delft, The Netherlands, 2019).

[180] E. Sarradj, *A fast signal subspace approach for the determination of absolute levels from phased microphone array measurements,* Journal of Sound and Vibration **329**, 1553–1569 (2010).

[181] Visaton, *FRWS 5 - 8 Ohm,* (Accessed 21 February 2022).

[182] A. O. Williams, *The Piston Source at High Frequencies,* Journal of the Acoustical Society of America **23**, 1–6 (1951).

[183] L. L. Pereira, R. Merino-Martínez, D. Ragni, D. Gómez-Ariza, and M. Snellen, *Combining asynchronous microphone array measurements for enhanced acoustic imaging and volumetric source mapping,* Applied Acoustics **182** (2021).

[184] B. von den Hoff, M. Snellen, and D. G. Simons, *Noise assessment of taxibotted versus conventional taxiing operations using a phased microphone array,* in *50th International Congress and Exposition of Noise Control Engineering* (The Institute of Noise Control Engineering of the USA, Inc., 2021).

[185] B. Von den Hoff, M. Snellen, and D. G. Simons, *Data and code underlying the publication "Noise assessment of taxibotted versus conventional taxiing operations using a phased microphone array",* (2025).

[186] A. L. Brown and I. van Kamp, *WHO environmental noise guidelines for the European region: A systematic review of transport noise interventions and their impacts on health,* International Journal of Environmental Research and Public Health **14** (2017), 10.3390/ijerph14080873.

[187] European Parliament, *Directive 2003/10/EC of 6 February 2003 on the minimum health and safety requirements regarding the exposure of workers to the risks arising from physical agents (noise),* (2008).

[188] D. Bresser and S. Prent, *Feasibility Study Sustainable Taxiing at Schiphol*, Tech. Rep. (Royal Schiphol Group, 2021).

[189] C. Asensio, R. Pagan, and J. M. Lopez, *Aircrafts' taxi noise emission,* Noise and Vibration Worldwide **39**, 10–15 (2008).

[190] National Academies of Science Engineering and Medicine, *Enhanced Modeling of Aircraft Taxiway Noise, Volume 1: Scoping*, Vol. 1 (The National Academies Press, Washington DC, 2009).

[191] K. Hein and S. Baumann, *Acoustical comparison of conventional taxiing and dispatch towing - Taxibot's contribution to ground noise abatement,* 30th Congress of the International Council of the Aeronautical Sciences, ICAS 2016 , 1–7 (2016).

[192] CAE Software und Systems GmbH, *Acoustic Camera Bionic M-112 Array Fact Sheet*, Tech. Rep. (2021).

[193] K. Attenborough, *Sound Propagation in the Atmosphere,* in *Handbook of Acoustics* (2014) pp. 45–2674.

[194] R. W. Sinnott, *Virtues of the Haversine,* Sky and Telescope **68**, 158–159 (1984).

[195] M. Śliwińska-Kowalska and K. Zaborowski, *WHO environmental noise guidelines for the European region: A systematic review on environmental noise and permanent hearing loss and tinnitus,* International Journal of Environmental Research and Public Health **14** (2017).

[196] B. Von den Hoff, *Data and code underlying Ch. 7 of PhD thesis: Phased microphone array noise measurements of a Cessna Skymaster at Teuge International Airport,* (2025).

[197] D. C. Mikkelson, G. A. Mitchell, and L. J. Bober, *Summary of recent NASA propeller research*, Tech. Rep. NASA TM-83733 (NASA, 1984).

[198] Ampaire, *Electric EEL,* (Accessed 14 November 2024).

[199] N. Peake and A. B. Parry, *Modern Challenges Facing Turbomachinery Aeroacoustics,* Annu. Rev. Fluid Mech **44**, 227–248 (2012).

[200] Voorsternieuws, *Testvliegtuig Cessna Skymaster voor onderzoek naar elektrisch vliegen aangekomen op Teuge Airport,* (Accessed 1 February 2025).

[201] R. H. Self, *Propeller Noise,* in *Encyclopedia of Aerospace Engineering* (John Wiley & Sons, Ltd, 2010).

[202] S. Werner, *Plane and Pilot: 1978 Aircraft Directory,* (1978).

[203] Cessna Aircraft Company, *Super Skymaster Owner's Manual*, Tech. Rep. (Wichita, Kansas, USA, 1971).

[204] Continental Motors, *Maintenance and Operator's Manual - IO-360*, Tech. Rep. (2011).

[205] Federal Aviation Administration, *Type Certificate Data Sheet No. A6CE - Model 337 Super Skymaster*, Tech. Rep. (Department of Transportation, 2015).

[206] S. Jekosch, *Methods for analyzing and characterizing sound sources in rotating systems*, Ph.D. thesis, Technischen Universität Berlin, Berlin, Germany (2023).

[207] R. Yupa-Villanueva, R. Merino-Martinez, C. Andino Cappagli, A. Altena, and M. Snellen, *Effect of unmanned aerial vehicle configuration on the acoustic and psychoacoustic signatures,* in *30th International Congress on Sound and Vibration* (Amsterdam, 2024).

[208] B. Von Den Hoff, D. G. Simons, and M. Snellen, *Breakdown of propeller aircraft noise by applying conventional beamforming jointly with imaging using the rotating source identifier,* in *9th Berlin Beamforming Conference* (Berlin, 2022).

[209] F. Yunus, B. von den Hoff, and M. Snellen, *Predicting tonal noise of full-electric propeller-driven aircraft in outdoor environments using low-order models,* 30th AIAA/CEAS Aeroacoustics Conference (2024).

[210] B. Von den Hoff, *Data and code underlying Ch. 8 and Ch. 9 of PhD thesis: Noise measurements of a Pipistrel Velis Electro and Pipistrel Virus aircraft at Teuge International Airport,* (2025).

[211] EASA, *Type-Certificate Data Sheet No.EASA.A.573 for Virus SW 121*, Tech. Rep. (European Union Aviation Safety Agency, 2022).

[212] Z. Huang, H. Yao, O. Sjögren, A. Lundbladh, and L. Davidson, *Aeroacoustic analysis of aerodynamically optimized joined-blade propeller for future electric aircraft at cruise and take-off,* Aerospace Science and Technology **107**, 106336 (2020).

[213] J. R. Hambrey, M. T. Kotwicz Herniczek, D. Feszty, S.-A. Meslioui, and J. Park, *Comparison of Three Popular Methods for the Prediction of High Speed Propeller Noise,* 23rd AIAA/CEAS Aeroacoustics Conference (2017).

[214] M. T. Kotwicz Herniczek, D. Feszty, S. A. Meslioui, and J. Park, *Applicability of early acoustic theory for modern propeller design,* 23rd AIAA/CEAS Aeroacoustics Conference (2017).

[215] M. T. Kotwicz Herniczek, D. Feszty, S.-A. Meslioui, J. Park, and F. Nitzsche, *Evaluation of Acoustic Frequency Methods for the Prediction of Propeller Noise,* AIAA Journal **57** (2019).

[216] A. Kvurt and O. Stalnov, *From the Blade Geometry to Prediction of Tonal Noise Component in Hover,* in *28th AIAA/CEAS Aeroacoustics Conference, 2022* (American Institute of Aeronautics and Astronautics Inc, AIAA, Southampton, 2022).

[217] M. H. Martins, L. A. Bonomo, A. R. da Silva, and J. A. Cordioli, *Evaluation of the helicoidal surface theory for the noise prediction of small UAS propellers,* Journal of the Brazilian Society of Mechanical Sciences and Engineering **46**, 1–14 (2024).

[218] M. Haddaoui, *Development of a Propeller Source Noise Model*, MSc. thesis, Delft University of Technology (2019).

[219] M. Drela, *XFOIL: An Analysis and Design System for Low Reynolds Number Airfoils,* in *Lecture Notes in Engineering*, Vol. 54 (Springer, Berlin, Heidelberg, 1989) pp. 1–12.

[220] M. Drela and H. Youngren, *XROTOR download page,* (Accessed 8 January 2025).

[221] Y. Fuerkaiti, E. Grande, D. Casalino, F. Avallone, and D. Ragni, *Efficient low-fidelity aeroacoustic permanence calculation of propellers,* Aerospace Science and Technology **123**, 107438 (2022).

[222] N. Elbers, *Assessment of an aircraft propeller noise model by verification and experimental validation*, MSc. thesis, Delft University of Technology (2021).

[223] F. Yunus, D. Casalino, G. Romani, and M. Snellen, *Efficient prediction of propeller noise at incidence,* in *Quiet Drones* (Manchester, 2024).

[224] B. von den Hoff, R. Merino-Martinez, R. Yupa Villanueva, and M. Snellen, *Noise Emissions and Noise Annoyance of a Single-propeller Electric Aircraft During Flyover,* in *30th International Congress on Sound and Vibration* (Society of Acoustics, Amsterdam, 2024) p. 558.

[225] B. Von den Hoff, R. Merino-Martínez, J. Pockelé, and R. M. Yupa Villanueva, *Data and code underlying Ch. 9 of PhD thesis: Psychoacoustic assessment of electric aviation noise,* (2025).

[226] Boeing, *Commercial Market Outlook 2020-2039*, Tech. Rep. (2020).

[227] D. Schweizer, E. Bühlmann, T. Saurer, J. Mercuriali, D. Milo, M. Strickler, and A. Stöcklin, *Noise emissions: What to expect from electric vehicles compared to combustion vehicles?* in *29th International Congress on Sound and Vibration* (Prague, 2023).

[228] EASA, *Type-Certificate Data Sheet for Noise No. EASA.A.573 for Virus SW 121*, Tech. Rep. (European Union Aviation Safety Agency, 2022).

[229] Pipistrel, *Velis Electro - Technical Characteristics,* (Accessed 29 April 2023).

[230] ICAO, *Environmental Protection: Annex 16 to the Convention on International Civil Aviation, Volume I Aircraft Noise*, Tech. Rep. (International Civil Aviation Organization, 2008).

[231] J. Pockelé, *Graphical User Interface for the Psychoacoustic Listening Laboratory (PALILA GUI) (version v1.0.0),* (2024).

[232] H. M. Miedema and C. G. Oudshoorn, *Annoyance from transportation noise: Relationships with exposure metrics DNL and DENL and their confidence intervals,* Environmental Health Perspectives **109**, 409–416 (2001).

[233] R. van Poll, M. Reedijk, J. Hoekstra, W. Swart, J. van de Kassteele, and D. Houthuijs, *Relaties vliegtuiggeluid – hinder en slaapverstoring 2020*, Tech. Rep. (RIVM, Bilthoven, 2023).

[234] A. L. Hansell, M. Blangiardo, L. Fortunato, S. Floud, K. De Hoogh, D. Fecht, R. E. Ghosh, H. E. Laszlo, C. Pearson, L. Beale, S. Beevers, J. Gulliver, N. Best, S. Richardson, and P. Elliott, *Aircraft noise and cardiovascular disease near Heathrow airport in London: small area study,* BMJ **347** (2013).

[235] P. Bazilinskyy, R. Merino-Martínez, E. Özcan, D. Dodou, and J. de Winter, *Exterior sounds for electric and automated vehicles: Loud is effective,* Applied Acoustics **214**, 109673 (2023).

[236] S. Kumar, W. S. Wing, and H. P. Lee, *Psychoacoustic Analysis of Vacuum Cleaner Noise,* Acoustics **3**, 545–558 (2021).

[237] S. Atamer and M. E. Altinsoy, *Vacuum Cleaner Noise Annoyance: An Investigation of Psychoacoustic Parameters, Effect of Test Methodology, and Interaction Effect between Loudness and Sharpness,* Applied Sciences **13**, 6136 (2023).

[238] S. Wagner, R. Bareiß, and G. Guidati, *Wind Turbine Noise* (Springer Berlin Heidelberg, 1996).

[239] O. Breugelmans, D. Houthuijs, R. Van Poll, Hajema KlaasJan, and R. Hogenhuis, *Predicting aircraft noise annoyance: Exploring noise metrics other than Lden,* in *12th ICBEN Congress on Noise as a Public Health Problem* (Zurich, 2017).

[240] G. F. Greco, L. Bertsch, T. P. Ring, and S. C. Langer, *Sound quality assessment of a medium-range aircraft with enhanced fan-noise shielding design,* CEAS Aeronautical Journal **12**, 481–493 (2021).

[241] Y. Huang, B. Lv, K. Ni, and W. Jiang, *Discomfort estimation for aircraft cabin noise using linear regression and modified psychoacoustic annoyance approaches,* The Journal of the Acoustical Society of America **154**, 1963–1976 (2023).

[242] S. A. Rizzi and A. Christian, *A psychoacoustic evaluation of noise signatures from advanced civil transport aircraft,* 22nd AIAA/CEAS Aeroacoustics Conference, 2016 (2016).

[243] B. Schäffer, S. J. Schlittmeier, R. Pieren, K. Heutschi, M. Brink, R. Graf, and J. Hellbrück, *Short-term annoyance reactions to stationary and time-varying wind turbine and road traffic noise: A laboratory study,* The Journal of the Acoustical Society of America **139**, 2949–2963 (2016).

[244] B. Schäffer, R. Pieren, S. J. Schlittmeier, and M. Brink, *Effects of Different Spectral Shapes and Amplitude Modulation of Broadband Noise on Annoyance Reactions in a Controlled Listening Experiment,* International Journal of Environmental Research and Public Health **15**, 1029 (2018).

[245] R. Pieren, L. Bertsch, D. Lauper, and B. Schäffer, *Improving future low-noise aircraft technologies using experimental perception-based evaluation of synthetic flyovers,* Science of The Total Environment **692**, 68–81 (2019).

[246] S. A. Rizzi, D. L. Huff, D. D. Boyd, P. Bent, B. S. Henderson, K. A. Pascioni, D. C. Sargent, D. L. Josephson, M. Marsan, H. B. He, and R. Snider, *Urban Air Mobility Noise: Current Practice, Gaps, and Recommendations*, Tech. Rep. (NASA, 2020).

[247] R. Merino-Martinez, R. Pieren, B. Schäffer, and D. G. Simons, *Psychoacoustic model for predicting wind turbine noise annoyance,* in *24th International Congress on Acoustics* (Gyeongju, Korea, 2022).

[248] H. H. Hubbard and C. A. Powell, *Acoustic facilities for human factors research at NASA Langley Research Center: Description and operational capabilities*, Tech. Rep. (NASA, 1981).

[249] I. Faller, Kenneth J., S. A. Rizzi, and A. R. Aumann, *Acoustic Performance of a Real-Time Three-Dimensional Sound-Reproduction System*, Tech. Rep. (NASA, 2013).

[250] J. Klos, *Overview of an Indoor Sonic Boom Simulator at NASA Langley Research Center,* in *INTER-NOISE 2012* (New York, 2012).

[251] F. Pausch and J. Fels, *MobiLab - A Mobile Laboratory for On-Site Listening Experiments in Virtual Acoustic Environments,* Acta Acustica united with Acustica **105**, 875–887 (2019).

[252] University of Salford, *Listening Room,* (Accessed 20 March 2023).

[253] R. Merino-Martínez, A. Rubio Carpio, L. T. Lima Pereira, S. van Herk, F. Avallone, D. Ragni, and M. Kotsonis, *Aeroacoustic design and characterization of the 3D-printed, open-jet, anechoic wind tunnel of Delft University of Technology,* Applied Acoustics **170** (2020).

[254] T. Sinnige, B. D. Corte, R. De Vries, F. Avallone, R. Merino-Martínez, D. Ragni, G. Eitelberg, and L. L. Veldhuis, *Alleviation of Propeller-slipstream-induced unsteady pylon loading by a flow-permeable leading edge,* Journal of Aircraft **56**, 1214–1230 (2019).

[255] International Standardization Organization, *ISO 11654:1997 - Acoustics — Sound absorbers for use in buildings — Rating of sound absorption,* (1997).

[256] Studiobricks, *Soundproof booths for music, recording, office,* (Accessed 20 March 2023).

[257] Akoestiekwinkel, *Akotherm Basic D40 - Akoestische plaat,* (Accessed 20 March 2023).

[258] *Studiobricks is excited to announce the launch of the Eco Sound Isolation Booth Line - Studiobricks,* (Accessed 20 March 2023).

[259] Akoestiekwinkel, *Studiobricks Corner bass traps,* (Accessed 20 March 2023).

[260] arc edition, *Master 198 - Service Collection,* (Accessed 20 March 2023).

[261] Sony, *Sony WH1000XM4/B Premium Noise Cancelling Wireless Over-The-Ear Headphones, Black,* (Accessed 20 March 2023).

[262] M. Kuntz, N. F. Bischof, and B. U. Seeber, *Sound field synthesis for psychoacoustic research: In situ evaluation of auralized sound pressure level,* The Journal of the Acoustical Society of America **154**, 1882–1895 (2023).

[263] GRAS Sound and Vibration, *GRAS 45BB-14 KEMAR for High-Frequency Test of Ear- and Headphones, 2-Ch CCP,* (Accessed 20 March 2023).

[264] American National Standards Institute, *ANSI/ASA S3.36 (R2018) - Manikin for Simulated in-situ Airborne Acoustic Measurements,* (2018).

[265] International Electrotechnical Commission, *IEC 60318-7:2022 - Electroacoustics - Simulators of human head and ear - Part 7: Head and torso simulator for the measurement of sound sources close to the ear,* (2022).

[266] GRAS Sound and Vibration, *GRAS 40AO 1/2" Prepolarized Pressure Microphone,* (Accessed 20 March 2023).

[267] GRAS Sound and Vibration, *GRAS AA0028 10 m SMB - BNC Cable,* (Accessed 20 March 2023).

[268] International Standardization Organization, *ISO/TS 15666:2021 - Acoustics — Assessment of noise annoyance by means of social and socio-acoustic surveys,* (2021).

[269] Brüel & Kjær, *User Manual Hand-held Analyzer Types 2250 and 2270*, Tech. Rep. (Brüel & Kjær, 2016).

[270] HBK, *Type 4189 - 1/2" free-field microphone, prepolarized,* (Accessed 20 March 2023).

[271] HBK, *Type 4179 - Condenser Microphone,* (Accessed 20 March 2023).

[272] HBK, *Type 2669-L Microphone Preamplifier,* (Accessed 20 March 2023).

[273] JBL, *JBL Flip 5 - Portable Waterproof Speaker,* (Accessed 20 March 2023).

[274] P. D. Welch, *The Use of Fast Fourier Transform for the Estimation of Power Spectra: A Method Based on Time Averaging Over Short, Modified Periodograms,* IEEE Transactions on Audio and Electroacoustics **15**, 70–73 (1967).

[275] International Standardization Organization, *ISO 226:2003 - Acoustics — Normal equal-loudness-level contours,* (2003).

[276] R. Pieren, *Auralization of Environmental Acoustical Sceneries*, Ph.D. thesis, Delft University of Technology (2018).

[277] T. Rossing, *Handbook of Acoustics*, 2nd ed. (Springer, 2007) Chap. 17.

[278] International Standardization Organization, *ISO 3382-3:2012 - Acoustics — Measurement of room acoustic parameters — Part 3: Open plan offices,* (2012).

[279] International Standardization Organization, *ISO 3745:2012 - Acoustics — Determination of sound power levels and sound energy levels of noise sources using sound pressure — Precision methods for anechoic rooms and hemi-anechoic rooms,* (2012).

[280] International Standardization Organisation, *ISO 717-1:2020 - Acoustics — Rating of sound insulation in buildings and of building elements — Part 1: Airborne sound insulation,* (2020).

[281] B. Schäffer, R. Pieren, U. Wissen Hayek, N. Biver, and A. Grêt-Regamey, *Influence of visibility of wind farms on noise annoyance – A laboratory experiment with audio-visual simulations,* Landscape and Urban Planning **186**, 67–78 (2019).

[282] M. Manyoky, U. Wissen Hayek, R. Pieren, K. Heutschi, and A. Grêt-Regamey, *Evaluating a visual-acoustic simulation for wind park assessment,* Landscape and Urban Planning **153**, 180–197 (2016).

[283] Netherlands Aerospace Centre, *Noise simulator,* (Accessed 20 March 2023).

Curriculum Vitæ

Bieke von den Hoff

04-10-1995	Born in Weert, the Netherlands
1999–2007	Primary School Montessori basisschool, Weert, the Netherlands
2007–2013	High School Philips van Horne SG, Weert, the Netherlands *Profile:* Science profile, with additional mathematics and economics (N&T, N&G) *Extra:* English A Language & Literature, standard level (IB)
2013–2016	Bachelor of Science in Aerospace Engineering Delft University of Technology, Delft, the Netherlands *Minor:* Noise and Emissions for vehicles, Kungliga Tekniska Högskolan, Stockholm, Sweden *Thesis:* MIRU: a purpose designed air safety investigation UAV
2016–2020	Master of Science in Aerospace Engineering Delft University of Technology, Delft, the Netherlands *Profile:* Control & Operations, Aircraft Noise and Climate Effects *Gap year:* Full-time voluntary work - board member study association *Thesis:* Assessment of the use of global optimisation techniques for aircraft noise source identification *Graduated cum laude*
2020–2025	PhD in Aircraft Noise Delft University of Technology, Delft, the Netherlands *Thesis:* Introducing sustainable systems in the aviation industry: their impact on noise emissions and annoyance *Promotor:* Prof. dr. ir. M. Snellen *Promotor:* Em. Prof. dr. D.G. Simons *Extra:* PhD council
2023–Current	Head of Acoustics MuTech B.V., Delft, the Netherlands

LIST OF PUBLICATIONS

PEER-REVIEWED JOURNAL ARTICLES

2. A.E. Vieira, **B. von den Hoff**, M. Snellen, D.G. Simons, *Comparison of Semi-Empirical Noise Models with Flyover Measurements of Operating Aircraft*, Journal of Aircraft (2022) 59:6, 1574-1587.

1. **B. von den Hoff**, R. Merino-Martínez, D.G. Simons, M. Snellen, *Using global optimization methods for three-dimensional localization and quantification of incoherent acoustic sources*, JASA Express Letters (online) **2** 054802 (2022).

CONFERENCE CONTRIBUTIONS

8. R. Merino-Martínez, R.M. Yupa Villanueva, **B. von den Hoff**, J.S. Pockelé, *Human response to the flyover noise of different types of drones recorded in field measurements*, Quiet Drones 2024, Manchester, the United Kingdom, (2024).

7. **B. von den Hoff**, R. Merino-Martínez, R.M. Yupa Villanueva, M. Snellen, *Noise Emissions and Noise Annoyance of a Single-propeller Electric Aircraft During Fly-over*, 30th International Congress on Sound and Vibration (ICSV), Amsterdam, the Netherlands (2024).

6. F. Yunus, **B. von den Hoff**, M. Snellen, *Predicting tonal noise of full-electric propeller-driven aircraft in outdoor environments using low-order models*, 30th AIAA/CEAS Aeroacoustics Conference, Rome, Italy (2024).

5. R. Merino-Martínez, I. Besnea, **B. von den Hoff**, M. Snellen, *Psychoacoustic Analysis of the Noise Emissions from the Airbus A320 Aircraft Family and its Nose Landing Gear System*, 30th AIAA/CEAS Aeroacoustics Conference, Rome, Italy (2024).

4. R. Merino-Martínez, **B. von den Hoff**, D.G. Simons, *Design and acoustic characterization of a psychoacoustic listening facility*, 29th International Congress on Sound and Vibration (ICSV), Prague, Czech Republic (2023).

3. R. Merino-Martínez, **B. von den Hoff**, D. Morata, M. Snellen, *Three-dimensional acoustic imaging using asynchronous microphone array measurements*, 9th Berlin Beamforming Conference (BeBeC), Berlin, Germany (2022).

2. **B. von den Hoff**, D.G. Simons, M. Snellen, *Breakdown of propeller aircraft noise by applying conventional beamforming jointly with imaging using the rotating source identifier*, 9th Berlin Beamforming Conference (BeBeC), Berlin, Germany (2022).

1. **B. von den Hoff**, M. Snellen, D.G. Simons, *Noise assessment of taxibotted versus conventional taxiing operations using a phased microphone array*, Inter-Noise 2021, Washington DC/online, USA (2021).

INTERVIEWS

4. D. Ragni, **B. von den Hoff**, F.H. Hartog, *This clever slipper with holes in it makes wind turbines significantly quieter*, TU Delft | Stories, Delft, 2 April 2024

3. H.G.C. Werij, G. Zoppini, X. Wang, R.P. Sampat, C. Borst, **B. von den Hoff**, B.C.P. Jongbloed, K. Masania, R. Vos, *Virtual lab tour Sustainable Aviation at Aerospace Engineering TU Delft*, TU Delft | Faculty of Aerospace Engineering, Delft, 3 February 2023

2. **B. von den Hoff**, X. in 't Veld, R. de Wit, *Hoe stil zijn elektrische vliegtuigen? Dat onderzoekt de TU Delft op Teuge: 'Omwonenden gaan merken dat het stiller wordt'*, de Stentor/Tubantia, Apeldoorn, 11 November 2022

1. **B. von den Hoff**, *Lockdown presents unique opportunity to study sustainable taxiing at Schiphol*, TU Delft | Stories, Delft, 13 July 2020

Acknowledgements

The way to achieve your own success
is to be willing to help somebody else get it first.

Iyanla Vanzant

I used to wonder; was the investment in time, energy, the many lost healthy life years due to stress, the sleepless nights all worth it? But as I write this, at the very end of the PhD, I can say: it was worth it. I learned an incredible lot, about various topics within the larger acoustics field, about conducting research, about knowledge dissemination, but above all, I learned more about myself.

This steep learning curve would not have been possible without the help and support of many people, to which I want to extend my heartfelt gratitude. Please forgive me if I missed someone, some parts of my brain (memory in particular) degraded in the process of this PhD.

Mirjam, thank you for encouraging me to pursue a PhD and allowing me to decide on topics of interest. I truly appreciate your help, throughout scheduled meetings as well as during unscheduled walk-ins during stressful moments on my side. We discussed a broad range of topics that I was interested in, not strictly limited to the topic of my PhD but also to the challenges that come with being a PhD candidate in general.

Dick, thank you for your help over the past few years, even as you retired. I appreciate that even in those last months, you took the time to answer my questions and read the final adjustments to my PhD. Your critical view and focus on details helped me improve many papers.

Fred and Menno, thank you for keeping me safe during experiments at airports! Your reminders of the importance (or actually, lack thereof) of 3rd-decimal-level accuracy helped me make decisions on measurement methods, or on the necessary number of flights. I truly appreciate how the two of you brightened up long measurement days and how you were always available to answer questions on engine details or airframes, even long after I finished the measurements.

To the pilots that helped me, Xander, Hans, and Evert-Jan, thank you for flying many circuits and low-passes over Teuge airport!

Simon, Dirk, and Wouter, thank you for the fun times at Schiphol airport during the TaxiBot research! I still can't believe that I was allowed on airside with my equipment.

Pieter, thank you for your help with propeller noise and cyclostationary sources. I sometimes needed a bit more time to understand the mathematical side of our discussions, but I appreciate that you were always willing to explain it.

Lisette and Marloes, thank you for the help with arranging any forms and documents that were not directly research related, but still very much necessary to actually do the research.

Henri, thank you for supporting me with recommendation letters and taking me seriously on faculty culture matters related to PhDs. Regarding the latter, I felt like you were open to listen and supported me in all the time I spent on advocating PhD rights and issues. Every meeting brought me one step closer to my ambitious goal: a positive and supportive culture for PhDs.

At times, I didn't feel heard or I felt like I had to tell the same story over and over again. At times I felt like everyone thought that change was not going to happen and that I was overly positive or naive. Yet, at the end of the day, all I can say is "at least I tried". I am lucky enough to not be in a vulnerable position, and hence I could speak out for those who couldn't. I will continue doing so when necessary, no matter the consequences, the worries, the time spent.

I believe PhDs are a crucial part of the future of academic institutions. We have to be involved, because if the younger generation is not part of change, we risk losing talent, time, and innovation. We lose our chance to change.

Roberto, you have always supported me and helped me voice concerns to improve social awareness. It was not only verbal, but also by actions. You set a high standard with your collaborative nature and support of others' work! Thank you for always being available to provide feedback and to discuss interesting findings. Attending BeBeC, as the only female participant, together with you was good fun! Thanks for always introducing me to literally everyone or automatically opening up a place to join in a conversation or in a collaboration.

Irina, we have been through many highs and lows together, through endless technical discussions, through endless life discussions. Yet here we are, finishing up our PhD at the same time, because finishing a MSc together was not sufficient struggle. Thank you for being there, always.

Jin, thank you for putting up with my large plant on (y)our desk. It was meant to hide us from potential visitors, but I am not sure that it sufficiently did the job.

Amy, thank you for taking over and improving all things equipment! It was such a relief to no longer be responsible for it all. Your positive mood and happiness were also much appreciated, especially as I was very stressed towards the end of the PhD.

Anique, thank you for supporting me through an intense measurement campaign at Teuge airport. I still feel awkward that we broke the record of noise complaints (twice), but let's hope it advanced science!

To all my colleagues at ANCE, thank you all for the fun breaks and group events! Seemingly unimportant discussions at the coffee machine sometimes sparked new ideas for my research.

While the students I guided have long moved on to jobs elsewhere, I want to thank them for their curiosity. They brought interesting new views on the research and consistently challenged me to improve my explanations.

To the team at MuTech, thank you for sparking my interest with out-of-the-box questions and collaborations on array design. What started out as just helping out, eventu-

ally led to a part-time job, and then a full-time job. I am incredibly grateful that you believed in me and gave me the chance to do a challenging yet rewarding job at MuTech, combined with finishing the PhD. I needed the change of pace and scenery for half of my working days. This dissertation wouldn't have been ready without my job with you; thank you for the incredible opportunity!

To all my housemates, thank you for all the coffee breaks, lunch breaks, and much-needed hugs. It was challenging to start a PhD on March 16, 2020, which marked the start of the first corona lockdown, but being home together made it much more fun. Over the years, some moved out, others moved in, but all of you made it feel like home.

To my friends outside of work, thank you! Having you by my side, to talk about anything and everything, to share laughter and tears, to go on adventures, means the world to me!

To mum and dad, thank you for always being by my side. Thanks for listening to my ups and downs, to the stories of amazing research by someone else, and to the depths of my own work. Your support has been crucial at times when I wanted to quit (but obviously didn't). Maybe you think I am stubborn, that I should have listened more to your advice, but I am pretty sure I got this character trait from both of you.

Ties and Douwe, both of you used to say that I received all "the brains", but you received an unfair share of all other skills in my opinion. Receiving "the brains" has been both a blessing and a burden. It allowed me to help you with reports and study, to hopefully help many people, but at the same time it makes me doubt and overthink more than I would prefer. Luckily, in those difficult times, you two are always there for me with jokes, hugs, and (funny) life advice.

To Philip, I don't even know where to begin to thank you. Thank you for your endless love, thank you for supporting me in chasing my dreams, thank you for being by my side through all the highs and lows, thank you for bringing laughter, positivity, and sunshine to every single day. Thank you for everything!

Bieke von den Hoff
Rotterdam, June 2025

TU Delft